# The molecular beam epitaxy technique for PbSe-based lead chalcogenide diode lasers

Norton, Peter Robert

*Award date:*
1986

*Awarding institution:*
University of Bath

# THE MOLECULAR BEAM EPITAXY TECHNIQUE

# FOR PbSe - BASED

# LEAD CHALCOGENIDE DIODE LASERS

Submitted by PETER ROBERT NORTON for the degree of

Ph.D. of the University of Bath.

1 9 8 6



P.R. Norton





ProQuest LLC
789 East Eisenhower Parkway
P.O. Box 1346
Ann Arbor, MI 48106-1346

To Sue .....

in appreciation of your assistance and endless patience

Abstract

This thesis describes the design, construction and commissioning of a molecular beam epitaxy system to fabricate lead chalcogenide semiconductor diode lasers emitting in the spectral range from 3.5μm to 20μm. The aim of the project is to cover this entire spectral range using a minimum number of alloy compounds, a common substrate and a unified structure. The lasers fabricated are to be optimised for low threshold currents, single mode spectra and high operation temperatures.

Careful system design considerations to grow lead chalcogenide semiconductors by the molecular beam epitaxy method enables different types of lasers to be made from the ternary materials $Pb_{1-x}Sn_xSe$, $PbS_{1-x}Se_x$ and $Pb_{1-x}Eu_xSe$. The best results can be achieved with lasers having graded refractive index confinement layers employing $Pb_{1-x}Eu_xSe$, a material which is used for the first time. This direct band gap alloy system exhibits a large absorption edge shift from 2250 $cm^{-1}$ ($x = 0$) to over 8000 $cm^{-1}$ ($x > 0.15$) thus permitting it's use in short wavelength IR diode laser confinement layers.

The doping of the lead chalcogenides has been achieved by the use of bismuth (n - type) and silver

(p - type) and carrier concentrations of over $10^{19}$ $cm^{-3}$ in both n - type and p - type material has been possible with correspondingly high mobility values of over 500 $cm^2V^{-1}s^{-1}$.

Lasers with wavelengths above 10μm are easier to fabricate than lasers with wavelengths below 10μm. The shortest wavelength achieved in the work presented here is 3.5μm and the longest is greater than 21μm. The highest operation temperature for a laser in continuous operation is 163K whilst for pulsed operation this figure is as high as 270K resulting in the simplification of necessary cooling apparatus associated with such a device used within measurement sytems.

CONTENTS

List of Figures

stimulated emission for a particular value of the quasi - Fermi level separation.

Fig(9). Emission wavelengths either presently or potentially available with III - V and IV - VI heterostructure lasers.

Fig(10). Square potential in a quantum - well heterostructure.

Fig(11). Schematic of the threshold current density dependence upon temperature for single and double heterostructure lasers.

Fig(12). Diagram of a single heterostructure laser.

Fig(13). Distribution of conduction and valence band bands, refractive index and light intensity perpendicular to the p - n junction in a single heterostructure laser under forward bias.

Fig(14). Diagram of a double heterostructure GaAs laser.

Fig(15). Distribution of conduction and valence bands, refractive index and light intensity perpendicular to the p - n junction in a double heterostructure laser under forward bias.

Fig(16). Schematic of the relation between threshold current density and active layer thickness in the GaAs - GaAlAs double heterostructure laser.

Fig(17). Diagram of a five - layer localised gain region heterostructure GaAs laser.

Fig(18). Distribution of conduction and valence bands, refractive index and light intensity perpendicular to the p - n junction in a five - layer localised gain region heterostructure laser under forward bias.

Fig(19). Comparison of threshold current density versus active layer thickness between GaAs - based LGR and DH lasers.

Fig(20). Dependence of threshold current density upon temperature in an LGR structure.

Fig(21). Diagram of a five - layer graded refractive index heterostructure GaAs laser.

Fig(22). Distribution of conduction and valence bands, refractive index and light intensity perpendicular to the p - n junction in a five - layer graded refractive index heterostructure laser under forward bias.

Fig(23). Cross - sectional views of various GaAs - based heterostructure lasers using advanced technology.

Fig(24). Known absorption bands of important gases.

Fig(25). Synthesis reactor with temperature profile for the synthesis of PbS.

Fig(26). Positioning of the ampoules within the temperature profile set for single crystal growth.

Fig(27) Pressure - temperature - composition diagram for the PbSe alloy system.

Fig(28). The sodium chloride crystal structure.

Fig(58). Details of the sublimed lead chalcogenide block formed within the stabilisation phase of a furnace.

Fig(59). Details of the selenium furnace.

Fig(60). Furnace shutter and position in the MBE system.

Fig(61). The shutter effect observed from one of the top three furnaces loaded with PbSe.

Fig(62). Details of the furnaces presently used showing the positioning of the thermocouple to reduce the shutter effect.

Fig(63). The decreased shutter effect resulting from the modified thermocouple position.

Fig(64). The substrate holder assembly.

Fig(65). Heated substrate holder assembly.

Fig(66). Side view of the beam flux monitor.

Fig(67). PbSe film thicknesses measured from a furnace in: a) Port 2; b) port 6.

Fig(68). Thickness distributions from four consecutive runs resulting from PbSe loaded in port 2.

Fig(69). Scanning electron microscope image of a 3µm thick PbSe film grown on cleaved $BaF_2$ at 620K.

Fig(70). Scanning electron microscope image of a 3µm thick PbSe film grown on cleaved $BaF_2$ using a low substrate temperature (570K).

Fig(71). Scanning electron microscope image of a 3µm thick PbSe film grown on a polished PbSe substrate at

620K.

Fig(72). Transmission spectrum of a 2μm thick $BaF_2$ slice.

Fig(73). Absorption spectrum of a 4.8μm thick PbSe layer on $BaF_2$ at300K.

Fig(74). Transmission spectrum of a 3μm thick PbS film on $BaF_2$ at 310K.

Fig(75). Secondary ion mass spectroscopy scan of a four - layer $Pb_{1-x}Sn_xSe$ structure on $BaF_2$.

Fig(76). X - ray diffractometer scan of a four - layer $Pb_{1-x}Sn_xSe$ structure on $BaF_2$.

Fig(77). Absorption edge measurements across a $Pb_{1-x}Sn_xSe$ film grown on $BaF_2$ showing the inhomogeneity of such films.

Fig(78). Secondary ion mass spectroscopy scan of a $Pb_{1-x}Sn_xSe$ structure grown on $BaF_2$ with five different deposition temperatures.

Fig(79). Reactor tube arrangement for thallium doping experiments.

Fig(80). Hole concentration versus silver dopant flux rate in PbSe at 77K and 300K.

Fig(81). Hole mobility versus silver dopant flux rate in PbSe at 300K.

Fig(82). The transmission spectrum of a 3μm thick $Pb_{1-x}Eu_xSe$ film on $BaF_2$ at 300K.

Fig(83). Absorption edge measurements across a

$Pb_{0.98}Eu_{0.02}Se$ film grown on $BaF_2$ showing the inhomogeneity of such films.

Fig(84). Absorption edge in $Pb_{1-x}Eu_xSe$ with varying Eu flux ratios at 77K and 300K.

Fig(85). Carrier concentration for undoped, Bi - and Ag - doped $Pb_{1-x}Eu_xSe$ films at 77K and 300K.

Fig(86). Carrier mobility for undoped, Bi - and Ag - doped Pb1-xEuxSe films at 77K and 300K.

Fig(87). Energy diagrams for Bi - doped $Pb_{1-x}Eu_xSe$ films at temperatures $T_1$ and $T_2$ showing the postulated donor levels within the conduction band.

Fig(88). The idea of a silver acceptor level lying within the valence band at 300K and 77K.

Fig(89). A qualitative explanation of the Ag acceptor level in the $Pb_{1-x}Eu_xSe$ alloy system showing schematically the location of the assumed acceptor gap as a function of the Eu content.

Fig(90). Temperature dependence of the hole concentration in a Ag - doped $Pb_{0.985}Eu_{0.015}Se$ layer.

Fig(91). Temperature dependence of the hole mobility in a Ag - doped $Pb_{0.985}Eu_{0.015}Se$ layer.

Fig(92). The effect of dopant flux ratios upon the carrier concentration of $Pb_{0.985}Eu_{0.015}Se$ layers.

Fig(93). The effect of the dopant flux rate upon the carrier mobility of $Pb_{0.985}Eu_{0.015}Se$ layers.

technique.

Fig(108). Qualitative explanation of the advantage in using $(PbS)_{1-x}(SnSe)_x$ in the active layer with $PbS_{1-x}Se_x$ confinement layers to reduce lattice mismatch.

Fig(109). Schematic of the $PbS_{1-x}Se_x$ / $(PbS)_{1-x}(SnSe)_x$ / $PbS_{1-x}Se_x$ laser structure.

Fig(110). Schematic of the PbS / PbSe / PbSnSe / PbSe / PbS localised gain region laser.

Fig(111). Temperature dependence of the threshold current for the localised gain region laser.

Fig(112). Injected carrier capture in the localised gain region laser showing the spill - over effect at low temperatures due to the lack of phonon interaction.

Fig(113). The graded refractive index laser energy diagram showing the concept of injected electron thermalisation into the active layer.

Fig(114). Schematic of the $Pb_{1-x}Eu_xSe$ graded refractive index lasers using the natural oxide technique for device passivation.

Fig(115). The temperature tuning spectrum of GRIN laser 431,9.

Fig(116). Schematic of the PbSe / $Pb_{1-x}Sn_xSe$ silver - doped DH laser.

List of tables

# 1) THE SEMICONDUCTOR DIODE LASER

## 1.1) Introduction

The work presented in this thesis concerns the molecular beam epitaxy (MBE) technique applied to lead chalcogenides for the fabrication of semiconductor laser diodes emitting in the infra - red region of the optical spectrum.

Chapter 1 introduces the basic theory and characteristics of semiconductor laser diodes based upon the gallium arsenide material system. This serves as an introduction to the field of semiconductor diode lasers and the GaAs material system has been used to indicate the necessary lasing conditions due to the advanced state of the technology concerned with this material. Chapter 2 is a summary of the properties of the materials used in this thesis - the lead chalcogenides. These material systems are well - suited to the MBE technique and, being direct band semiconductors, to the fabrication of diode lasers.

Arguments for using MBE are presented in chapter 3 followed by a description of the MBE apparatus developed by the author with specific emphasis given to the optimisation of design concepts. The performance of

the system is considered in chapter 4 where the properties of the epitaxial layers are described and assessed.

The properties of seven different types of diode lasers fabricated during the course of this project are given in chapter 5. Conclusions and suggestions for improvements in future work are presented in chapter 6. During the course of this work, other MBE work not directly concerned with lasers has been performed. This work will not be described here but a description can, however, be found under the list of author's publications in chapter 9.

## 1.2) Historical development

The concepts of stimulated emission and electromagnetic radiation absorption were founded by Einstein in 1917 [1]. In his work he suggested that atoms could be stimulated to give up or receive energy due to the interaction with electromagnetic radiation.

The first use of the principle to amplify electromagnetic radiation by stimulated emission was made by Weber in 1953 [2]. The principle was discussed further by Basov et al [3] in which the concept of population inversion of energy states was put forward as being a fundamental requirement necessary for the sustained

production of stimulated emission. In 1958 Schawlow et al {4} outlined the difficulties and technical aspects of applying the stimulated emission concept to producing coherent light sources and suggested that the Fabry - Perot interferometer could be employed to produce the required optical feedback required for such laser emission (laser - light amplification by stimulated emission of radiation). In 1960 Maiman {5} demonstrated the first successful laser of any type - the ruby laser, and two years later the first gas laser was demonstrated by Javan et al {6}.

The original concept to produce stimulated emission of photons in semiconductors by the recombination of carriers injected across a p - n junction dates back to 1961 {7}. Population inversion is not in this case produced by radiation from an incoherent light source but through the injection of electrons and holes into a recombination area. Due to the direct conversion of the laser current into coherent light, an extremely high power efficiency and a high output intensity over a narrow band width can therefore be expected in continuous operation. A consequence of the injection principle and the short lifetimes of the injected carriers is that modulation is possible at microwave frequencies through direct modulation of the

device current.

The semiconductor laser has taken a much longer time than other types of laser to become established as a functional and practical device. This has been due to the necessity of building up a new semiconductor technology and overcoming difficult technical problems inherent to the device. The intense stimulated emission and non - radiative processes present in the semiconductor laser produce large rates of energy generation and heat dissipation becomes a difficult problem. In the course of its development, the semiconductor laser has undergone considerable alterations in its design. The simple p - n junction from 1961 has been superceded by structures consisting of several layers of semiconducting materials of different compositions and band gaps.

## 1.3) Stimulated emission and population inversion

Three types of electronic transitions can occur between two energy levels and these are illustrated in Fig(1a) - Fig(1c). The figure shows the absorption, spontaneous emission and the stimulated emission transitions between two energy levels $E_1$ (ground state) and $E_2$ (excited state) [8]. $E_2$ corresponds to a state near the bottom of the conduction band (CB) and $E_1$ to a state near the top of the valence band (VB) of a direct

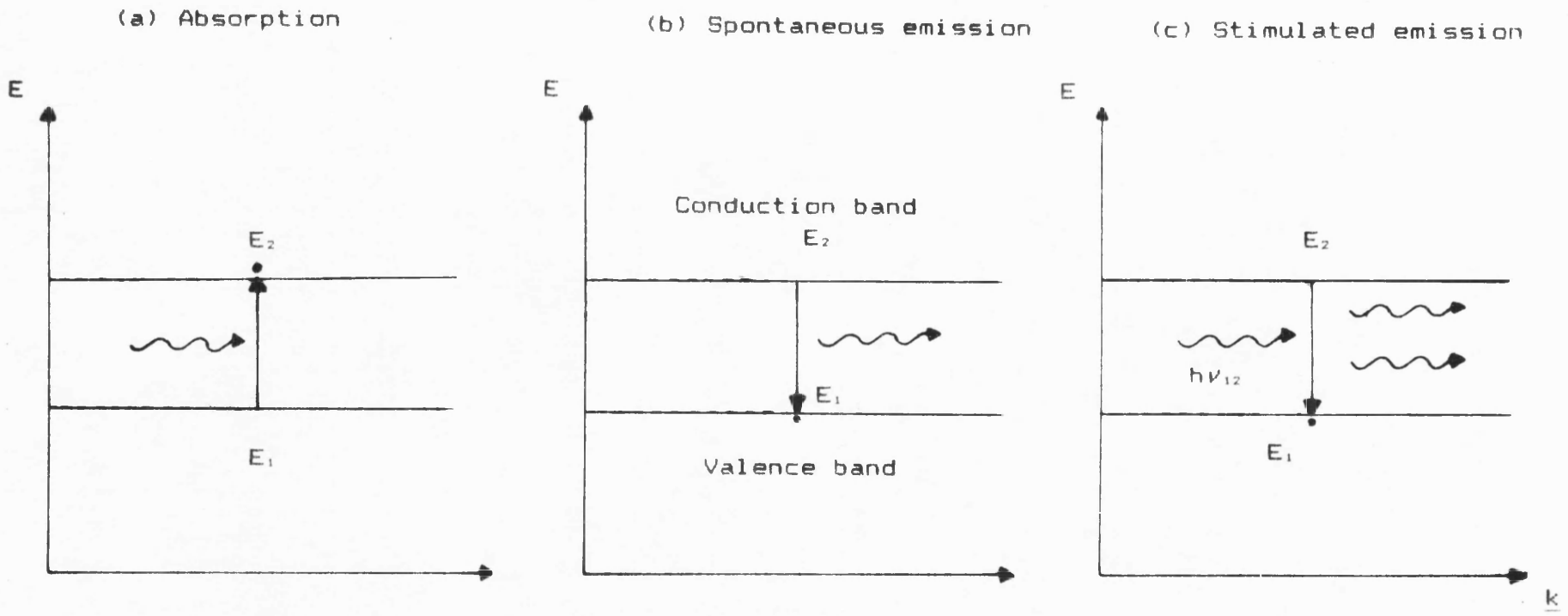


Fig(1). The three basic transition processes between two energy levels $E_2$ and $E_1$.

gap semiconductor. Transitions between these two states involve the emission or absorption of a photon with an energy

$$h\nu_{12} = E_2 - E_1 \qquad (1)$$

where h is Planck's constant and $\nu$ is the photon frequency.

The equilibrium electron distribution is disturbed when a photon having an energy exactly equal to $h\nu_{12}$ impinges upon the system. An electron at $E_1$ is excited to $E_2$ as a result of photon absorption as indicated in Fig(1a). This excited state is shortlived and returns spontaneously to the ground state emitting a photon of energy $h\nu_{12}$ (after $1\times10^{-3}$ - $1\times10^{-8}$ s depending upon the system). This is the process of spontaneous emission (Fig(1b)).

The third transition is that of stimulated emission shown in Fig(1c). Here a photon of energy $h\nu_{12}$ interacts with the system which is in an excited state. In this case, an electron at $E_2$ is stimulated to drop to $E_1$, emitting a photon of energy $h\nu_{12}$ which is in phase with the incident photon. The probability of a particular electron transition with energy $h\nu_{12}$ increases with increasing photon density of energy $h\nu_{12}$.

In thermal equilibrium, the number of systems

with electrons at $E_1$ is very much greater than that at $E_2$. Therefore the absorption process (Fig(1a)) dominates over stimulated emission (Fig(1c)). Population inversion, where the number of states at $E_2$ is greater than that at $E_1$, is required before stimulated emission becomes significant.

The simple two level system shows the basic concept of stimulated emission. A semiconductor, however, has a continuous range of allowed energy levels within the VB and the CB. It is important to note this difference to the two level system since it results in there being different photon energies $h\nu$ contributing to the energy of the laser output radiation.

Population inversion in semiconductors has been accomplished using several excitation methods. The avalanche process of electron - hole pair production through the application of a large current pulse, electron beam irradiation, or optical pumping by an external light source are three methods which have been investigated by various groups of workers {9} - {14}. The most important process for semiconductor lasers is based upon creating population inversion by the injection of electrons and holes across a p - n junction by the application of a forward current.

In a real system, the energy released in an

electronic transition is not always in the form of radiative transitions. Non - radiative transitions involving lattice and impurity interactions often dominate. The materials used in this work exhibit a large non - radiative process probability and hence strong stimulated emission is required for lasing conditions to be satisfied.

## 1.4) Threshold current

A semiconductor that is pumped into an inverted state imparts optical gain to a propagating wave but will not cause laser oscillation until it is enclosed within a suitable optical resonator. The resonator provides the required feedback by reflecting a proportion of the generated photons back into the inverted region.

Fig(2) shows the basic structure of a junction laser in the form of a Fabry - Perot cavity. The criterion to be satisfied for lasing to commence is that the stimulated emission should compensate for the photon loss at the output and elsewhere in the resonator. According to this concept, the coherent laser output shows a threshold current at which the condition of photon balance is first fulfilled. The reflection from the ends of the optical resonator provides maximum feedback at a specific set of optical frequencies which

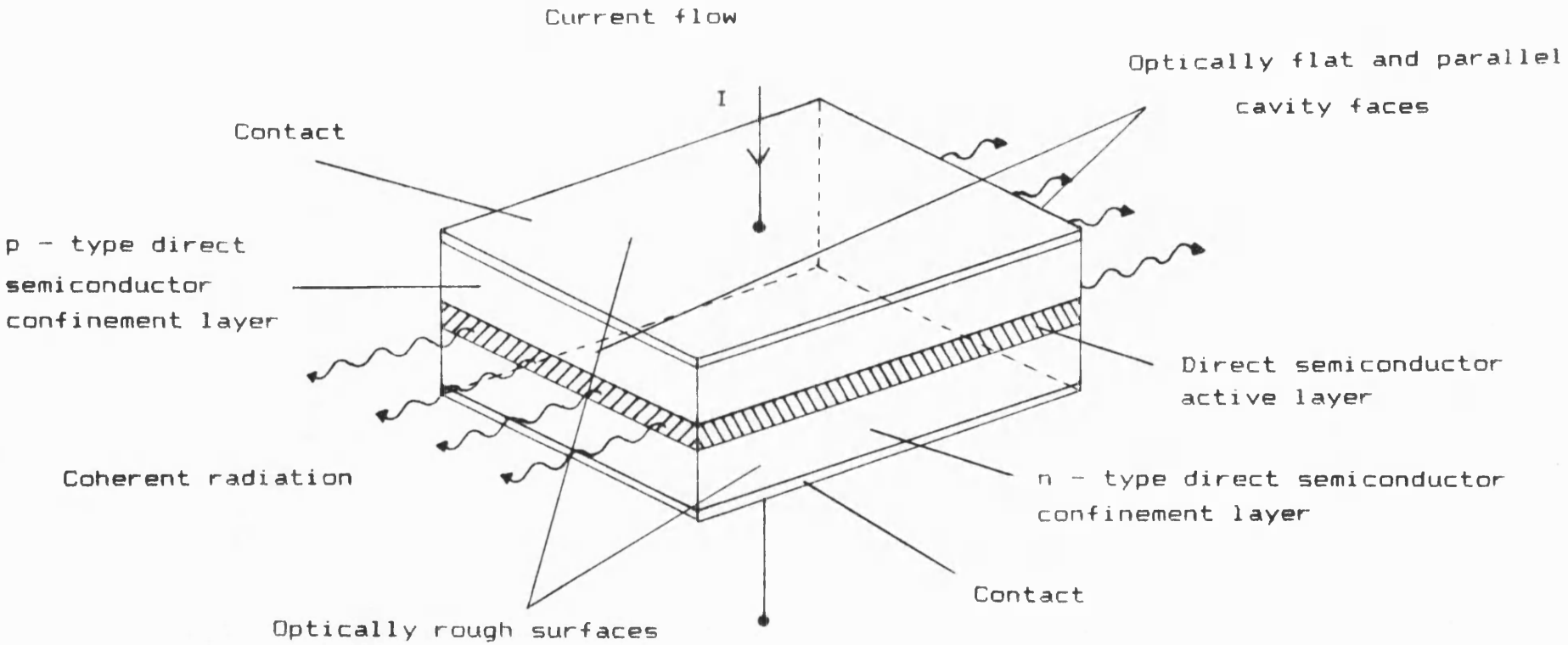


Fig(2). Basic structure of a diode laser in the form of a Fabry - Perot cavity.

give an integral number of half wavelengths within the space between the two ends. This produces emission with a set of radiation modes, each having a different frequency and energy distribution.

An idealised output power - device current characteristic is shown in Fig(3a). No emission is produced until the device current reaches the threshold value where photon balance is achieved. As the current is raised above threshold, the output increases approximately linearly with the current which is the result of a number of different mechanisms. The instantaneous effect of increasing the current is to cause the stimulated emission to exceed the losses from the optical resonator. For a period of approximately 100 ps the photon population builds up and the drain of the increasing stimulated emission lowers the injected carrier rate back to a point where the stimulated emission once again balances the losses. The photon population of the resonator stabilises at a value where the additional photon output compensates the increase in the device pump level. Fig(3b) illustrates the emission spectrum and shows that at threshold the radiation becomes coherent and narrow.

In a semiconductor laser, the pumping is supplied by direct injection of carriers and if all photons lost

Fig(3a). Current - power characteristic of a semiconductor diode laser.

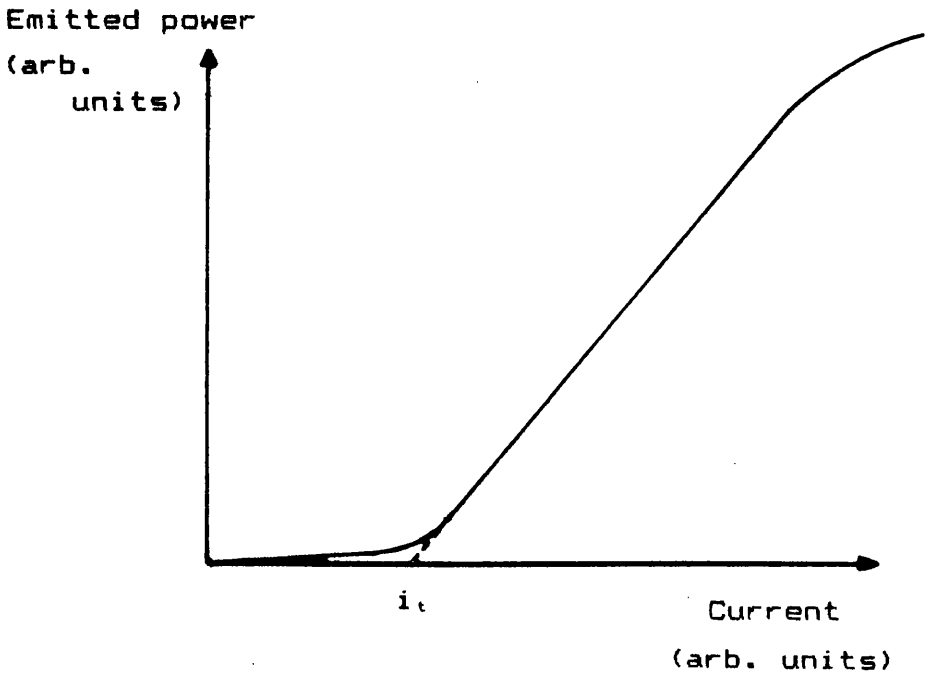


Fig(3b). Spectrum of a GaAs DH laser.

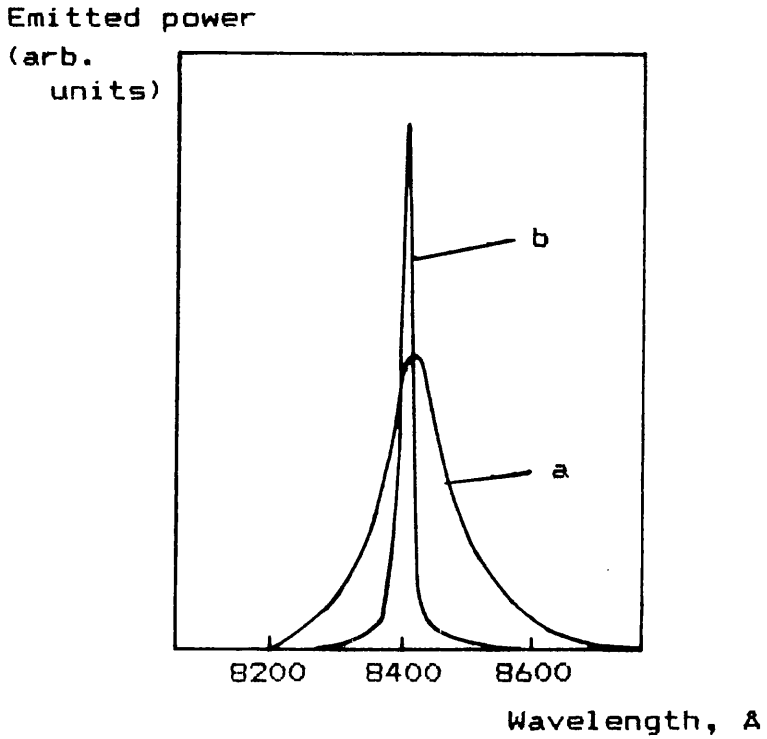


a) incoherent $i < i_t$

b) coherent $i > i_t$

from the resonator appeared in the output, the laser would have a 100% efficiency in converting electrons into photons. Optical losses and light scattering in the resonator reduces this and since these losses are linear, the output of the laser should remain a linear function of the input current.

The peak power capability of a semiconductor laser is determined by the breakdown strength of the output facets since these suffer catastrophic damage when subjected to an optical flux density greater than a critical value {15}. In general, the threshold current depends linearly upon the active layer thickness and hence lasers with relatively high output powers will tend to have high threshold currents due to the necessity of a thick active layer.

The threshold current density in heterostructure diode lasers depends upon two main general factors which will be discussed in more detail in the following two sections. In most laser applications it is an advantage to have a low threshold current density to reduce both energy dissipation and give a lower total operating current. The efficiency with which carriers are injected into, and confined within the active layer, are properties of the heterojunctions themselves and the effect of such mechanisms upon the threshold current density will be

discussed in section 1.7.

1.4.1) Optical gain

The first main factor governing the threshold current density is the magnitude of the optical gain required. An optical wave will experience gain as it passes through an inverted region of a semiconductor as a result of the effect of stimulated emission. When P(z) is the photon flux per unit area and dP(z)/dz is the change in photon flux in the direction z along the resonator axis, the gain of a wave is given by [16]

$$g = \frac{dP(z)}{dz} \quad \frac{1}{P(z)} \qquad (2)$$

Equation 2 has the solution

$$P(z) = P_o \exp(gz) \qquad (3)$$

where $P_o$ is a constant.

In a semiconductor laser the photon flux is not totally confined to the active layer. The confinement layers shown in Fig(2) will also contain a certain percentage of the total photon flux. The ratio of the photon flux within the active layer to the total photon flux is denoted by $\Gamma$ and is called the confinement factor. This gives an average rate of useful stimulated emission equal to $\Gamma r_{stim}$, where $r_{stim}$ is the rate of

stimulated emission within the active layer. The theory deducing $\Gamma$ is outside the scope of this thesis, however, a treatment can be found by Sze {17} in which practical comparisons are made with work from Casey et al {18}. The main conclusion to be drawn from the work is that $\Gamma$ decreases rapidly for active layer thicknesses, d, for $d < \lambda/\Delta n$, where $\Delta n$ is the difference in refractive index between the material in the active layer and that in the confinement layers.

The waves in the laser are enclosed within a cavity to increase the photon density within the active region. Spontaneous and stimulated emission couple to radiation modes which leave the laser in all directions, but predominantly in the direction of the guided modes of the laser axis. This axial beam increases in intensity as it travels back and forth in the active layer, reflected by the mirrors. The optical feedback provided by the cavity converts the system into an oscillator and hence a light source.

The wave takes on a standing wave configuration and Fig(4a) shows a typical distribution along a laser length of the wave intensity. The cavity, length L, only resonates when there is an integral number, q, of half wavelengths bridging the region between the two mirrors. Hence

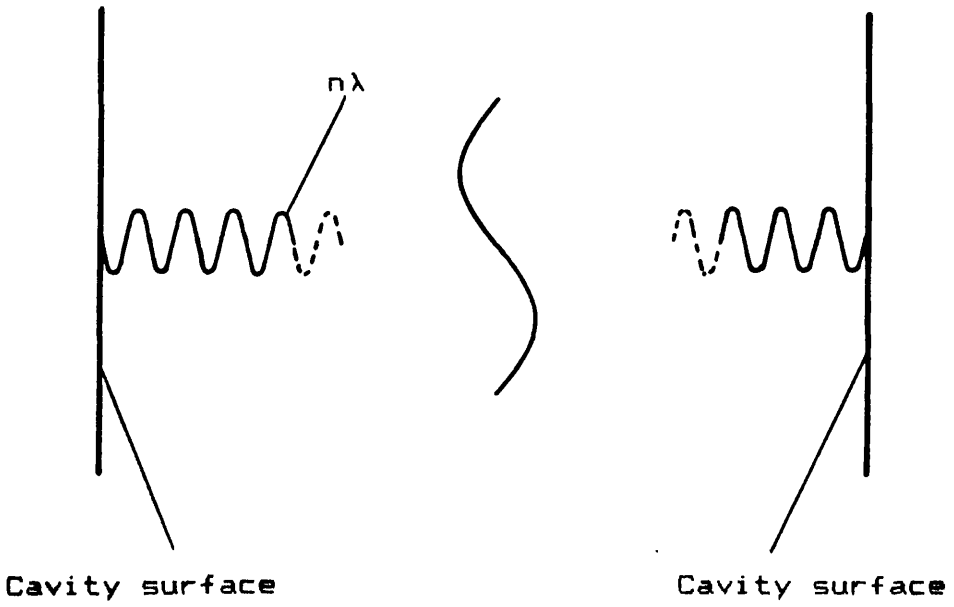


Fig(4a). The Fabry - Perot resonator with an allowed standing - wave form.

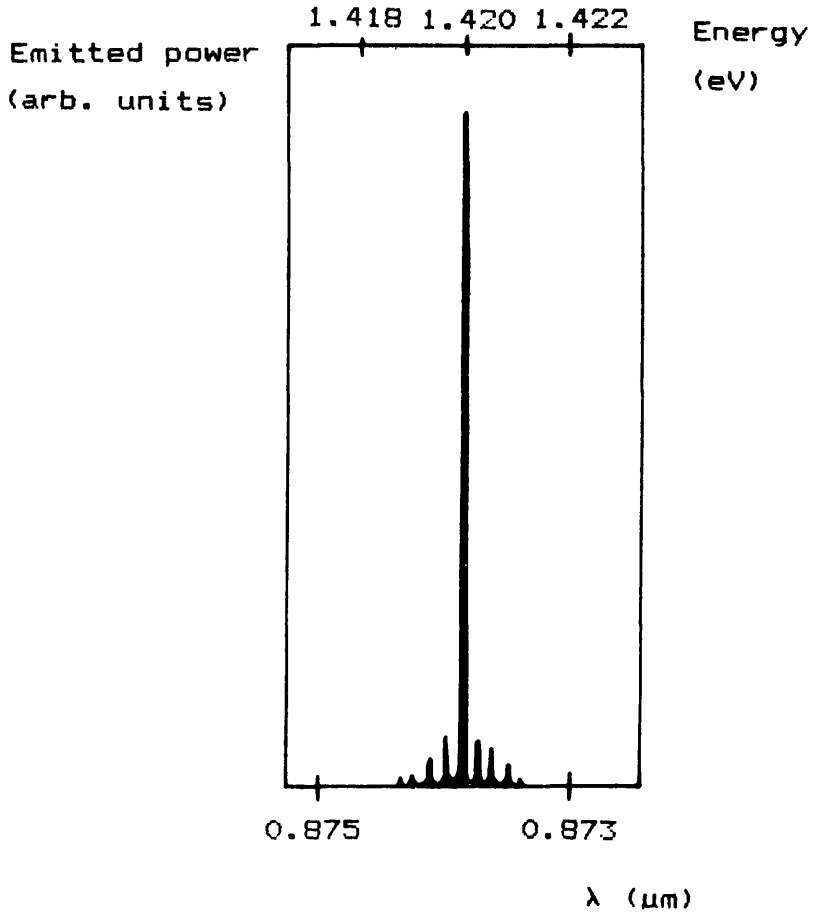


Fig(4b). Relative emission intensity of a GaAlAs - GaAs DH laser at 300K {17}.

$$q\left(\frac{\lambda}{2}\right) = L\ n \qquad (4)$$

where n is the effective refractive index of the layer structure. If $V_w$ is the wave velocity of the mode, c the velocity of light in free space and since $n = c/V_w$, equation 4 can be written

$$\frac{c}{\lambda} = q\left(\frac{V_w}{2L}\right) \qquad \text{Hz} \qquad (5)$$

Therefore, a large number of oscillatory longitudinal modes are possible, each having its own distinct frequency $c/\lambda$. The mode separation is then given by

$$\Delta\left(\frac{1}{\lambda}\right) = \frac{1}{2nL} \qquad \text{cm}^{-1} \qquad (6)$$

Fig(4b) illustrates the intensity versus wavelength characteristic of a diode laser which shows that above threshold one main mode is present. Under the condition where the optical gain is constant over the whole length of the laser, the intensity has an exponential distribution with position z along the laser axis as seen in equation 3. In an adaptation of equation 2 by Pilkuhn {19}, in which the net change in photon flux dP(z)/dz is integrated over a closed path, 2L, an expression is derived for the photon flux distribution along the resonator length. If $\alpha$ is the absorption losses

per unit length due to diffraction, scattering, free carrier absorption and other losses, then

$$P(z)\pm = P_{o}\pm \exp\pm(g-\alpha)z \qquad (7)$$

where the positive and negative subscripts refer to the forward and reverse components of the wave and $P_{o+}$ and $P_{o-}$ are appropriate constants to be determined.

If $R_1$ and $R_2$ are the power reflection coefficients at the two resonator ends the following condition will apply when the end boundary conditions are fulfilled for a wave within the resonator

$$R_1 \exp L(g-\alpha) \times R_2 \exp L(g-\alpha) = 1 \qquad (8)$$

This can be rearranged as follows

$$\exp 2L(g-\alpha) = \frac{1}{R_1 R_2} \qquad (9)$$

From this expression a relation between the nominal gain g and $R_1$, $R_2$ and L can be obtained

$$g = \alpha + \frac{\ln\left(\frac{1}{R_1 R_2}\right)}{2L} \qquad (10)$$

In practice, $R_1 = R_2 = R$ and equation 10 becomes

$$g = \alpha + \left(\frac{1}{L}\right) \ln\left(\frac{1}{R}\right) \qquad (11)$$

If $\beta_{eff}$ is the amplification factor related to the diode laser current ($cmA^{-1}$) then, with a threshold current

density of $i_t$

$$g = \beta_{eff} \times i_t \qquad (12)$$

It follows that

$$i_t = \frac{\alpha + \left(\frac{1}{L}\right) \ln\left(\frac{1}{R}\right)}{\beta_{eff}} \qquad (13)$$

As a means of simplifying equation 13, Lasher and Smith {20} have introduced a characteristic length $L_\alpha$ such that

$$L_\alpha = \frac{\ln\left(\frac{1}{R}\right)}{\alpha} \qquad (14)$$

If $L_\alpha/L >> 1$ then equation 13 now becomes

$$i_t = \left(\frac{\alpha}{\beta_{eff}}\right)\left(1 + \frac{L_\alpha}{L}\right) \qquad (15)$$

Equation 15 shows that the threshold current depends inversely upon the length of the resonator and also upon the natural logarithm of the inverse of the end power reflection coefficients. The end power reflection coefficients are dependent upon the semiconductor refractive index n for the semiconductor - air interface according to the following relationship

$$R = \left(\frac{n - 1}{n + 1}\right)^2 \qquad (16)$$

For completeness, as L approaches infinity, $i_t$ approaches the limiting value of

$$i_t = i_{t\ min} = \frac{\alpha}{\beta_{eff}} \qquad (17)$$

and when $L = L_\alpha$

$$i_t = 2\ i_{t\ min} \qquad (18)$$

The conclusions to be drawn from the above arguements are that to keep the threshold current advantageously low, the following laser design factors should be considered:

a) the cavity length, L, can be extended as implied by equation 15, however a practical limit is reached as far as mode separation is concerned when equation 6 is consulted;

b) equation 15 also shows that the reflection coefficient, R, should be kept as high as possible. Through equation 16 this is seen to be dependent upon the refractive index, n, of the semiconductor;

c) $\Gamma$ can be increased by careful choice of the confinement layers relative to the active region and the active region width;

d) for the case of double heterostructure lasers, the active layer thickness, d, can be reduced. At very small values of d, however, the confinement factor $\Gamma$ decreases and the threshold current increases again;

e) the absorption factor, $\alpha$, can be decreased by

employing purer materials hence reducing free carrier absorption and impurity scattering.

1.4.2) The Bernard and Duraffourg condition

The second factor governing the threshold current density is the way in which the optical gain of the laser active region depends upon injected current densities. To understand these effects it is necessary to discuss the density of states and occupation probability of a semiconductor to find the required electrical condition for stimulated emission. It is only then that conclusions over the threshold current can be drawn.

The CB and VB of a direct gap semiconductor are shown in Fig(5) as functions of energy in momentum space or $\underline{k}$ space. The parabolic form of the bands illustrates the allowed $E - \underline{k}$ relations for electron states in the CB and VB. Band theory shows that the electrons and holes in bands generally have values of effective masses that are different to that of a free electron. These are $m^*_c$ and $m^*_v$ respectively. If $E_c$ is the bottom of the CB and $E_v$ the top of the VB, then the $E - \underline{k}$ relation for the CB states is given by {21}

$$(E - E_c) = \frac{h^2 k^2}{8\pi^2 m^*_c} \qquad (19)$$

and for VB states is given by

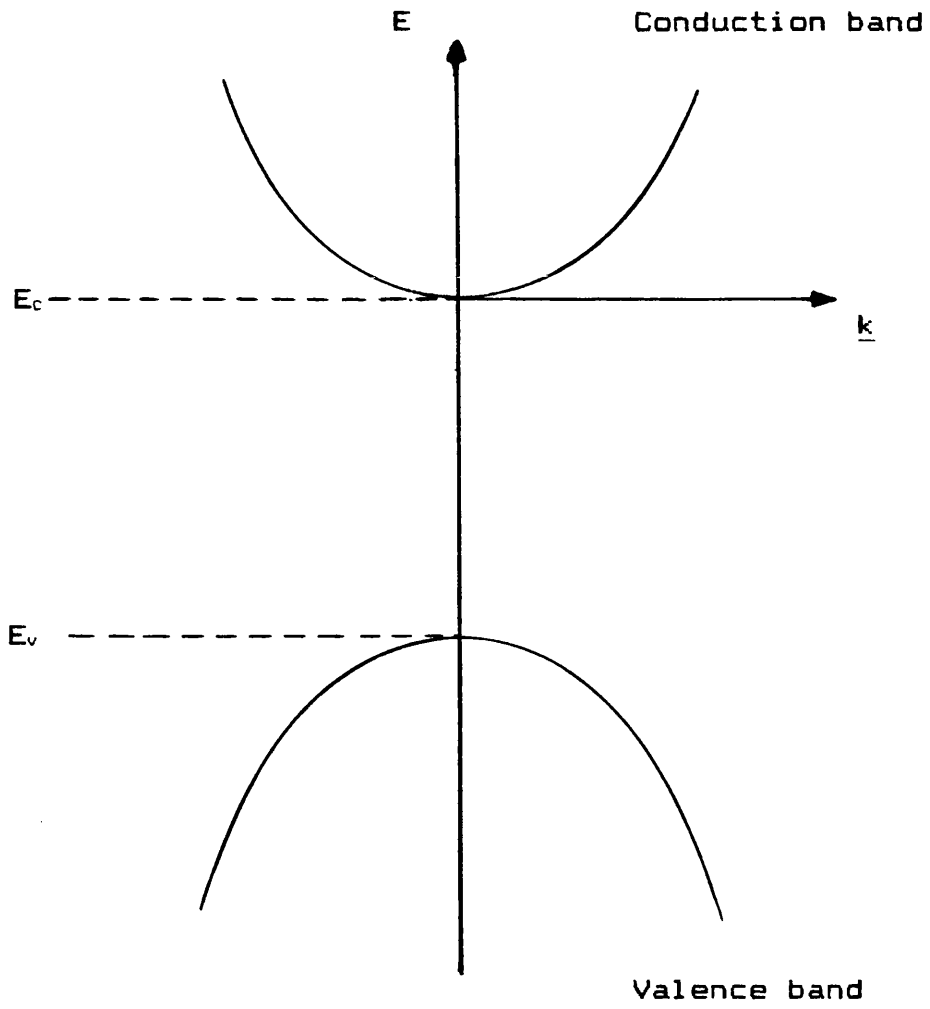


Fig(5). E/k diagram of an intrinsic semiconductor. showing $E_c$ and $E_v$.

$$(E_v - E) = \frac{h^2 k^2}{8\pi^2 m^*_v} \qquad (20)$$

The distribution of electrons in the conduction band and in the valence band of a semiconductor can be expressed in terms of the density of states $p(E)$ at any particular energy E and the fractional occupation of the states F(E). The occupation of energy states is determined by Fermi - Dirac statistics since electrons are subject to the Pauli exclusion principle which prevents more than one electron occupying an identical state. The Fermi - Dirac distribution function is given by

$$F(E) = \frac{1}{1 + \exp\left(\frac{E - E_f}{kT}\right)} \qquad (21)$$

where k is the Boltzmann constant, T the absolute temperature and $E_f$ the Fermi energy. If it is true that $\exp((E_c - E_f)/kT) \gg 1$, then the concentration of electrons in thermal equilibrium can be expressed by

$$n = N_c \exp\left(-\frac{E_c - E_f}{kT}\right) \qquad (22)$$

$N_c$ is the effective density of states in the CB {22}. Similarly for holes in the valence band

$$p = N_v \exp\left(-\frac{E_f - E_v}{kT}\right) \qquad (23)$$

where $N_v$ is the effective density of states in the VB.

The density of states per unit energy for electrons in the CB and the VB within a semiconductor are given by [23]

$$p_c = \frac{8\pi\, m^*_c \sqrt{2m^*_c\,(E - E_c)}}{h^3} \qquad (24)$$

and

$$p_v = \frac{8\pi\, m^*_v \sqrt{2m^*_v\,(E_v - E)}}{h^3} \qquad (25)$$

Fig(6) illustrates the Fermi Dirac function, the carrier concentrations and the density of states for an intrinsic, an n - type and a p - type semiconductor.

It can be seen from equations 24 and 25 that the density of states in the two bands is proportional to $m^{*3/2}$ and hence the difference between the electron and hole effective masses can lead to conduction band and valence band density of states diagrams showing large anti - symmetrical properties.

High injected carrier concentrations and, in particular, high doping modifies the distributions described by equations 22 and 23. It is therefore important to see how these properties effect the condition for stimulated emission in a semiconductor.

Fermi - Dirac statistics describes the occupation of the available states in terms of the Fermi energy. If the average proportion of occupied states in the

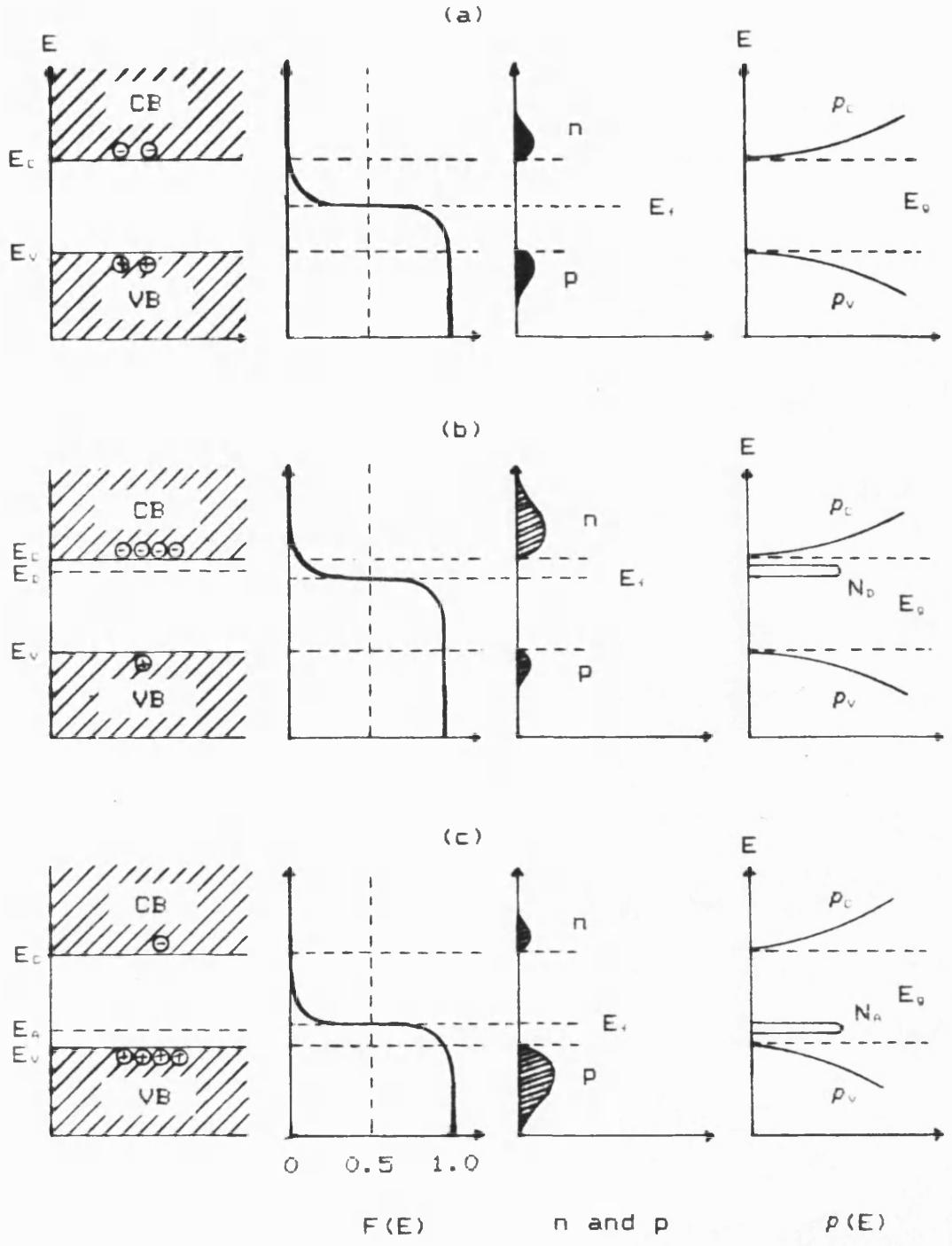


Fig(6). Schematic band diagram, Fermi - Dirac distribution, carrier concentrations and density of states for: (a) intrinsic; (b) n - type; (c) p - type semiconductors at thermal equilibrium and room temperature.

conduction band at some particular energy is $f_c$ and that in the valence band is $f_v$ then, when there is thermal equilibrium between the two bands, a single Fermi level exists. Injection of minority carriers into one or both bands upsets this equilibrium. If, however, the injection rate is not too large, the carriers in each of the bands can keep in close equilibrium with one another and two different Fermi levels can be defined in such a way so as to give a good approximation to the distribution of carriers within the bands. These are called the quasi - Fermi levels and are denoted $F_c$ and $F_v$ for the conduction band and the valence band respectively. The occupation factor F(E) for CB states is given by

$$F(E) = \frac{1}{1 + \exp\left(\frac{E - F_c}{kT}\right)} \qquad (26)$$

and for VB states

$$F(E) = \frac{1}{1 + \exp\left(\frac{E - F_v}{kT}\right)} \qquad (27)$$

The quasi - Fermi levels $F_c$ and $F_v$ represent the energy levels where the states are 50% occupied. Fig(7) is a schematic of the energy versus density of states in an inverted semiconductor for the two cases $T << E_g/k$ and $T = E_g/k$ showing the concept of the quasi - Fermi levels $F_c$ and $F_v$ [24].

Consider a transition from the state $E_1$ in the VB

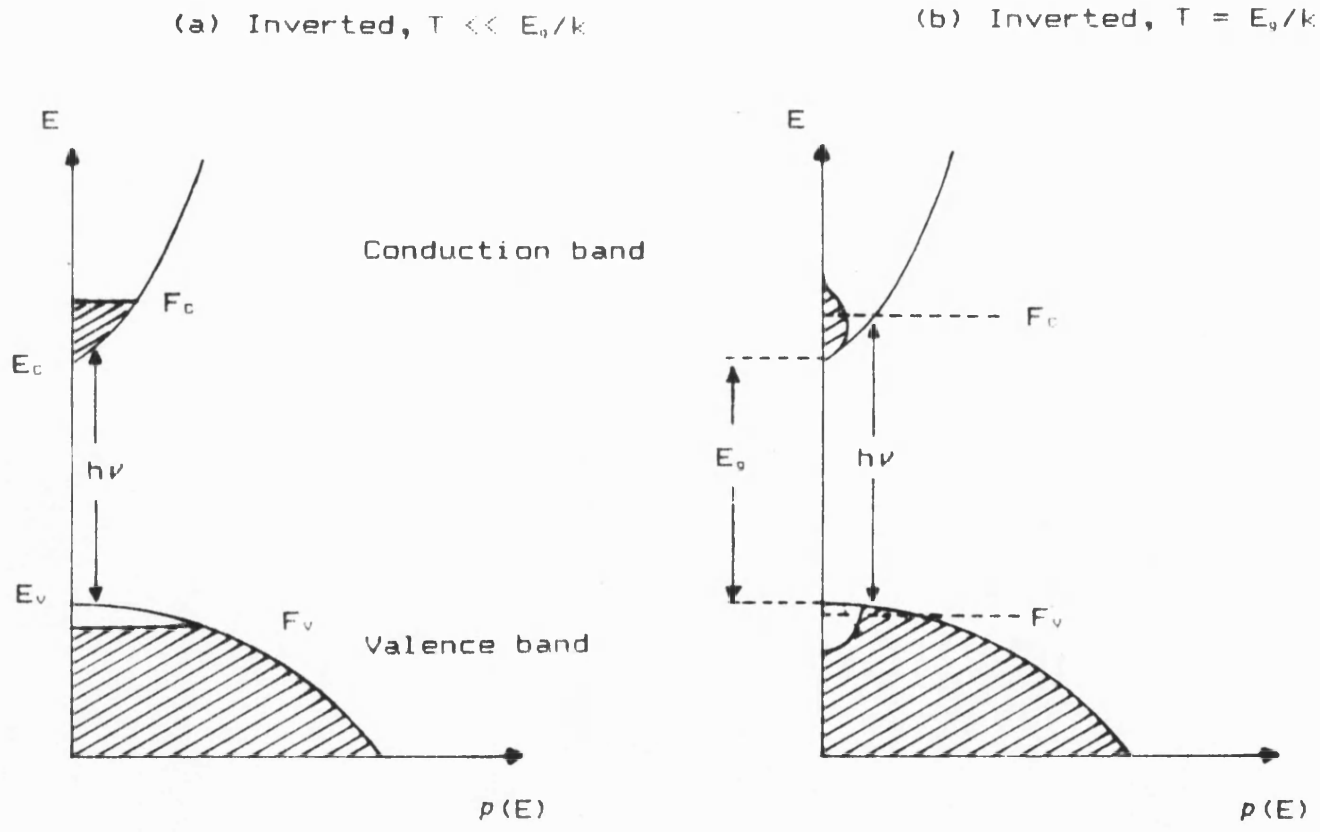


Fig(7). Energy versus density of states in a semiconductor (24).

to $E_2$ in the CB occuring due to absorption of a photon of energy $E_2 - E_1 = E_t$. The rate for this process depends upon the following factors:

a) the transition probability $B_{12}$;

b) the density of photons, energy $E_t$, $P(E_t)$;

c) the probability that the initial state $E_1$ contains an electron $F(E_1)$;

d) the probability that the final state $E_2$ is empty $[1-F(E_2)]$.

The upward transition rate, $r_{12}$, is

$$r_{12} = B_{12} F(E_1) [1-F(E_2)] P(E_t) \qquad (28)$$

Similarly, the photon can produce stimulated emission of a photon by the transition of an electron from $E_2$ to $E_1$. If $r_{21}$ is the downward transition rate, then

$$r_{21} = B_{21} F(E_2) [1-F(E_1)] P(E_t) \qquad (29)$$

For completeness, electrons at $E_2$ can also return to $E_1$ spontaneously and if $A_{21}$ is the transition probability, then this process can be written as

$$r_{21\ (spon)} = A_{21} F(E_2) [1-F(E_1)] \qquad (30)$$

Stimulated emission occurs when $r_{21} > r_{12}$ and using 28 and 29,

$$B_{21}F(E_2)[1-F(E_1)]P(E_t) > B_{12}F(E_1)[1-F(E_2)]P(E_t) \quad (31)$$

Using the Einstein relation that $B_{12} = B_{21}$, equation 32 becomes

$$F(E_2)\ [1-F(E_1)] > F(E_1)\ [1-F(E_2)] \quad (32)$$

Using equations 26 and 27

$$\exp\left(\frac{F_c - F_v}{kT}\right) > \exp\left(\frac{E_2 - E_1}{kT}\right) \quad (33)$$

or

$$F_c - F_v > E_2 - E_1 \quad (34)$$

The minimum value for this transition is $E_2 - E_1 = E_g$ and hence equation 35 reduces to the Bernard and Duraffourg condition {7}

$$F_c - F_v > E_g \quad (35)$$

The E/$\underline{k}$ diagram in Fig(8) illustrates the concept of the above condition. Typical values of the Fermi energies are indicated and the range of transitions is shown that can produce net stimulated emission.

In a semiconductor laser, therefore, the gain depends upon the energy - band structure and is a complicated function of doping levels and temperature. As

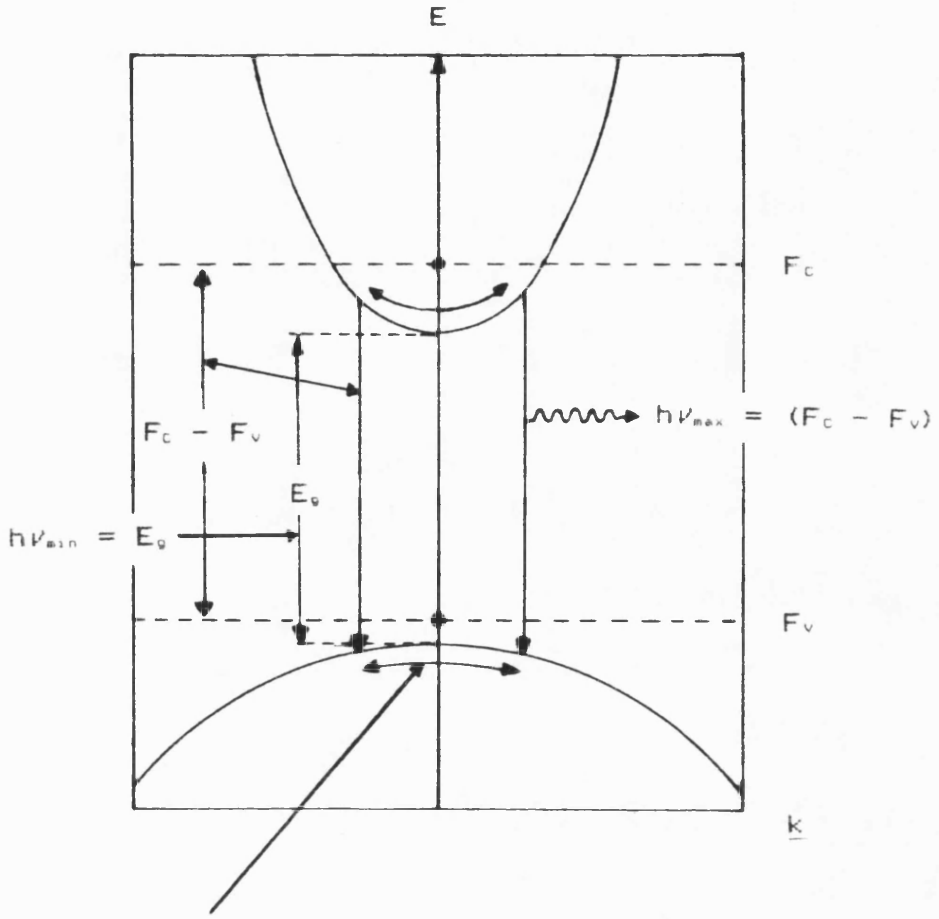


Fig(8). Illustration of lasing condition in a semiconductor showing range of $\underline{k}$ for transitions with net stimulated emission for a particular value of the quasi - Fermi level separation.

the forward current is increased, the quasi - Fermi levels $F_c$ and $F_v$ change, leading to increased gain and an increased range of possible emission frequencies.

It is possible to calculate the electron and hole concentrations at zero gain for any initial doping level. The calculations can then be used to find suitable doping levels to minimise the threshold current density. In the gallium arsenide system, for example, it is found that due to the density of states in the CB being less than that in the VB, n - doping should considerably reduce the threshold current density whereas p - doping should have little effect.

## 1.5) Laser Emission frequency

It has been discussed above that the state of population inversion is necessary for laser emission to be possible in a semiconductor and that this can be achieved by injecting carriers across a p - n junction into a recombination region. Equation 36 describes the condition in terms of the difference between the two quasi - Fermi levels present in the CB and the VB. The laser emission frequency, therefore, is dependent upon this difference which is approximately the band gap $E_g$ of the active recombination region. The active layer of a diode laser, therefore, controls the emission frequency which can be influenced by the following aspects:

a) The use of a mixed crystal system $X_{1-x}Y_xZ$ gives the opportunity through the choice of x of producing a variety of frequencies between those of the two binary materials XZ and YZ due to the composition dependence of the band gap $E_g$. Fig(9) presents the emission frequencies which are either available or potentially available with III - V and II - VI compound semiconductor lasers {18}. The list of materials being used for laser diode work is expanding and there are a whole number of new materials to be investigated.

b) The band gap of a material is in general temperature dependent and enables, through the control of the laser temperature, the emission frequency to be tuned about the wavelength controlled by the active layer composition. The tuning rate will depend upon the material band gap temperature coefficient $dE_g/dT$.

c) A significant range of emission frequency tuning can also be achieved through control of the diode current. As more current and hence power is delivered to the device, Joule heating occurs and the diode temperature will increase. This has the effect of changing the band gap of the active layer and the emission frequency will change as described above.

d) If the thickness of the active layer is reduced to the order of the de Broglie wavelength, $\lambda = h/p$, where h

Fig(9). Emission wavelengths either presently or potentially available with Ⅲ - Ⅴ and Ⅳ - Ⅵ heterostructure lasers (18).

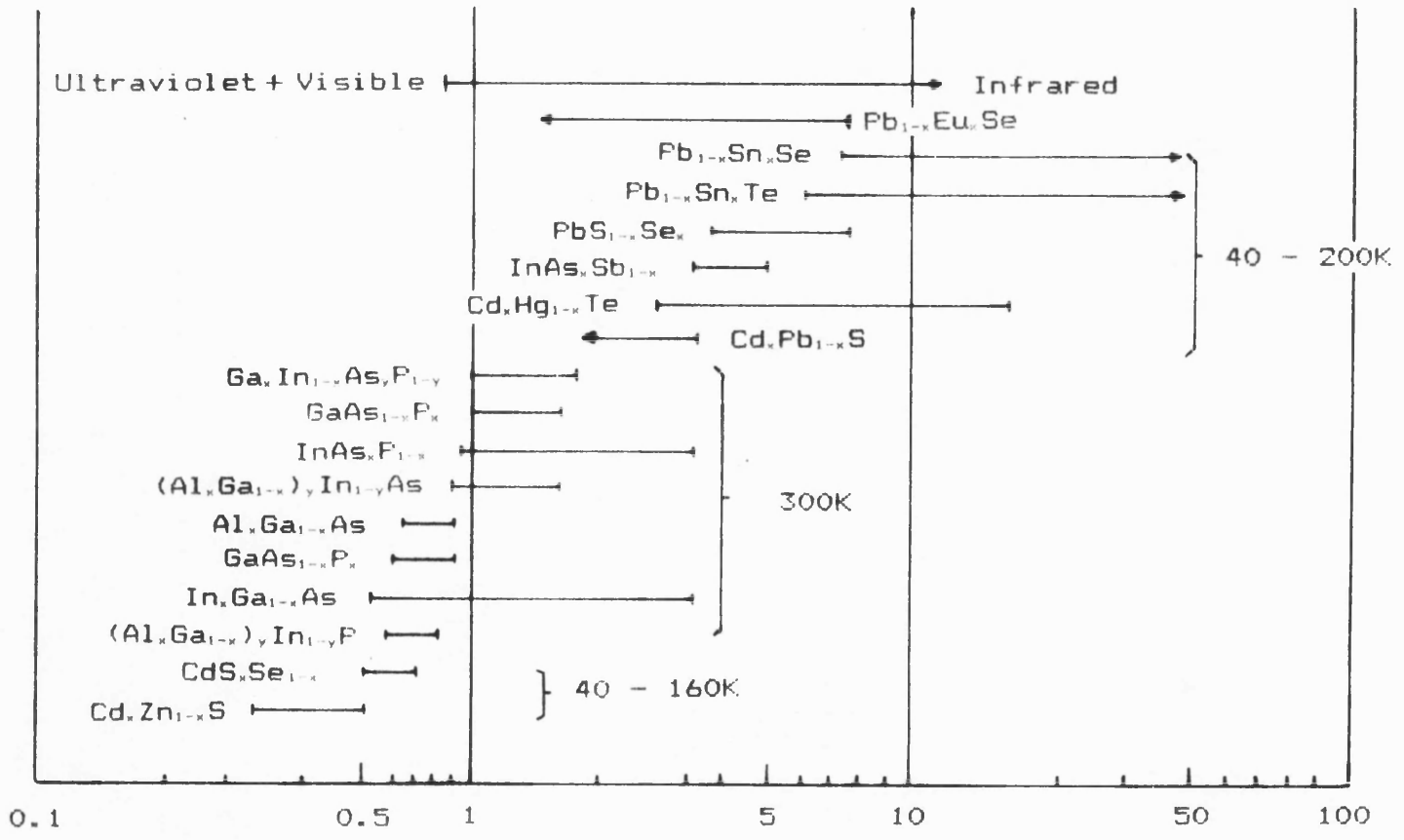

is Planck's constant and p the electron momentum, two - dimensional quantisation occurs and results in a series of discrete energy levels given by the bound - state energies of a finite square well. Fig(10) schematically shows the concept of the quantum well in which the energy eigenvalues are designated by $E_{e1}$ and $E_{e2}$ for electrons and $E_{h1}$ and $E_{h2}$ for holes (25). Interband recombination transitions ($\Delta n = 0$ selection rule) occur from a bound state in the CB (for example at $E_{e1}$) to a bound state in the VB (for example at $E_{h1}$). The energy of the transition is given by

$$h\nu = E_{g2} + E_{e1} + E_{h1} \qquad (36)$$

Thus the recombination can occur between two energy levels in contrast to a bulk semiconductor. The thin active region under the quantum effect, therefore, produces emission frequencies that would normally be emitted from a material with a larger band gap.

Aspects a) - d) enable lasers to be fabricated which can cover a large range of pre - determined frequencies without the need to change the semiconductor composition.

## 1.6) Temperature effects upon threshold current

Section 1.4.2 shows that temperature affects the

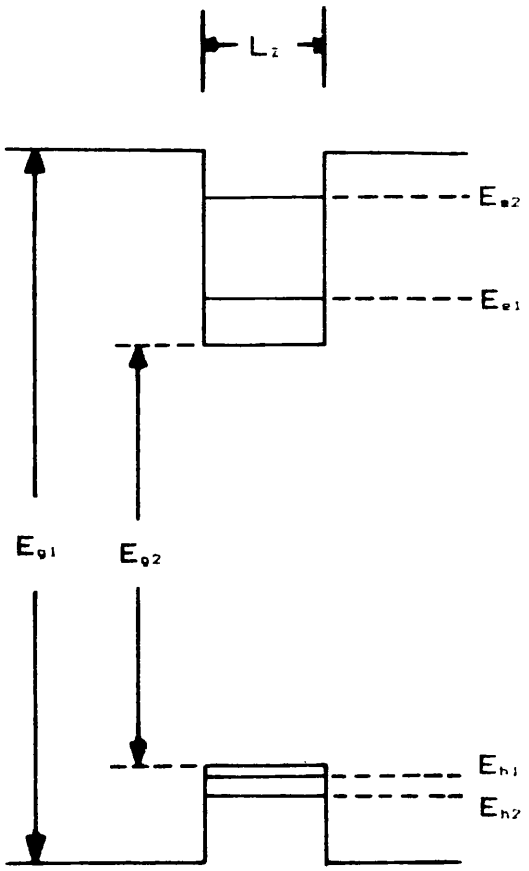


Fig(10). Square potential in a quantum - well heterostructure {25}.

threshold current density. This dependence results from a combination of the fundamental temperature variation of the gain / current characteristic of the active layer with various other temperature dependent mechanisms associated with the particular structures such as carrier and optical confinement. Typical variations of two types of laser are shown in Fig(11) {26}. Empirically a law of the form

$$i_t \propto \exp\left(\frac{T}{T_o}\right) \qquad (37)$$

often applies where T is the heat - sink temperature and $T_o$ a device - specific constant which can be experimentally evaluated {27}. The temperature dependence of the various laser types will be dealt with in more detail in the following section.

## 1.7) Diode laser structures

The work presented in chapter five covers double heterostructure (DH) lasers, localised gain region (LGR) lasers and graded refractive index (GRIN) lasers fabricated from lead chalcogenides. These types of semiconductor lasers are introduced in sections 1.7.2 to 1.7.4 in which the the physical appearance and expected characteristics are described for the gallium arsenide (GaAs) - based system. GaAs and its ternary and

Fig(11). Schematic of the threshold current density dependence upon temperature for single and double heterostructure lasers. Values of $T_o$ are taken from GaAs laser structures (26).

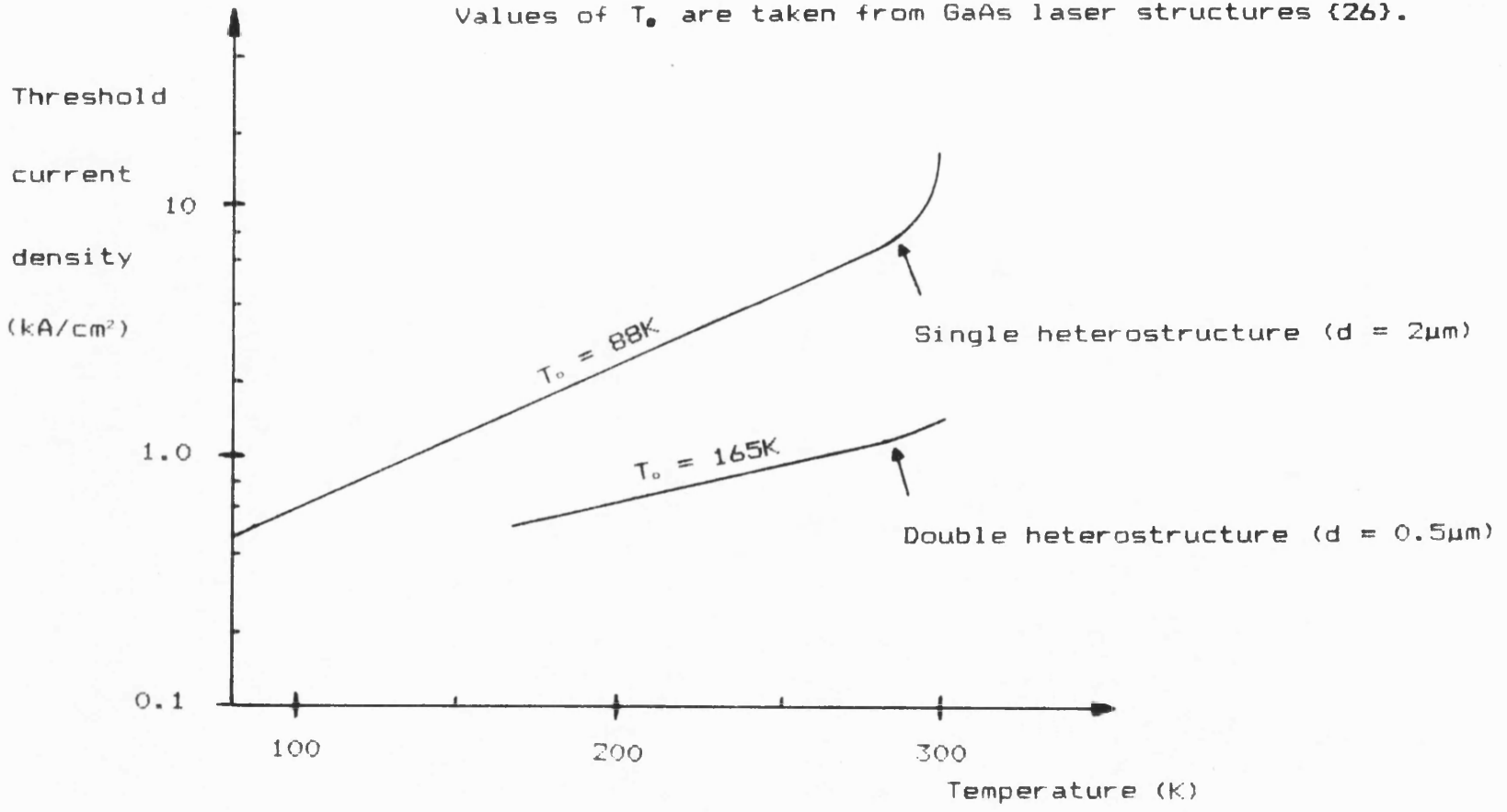

quaternary compounds are well - documented and in the following sections, these materials will be referenced, giving a basis for the interpretation of lead chalcogenide lasers grown by the author. Section 1.7.1 introduces the basic concept of the heterostructure in the form of the single heterostructure (SH) laser.

### 1.7.1) Single heterostructure laser (SH)

Kressel and Nelson {28} and Panish et al {29} introduced the single GaAs heterostructure (SH) laser in 1969. The SH laser is shown in Fig(12) and is physically the simplest device described in connection with this work.

The central region of the laser has one wider band gap layer lying adjacent to it. A p - n junction is formed in the smaller band gap material and the heterojunction is placed at a distance away on the p - side where it can prevent the unrestricted diffusion of electrons injected into the p - layer. This provides an optical waveguide resulting from the barrier due to the bandgap and refractive index differences between the two materials. The p - n junction itself provides the second injecting contact and the other boundary of the waveguide. To achieve satisfactory confinement, the n - side of the junction must be highly doped. The band

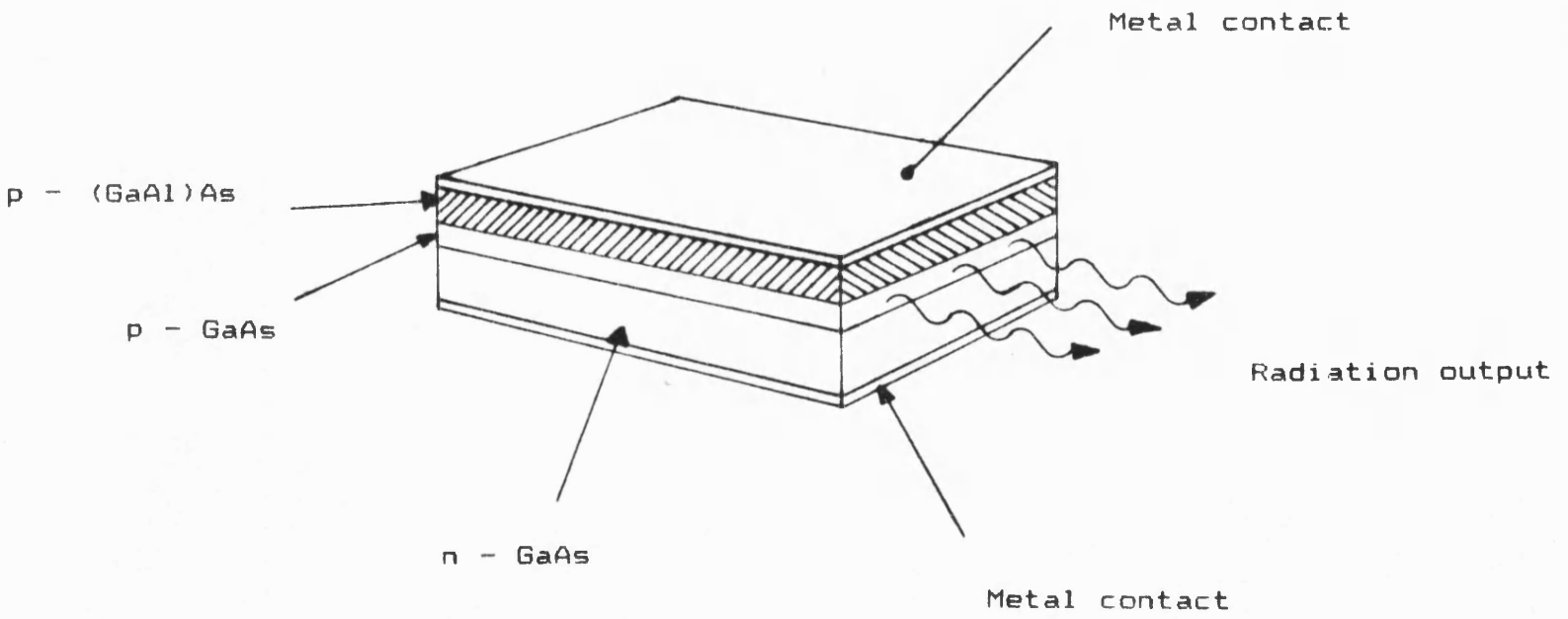


Fig(12). Diagram of a single heterostructure GaAs laser.

diagram under forward bias and the distributions of refractive index n and light intensity I are shown in Fig(13).

The use of a single heterostructure yields a relatively low injection efficiency of electrons and produces an asymmetric optical waveguide. The lower limit for the threshold current density is set by the minimum thickness to which the p - type layer may be reduced before optical guiding and the injection efficiency at the p - n junction become unsatisfactory. This minimum is of the order of 1μm. A lower threshold current density can be achieved in more elaborate structures as described below.

### 1.7.2) Double heterostructure laser (DH)

In the double heterostructure (DH) laser the active layer is sandwiched between n - and p - type layers of larger band gap material. The DH laser is shown schematically in Fig(14). The first reported successful operation of such a structure was a GaAs device made by Alferov in 1970 {30}.

Fig(15) shows the band energy diagram under forward bias and the distributions of the refractive index and light intensity in a DH laser. Optical confinement deteriorates when the thickness of the

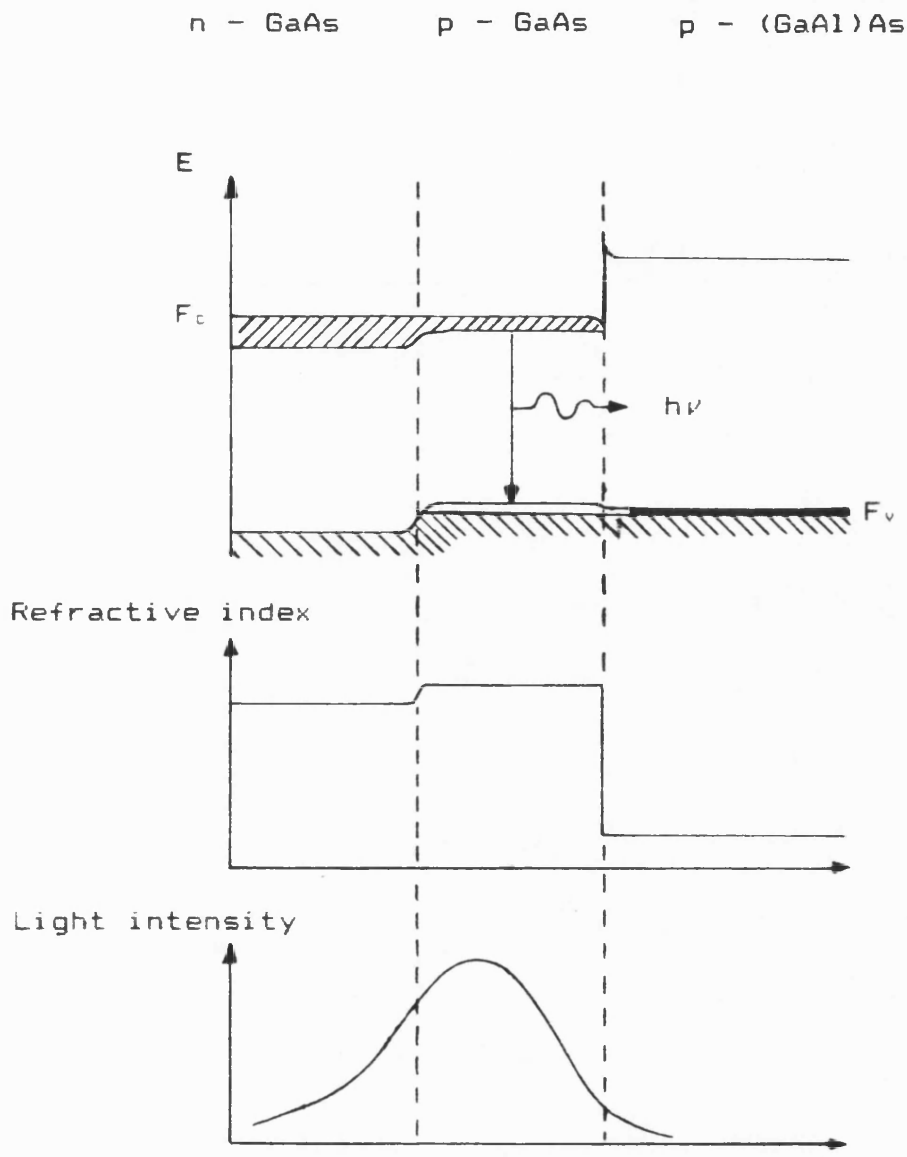


Fig(13). Distribution of conduction and valence bands, refractive index and light intensity perpendicular to the p - n junction in a single heterostructure laser under forward bias.

central active layer is reduced below a certain critical value. The critical value can be made smaller by increasing the refractive index difference between the active and confinement layers. It is this optical guiding effect which sets the lower limit to the possible threshold current density.

Fig(16) shows the expected relationship of the threshold current density to the active layer thickness (d). For large values of d (> 0.5μm) the behaviour is a straightforward linear dependence between the threshold current density and d as discussed in section 1.3.1. As d is reduced the confinement factor Γ of the optical distribution decreases and for d less than about 0.2μm, the threshold current density increases with a further reduction of d. The minimum threshold current density occurs at an appreciably smaller value of d than does the minimum optical spread on account of the non - linear gain / current characteristic {31}.

### 1.7.3) Localised gain region laser (LGR)

It can be an advantage to construct heterostructures in which the injected carriers are confined to a narrow part of the total region in which the light is confined. The light is as closely confined as the wave guiding structure allows but a further

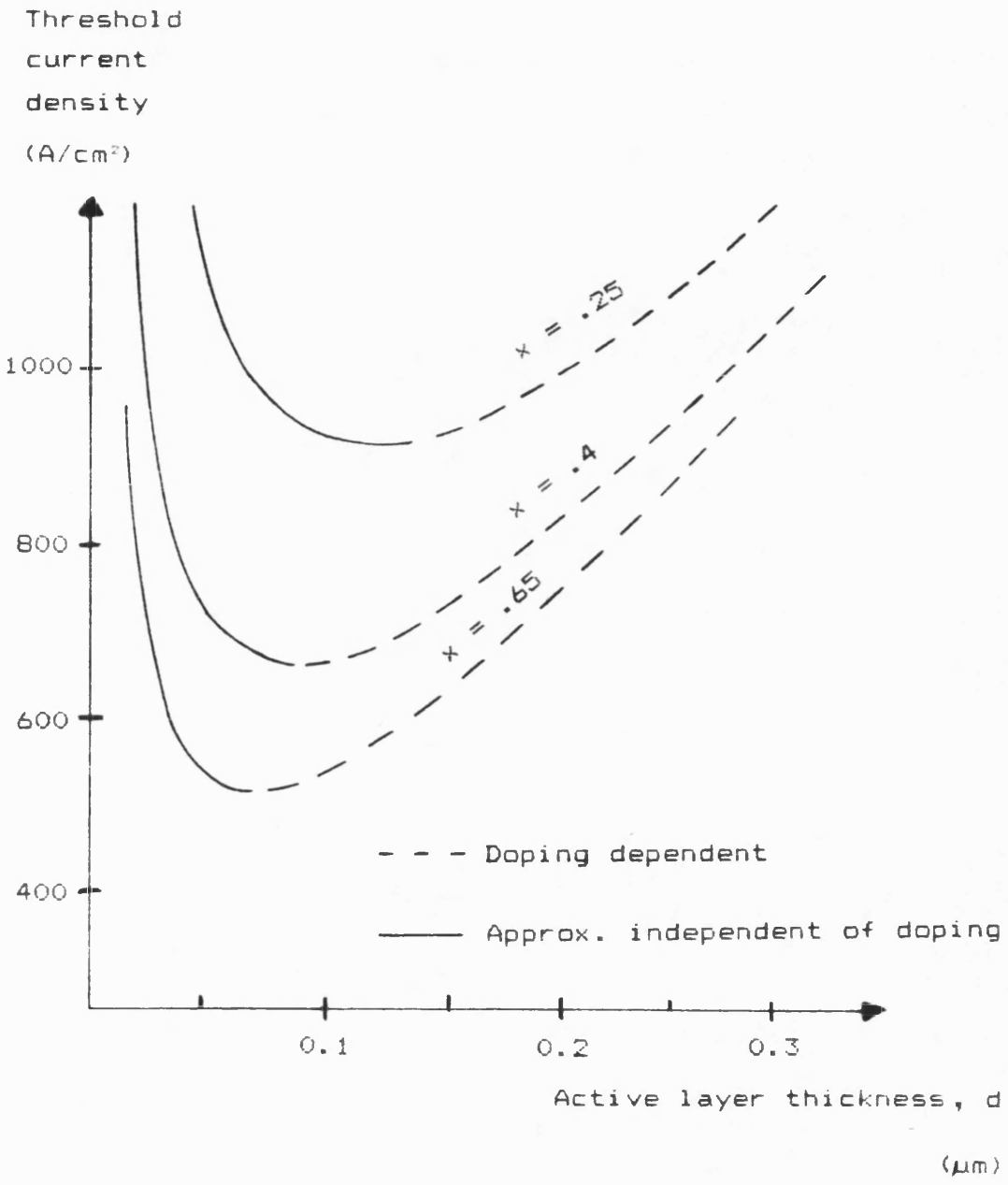


Fig(16). Schematic of the relation between threshold current density and active layer thickness in the GaAs - $Ga_{1-x}Al_xAs$ double heterostructure laser.
The different curves are for different $Ga_{1-x}Al_xAs$ compositions {31}.

reduction in the threshold current density is obtained by confining the injected carriers to an even narrower layer. The threshold current density can be drastically reduced {32} or the LGR form can be used to increase output power with similar threshold currents to that of the DH laser {33}.

The type of LGR laser investigated with regards to this work is a five - layer device in which the inner heterojunctions are used for carrier confinement and the outer heterojunctions are used for optical confinement. Fig(17) shows the structure of such a device using GaAs and Fig(18) is a schematic of the distributions perpendicular to the junction of the CB and VB, refractive index and light intensity.

In Fig(19) the dependence of the threshold current density upon the active layer thickness d is shown. The critical thickness for optical confinement in this structure can be avoided due to the carriers being confined in the narrow inner cavity. Here the active layer can be made very thin in comparison to that of the DH laser thus enabling the threshold current to be maintained at a low level. Fig(20) illustrates the temperature dependence of the threshold current density. In the LGR the increase in threshold current density is expected to be similar to that of a DH laser with good

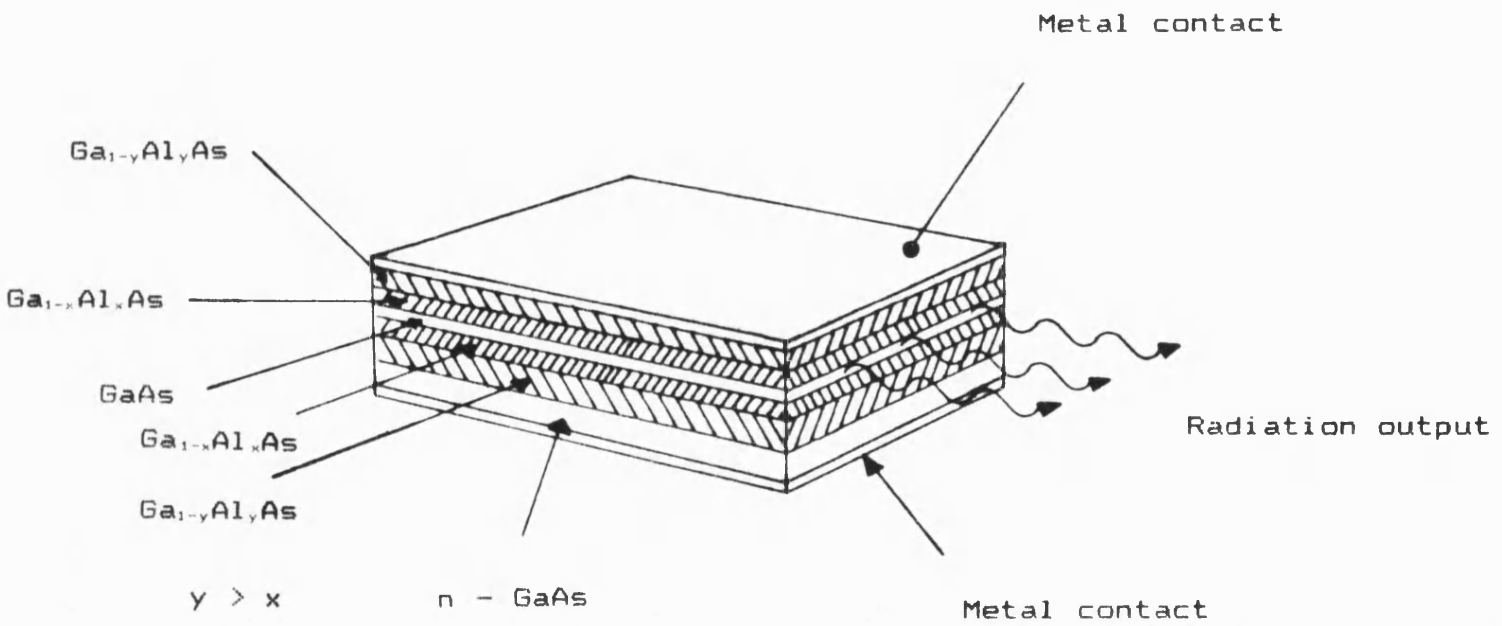


Fig(17). Diagram of a five - layer localised gain region heterostructure GaAs laser.

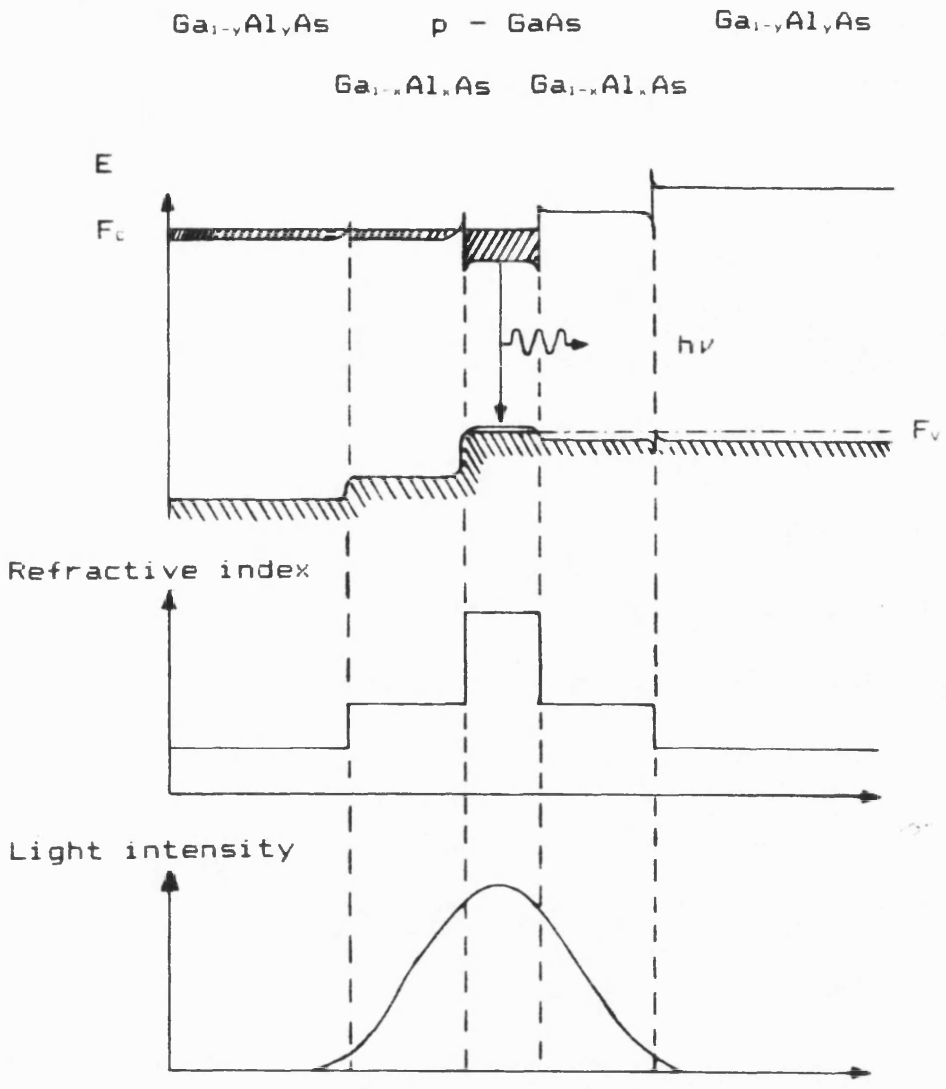


Fig(18). Distribution of conduction and valence bands, refractive index and light intensity perpendicular to the p - n junction in a five - layer localised gain region heterostructure laser under forward bias.

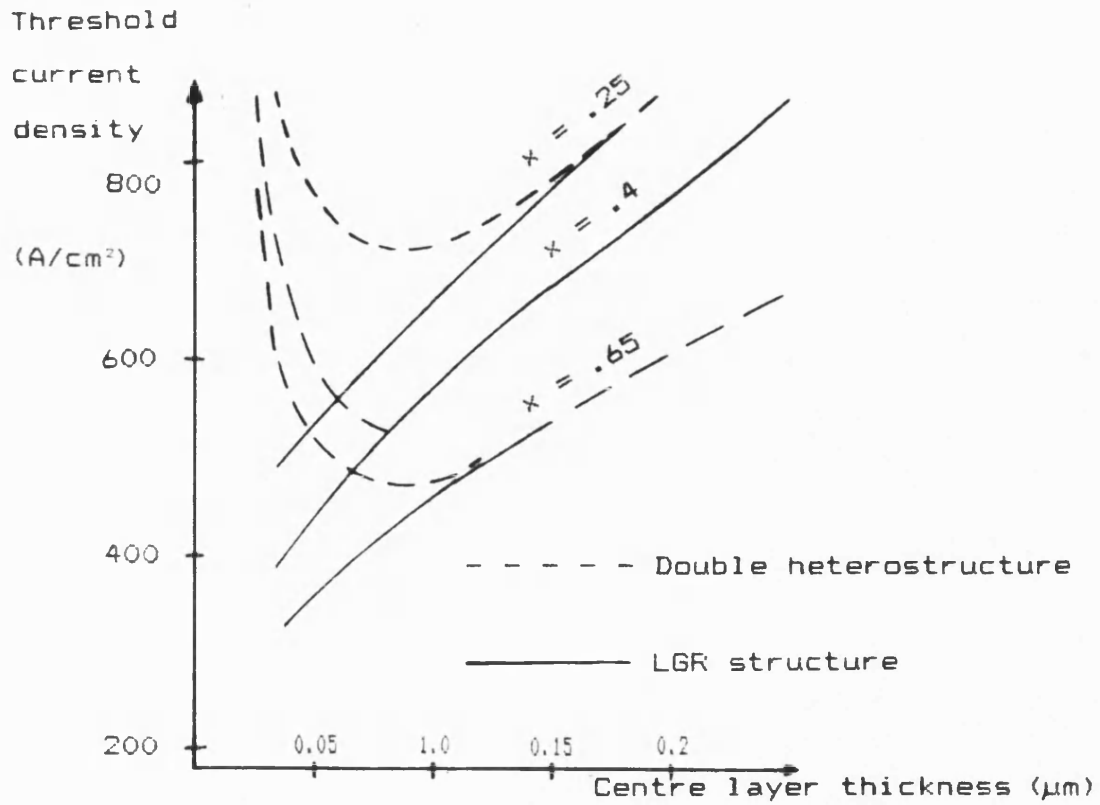


Fig(19). Comparison of threshold current density versus active layer thickness between GaAs - based LGR and double heterostructure lasers {34}.

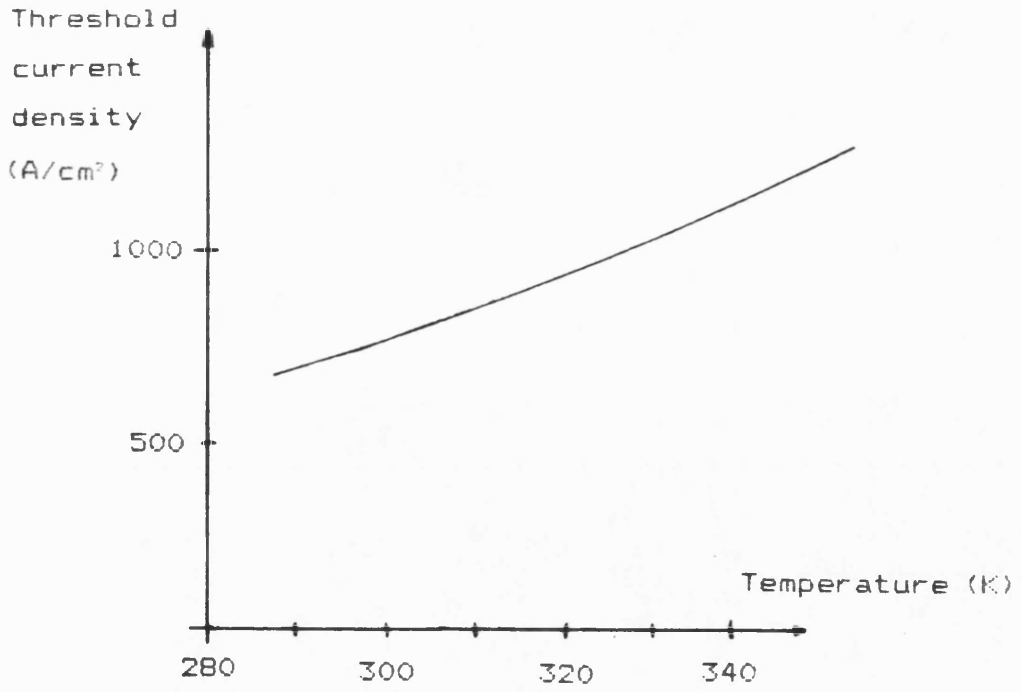


Fig(20). Dependence of threshold current density upon temperature in an LGR structure {34}.

confinement (34).

### 1.7.4) Graded refractive index laser (GRIN)

The laser structures described above use abrupt heterojunctions. The fourth type of laser of interest to this work is the graded refractive index (GRIN) laser which differs from the DH laser by the fact that the outer confinement layers have graded material composition profiles in the vicinity of the active layer. Fig(21) shows the structure investigated and Fig(22) schematically presents the energy and refractive index distributions perpendicular to the laser.

The effect of the graded composition confinement layers is to ease the thermalisation of the injected carriers through the resulting change of the material band gap and hence refractive index. Since the funnel can be made as deep as required, the threshold current density dependence upon active layer thickness and temperature can be expected to behave like that of the LGR laser as suggested by Fig(19) and Fig(20).

## 1.8) Heterostructure technology

Most heterostructure semiconductor diode lasers have a method of limiting the spread of injected carriers and lasing emission in the plane parallel to the

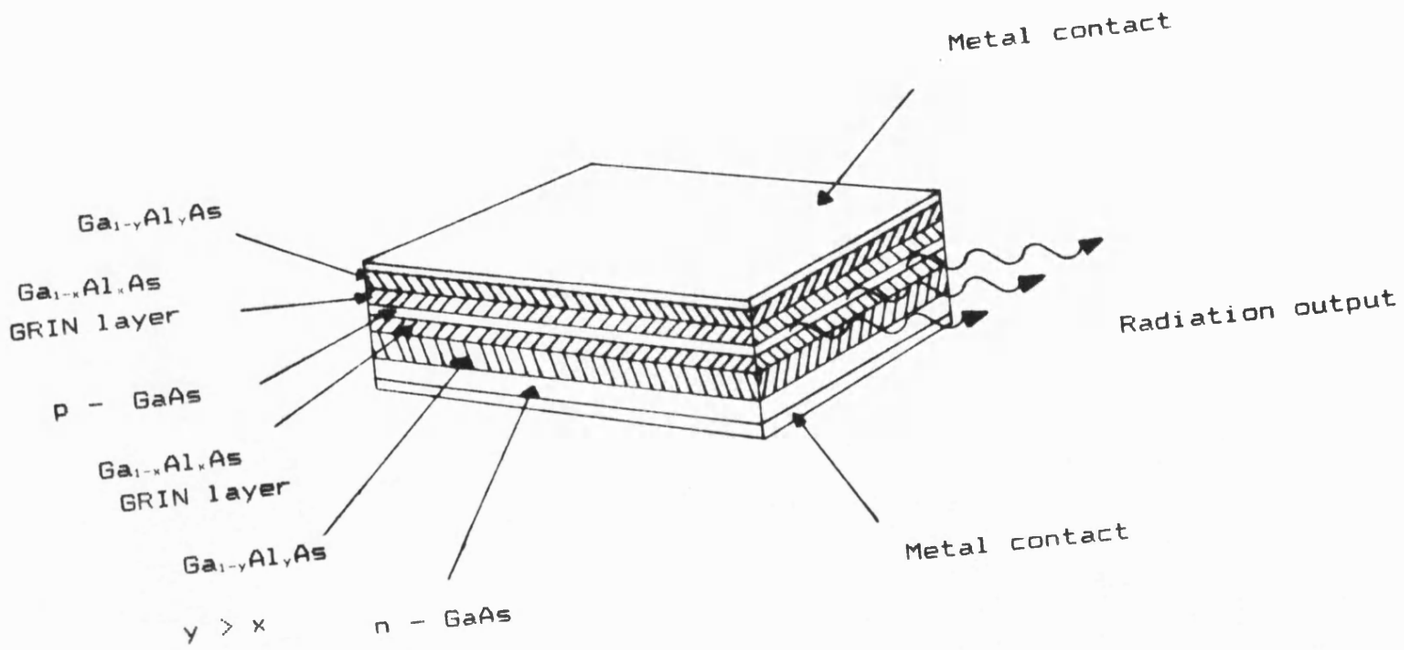


Fig(21). Diagram of a five - layer graded refractive index heterostructure GaAs laser.

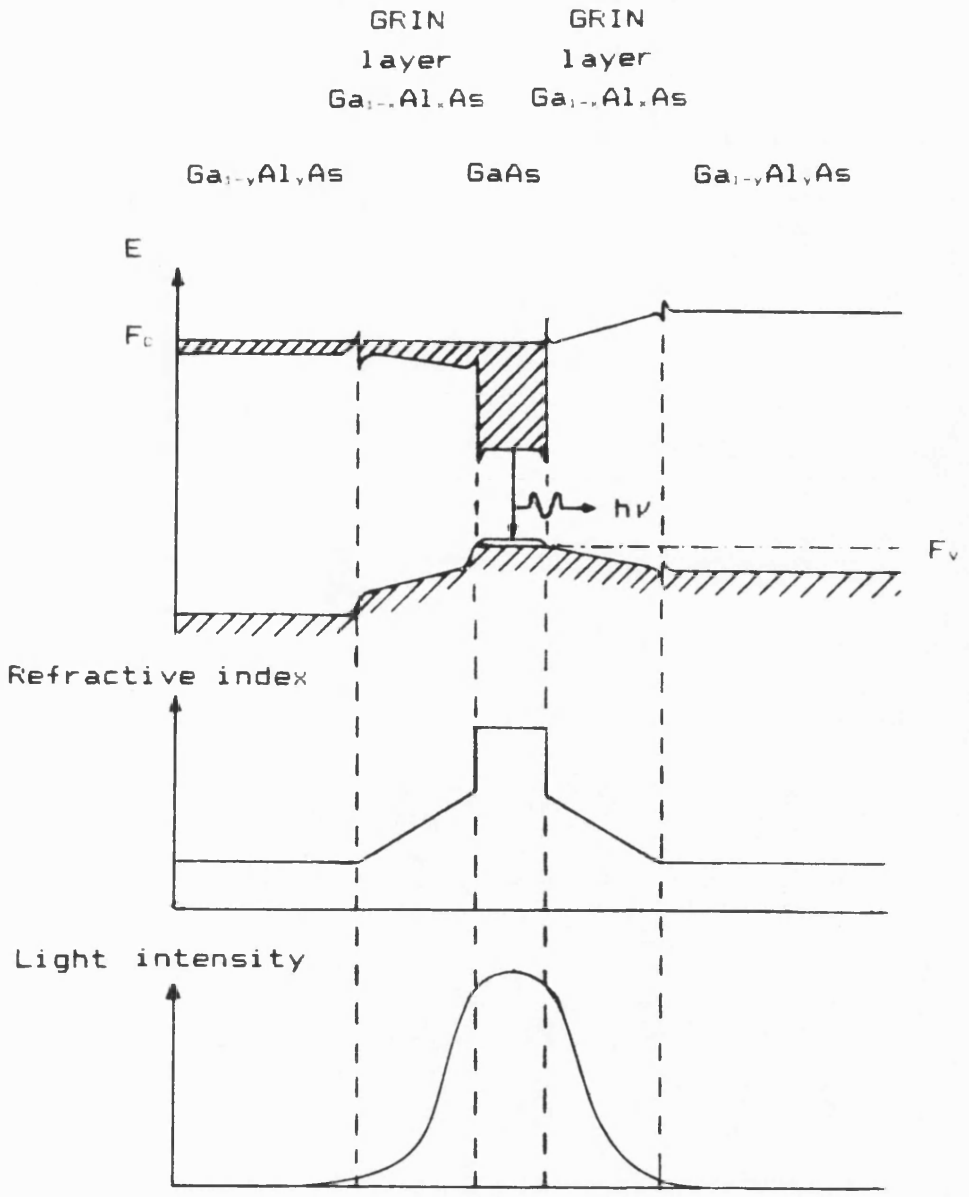


Fig(22). Distribution of conduction and valence bands, refractive index and light intensity perpendicular to the p - n junction in a five - layer graded refractive index heterostructure laser under forward bias.

junction. This is easily achieved by the simple stripe geometry contact and the necessary insulation to confine the current outside the stripe can be incorporated in several ways leading to a range of different devices. This type of simple stripe contact geometry laser is covered in detail in chapter 5 and will not be discussed further here.

Fig(23), on the other hand, shows cross - sectional views of various heterostructure lasers which use advanced heterostructure technology to limit injected carrier spread. The forms shown in Fig(23) will theoretically yield better laser characteristics and a detailed description of the fabrication and function of the various types can be found in good text books upon diode lasers {35}. Such contact technologies must also be investigated in the future for the work described in this thesis but for the simplification in understanding the results of lasers grown by the MBE technique, only simple stripe geometries are considered here.

## 1.9) Applications of semiconductor lasers

Due to its compact size and capability for high - frequency modulation, the semiconductor diode laser is one of the most important radiation sources for optical fibre communication systems. There are currently three

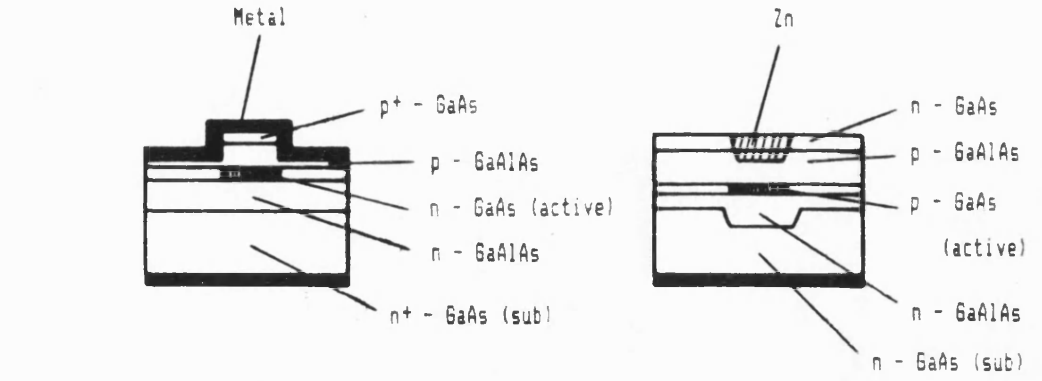


a) Mesa stripe b) Channeled substrate

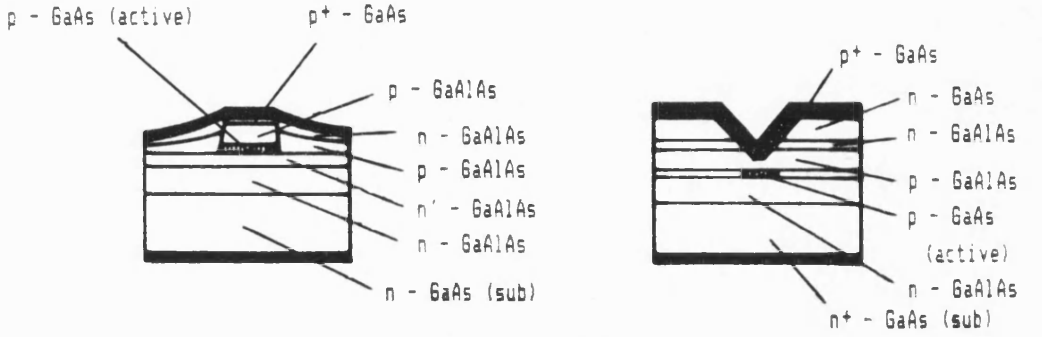


c) Buried stripe d) V - groove

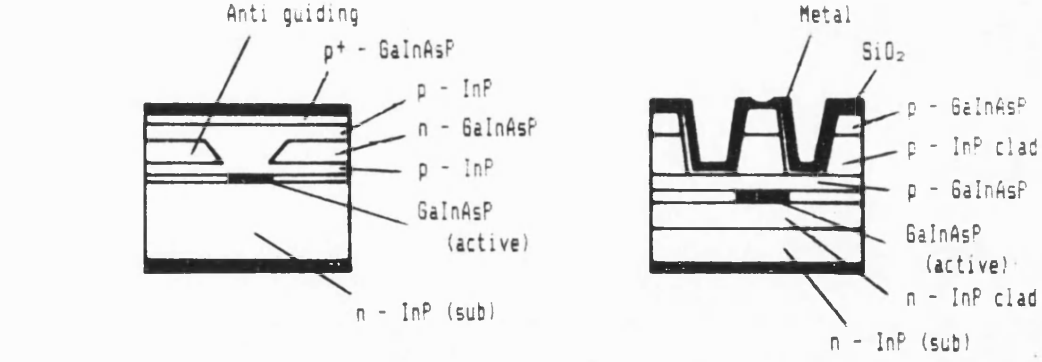


e) Self - aligning f) Ridge waveguide

Fig(23). Cross - sectional views of various GaAs - based heterostructure lasers using advanced technology {35}.

wavelengths of particular interest due to the absorption loss minima of the silica fibres. These occur at 0.9μm for GaAs and at 1.3μm and 1.55μm where the absorption coefficient (0.2 dB/km {36}) and dispersion cofficients are low. For this wavelength, III - V quaternary compound lasers, such as $Ga_xIn_{1-x}As_yP_{1-y}/InP$ lasers, have been intensively researched. Longer wavelengths on the other hand (for example at 4μm for the new fluoride - based fibres) have much smaller absorption coefficients {37} and Fig(9) shows that possible material candidates are the lead chalcogenides.

Due to the fact that in 1970, narrow spectral linewidths were observed in a semiconductor diode laser of $Pb_{1-x}Sn_xSe$, research has spread to other applications for the diode laser. The current tuning of this single mode with and a high degree of stability and reliability in the lead chalcogenide diode lasers allows their potential use for applications in technology and basic research. Fields of interest include ultra - fine resolution gas spectroscopy (e.g. $SF_6$, $NH_3$, $C_2H_4$, CO, $CO_2$, $N_2O$, $NO_2$, NO, $SO_2$ etc.), molecular spectroscopy (nuclear spectroscopy and Zeemann splitting) and local oscillators for use in infra - red heterodyne detectors and isotope analysis ($U^{238}F_6$ and $U^{235}F_6$ in the 16μm region).

Fig(24) shows the centres of the vibrational - rotational absorption wavelength bands of a large number of molecular gases (38). Laser alloys with band gaps corresponding to these wavelengths are also included. It can be seen that lasers based upon the IV - VI group of compounds cover this range. Lead chalcogenide lasers in fact allow the spectral region 2.5 - 34μm to be covered thus including the environmentally dangerous gases listed above which forms the basis of the goal set for this work. The physical, electrical and optical properties of lead chalcogenides will be discussed in detail in the following chapter.

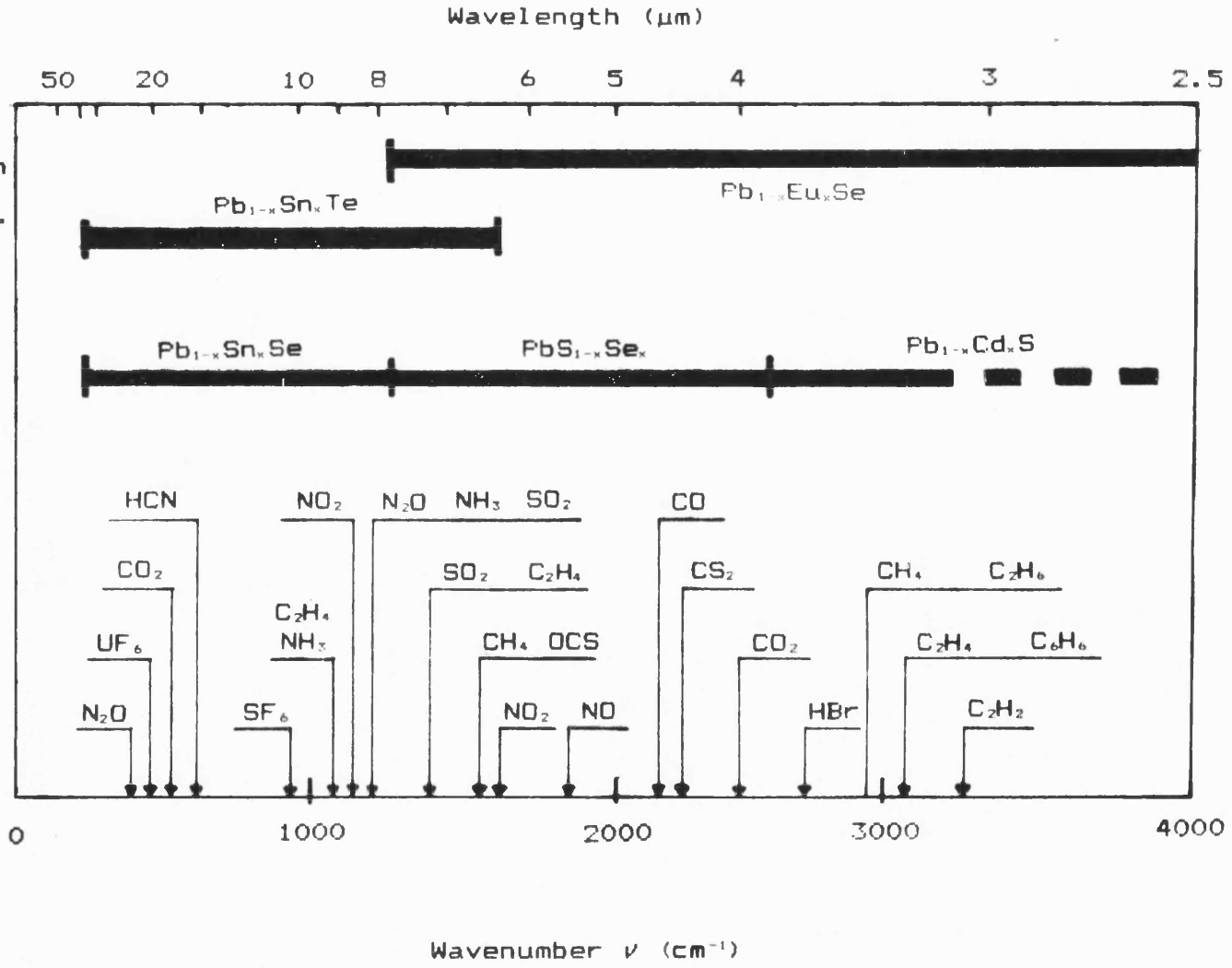


Fig(24). Known absorption bands of important gases. Also shown are the regions in which diode - laser spectroscopy has been performed with the stated lead - salt compositions {38}.

## 2) IV - VI COMPOUNDS AND GROWTH TECHNIQUES

### 2.1) Introduction

This chapter presents the properties and characteristics of the lead chalcogenide materials used for the fabrication of diode lasers emitting in the 3.5µm to 20µm range as described in chapter 1.

Section 2.2 lists the production steps and properties of the IV - VI binary compounds and section 2.3 discusses similar aspects of ternary compounds relavant to this work.

### 2.2) IV - VI binary compounds

The group IV elements germanium, tin and lead form nine binary compounds with the group VI elements sulphur, selenium and tellurium. The most interesting group IV - VI binary compounds for this work are the cubic $B_1$ structured PbSe, PbS and PbTe (lead chalcogenides) and the orthorhombic $B_{29}$ structured SnSe. These compounds and SnSe are direct, narrow - gap semiconductors.

#### 2.2.1) Crystal growth techniques

The compounds PbS, PbSe, PbTe and SnSe may be synthesised by direct reaction of the elements in vacuum.

The elements are first purified using a simple heated quartz reactor tube with flowing hydrogen to reduce the contaminants. The purified materials are then placed into a synthesis reaction chamber under a pressure of 1 mbar of hydrogen as shown in Fig(25). Care must be taken to ensure that the anion (Se, S, or Te) does not volatilise excessively before the reaction and generate explosively dangerous pressures. Temperatures required for the synthesis of PbS, for example, are shown in the diagram next to the profile.

Crystals of PbS, PbSe, PbTe and SnSe may be grown by a variety of techniques {39} - {42}. The method used to grow single crystals in the work described here is that of vapour transport growth. This is the technique of subliming the compound in an evacuated ampoule to a cooler position within the ampoule.

The synthesised binary material is weighed into 12g portions and is placed into a quartz ampoule with a length of approximately 150 mm. Under a vacuum of better than $1x10^{-5}$ mbar, a quartz stopper is fused into the ampoule forming an evacuated ampoule of 100 mm in length. This is now placed into a furnace with the temperature profile shown in Fig(26) to produce a single crystal, the crystal growth time being over a week {43}.

This method of single crystal fabrication

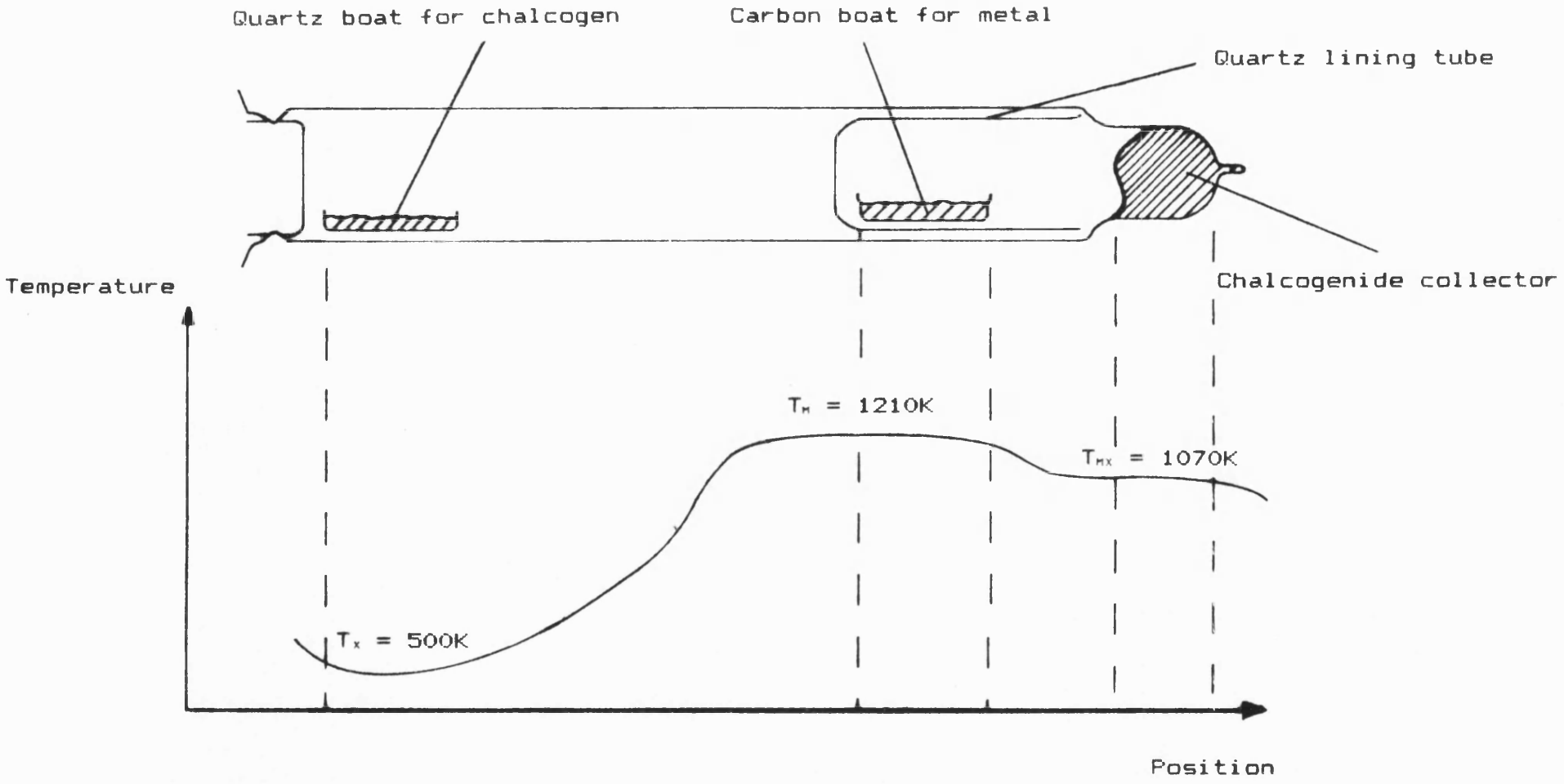


Fig(25). Synthesis reactor with temperature profile for the synthesis of PbS.

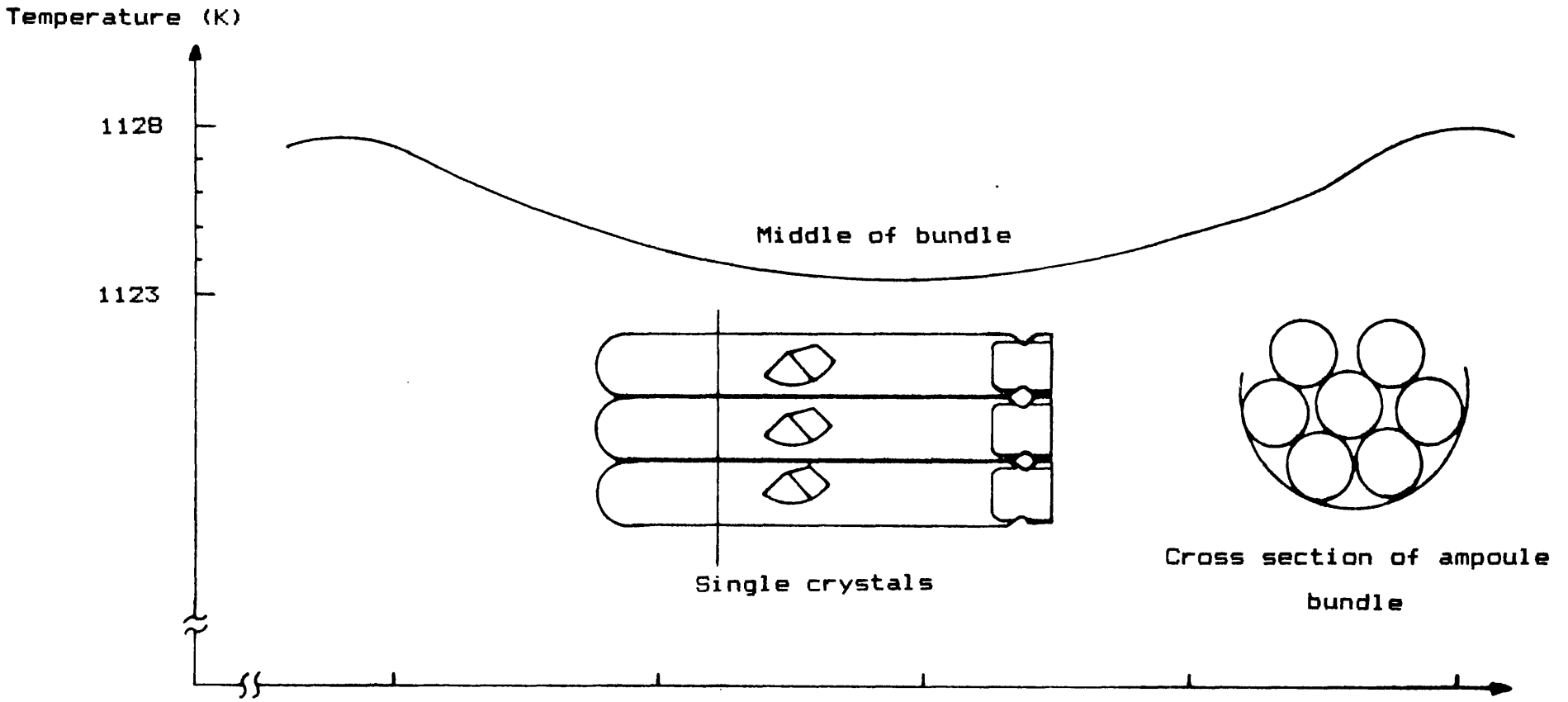


{43}.

Fig(26). Positioning of the ampoules within the temperature profile set for single crystal growth.

produces crystals with [100] facets of approximately 1 $cm^2$ substrate area. From the 12g of material loaded, an average of 50% will be effectively used for further laser manufacture. Bartel Metallphysik in Göttingen, West Germany have measured the dislocation density of the crystals to be $1x10^3$ - $1x10^4$ $cm^{-2}$. This low level of dislocation density is over an order of magnitude smaller than commercially available lead chalcogenide substrate material.

The single crystals of PbX (X=S, Se, or Te) prepared by these methods will exhibit compositions which, according to preparation, deviate from stoichiometry. For this reason and since an excess of either lead atoms or X atoms will introduce charge carriers, single crystals usually yield carrier concentrations in the range $1x10^{17}$ - $1x10^{19}$ $cm^{-3}$.

The composition (and thus the carrier concentration) of a crystal may be modified by annealing in either a lead - rich or an X - rich vapour. Either a two - temperature anneal or an isothermal anneal may be used. PbSe {44} and PbTe {45} have been annealed using the former method with the crystal being at a temperature $T_1$ in a vapour of partial pressure p of either lead or $X_2$ obtained from material in a second region at a temperature $T_2$ where $T_1 > T_2$. The latter isothermal

method developed by Brebrick and Allgaier {46} anneals the crystal in the presence of a lead - rich or X - rich two - phase PbX alloy until equilibrium is achieved. This technique has been applied to PbTe {47} and to diffusion experiments in PbSe {48}. Both techniques shift the equilibrium composition of the crystal in accordance with the phase diagram of the system. The equilibrium conditions can then be kept by rapidly cooling the crystal to room temperature.

The pressure - temperature - composition diagram for PbSe is shown in Fig(27) {49}. The diagram shows the partial pressure $pSe_2$ of $Se_2$ in equilibrium with with solid (or solid plus liquid) PbSe at a given temperature. In the figure, the contour BAFCDE is the line along which solid PbSe and liquid coexist in the presence of Se vapour and encloses the region in which solid exists. Compositions are given as carrier concentrations n - or p - type by assuming that two electrons correspond to one selenium vacancy {50}. Thus the line KJF marked $5x10^{17}$ electrons $cm^{-3}$ corresponds to a non - stoichiometric composition containing $1x10^{18}$ excess lead atoms $cm^{-3}$. A similar arguement is also applicable on the p - type side of the solid region. The intrinsic line FG corresponds to n = p and hence to stoichiometry. Similar diagrams are available for PbS {51} and PbTe {52}, but will not,

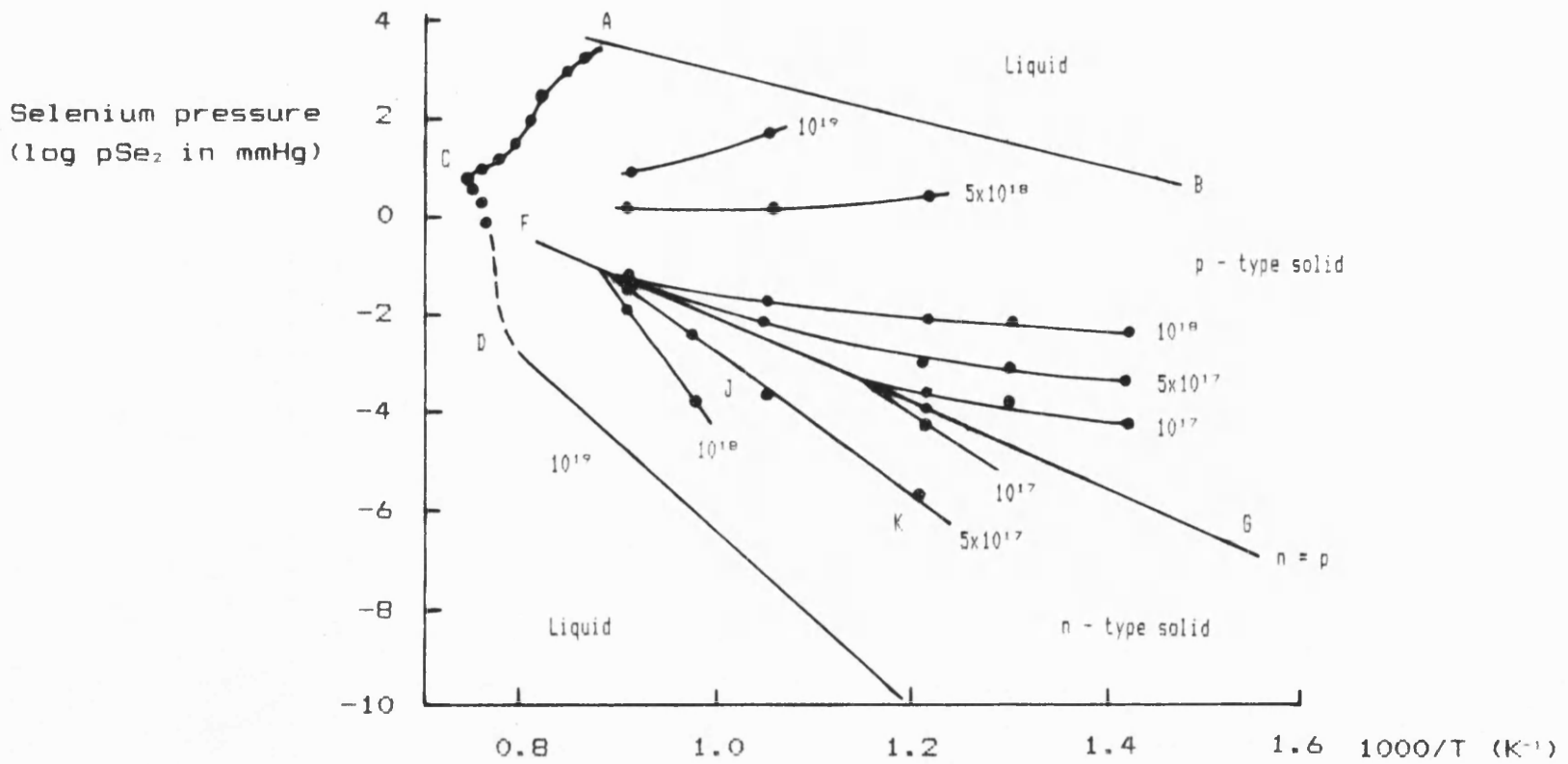


Fig(27). Pressure - temperature - composition diagram for the PbSe alloy system **{49}**.

however, be presented here.

Of particular interest to the work described in this thesis, a mass spectrometric study indicates that PbSe, PbS and PbTe sublime primarily as molecular PbSe(g), PbS(g) and PbTe(g) respectively [(g) = gaseous] {53}. Also the partial pressure p of PbX(g) in equilibrium with solid PbX is independent of the composition of the solid PbX. However, the partial pressure of $X_2(g)$ in equilibrium with solid PbX varies strongly with the composition of the solid phase. The sublimation of solid PbX must therefore be described in terms of the partial pressures of both PbX(g) and $X_2(g)$ in equilibrium with the solid.

### 2.2.2) Crystal structure

Lead selenide, sulfide and telluride are polar semiconductors in which the bonding is due to a large extent to the electrostatic forces between the ions forming the crystal. This type of system, in which there is a strong ionic contribution to the bonding of the compounds, is characteristic of the sodium chloride or rock salt structure which all three above compounds exhibit {54}. The space lattice is face - centred cubic, with a basis of one lead ion and one X ion associated with each lattice point {55}. The structure is shown in

Fig(28) where the lead and X ions forming the basis are separated by a distance d/2, d being the body diagonal of the unit cube formed by eight lead ions (or eight X ions). The distance, a, is the customary lattice constant. If A = a/2, then the positions of the ions in the unit cell are

Pb: (000); (AA0); (A0A); (0AA) (38)

and

X : (AAA); (00A); (0A0); (A00) (39)

Thus the lead ion at (000) and the X ion at (AAA) (separated by a distance d/2 = a$\sqrt{3}$/2) form the PbX basis associated with the lattice point (000). There are four PbX units in each unit cube of volume a$\sqrt{3}$. Table (1) gives values of the lattice constant a for nominally stoichiometric PbX {56} and that of $BaF_2$ {57}.

Table (2) shows the thermal expansion of PbSe, PbS and PbTe, measured from 20 to 340K using polycrystalline samples {58}, with $BaF_2$ {57} for comparison. $BaF_2$ data is included here since it proves to be an excellent cubic structured substrate material upon which lead chalcogenides can be epitaxially deposited.

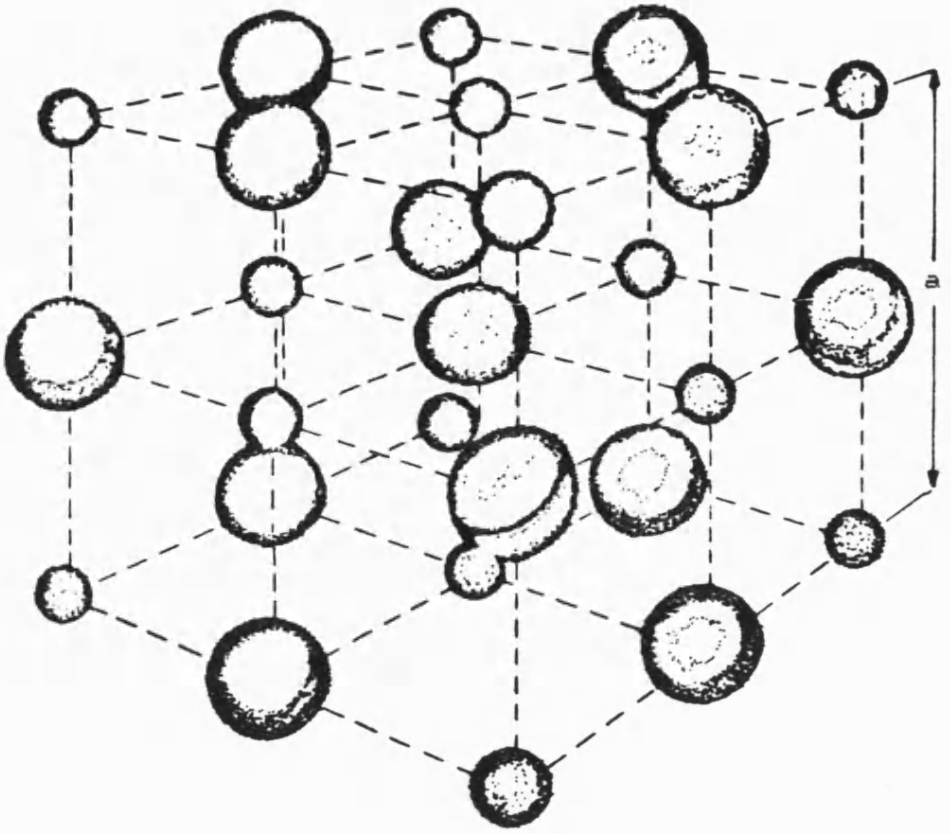


Fig(28). The sodium chloride crystal structure.
The space lattice is face centred cubic.

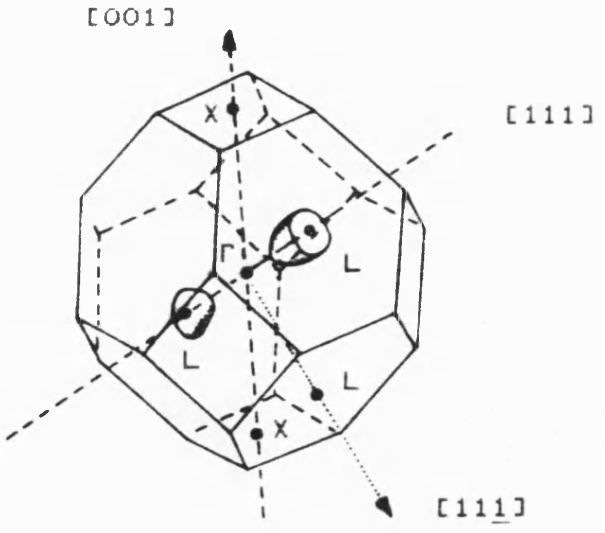


Fig(29). The first Brillouin zone for PbSe, PbTe and PbS. The symmetry points Γ, L and X are shown, as are two ellipsoids of constant energy {59}.

| Compound | a (Å) | Volume of unit cube ($Å^3$) | Volume of one PbX ($Å^3$) | Experimental density ($gcm^{-3}$) |
|---|---|---|---|---|
| PbSe | 6.124 | 229.7 | 57.43 | 8.10 |
| PbTe | 6.462 | 269.8 | 67.45 | 8.16 |
| PbS | 5.936 | 209.2 | 52.30 | 7.50 |
| $BaF_2$ | 6.120 | ----- | ----- | ---- |

Table (1). Lattice parameters and density for PbSe, PbTe, PbS and $BaF_2$ at 300K {56}, {57}.

| Temperature (K) | PbSe | PbTe | PbS | $BaF_2$ |
|---|---|---|---|---|
| 30 | 7.65 | 9.02 | 7.54 | ----- |
| 50 | 12.92 | 14.30 | 12.43 | ----- |
| 70 | 15.63 | 15.38 | 15.42 | 14.80 |
| 100 | 17.37 | 17.70 | 17.55 | ----- |
| 300 | 19.40 | 19.80 | 20.27 | 18.20 |

Table (2). Linear expansion coefficient for PbSe, PbTe, PbS and $BaF_2$ in units of $10^{-6}K^{-1}$ {58}, {57}.

| Material | 77K (eV) | 300K (eV) |
|---|---|---|
| PbSe | 0.176 | 0.279 |
| PbTe | 0.217 | 0.310 |
| PbS | 0.307 | 0.410 |

Table (3). Minimum energy gap of PbSe, PbTe and PbS {61}.

2.2.3) Band structure

The band structures of PbS, PbSe and PbTe have been extensively investigated. The first Brillouin zone is shown in Fig(29) and is that of a face - centred cubic lattice {59}. The eight equivalent L points are each at the centre of a hexagonal Brillouin zone face at its intersection with a [111] direction {60}. The six equivalent X points are each at the centre of a square zone face at its intersection with a [001] direction. The $\Gamma$ point is at the centre of this zone.

Experimental results indicate that the surfaces of constant energy for both the conduction and valence bands are prolate ellipsoids of revolution. The centres of the ellipsoids are at L points and the major axes are in [111] directions. Hence, there are eight equivalent constant energy ellipsoids for the conduction band states and eight for the valence band states. Portions of two such ellipsoids are shown in the figure.

The general features of the band structures of PbS, PbSe and PbTe are similar {61}. In each case, the valence band maximum and the conduction band minimum both occur at the L point. This results in a direct minimum energy gap $E_g$. At room temperature and above, $E_g$ can be estimated from the positions of peaks in the refractive index as a function of incident photon energy. A summary

of these results is given in Table (3) and it can be seen that the data show the unusual positive temperature coefficient of the energy gap $E_g$ ($dE_g/dT$). The variation of $E_g$ between 80 and 373K is linear and these values are plotted in Fig(30). From the plot, values for $dE_g/dT$ between 80 and 373K are calculated to be $4.5 \times 10^{-4}$, $4.5 \times 10^{-4}$ and $4.2 \times 10^{-4}$ eV $K^{-1}$ for PbS, PbSe and PbTe respectively. Although these values are very similar, the band gap variation below 80K for each of the above compounds is different as shown in the plot.

2.2.4) Optical properties

Fig(31) shows the optical absorption $\alpha$ of PbS, PbSe and PbTe as a function of photon energy $h\nu$ at 300K {62}. For each compound there is a sharp threshold for absorption and for direct transitions across the energy gap, a plot of $\alpha$ against $\sqrt{(h\nu - E_g)}$ is linear {63}.

Fig(32) shows the reflectivity of PbS, PbSe and PbTe at 300K {64}. The values of the reflectivity are important for determining the quality of the resonator in a diode laser made with these materials in the active region.

The refractive index of PbS, PbSe and PbTe at 77, 300 and 373K is shown in Fig(33) as a function of photon energy {65}. As quoted in equation 16, the reflection

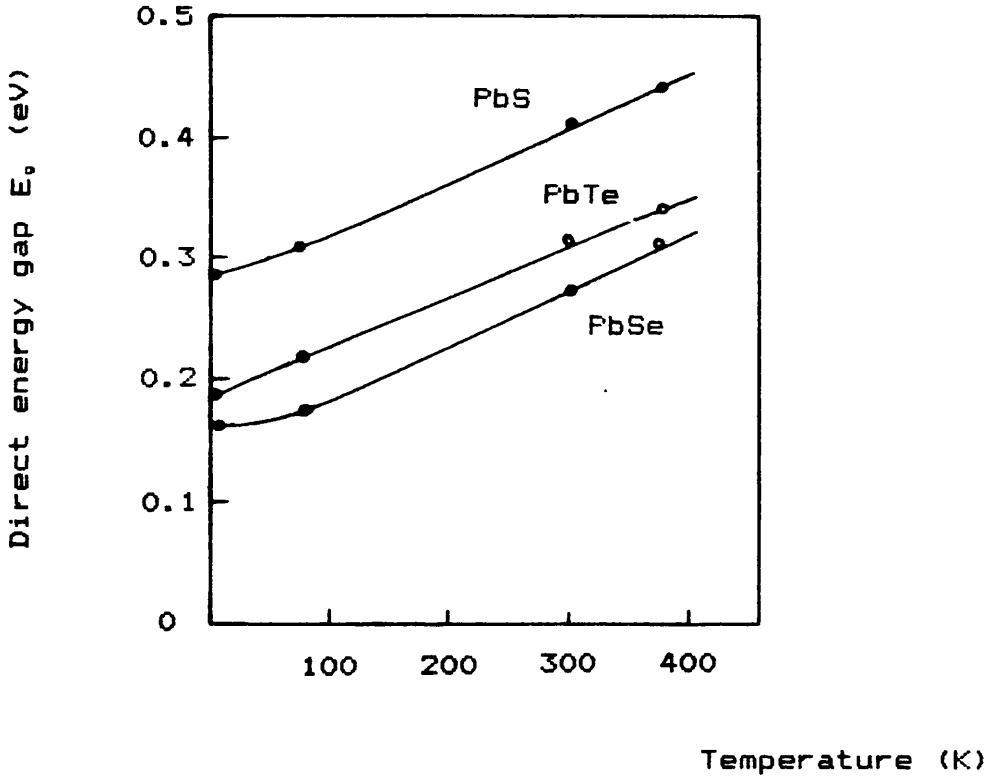


Fig(30). Variation of energy gap $E_0$ with temperature for PbS, PbSe and PbTe {61}.

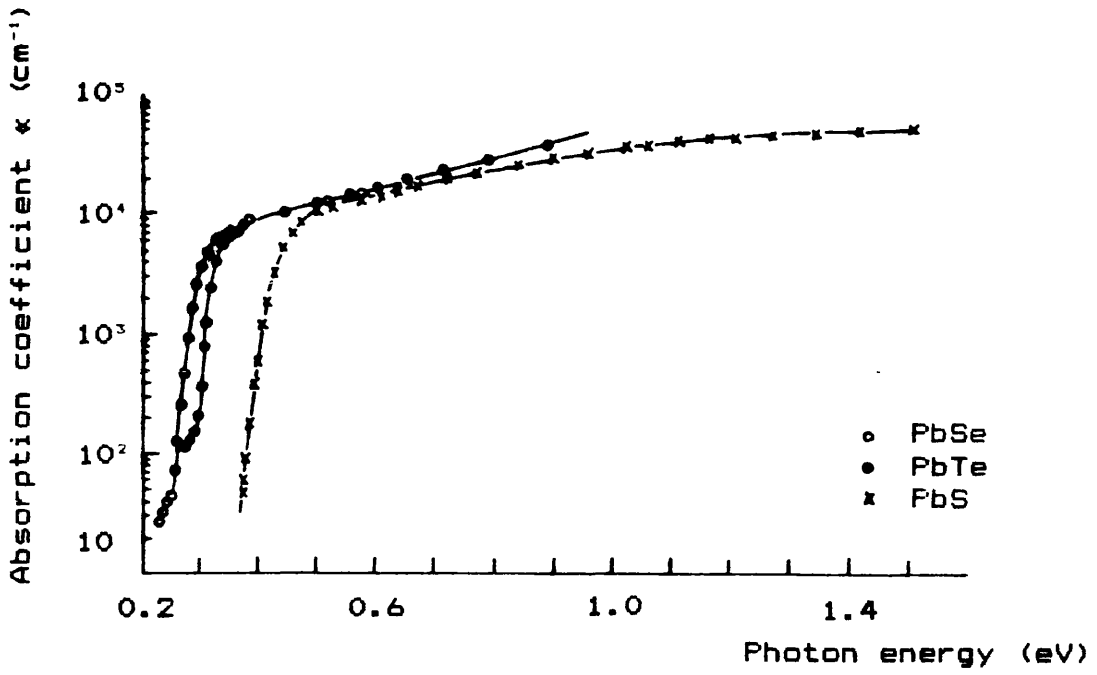


Fig(31). The optical absorption spectra of PbS, PbSe and PbTe at room temperature {62}.

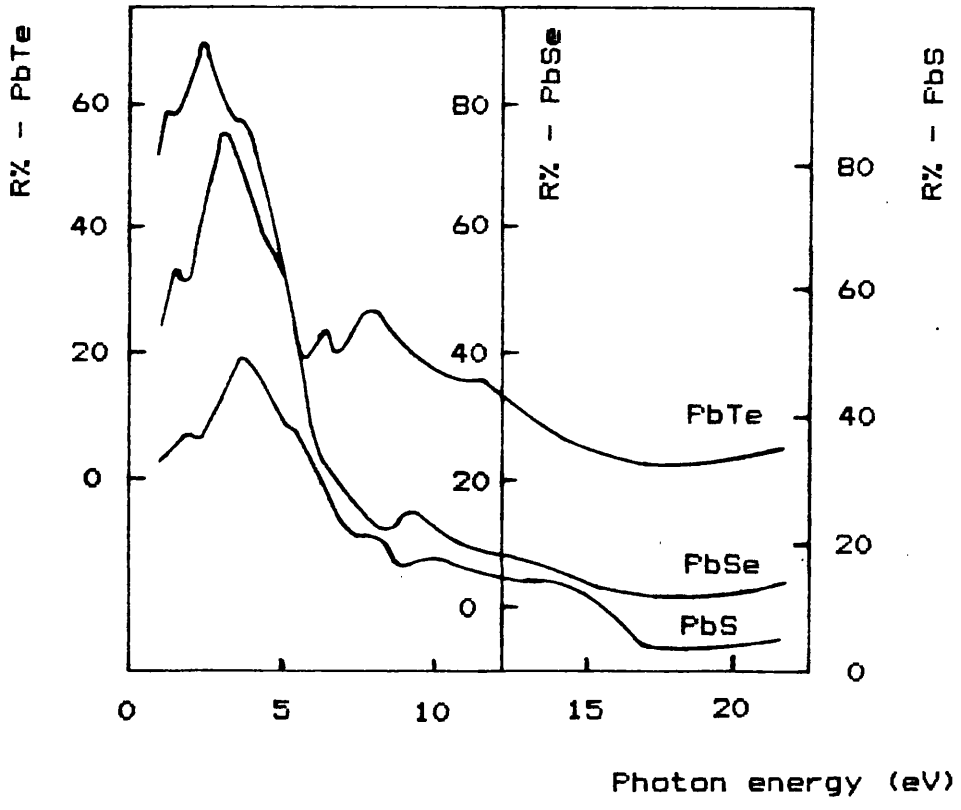


Fig(32). Reflectivity of PbS, PbSe and PbTe at 297K {64}.

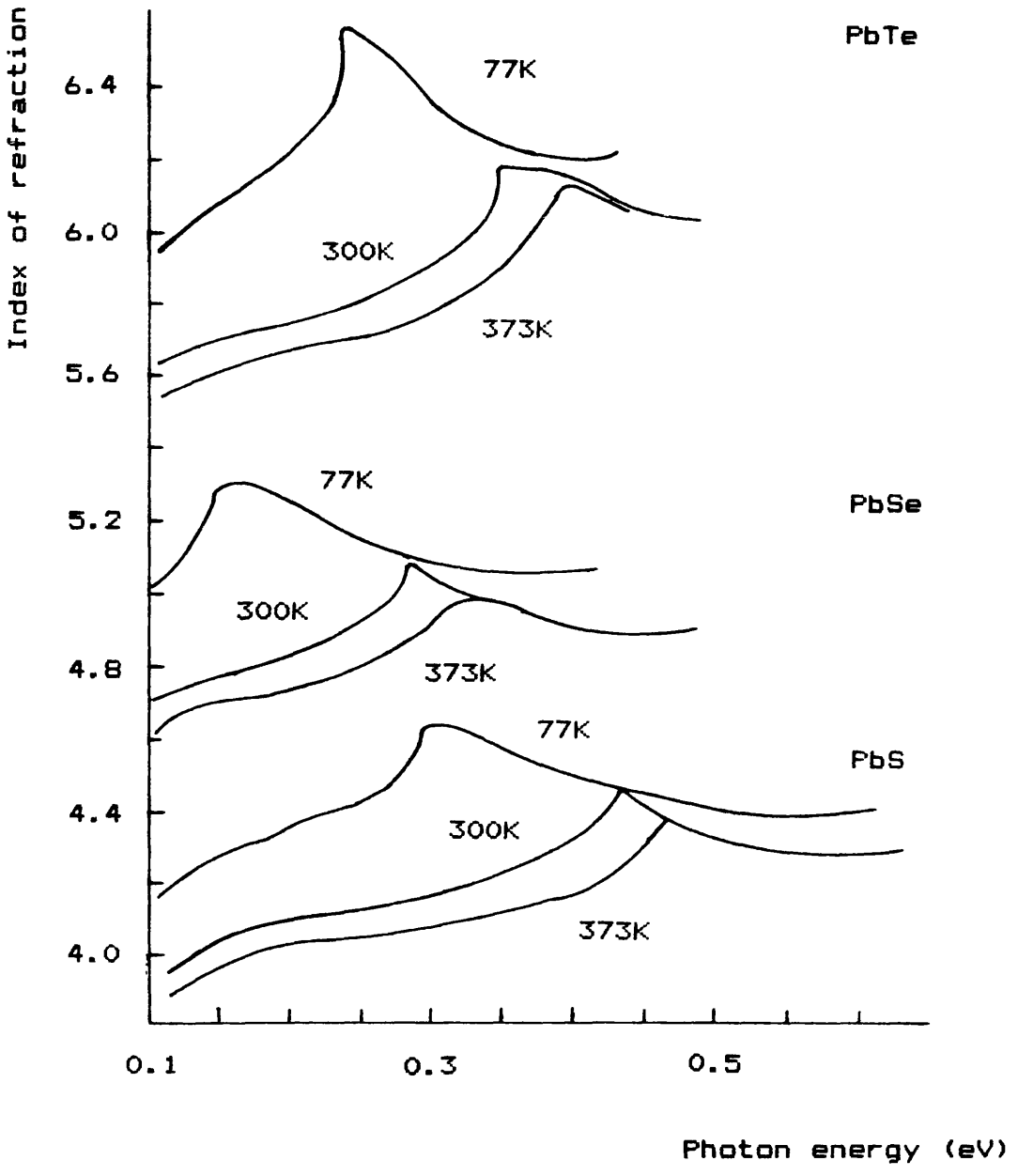


Fig(33). Variation of the refractive index of PbS, PbSe and PbTe with photon energy at 77, 300 and 373K {65}.

coefficient is dependent upon the refractive indices of the materials forming the interface. Hence the refractive index at photon energies greater than 0.6 eV can be calculated from the measured reflection coefficients shown in Fig(32) and reflection coefficients in the 0 - 0.6 eV range can be calculated from the refractive indices shown in Fig(33) thus providing information over a large range.

2.2.5) Electrical properties

The electrical conductivity $\sigma$ and the Hall coefficient $R_H$ yield useful information on the carrier density and mobility in a semiconductor. There have been a number of investigations of these characteristics over wide temperature ranges {66}. The data indicate that $R_H$ is practically constant over the entire temperature range 4K - 300K, implying that the extrinsic carrier concentration n (or p) = $(1/eR_H)$ is also independent of temperature. This, in turn, implies that at 295K in these samples, intrinsic carriers are not numerous enough to influence the conduction process. With the exception of rare samples with very low carrier concentrations, PbS, PbSe and PbTe are not intrinsic at 300K or below. The intrinsic carrier concentration $n_i$ at 300K has been calculated to be $8\times10^{15}$ $cm^{-3}$ for PbS, $3\times10^{14}$ $cm^{-3}$ for

PbSe and $1.5 \times 10^{16}$ $cm^{-3}$ for PbTe {67}.

The mobility $\mu$ of both electrons and holes in PbS, PbSe and PbTe has been studied and data between liquid helium temperature and room temperature is given for PbS in Fig(34), PbSe in Fig(35) and PbTe in Fig(36) {66}. All plots have similar forms and as the temperature is decreased, $\mu$ increases as $T^{-C}$ where C is a number dependent upon the carrier concentration. The absolute values of carrier mobility are given in the following table (Table (4)) {68}.

| Material | Electrons | Holes |
|---|---|---|
| PbS | 600 | 700 |
| PbSe | 1200 | 1000 |
| PbTe | 1800 | 900 |

Table (4). Mobility of PbS, PbSe and PbTe at 300K in units of $cm^2V^{-1}s^{-1}$ {68}.

2.2.6) Impurity and stoichiometric effects

Both impurities and defects due to deviations from stoichiometry may produce electrically active centres in the lead compounds. Extrinsic carrier concentrations as high as $2 \times 10^{20}$ $cm^{-3}$ have been obtained,

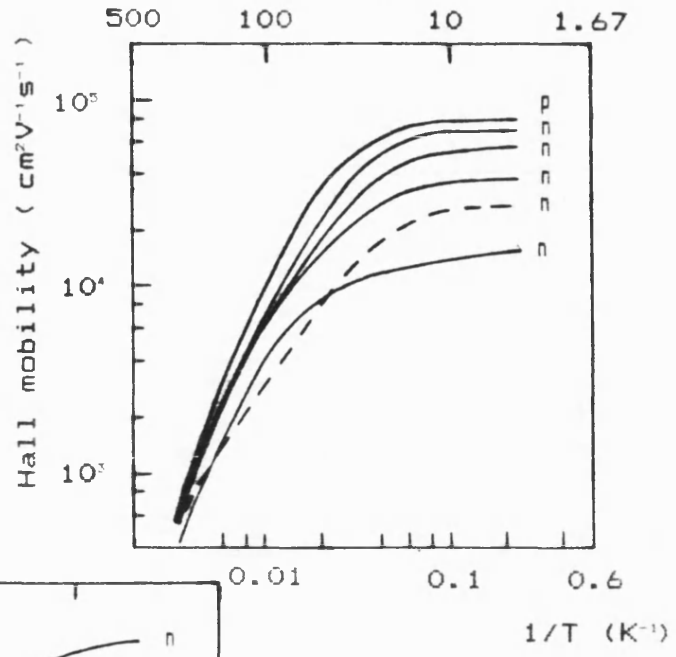


Fig(34). Mobilities in PbS from 300 to 4.2K {66}.

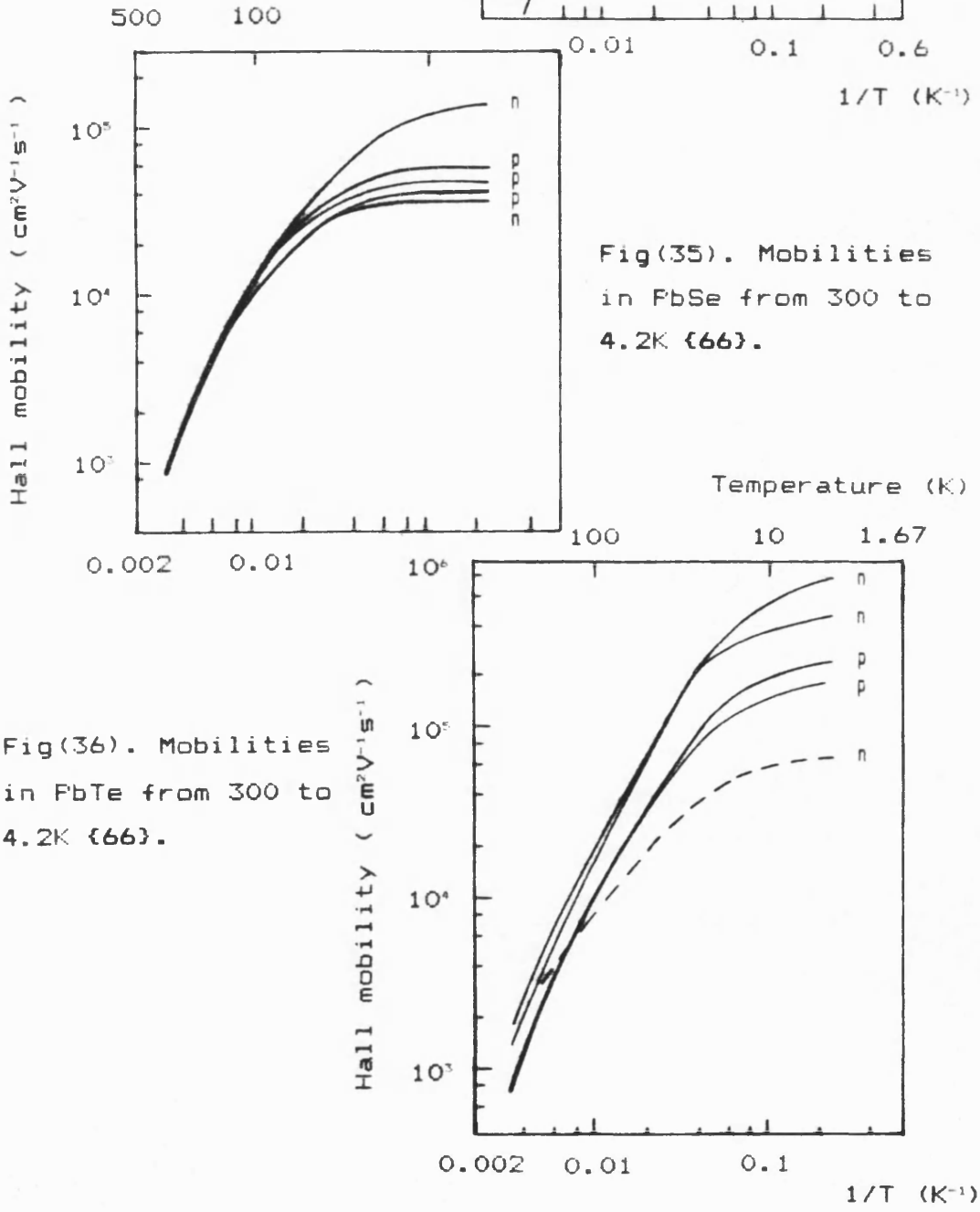


Fig(35). Mobilities in PbSe from 300 to 4.2K {66}.

Fig(36). Mobilities in PbTe from 300 to 4.2K {66}.

for example, by the incorporation of bismuth {69}. In section 2.2.1 it has been stated that two electrons in the lead chalcogenides are associated with one chalcogenide vacancy. However, it is not clear whether the crystal defects giving rise to these centres are of the Schottky (vacancy) type, the Frenkel (interstitial) type or a combination of the two. The energy of formation of a lead vacancy, for example, has been reported to be 0.3 eV and for that of a tellurium vacancy to be 1.2 eV {70}.

There have been a number of investigations of the electrical activity of impurity atoms in the lead compounds. Sodium {71}, silver and thallium {72} are acceptors whilst copper {72}, iron {73}, bromine {74} and bismuth {72} are donors. These examples do not exhaust the list of possible dopants and more about the two dopants important to the work here, namely bismuth and silver will be presented in chapter 4.

## 2.3) Lead chalcogenide ternary compounds

As mentioned in section 2.2, the lead chalcogenide binaries (and SnTe) crystallise in cubic $B_1$ and SnSe in orthorhombic $B_{2_7}$ structures. Therefore, for example, the ternaries $Pb_{1-x}Sn_xTe$ and $PbS_{1-x}Se_x$ exist for all compositions x, whilst the existence range for

$Pb_{1-x}Sn_xSe$ with cubic $B_1$ structure is restricted (to $x \leqslant 0.4$). Fig(37) schematically shows the dependence of energy gap $E_g$ and lattice constant a upon the composition x for the lead chalcogenide systems existing between the binaries SnTe, PbTe, PbS, PbSe and SnSe {75}.

2.3.1) Requirements of the project

Fig(38) shows the band gap $E_g$ plotted against the lattice constant a for important lead and tin systems. The binary PbSe was chosen as the substrate material due to its central lattice constant value in the figure and to the relative ease of producing good quality p - type single crystals and the ability of polishing sawn substrates to a high standard.

In the simple DH laser, the PbSe substrate is buffered by the first confinement layer giving a choice of confinement band gap energy and refractive index and isolating the active layer from strain caused by lattice mismatch. SnSe can be added to the active layer of a laser structure to produce wavelengths longer than 8μm at 77K without significant lattice mismatch occuring between the layers. Any mismatch may be reduced by the addition of Te in the active layer if this is found to be necessary.

Two different approaches have been used to

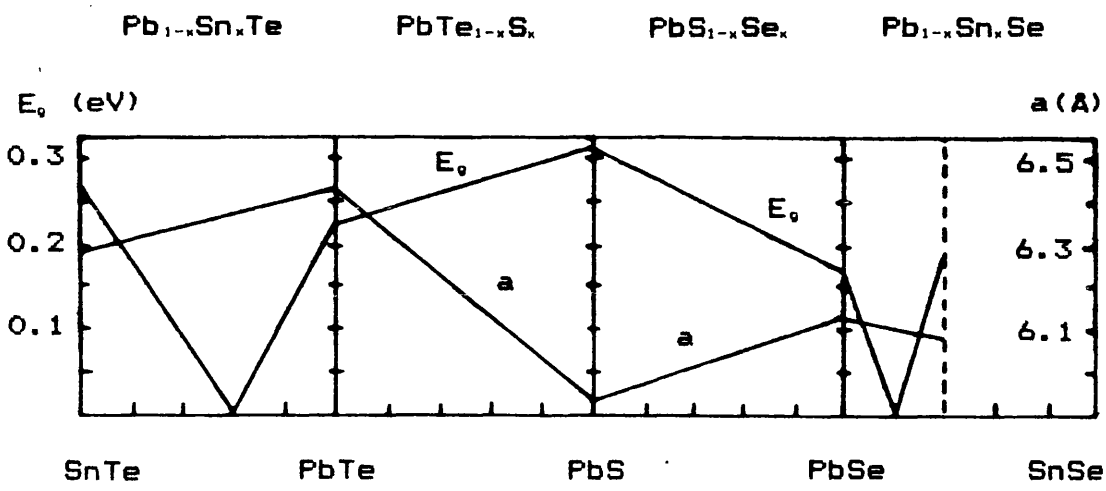


$E_g$ = bandgap at 77K

a = lattice constant at 300K

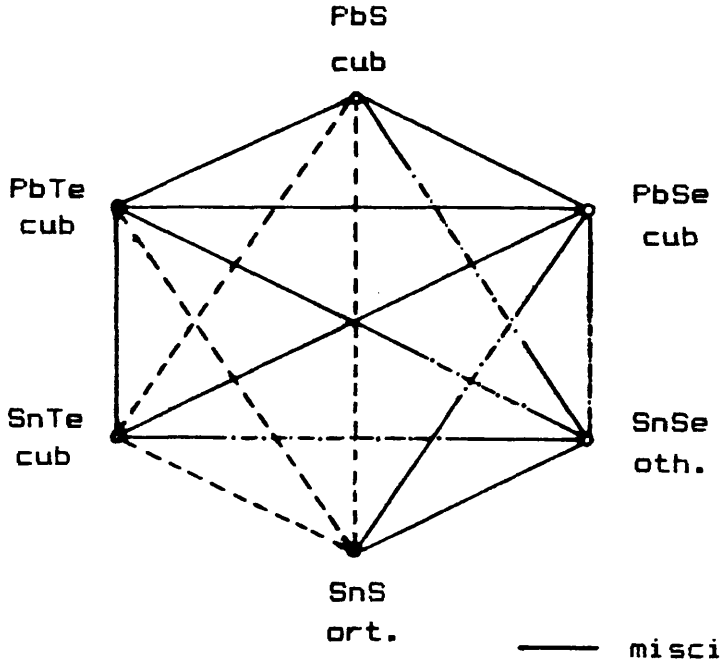


cub = cubic $B_1$

ort. = orthorhombic $B_{29}$

Fig(37). Solubility, band gap and lattice constant of important binary IV - VI alloys {75}.

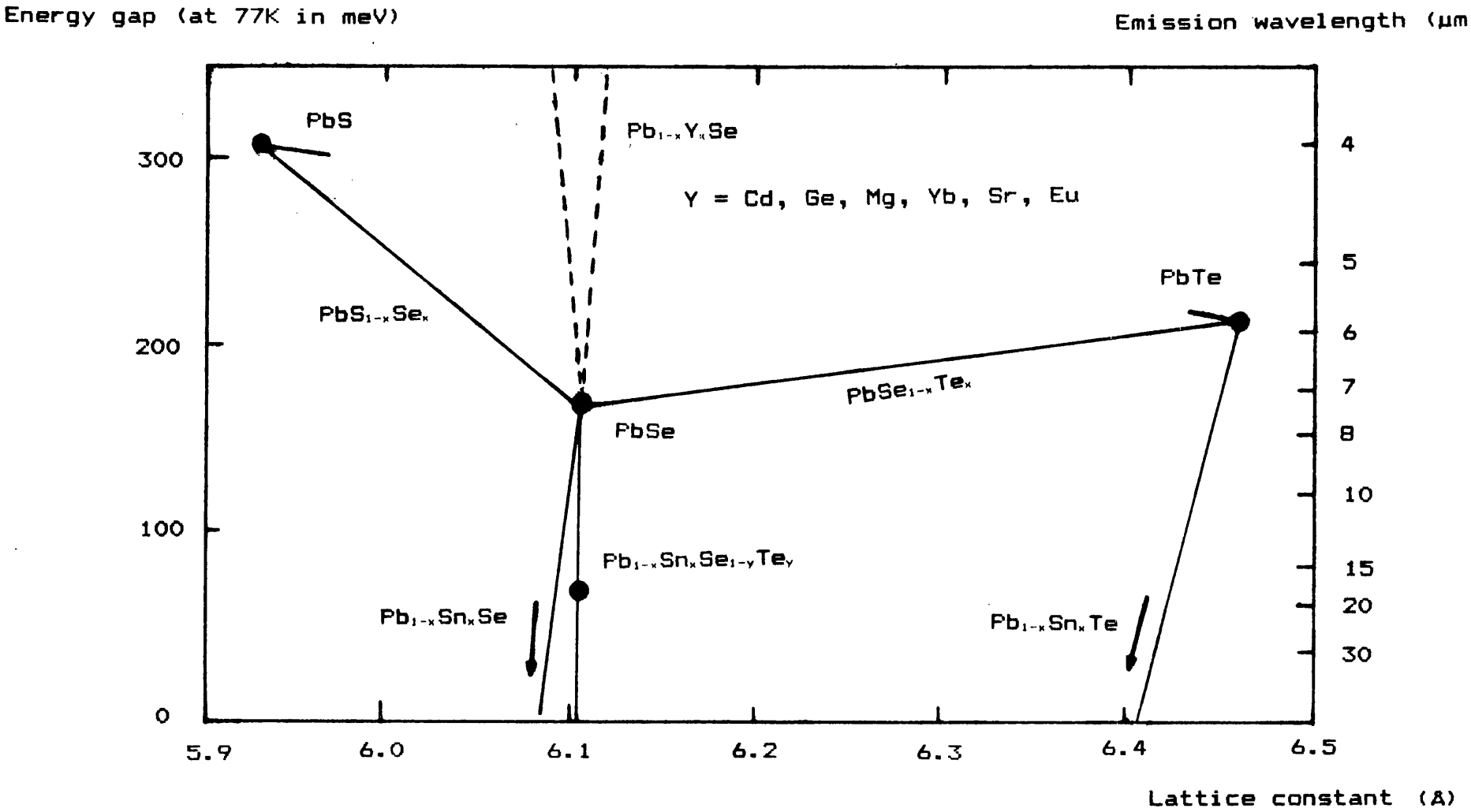


Fig(38). Energy gap versus lattice constant.

obtain wavelengths below 8µm. Confinement layers of PbS may be used with an active layer of $PbS_{1-x}Se_x$ to produce lasers having wavelengths as low as 5µm. However for the case of the PbS / $PbS_{1-x}Se_x$ system below 5µm, the optical confinement in a simple DH laser becomes too small between the layers and a more complicated structure has to be used employing compounds of PbS which increase the band gap $E_g$ beyond that of pure PbS. Therefore, other ternary compounds based upon PbSe have been investigated to obtain large band gap materials. This enables a unified technology for laser production covering the spectral range required using a minimal number of alloys. The dotted lines in Fig(38) illustrate the course of action to be taken by using $Pb_{1-x}Y_xSe$ compounds.

Cadmium, germanium, manganese and strontium and the rare earths europium and ytterbium all form compounds of the form $Pb_{1-x}Y_xSe$ with PbSe. Each compound has the property of producing an increasing band gap $E_g$ with an increasing composition factor x. Of these, cadmium {76}, {77}, germanium {78} and manganese {77} have alloying problems and ytterbium {79} acts as a donor. The $Pb_{1-x}Eu_xSe$ alloy has been investigated as a suitable material having a sufficiently large band gap for laser devices working near the 3µm region of the IR spectrum and is introduced in section 2.3.4.

2.3.2) $Pb_{1-x}Sn_xSe$ alloys

Fig(39) shows the temperature - composition diagram for the PbSe - SnSe system {80}. The phase diagram is of the eutectic type, the eutectic temperature being 1143K. There is considerable separation between the liquidus and solidus for the cubic $B_1$ structure alloys. For the orthorhombic $B_{2v}$ this difference is negligible since the eutectic temperature is only 2K lower than the melting point of SnSe. In this work, the shorter wavelength material is important thus all discussions on $Pb_{1-x}Sn_xSe$ will be limited to the cubic $B_1$ alloy with $x \leqslant 0.43$.

In Fig(40), the existence range for PbSe is presented {81}, {82}. It can be seen that the existence range for PbSe is approximately symmetrical with respect to the stoichiometric composition and shifts towards the Se side of the diagram as the SnSe content increases.

In the range of solubility of $Pb_{1-x}Sn_xSe$, the variation in band gap is nearly proportional to the composition x. Fig(41) shows in detail the dependence of the band gap upon the composition for the $Pb_{1-x}Sn_xSe$ system {83}. Laser emission has been obtained in $Pb_{1-x}Sn_xSe$ diodes with x upto 0.28 {84}. The results of the work from Harman et al support a band model in which

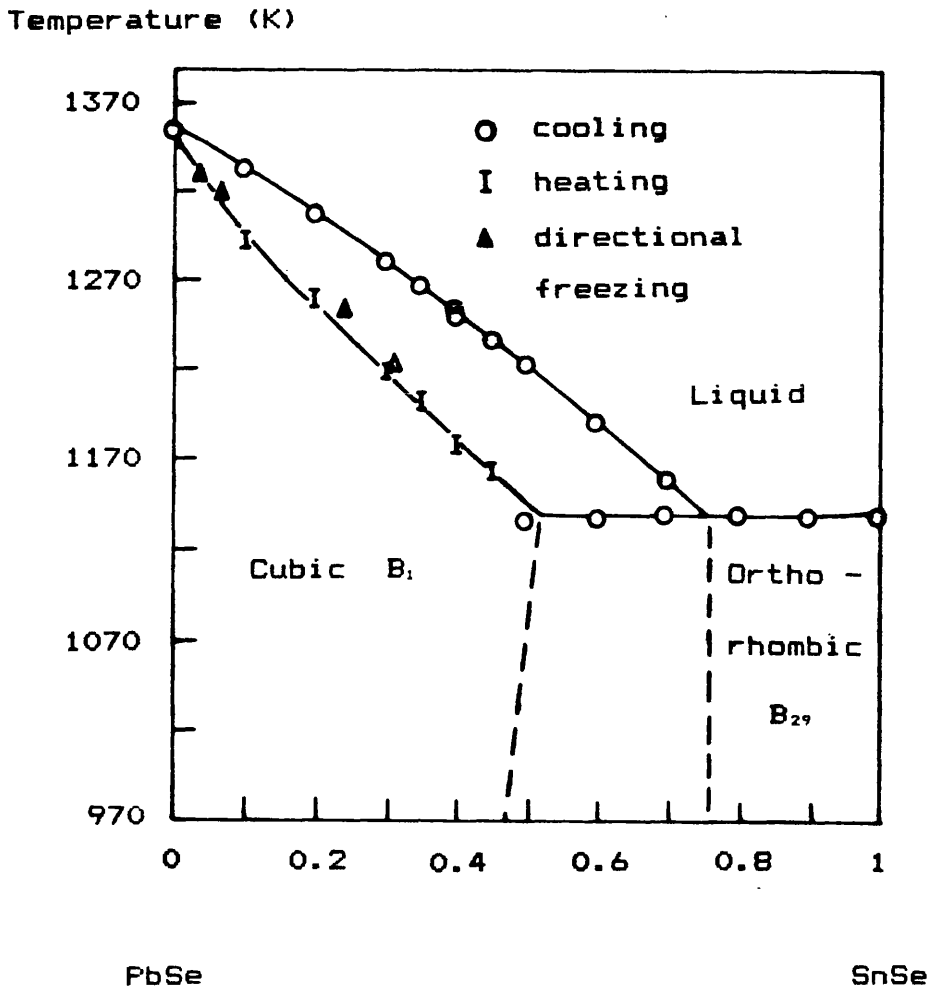


Fig(39). Temperature - composition diagram for the PbSe - SnSe system {80}.

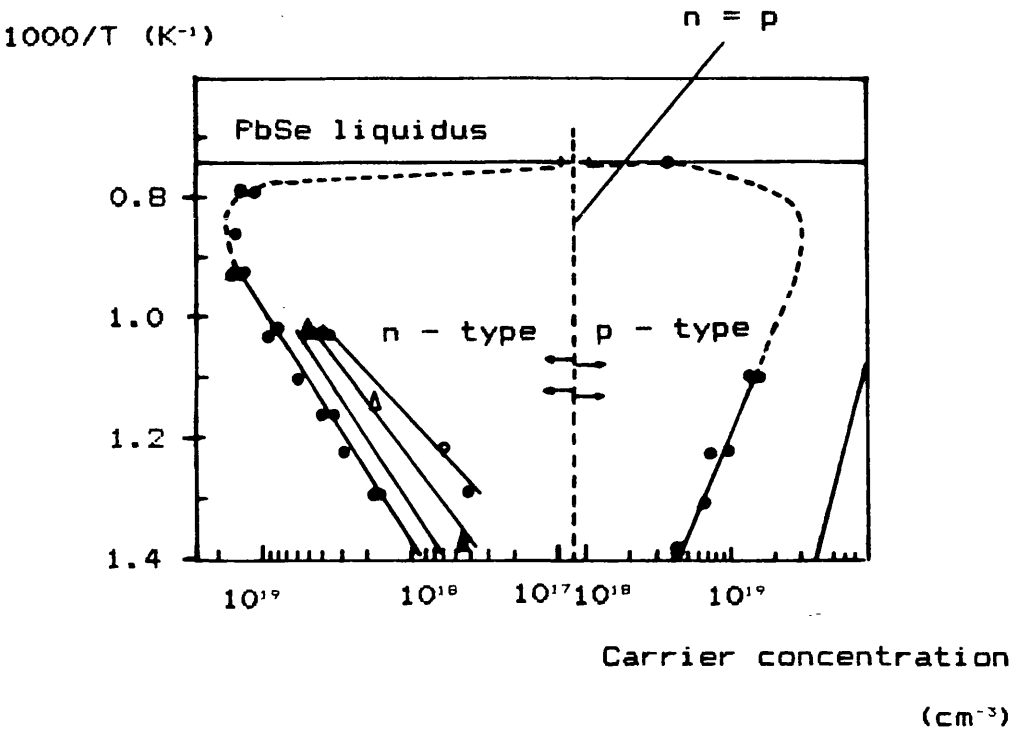


Fig(40). Carrier concentration versus isothermal annealing temperature for $Pb_{1-x}Sn_xSe$ {81}, {82}.

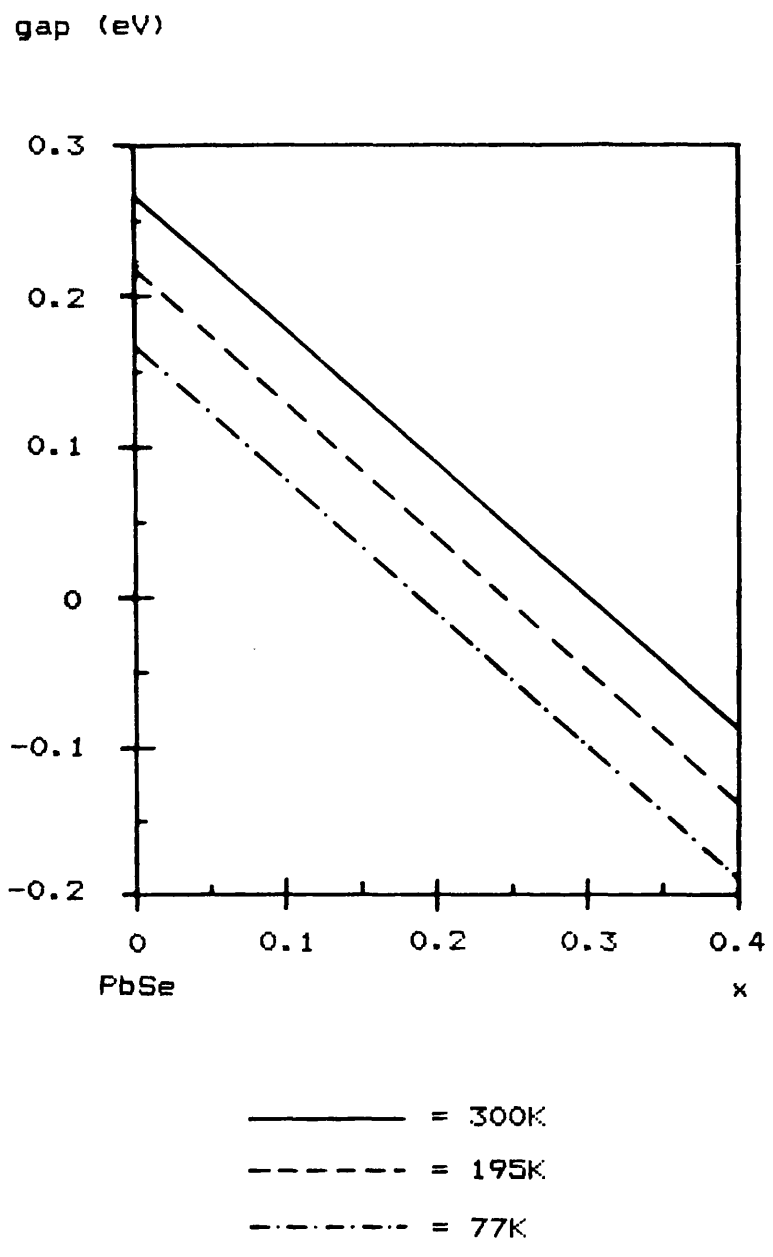


Fig(41). Variation of energy gap with composition and temperature for $Pb_{1-x}Sn_xSe$ alloys {83}.

the conduction and valence band edge states cross as the Sn content is increased from 0 to 0.28. For $x < 0.1$, the temperature coefficient of the energy is positive whereas for $x > 0.19$, the temperature coefficient is negative. The results also indicate that the band gap is direct on both sides of the crossover point which at 4.2K occurs for $x = 0.15$.

### 2.3.3) $PbS_{1-x}Se_x$ alloys

The temperature - composition phase diagram for the $PbS_{1-x}Se_x$ system is presented in Fig(42) {85}. Unlike the $Pb_{1-x}Sn_xSe$ system, the $PbS_{1-x}Se_x$ alloys exhibit complete solubility and solidus lines for the $PbS_{1-x}Se_x$ alloy system are shown in Fig(43) {86} where the metal - rich data are taken from work by Strauss {87}. As in the case for PbSe, the solidus field for PbS is approximately symmetrical with respect to the stoichiometric composition.

The dependence of the optical energy gap $E_g$ with the composition factor x is nearly a linear relation, similar to the $Pb_{1-x}Sn_xSe$ system {88}. Fig(44) shows in detail the dependence of the energy gap with composition. Lasers fabricated using the $PbS_{1-x}Se_x$ system theoretically have emission wavelengths ranging from 4μm ($x = 0$) to 7.5μm ($x = 1$) at 77K.

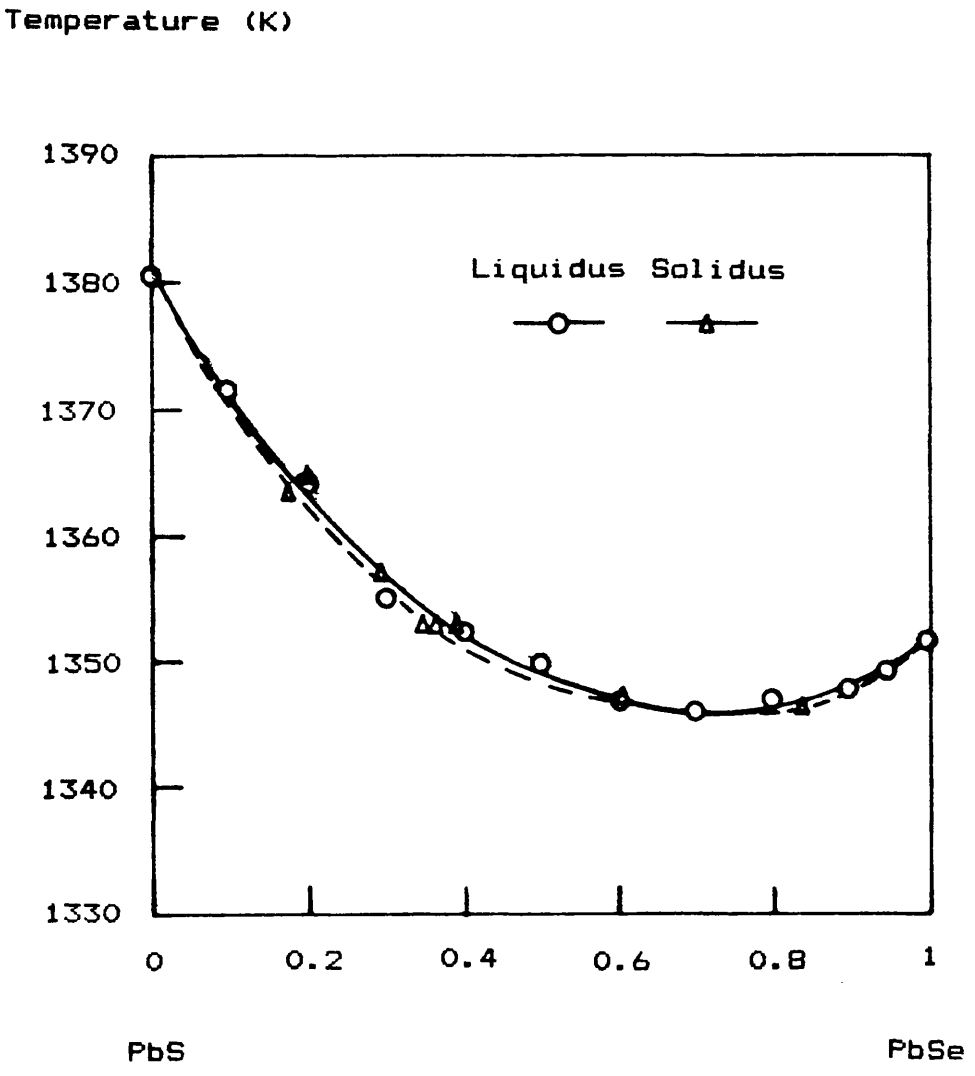


Fig(42). Temperature - composition diagram for the PbSe - PbS system (85).

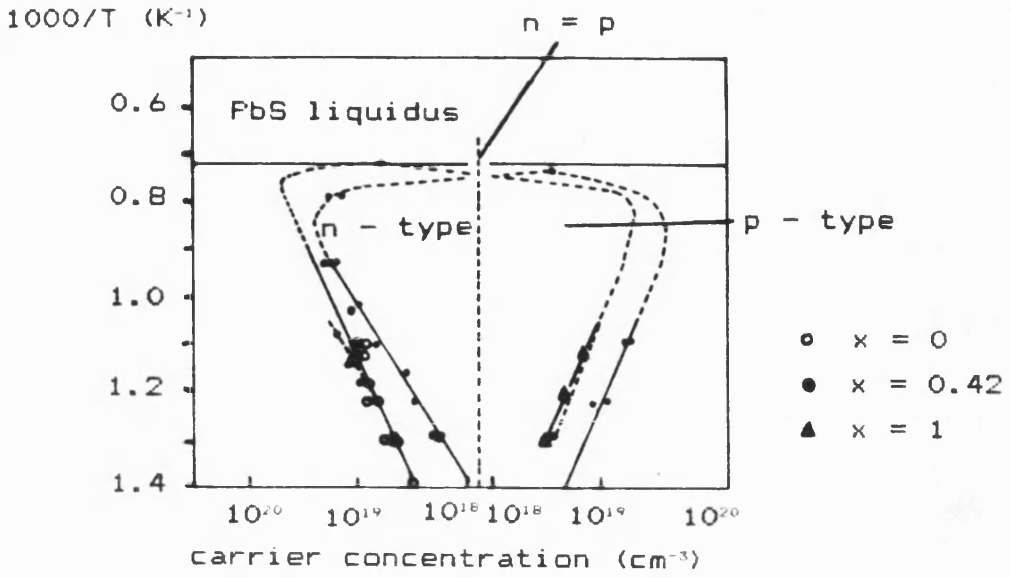


Fig(43). Carrier concentration versus isothermal annealing temperature for $PbS_{1-x}Se_x$ {86}, {87}.

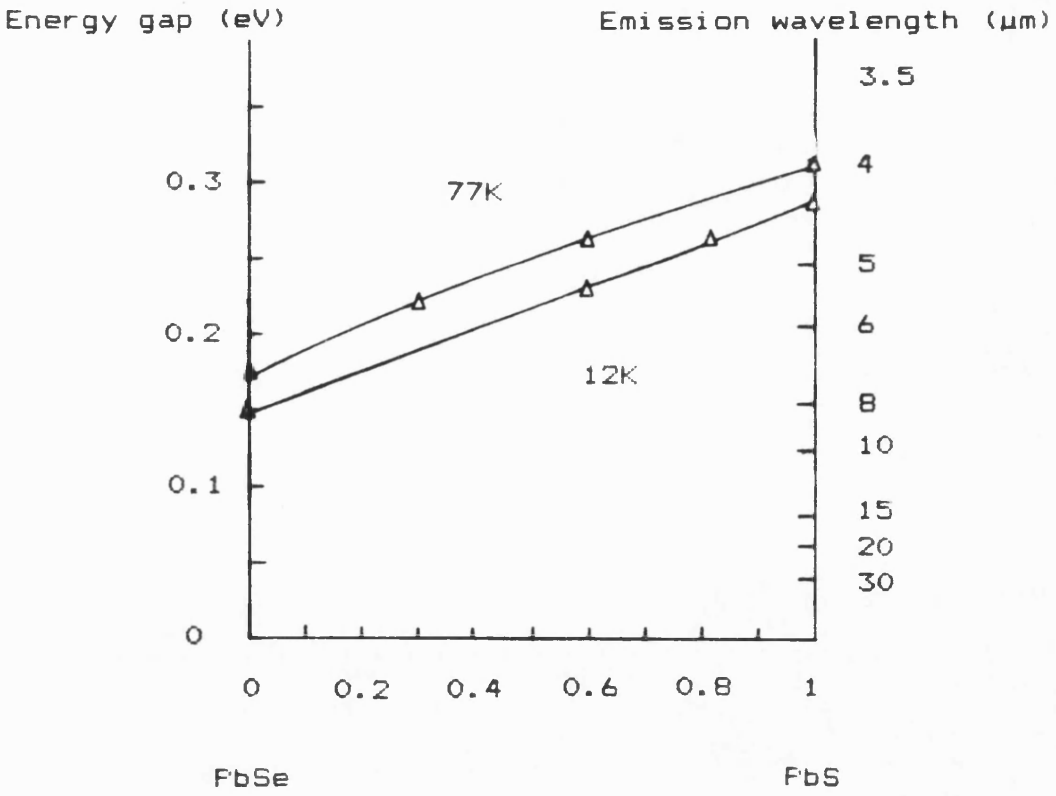


Fig(44). Composition dependence of the energy gap in $PbS_{1-x}Se_x$ {87}.

2.3.4) $Pb_{1-x}Eu_xSe$ alloys

The $Pb_{1-x}Eu_xSe$ alloy is interesting for covering the short wavelength range of lead chalcogenide diode lasers. The information upon the $Pb_{1-x}Eu_xSe$ system available at present is described below, and section 4.5 covers the work performed by the author.

The rare earth selenide compounds are face centred cubic. Eu tends to be divalent in monochalcogenides due to the relative stability of the half - full 4f shells. The divalent Eu ions are larger than the trivalent ions, thus resulting in a slightly larger lattice constant than other rare earth selenides (exceptions are SmSe and YbSe). EuSe has a lattice constant of 6.191Å {89} compared to the PbSe lattice constant of 6.126Å thus providing the possibility of good lattice - matched systems.

The $Pb_{1-x}Eu_xTe$ system shows a large increase in band gap with relatively small concentrations of Eu {90}. Assuming that EuTe and EuSe have similar properties, it is to be expected that the $Pb_{1-x}Eu_xSe$ system also exhibits this strong dependence of the band gap upon Eu content. The band gap of EuSe at 300K has been found to be 1.8 eV {91}.

# 3) MOLECULAR BEAM EPITAXY SYSTEM

## 3.1) Laser fabrication techniques

Lead chalcogenide semiconductor diode lasers have been prepared by a variety of techniques and these can be listed as follows:

a) Diffusion of foreign atoms;

b) compositional interdiffusion;

c) liquid phase epitaxy;

d) vapour phase epitaxy;

e) hot wall vapour deposition;

f) molecular beam epitaxy.

In this chapter methods a) - e) will be briefly described in the first two sections. MBE is introduced in section 3.1.3, followed by a detailed discussion of the technique which has been developed by the author for the growth of lead chalcogenide films and diode lasers. Emphasis is put upon the important factors governing the successful growth of lead chalcogenide compounds under MBE conditions and the inherent problems that arise from the properties of these materials.

### 3.1.1) Diffusional techniques

Cadmium is a suitable laser diffusant since it

has been shown that Cd produces low carrier concentration n - type material with a high mobility. At a Cd partial pressure of $1x10^{-3}$ mbar, the electron concentration becomes saturated to a value of $1.2x10^{18}$ $cm^{-3}$ in PbTe and is practically independent of the substrate type and concentrations. Electron mobilities of $3.8x10^{6}$ $cm^{2}V^{-1}s^{-1}$ have also been reported {92}.

A schematic diagram of a Cd diffused diode laser is shown in Fig(45). The Cd diffusion is performed with temperatures of the order of 670K using prepared p - type substrates with a hole concentration of between $1x10^{18}$ and $1x10^{19}$ $cm^{-3}$. The junction depth is proportionally dependent upon the square root of the diffusion time and is a function of the substrate hole concentration p {93}. Junction depths are of the order of a few microns after 1 hour and the depth can be controlled to ± 1μm.

Another diffusion technique is to anneal p - type $Pb_{1-x}Sn_xSe$, $PbS_{1-x}Se_x$ or $Pb_{1-x}Sn_xTe$ substrates in the presence of $Pb_{1-y}Sn_ySe$, $PbS_{1-y}Se_y$ or $Pb_{1-y}Sn_yTe$ powder respectively, thus forming heterostructures. This is the compositional interdiffusion technique (CID). Results from this type of laser are comparable to those of the Cd - diffused laser. Linden et al {94} have grown $PbS_{1-x}Se_x$ and $Pb_{1-x}Sn_xSe$ lasers based upon the CID technique.

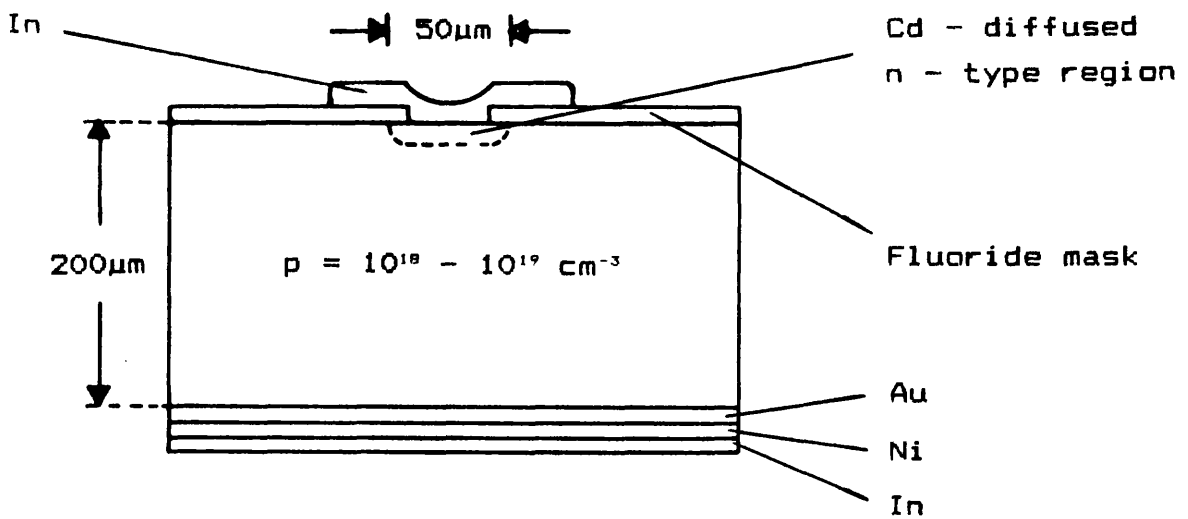


Fig(45). Schematic of Cd - diffused stripe lasers {93}.

3.1.2) Epitaxial film deposition

Lasers produced by the two above techniques suffer from poor electrical and optical confinement giving high threshold currents, low internal quantum efficiencies and low operating temperatures.

To obtain electrical and optical confinement, heterostructures must be used and can be produced by a number of techniques: liquid phase epitaxy (LPE); vapour phase epitaxy (VPE); MBE and hot wall vapour deposition (HWVD). Evaporative techniques are particularly attractive because the IV - VI semiconductors have convenient vapour pressures and sublime predominantly as diatomic molecules. Of the methods listed above, MBE and HWVD are best suited to growing multi - layers with thickness control in the 1μm range. This is required for active regions for lasers with lowest threshold currents, although liquid phase epitaxy does produce interfaces of superior quality.

Epitaxial layers of $Pb_{1-x}Sn_xTe$ grown by cooling from 800 - 780K in an LPE system yield hole concentrations of $1 \times 10^{18}$ $cm^{-3}$ (95). Results from X - ray diffractometry measurements indicate that for a 1μm thick epitaxial layer, the composition changes from 78.5% to 100% PbTe in a distance of less than 0.75μm. Although the

surfaces and interfaces produced by LPE are superior to the HWVD and MBE methods of film deposition, such a composition inhomogeneity is unacceptable.

Epitaxial layers of $Pb_{1-x}Sn_xTe$ grown upon PbTe substrates by the VPE technique show an even larger region of graded composition. Carrier densities of lead chalcogenides grown by VPE are approximately $2x10^{18}$ $cm^{-3}$ and electron microprobe analysis indicates that due to the relatively high deposition temperatures of 900K, some Sn diffuses from the layer into the substrate producing a graded composition layer of the order of 5μm thickness {96}.

The HWVD method has been applied to many lead chalcogenide alloy systems and Kasai et al {97}, for example, have grown $Pb_{1-x}Sn_xTe$. Growth rates are possible in the range 0.3 - 4.8 $\mu m hr^{-1}$ with typical source and baffle temperatures of 720 - 830K and a substrate temperature of 600K. Carrier concentrations of as - grown layers are in the range $1x10^{16}$ - $1x10^{17}$ $cm^{-3}$. The carrier mobility is of the order of $1x10^{4}$ $cm^2V^{-1}s^{-1}$ at 77K and hence the HWVD method is very acceptable for the growth of lead chalcogenide diode lasers.

### 3.1.3) The molecular beam epitaxy technique

The MBE technique dates back to the middle 1960's

when work in the optoelectronic field caused the start of intensive research and since then MBE has developed to the extent that reproducible control over lattice composition and thickness is now possible.

The basic MBE process achieves epitaxial growth through the reaction of multiple molecular beams of material with a heated single crystal substrate. This is illustrated in Fig(46) for the growth of doped $Pb_{1-x}Sn_xSe$. Each furnace encloses a crucible containing one of the constituent elements or compounds of the desired film. The temperature of each furnace is chosen so that the vapour pressures of the materials are sufficiently high for free evaporation of thermal energy molecular 'beams'. The furnaces are arranged so that the intersection of their axes coincide with the centre of the substrate surface. Through the choice of appropriate furnace and substrate temperatures, epitaxial films of the desired chemical composition can be obtained. Additional control over the growth process is achieved by means of individual furnace shutters situated between the furnace orifice and the substrate thus allowing abrupt interfaces to be fabricated.

The standard MBE system also incorporates a preparation chamber connected to the growth chamber via a transfer rod system to allow the possibility of loading

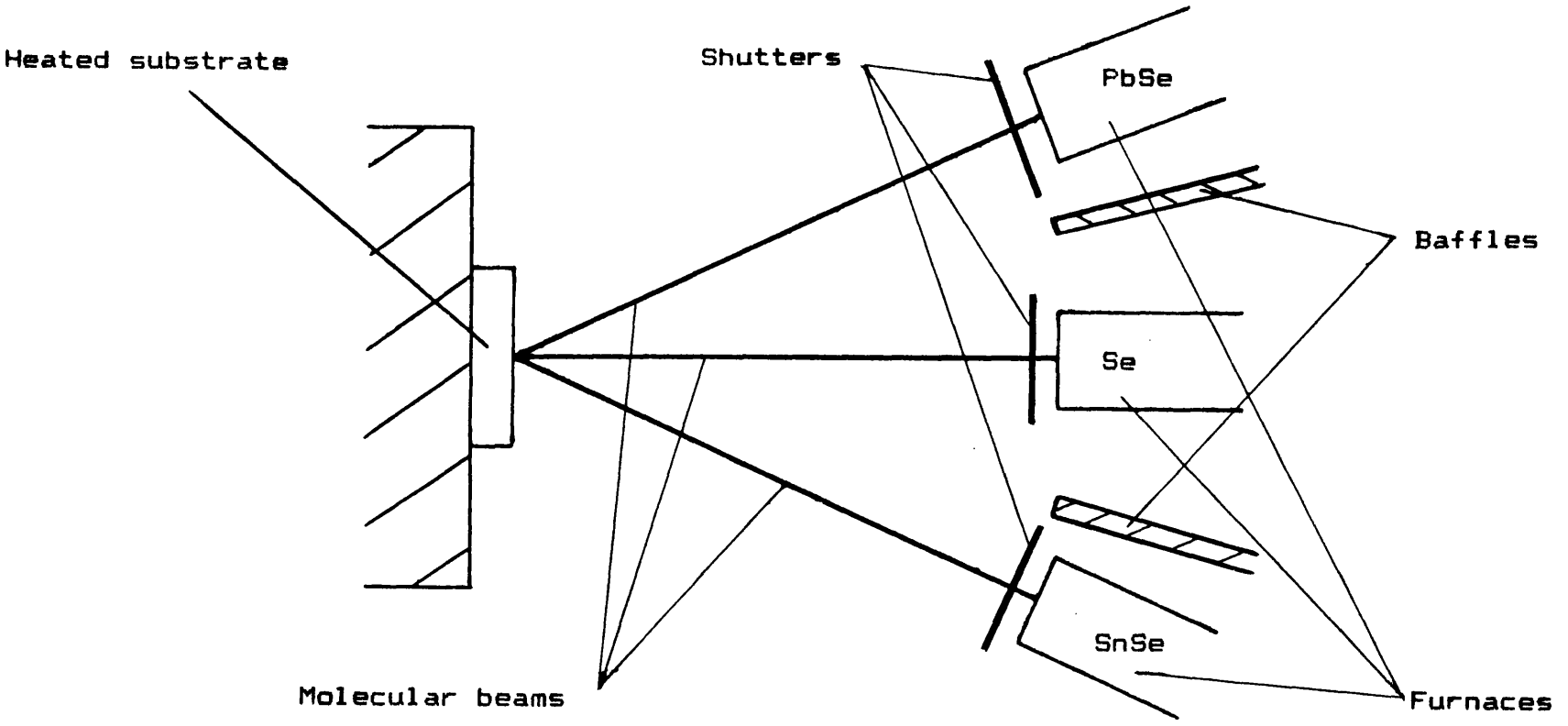


Fig(46). Illustration of the molecular beam epitaxy technique (furnaces shown are for the p - type growth of $Pb_{1-x}Sn_xSe$).

## 3.2) MBE vacuum system details

The original system concept was co - planned with Varian GmbH, Stuttgart, West Germany, the final welding work upon the chambers being performed by Varian S.p.A in Torino, Italy. Many other MBE - specific parts are also of Varian origin and the contrary will be mentioned where appropriate.

The system is an ultra - high vacuum (UHV) system consisting of two chambers (the working chamber and the loading chamber), pumps and ancilliary equipment. Fig(47) and Fig(48) show pictures of the vacuum system and the electronic racks respectively. Fig(49) and Fig(50) are diagrams to supplement the details of the MBE system. The working chamber houses the furnaces, substrate holder, beam flux monitor, mass spectrometer and cryoshield, the details being given in Fig(51a) and Fig(51b). This is connected to the loading chamber via a gate valve through which a magnetically operated transfer rod arrangement can pass. This rod is mounted in the loading chamber which accomodates upto seven substrates stored in holders on a rotating wheel. A side view of the loading chamber is shown in Fig(52).

The need for UHV conditions arises from the relatively slow growth rate of approximately 2 $\mu m hr^{-1}$ in comparison, for example, with LPE where growth rates can

Fig(47). Photograph of the molecular beam epitaxy system built by the author for the growth of lead - salts.

Fig(48). Photograph of the three electronic racks housing control equipment for the MBE system.

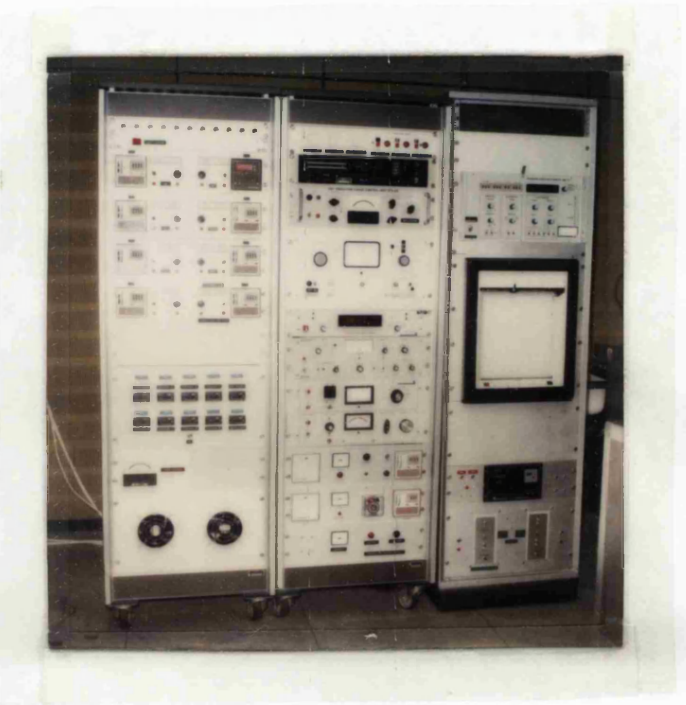

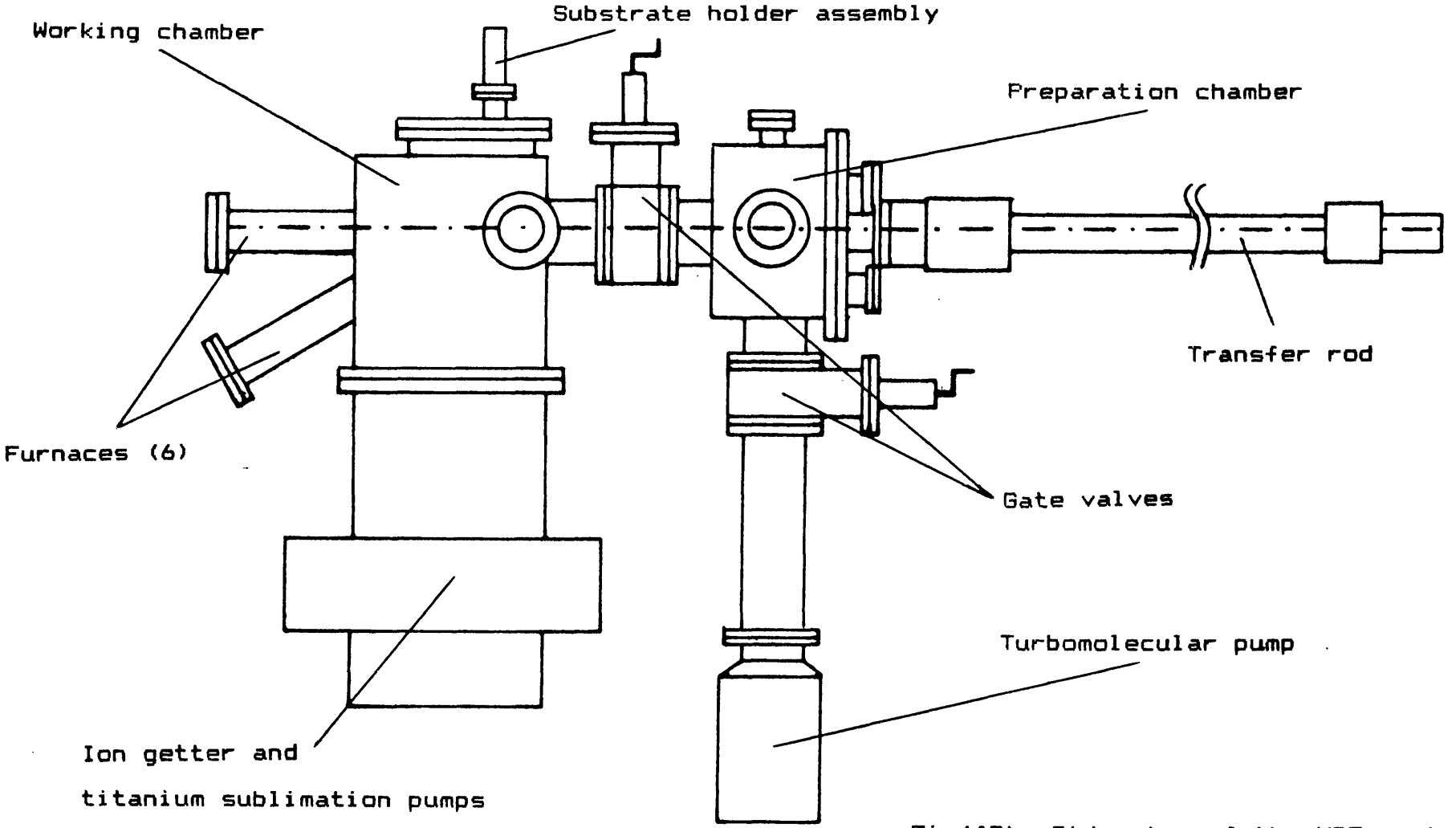


Fig(49). Side view of the MBE system.

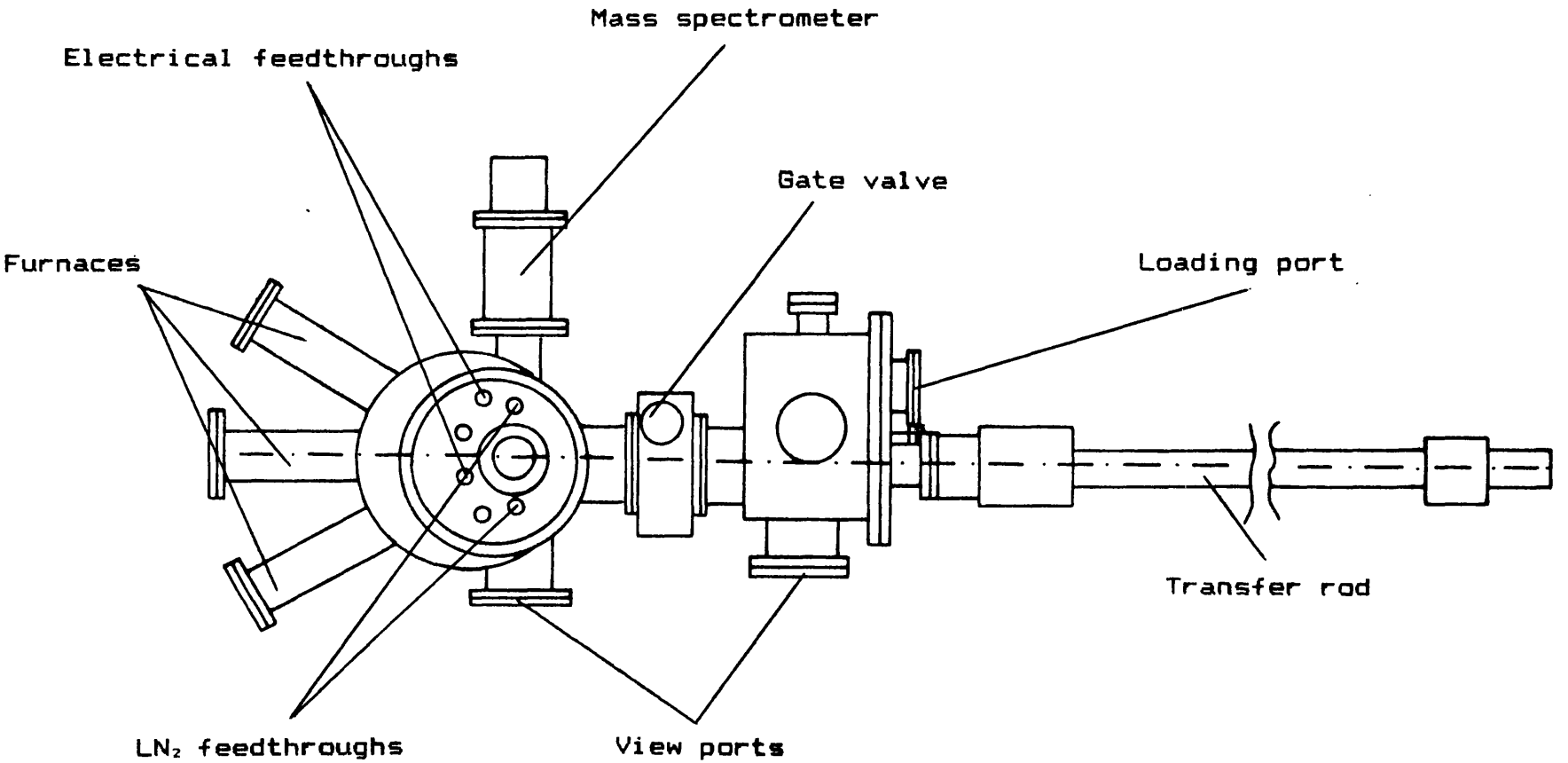


Fig(50). Top view of the MBE system.

Fig(51a). Details of the working chamber (side view).

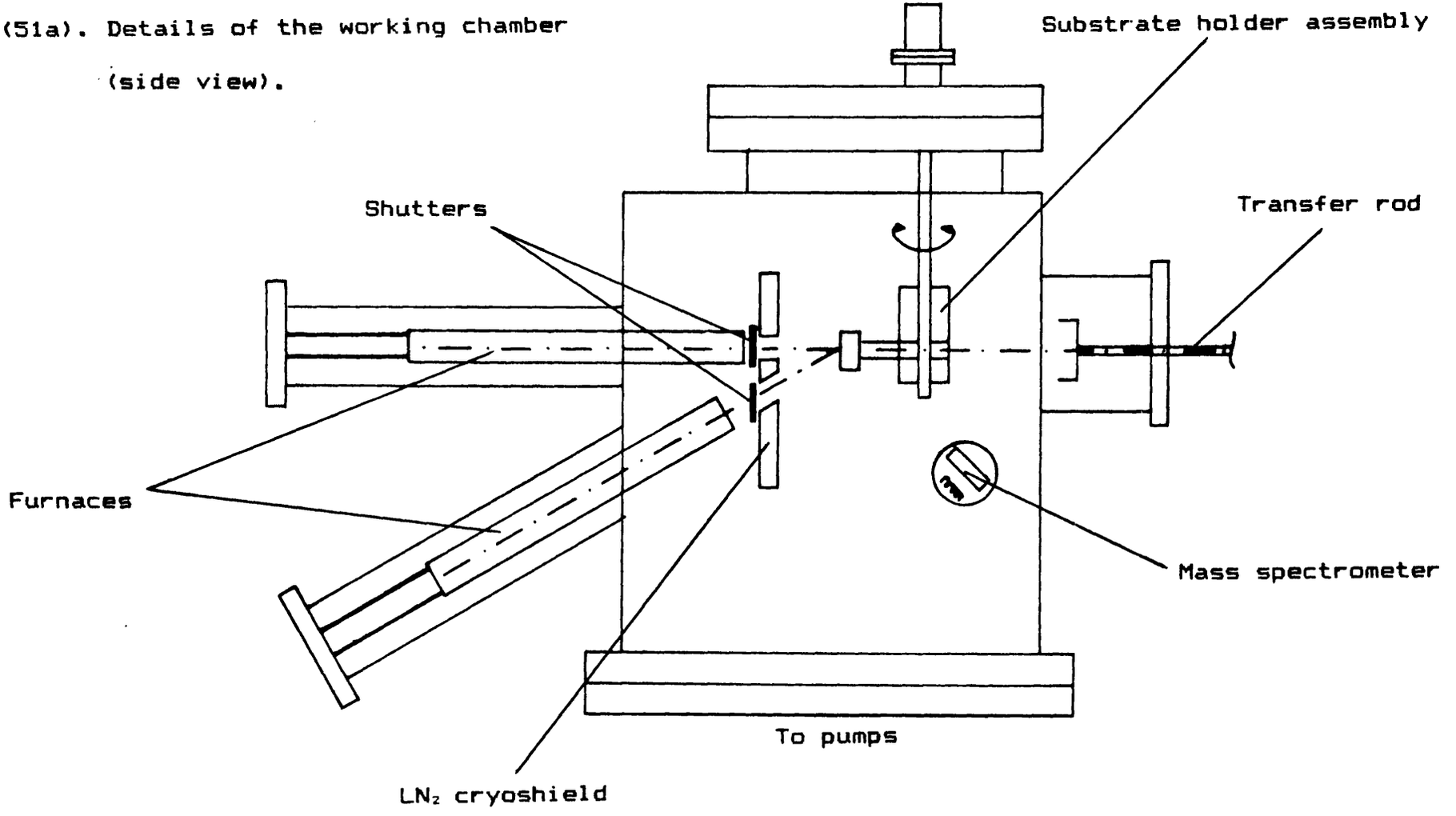

Fig(51b). Details of the working chamber (top view).

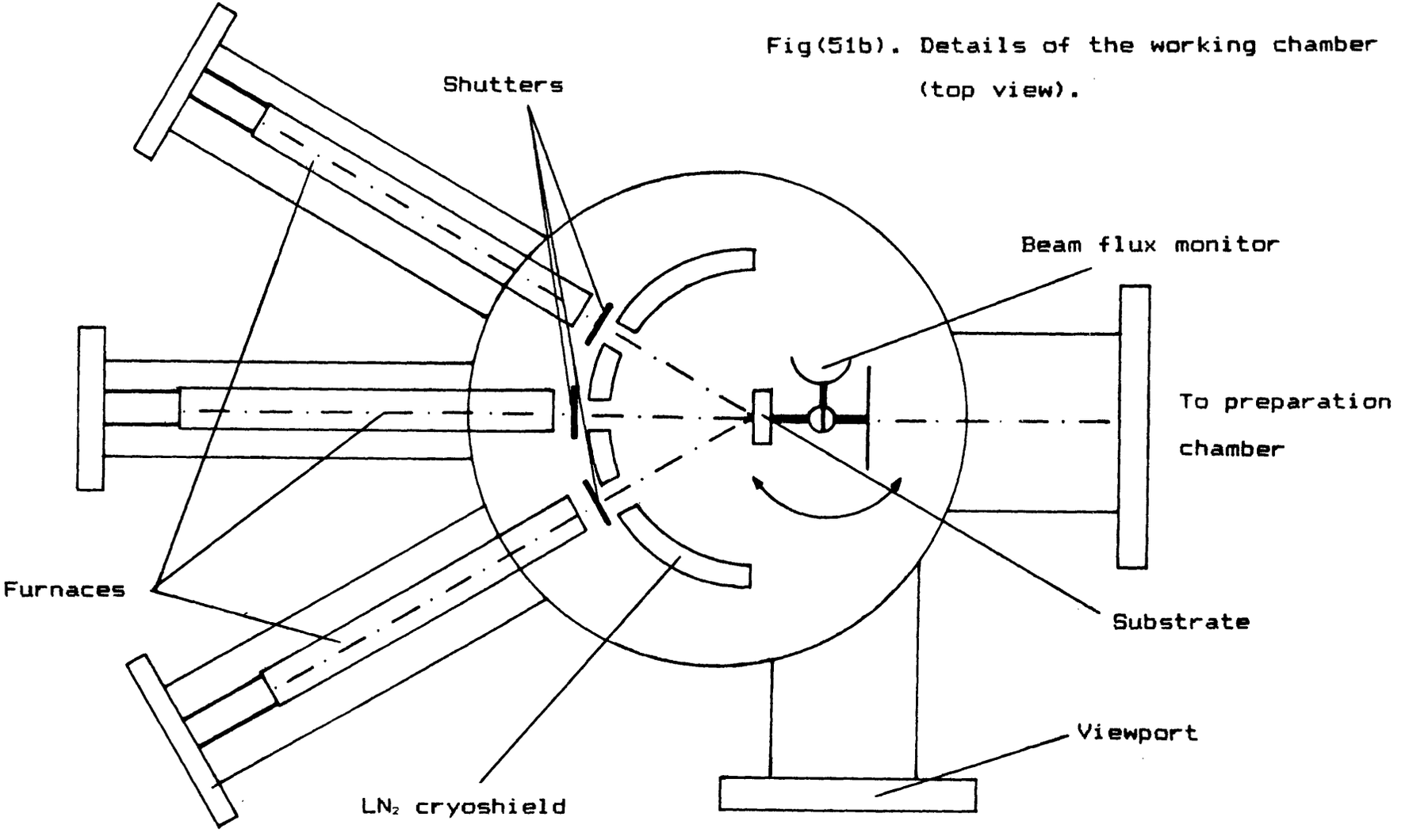

Fig(52). Preparation chamber in detail (side view).

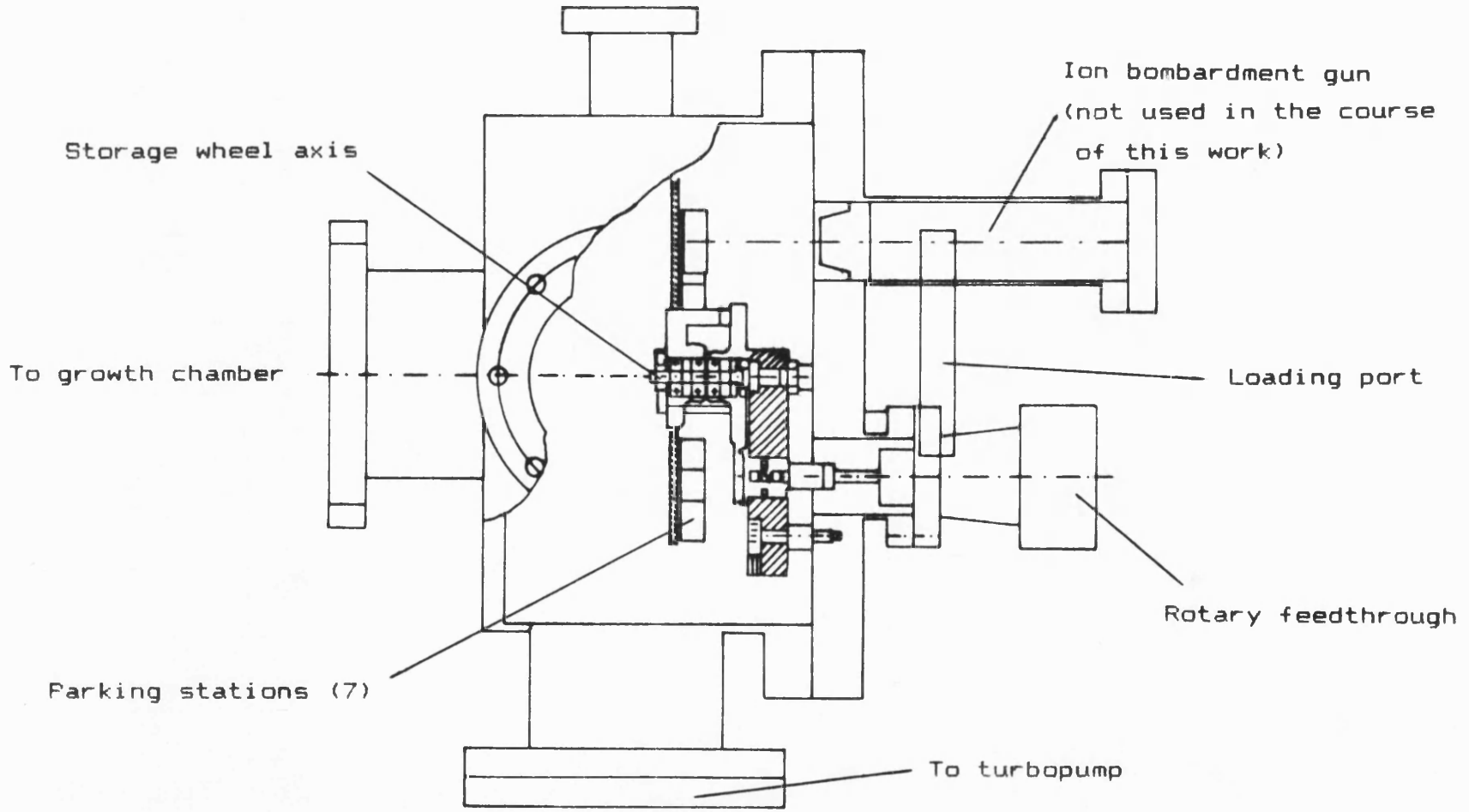

be as high as 60 $\mu mhr^{-1}$ {98}. If a background gas species with a unity sticking coefficient on the growth surface were present in the vacuum chamber at pressures of $1x10^{-6}$ mbar, roughly half of the grown film would be contaminants. Partial pressures of gases with high sticking coefficients must therefore be maintained to a very low value to avoid incorporation. This value has been estimated as having to be better than $1x10^{-10}$ mbar {99}.

To obtain such a low vacuum, the system is constructed of low vapour pressure stainless steel (type BS 304S15 with composition: S-0.03%; P-0.045%; C-0.08%; Si-1%; Mn-2%; Ni-10%; Cr-19% and Fe-68%) which can be baked out to 650K. The system constructed in this work is restricted to a bakeout temperature of 470K due to the fluorelastomer gaskets used in the two gate valves. After bakeout, the stainless steel has the negligible outgassing rate of $1x10^{-12}$ - $1x10^{-14}$ mbar 1 $s^{-1}cm^{-2}$. The growth chamber is equipped with a maintenance - free 200 l $s^{-1}$ Ultek ion getter pump and an Ultek titanium sublimation pump which maintains the background pressure (measured at the circumference of the chamber with hot furnaces) to a level of $1x10^{-9}$ mbar. The integral cryoshield surrounding the substrate holds the vacuum well below this value in the vicinity of the substrate to

minimise the incorporation of contaminants.

The UHV achieved in the working chamber takes over 48 hours to produce, therefore a load - lock system has been incorporated. The loading chamber is pumped via a versatile and quick 360 l $s^{-1}$ Leybold Heraeus turbomolecular pump which can achieve a vacuum of $1x10^{-7}$ mbar within 5 minutes thus permitting substrate transfer 90 minutes after loading without allowing a significant amount of water vapour to enter the working chamber.

This chapter will concentrate upon the important pieces of MBE apparatus. Section 3.3 discusses the MBE furnace in terms of requirements and results, section 3.4 shows the problems of MBE shutters and section 3.5 describes the substrate holder assembly.

## 3.3) Sources

One of the most important pieces of apparatus in an MBE system is the molecular beam source. Control and stability over long periods of time and beam characteristics govern the accuracy with which the stoichiometry and composition of the deposited film can be controlled.

Flexibility is one of the main advantages of the MBE technique. For example, with the binaries PbSe, PbS,

PbTe and SnSe as the separate source materials, layers of binary, ternary and quaternary material can be produced. The system described in this work was designed with six furnace ports, two for doping materials and the remaining four for combinations of the above materials. As the project proceeded, other materials such as europium, strontium and silver have been loaded for the use in the lead chalcogenide alloy systems.

### 3.3.1) Source flux rate requirements

The growth rate of the growing film is directly proportional to the main material furnace flux rate. When the sticking coefficient of the material on the substrate is unity then a flux rate of $1 \times 10^{15}$ molecules $s^{-1}cm^{-2}$ arriving at the substrate surface corresponds to a deposition rate of approximately a monolayer per second. This gives an acceptable overall growth rate of $2\ \mu m hr^{-1}$.

Fig(53) illustrates two possible forms of furnace construction namely the open ended type and the Knudsen cell. The governing factors for the flux rates are the furnace temperature $T_s$, the orifice diameter d (in the open ended type, $d = d_{furnace}$) and the material surface area $A_m$ (in the Knudsen cell, $A_m$ is not important due to the fact that $d \ll d_{furnace}$).

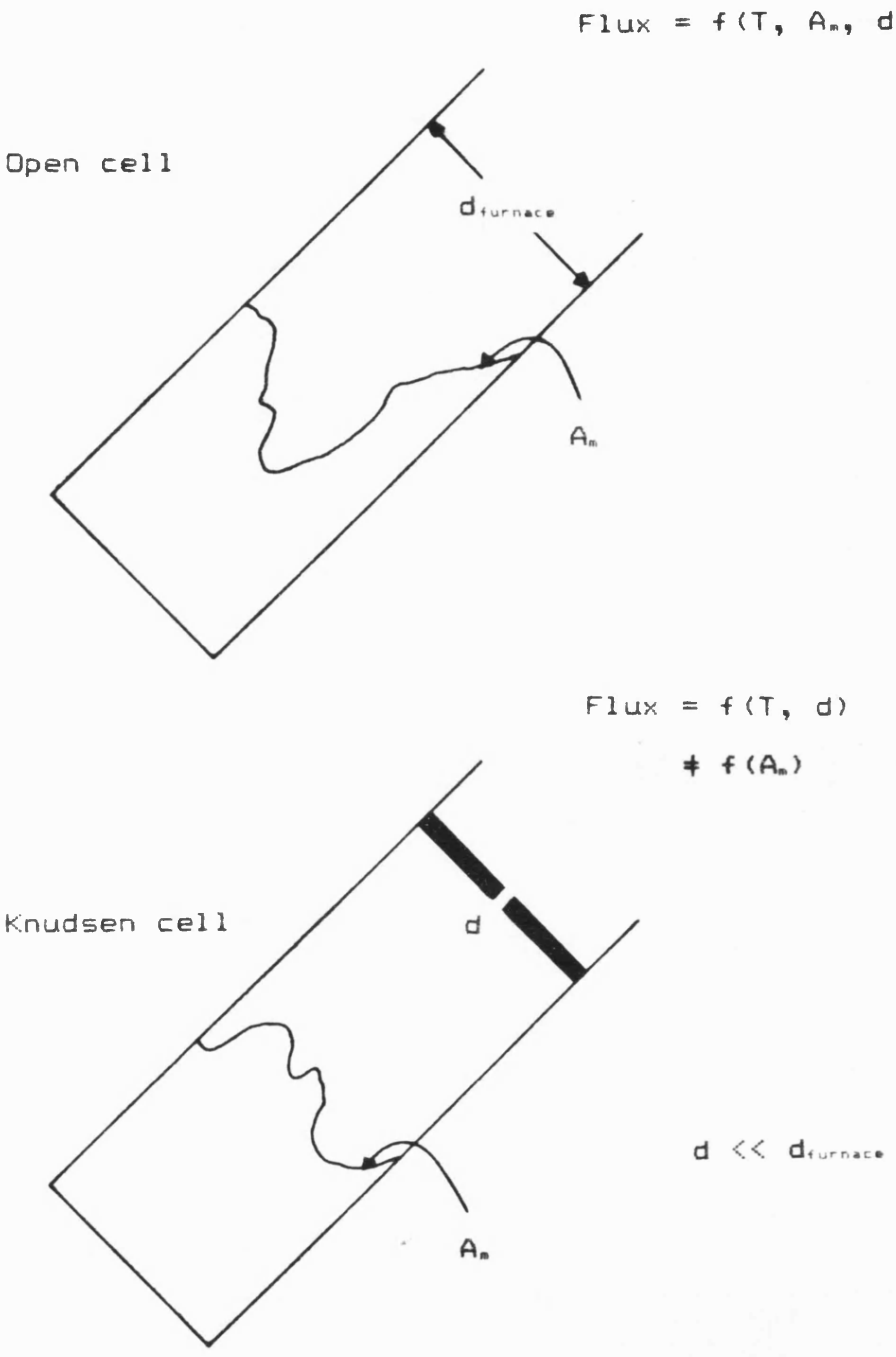


Fig(53). Schematic of two types of source used in MBE systems.

The open ended source is frequently used in the II - VI compound semiconductor system due to the low vapour pressures of the materials at temperatures where the materials are liquid hence producing a constant $A_m$. The lead chalcogenides have relatively high vapour pressures suggesting that an open ended type of furnace will require a low operating temperature to obtain the same flux rate. Low temperatures are difficult to control in a UHV environment due to the lack of heat conduction through the vacuum, meaning that the lead chalcogenides are solid at the operating temperatures. This is a disadvantage in the open ended source due to a continuous variation in $A_m$ and hence the Knudsen cell arrangement was necessary for the work presented here.

The expected flux rate from an ideal Knudsen cell with a particular source material can be calculated. The source material is assumed to effuse from the thin - walled furnace orifice in a hemispherical pattern in which the flux at any position on the hemisphere is proportional to the cosine of the angle from the orifice normal. The cosine law distribution is such that the flux at the normal is twice the average flux over the hemisphere and is given by

$$2\pi D^2 \left(\frac{\Gamma}{2}\right) = \frac{\pi}{4} \; 4r^2 \; \Psi \qquad (40)$$

where $\Gamma$ is the flux (molecules $cm^{-2}s^{-1}$) incident on a substrate positioned at a distance D (cm) from an orifice of radius r (cm) emitting a flux $\Psi$ (molecules $cm^{-2}s^{-1}$). Rearranging, equation 40 becomes

$$\Gamma = \left(\frac{r}{D}\right)^2 \Psi \qquad \text{molecules } cm^{-2}s^{-1} \qquad (41)$$

Assuming a true Knudsen cell where the pressure p (mbar) of the cell is kept low enough to maintain molecular flow through the orifice and where vapour - solid equilibrium is maintained, it can be shown that

$$\Psi = \frac{p}{\sqrt{2\pi\ mM\ kT_e}} \quad \text{molecules } cm^{-2}s^{-1} \qquad (42)$$

Here k ($JK^{-1}$) is the Boltzmann constant, M (kg) is the atomic mass unit, m the atomic weight of the effusand and $T_e$ (K) is the isothermal temperature of the furnace. Vapour pressures $p_{(atm)}$ of the effusand are given by the standard Clausius - Claperion equation {100}

$$\log_{10} p_{(atm)} = b - \frac{a}{T_e} \qquad (43)$$

where a ($K^{-1}$) and b are material constants given in Table (5) {101}. Combining the equations 41, 42 and 43, the flux rate impinging upon the substrate can be quantitatively written in terms of molecules $cm^{-2}s^{-1}$ as

$$\Gamma = \frac{2.7\times10^{19}}{\sqrt{mT_e}} \left(\frac{r}{D}\right)^2 \exp\left(2.3\left(b - \frac{a}{T_e}\right)\right) \qquad (44)$$

| Material | a ($K^{-1}$) | b | atomic weight m |
|---|---|---|---|
| PbSe | 11032 | 7.302 | 286.15 |
| SnSe | 10495 | 7.318 | 197.65 |
| PbTe | 11636 | 7.946 | 334.79 |
| PbS | 11780 | 7.448 | 239.25 |

Table (5). The material constants a, b and m for selected lead chalcogenides (101).

This numerical equation can be used to find the approximate operation temperature required for a given flux rate and furnace geometry. Fig(54) shows a computer plot of flux rate versus furnace temperature for PbSe in a furnace having an orifice diameter of 2mm and a substrate to orifice distance of 190mm which corresponds to the system distance for one of the lower furnace ports.

### 3.3.2) Source stability requirements

Due to the fact that interface states between two non - lattice - matched layers can give rise to undesirably short carrier lifetimes, it might be necessary to lattice - match epitaxial layers to the PbSe substrate {102}. This can be achieved by the addition of Te thus correcting the mismatch in the form of the quaternary material $Pb_{1-x}Sn_xSe_{1-y}Te_y$. It is of utmost importance to design furnaces that are stable enough to produce the minimum amount of deviation from the required stoichiometery necessary to produce lattice - matched layers. The amount of mismatch that an active layer can allow without having a detrimental effect upon lasing characteristics is dependent upon its composition and its thickness. It has been suggested that with active layer

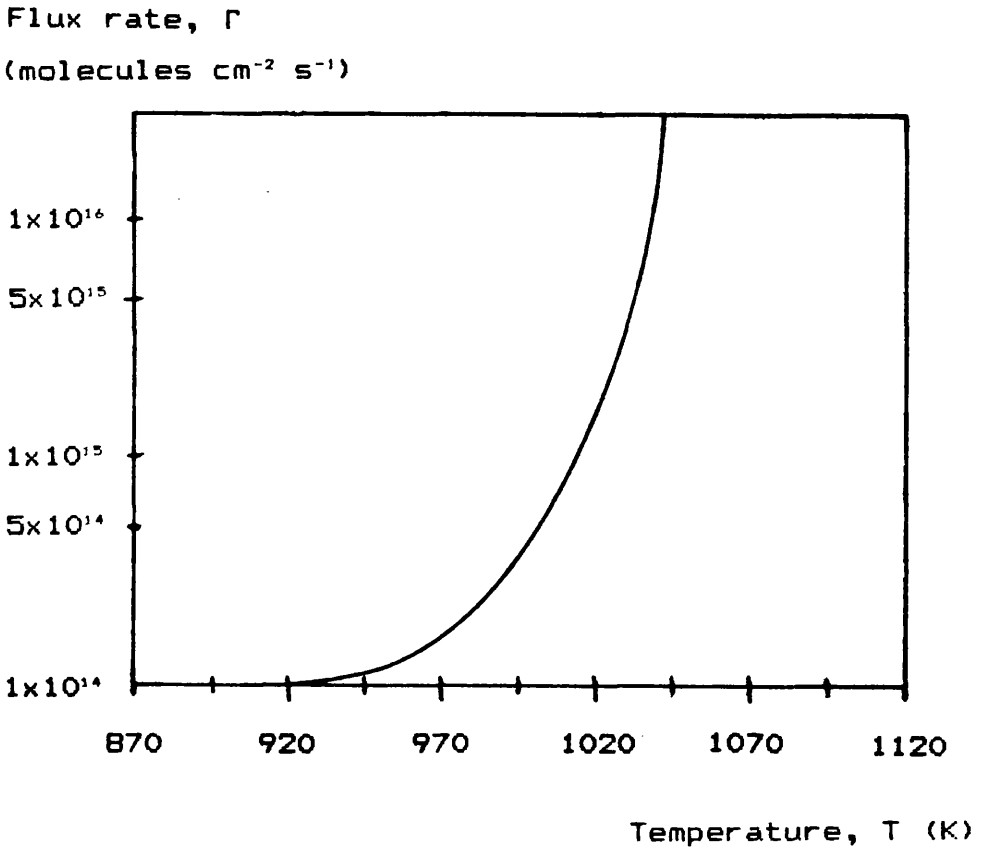


Fig(54). Plot of PbSe flux versus furnace temperature for an orifice - substrate distance of 190mm and an orifice diameter of 2mm according to **equation 44.**

thicknesses of 0.5μm in the PbSe rich area of the $Pb_{1-x}Sn_xSe$ system, lattice - matching of better than 0.01% is necessary {102}.

If $a_1$ is the lattice constant of the cladding layers and $a_2$ is the lattice constant of the active region, then this requirement can be written as

$$\frac{\Delta a}{a} = \frac{2\ (a_1 - a_2)}{a_1 + a_2} = 1 \times 10^{-4} \qquad (45)$$

In order to find the lattice - matching composition, it is necessary to use the generalised modification of Vegard's Law as derived by Moon et al {103}. According to this model, the lattice constant of the quaternary compound $Pb_{1-x}Sn_xSe_{1-y}Te_y$ is given by

$$a_{PbSnSeTe} = xya_{SnTe} + x(1-y)a_{SnSe} + (1-x)a_{PbTe} + (1-x)(1-y)a_{PbSe} \qquad (46)$$

where $a_{PbTe}$ = 6.460 Å {104}

$a_{PbSe}$ = 6.126 Å {104}

$a_{SnTe}$ = 6.328 Å {105}

and $a_{SnSe}$ = 6.003 Å {106} at 300K.

Inserting these parameters into equation 46

$$a_{PbSnSeTe} = 6.126 + 0.334y - 0.123x - 0.009xy \quad \text{Å} \qquad (47)$$

In the PbSe rich area, $x \ll 1$ and $y \ll 1$ and equation 47 reduces to

$$a_{PbSnSeTe} = 6.126 + 0.334y - 0.123x \quad \text{Å} \qquad (48)$$

For lattice - matching

$$\left(\frac{da}{dx}\right)_y = -0.123 \qquad (49)$$

Therefore

$$\frac{\Delta a}{a} = -\frac{0.123\Delta x}{a_{PbSe}} = 0.02\Delta x \qquad (50)$$

The required lattice - match as stated above is $\Delta a/a = 1\times10^{-4}$. Hence from equation 50

$$\frac{\Delta x}{x} = \frac{5\times10^{-3}}{x} \qquad (51)$$

For lasers emitting in the 10μm region at 80K, $x = 0.05$ and implies from equation 51 that the acceptable error in the x value $\Delta x/x$ is approximately 0.1. Similarly for y, $\Delta y/y$ is approximately 0.03. DH lasers of wavelengths approaching 8μm using the $Pb_{1-x}Sn_xSe_{1-y}Te_y$ system reach their lower wavelength limit due to the inherent lack of confinement. Here $\Delta x/x = \Delta y/y = 0.02$ and this was set as the goal for the stability of the main material furnaces.

Similar results are found for the stability required to fix a certain laser emission wavelength to within 1% accuracy around 16μm. At wavelengths around 10μm, acceptable errors in composition are of the order

2 - 3%.

As mentioned above, the flux rate of the furnace is directly proportional to the furnace temperature. Here the stability of a furnace is dependent mainly upon the temperature stability. The required temperature stability can be estimated assuming that chemical potential equilibrium is present within the Knudsen cell. Thermodynamic considerations lead to an empirical equation relating the pressure fluctuations $\Delta P/P$ within a Knudsen cell at a temperature T = 1000K to the temperature fluctuations $\Delta T/T$

$$\frac{\Delta P}{P} = 25.334 \quad \frac{\Delta T}{T} \qquad (52)$$

Therefore, in an MBE furnace loaded with PbSe, PbS, PbTe or SnSe, a temperature stability of $\Delta T = 0.8K$ is required if a flux stability of 2% is to be maintained. This is calculated by assuming that the local pressure fluctuations $\Delta P/P$ are directly responsible for the flux variations. This is a stability which can be achieved by the use of modern temperature regulators. Standard furnaces from the Varian company have been used and the resulting flux stability is described in the next section.

### 3.3.3) Practical binary material sources

The characteristics of a furnace with a 2mm diameter orifice in a lid placed in the middle of the standard 130mm long Varian crucible are discussed here. The furnace details are given in Fig(55). The furnace itself is constructed from tantalum and the crucible from surface - treated graphite rather than pyrolytic boron nitride since this is easier to machine. Due to the inherent reactive nature of selenium and its compounds, the thermocouple is tungsten / 26% rhenium - tungsten / 5% rhenium.

Fig(56) shows that the flux rate from this furnace is stable and free from variations upon the minute scale which is important for laser active layer growth where the emission wavelength depends upon the stoichiometric composition and where active layer growth times are short. Flux rates are given in millibar due to the method of measurement. An open ionisation gauge is used and a direct calibration of the measured pressure values into actual flux rates is not necessary. Relative, and not absolute, flux rates are of importance to the work here in determining growth rates and setting film compositions. An overall constant fall rate of approximately 2% $hr^{-1}$ can be seen in the charge -

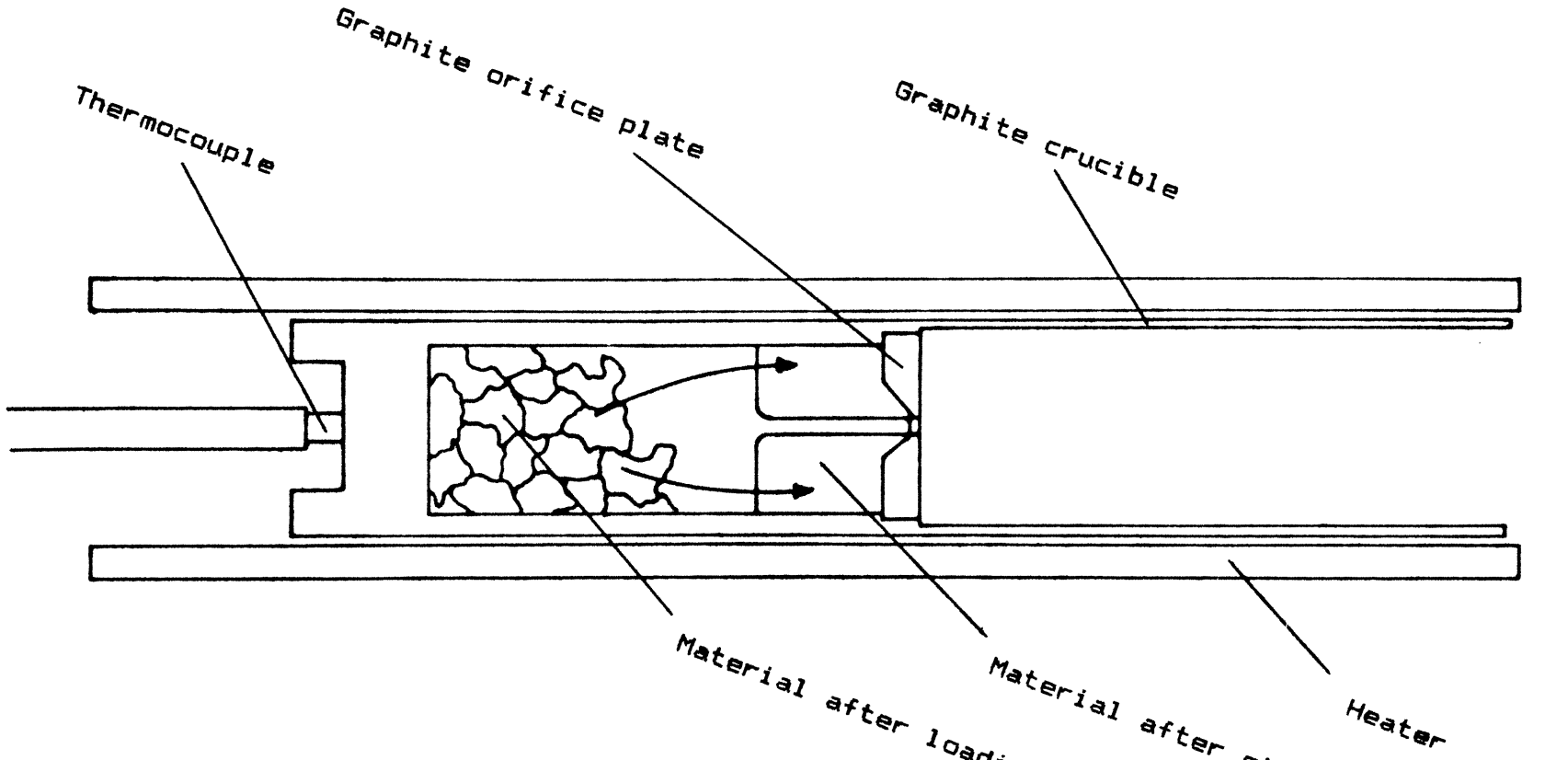


Fig(55). Details of the modified Varian crucible housed in a typical furnace.

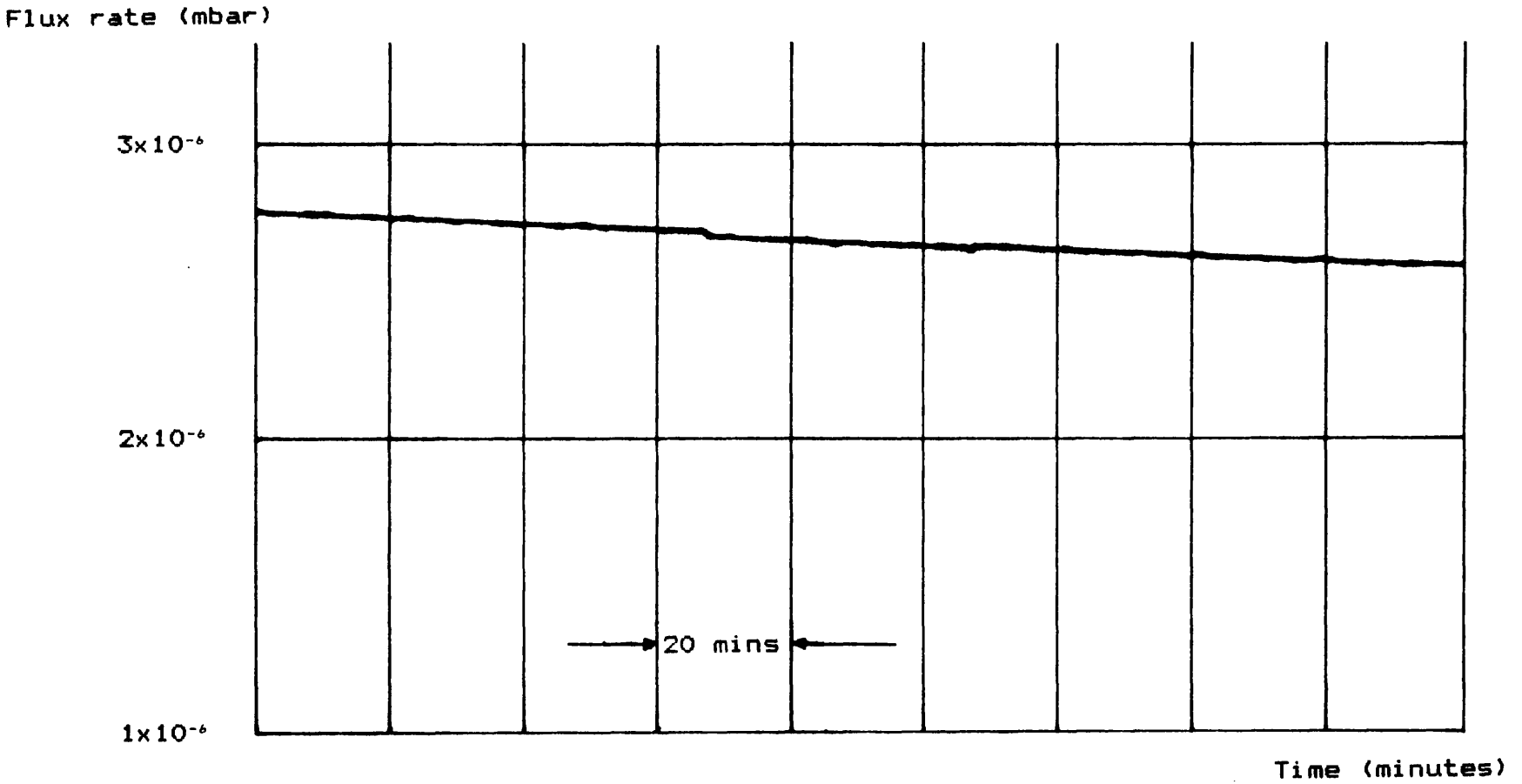


Fig(56). Minute - scale flux rate resulting from a modified furnace filled with PbSe.

lifetime profile in Fig(57).

The observed 2% fall rate can be directly related to the Varian furnace heating construction. In the stabilisation phase (approximately five hours after the loading of the charge) the lead chalcogenide has sublimed to form a block behind the cover through which an axial hole is formed. The diameter of this hole corresponds to that of the orifice and Fig(58) shows the material form created. This means that the vapour pressure in the crucible is dependent only upon the block surface facing backwards into the crucible ($T_s$ is constant). As the material is used up, the surface moves towards the cover and into a lower temperature zone hence producing a continually declining overall flux rate. This declining flux rate has been measured with lids in different positions within the crucible length and the 2% quoted fall rate is that from the best cover position found. A position well into the hot crucible does not bring any increased advantage as far as stability is concerned and the filling capacity would also become impractical.

At growth rates of 2 $\mu m hr^{-1}$, a constant drift rate of 2% $hr^{-1}$ is acceptable when it is remembered that all main component furnaces will have very similar flux rate decay characteristics and so film composition variations will be smaller than the required limits

Fig(57). Charge - lifetime profile of a furnace initially loaded with 40g of PbSe.

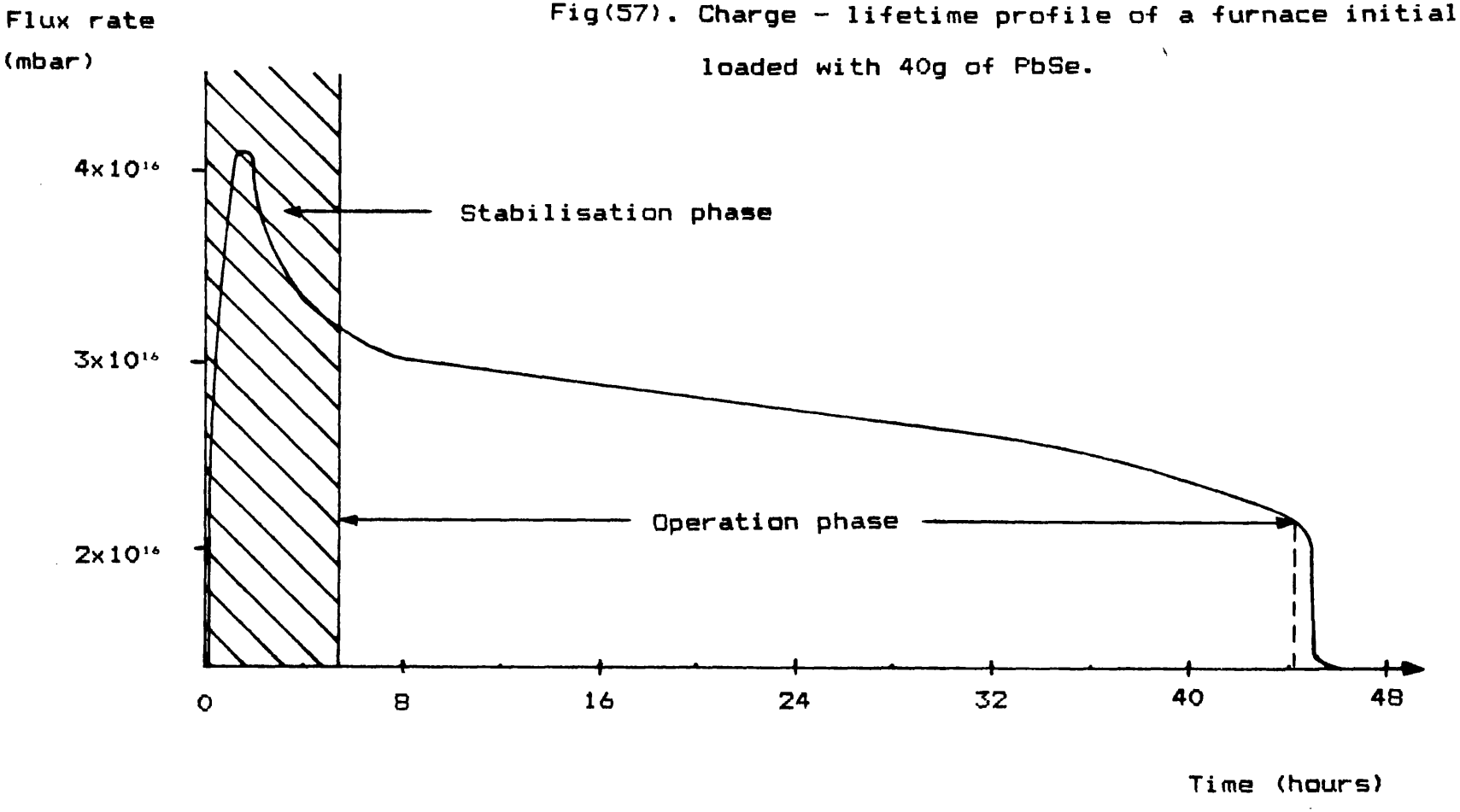

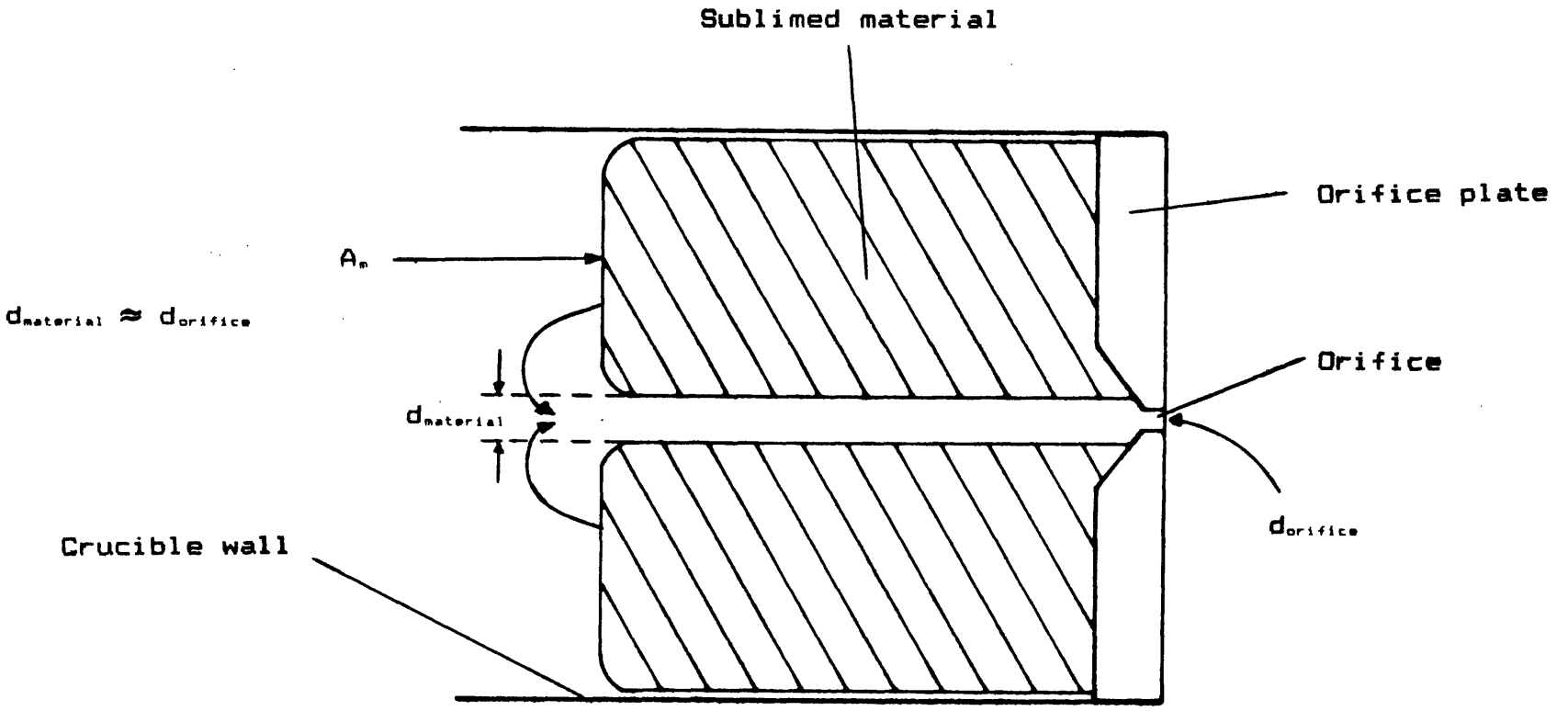


Fig(58). Details of the sublimed lead chalcogenide block formed within the stabilisation phase of a furnace.

quoted in the previous section.

Although the used furnace is stable, section 3.4 will show that it is very sensitive to the position of the shutters. The final modified version of this furnace can be found in that section.

### 3.3.4) Doping material sources

In section 4.3 it will be seen that the dopants for the lead chalcogenides used in conjunction with this work are Bi for n - type layers and Ag and Se for p - type layers. Bi is sublimed as $Bi_2Se_3$ for reasons to be described later. The materials $Bi_2Se_3$ and Ag have slightly lower vapour pressures than the lead chalcogenides. This does not, however, present any problems due to the much lower dopant flux rate required (approximate beam flux ratios are $Bi_2Se_3$ : PbSe = 0.0005). This fact means that it is possible to use the Varian furnace and customised graphite crucible described for the main lead chalcogenide components in the previous section. It will also be seen from the initial experiments that this step is justified due to the excellent flux rate stability that can be achieved at the required doping levels.

P - type doping with the use of Se on the other hand is more difficult. Se has an extremely high vapour

pressure compared to all the other materials present in the system, and would need low temperatures for the required flux rates if placed into one of the above furnaces. Therefore, an entirely new type of furnace has had to be designed. This is shown in Fig(59) and features the following three main differences to the standard type:

a) All forms of heat insulation have been omitted and silver thermal conduction paths to the mounting flange are present to assist heat dissipation;

b) the orifice diameter has been reduced and lengthened and opens not directly to form a Se beam but first passes to an area enclosed by a disk with a 2mm diameter axial orifice. This area serves as a vapour pressure equaliser and regulator;

c) to avoid the risk of Se precipitation near the primary orifice, the heating elements have been designed to heat the crucible in three zones, the hottest being near the top and the coldest at the bottom.

These alterations to the standard furnace have produced a selenium furnace with rates of acceptable stability. The stability tolerances of this quasi - compensation source are not as stringent as other furnace requirements and the fluctuations of 10% about the average value are within the necessary limits.

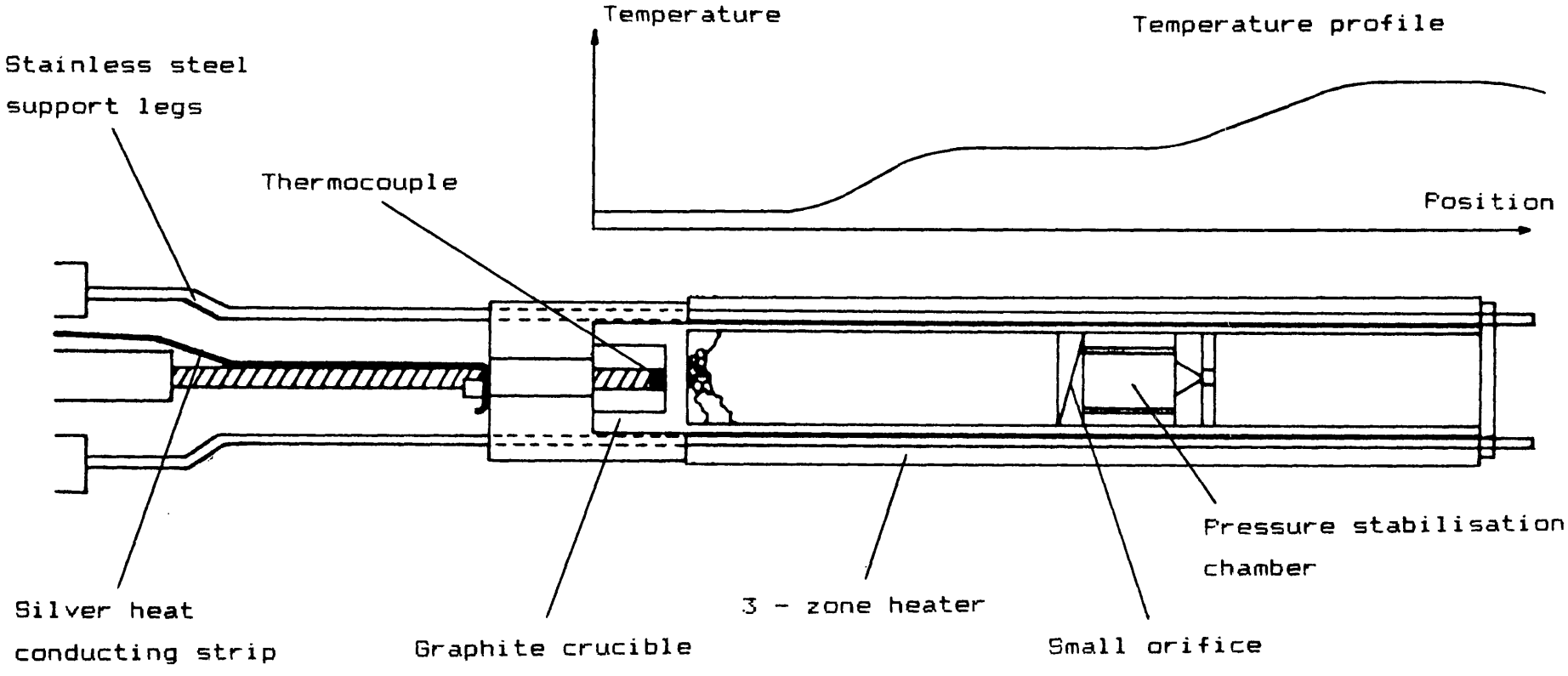


Fig(59). Details of the selenium furnace.

It must be mentioned here, however, that the selenium flux rate is difficult to measure due to the material's volatility. The beam flux monitor components can, therefore, be coated with a thin layer of Se within seconds. This consequently becomes a secondary source, heated by the monitor filament. As a consequence, flux values are measured within 3 seconds after opening the selenium shutter. As soon as the value is taken, the shutter is reclosed preventing further selenium being deposited onto the measuring head.

### 3.4) Furnace shutters

Section 3.2 stated the growth rate as 5 $As^{-1}$ and hence abrupt interfaces on the interatomic scale are possible when growing heterostructures using the MBE technique. Separate mechanical shutters placed directly in front of the individual furnaces enable each beam to be independently interrupted without changing the furnace temperature. By operating the furnace shutters alone, multi - layer, multi - composition structures such as double heterojunction (DH) lasers and quantum superlattices can be fabricated.

The shutters are manually operated and constructed of tantalum sheet on stainless steel frames. This is shown in Fig(60). Tantalum is used due to its

Fig(60). Furnace shutter and position in the MBE system.

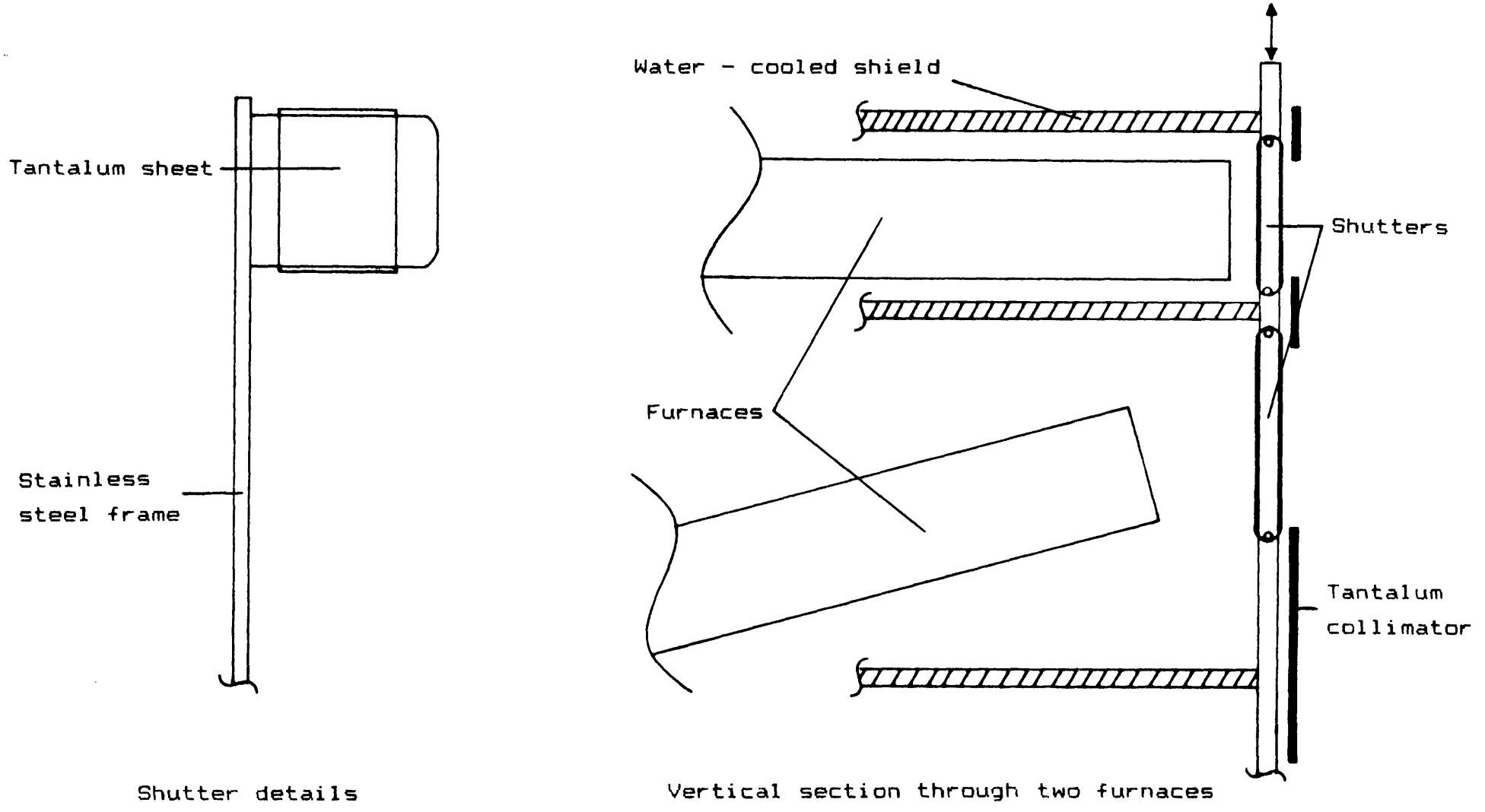


Shutter details

Vertical section through two furnaces

high melting point and low contamination rate which is important when a hot furnace 'sees' a closed shutter. The frames move vertically through guiding lugs in the water - cooled shield. The movement is achieved through a stainless steel band system pulling the shutter down against the force of a return spring.

Tantalum collimators sandwich the shutters onto the shield. The collimators restrict the sublimation of source material onto parts of the vacuum system where it could cause electrical short circuits. Placing the shutters between the collimators and the cooling shield ensures that the shutters are tight when in the closed position.

The reaction of source flux rates to changes of the shutter position is, however, very unsatisfactory. Fig(61) shows the flux rate of a main material furnace and the effect that a shutter closed in front of the furnace has upon the flux rate after reopening the shutter. A stabilised PbSe furnace, for example, shows increases of 10 - 20% of the original flux rate when the shutter is reopened after being closed for 10 minutes. This increase diminishes within a period of 10 - 15 minutes and the furnace assumes its original flux value. The increase can be explained by the fact that a certain amount of heat will be reflected back into the crucible

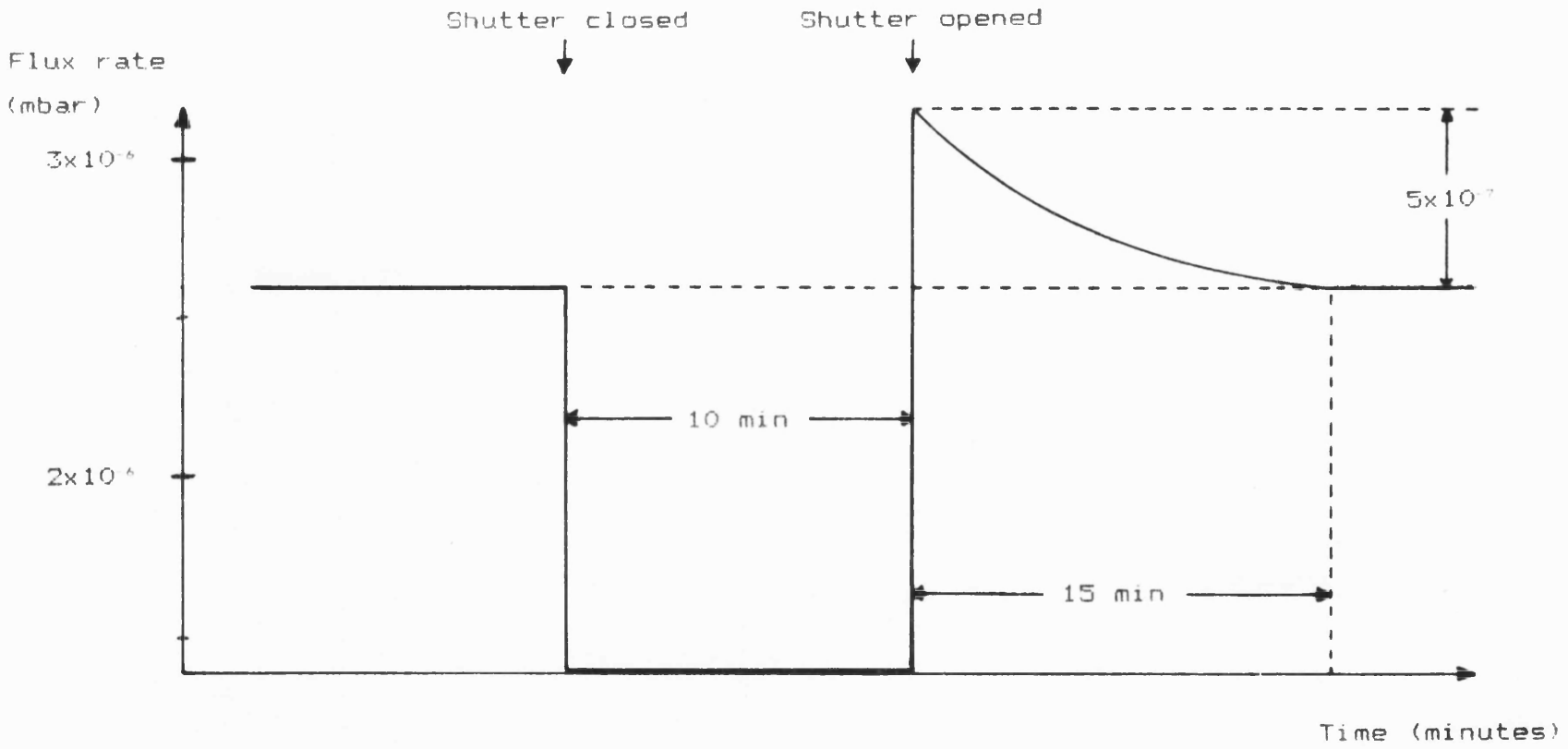


Fig(61). The shutter effect observed from one of the top three furnaces loaded with PbSe.

from the closed shutter thus increasing the temperature of the furnace orifice and hence changing the furnace temperature profile. The three horizontally positioned furnaces with a small orifice - shutter distance show a more pronounced effect than the three 30° - tilted furnaces with a correspondingly larger distance. The effect in the latter case is further reduced by the fact that the shutters are not angled at 90° to the furnace axis and so a certain amount of heat will be reflected up to the water cooled shield and not directly back into the furnace.

The temperature increase $\Delta T$ responsible for this effect can be estimated from the measured flux rate deviation using equation 44 since the material effusion rate is directly proportional to the furnace temperature. The figure shows that for the case of PbSe loaded in a top furnace position (D = 16.0cm, r = 0.1cm, m = 286.15, a = 11032K, b = 7.203) the deviation can be as high as 10 - 20%. If $\Gamma_1$ is the original flux rate corresponding to a temperature $T_1$ and $\Gamma_2$ is the flux rate after re - opening the shutter corresponding to a temperature $T_2$, then the numerical equation is found which relates $\Gamma_1$ and $\Gamma_2$ to $T_1$ and $T_2$

$$\frac{\Gamma_1}{\Gamma_2} = \sqrt{\left(\frac{T_2}{T_1}\right)}\ \exp\left(2.3a\left(\frac{1}{T_2} - \frac{1}{T_1}\right)\right) \qquad (53)$$

For a 20% deviation,

$$\frac{\Gamma_1}{\Gamma_2} \approx 0.8 \qquad (54)$$

Equating 53 and 54, substituting for a = 11032K and inserting a typical original operation temperature $T_1$ = 1100K, iteration shows that $T_2$ = 1111K, or $\Delta T$ = 11K, which is a relative temperature shift of only 1%. This temperature change is not compensated by the temperature controller due to the temperature profile for the case of an open shutter being different to that when the shutter is closed. If the temperature of the material block is held constant by positioning the thermocouple just behind the orifice, temperature distributions are created where the differences between the open and closed shutter cases are minimised. A furnace equipped with such a modified thermocouple system is shown in Fig(62) and the results of this arrangement are presented in Fig(63). Although the effect has not been completly eliminated, the 10 - 20% flux variation quoted above has been reduced to an acceptable value of 3 - 5% and the recovery time is reduced to 2.5 minutes.

## 3.5) Substrate Holder Assembly

The substrate holder assembly hangs from the top flange of the working chamber via a precision rotary

Fig(62). Details of the furnaces presently used showing the positioning of the thermocouple to reduce the shutter effect.

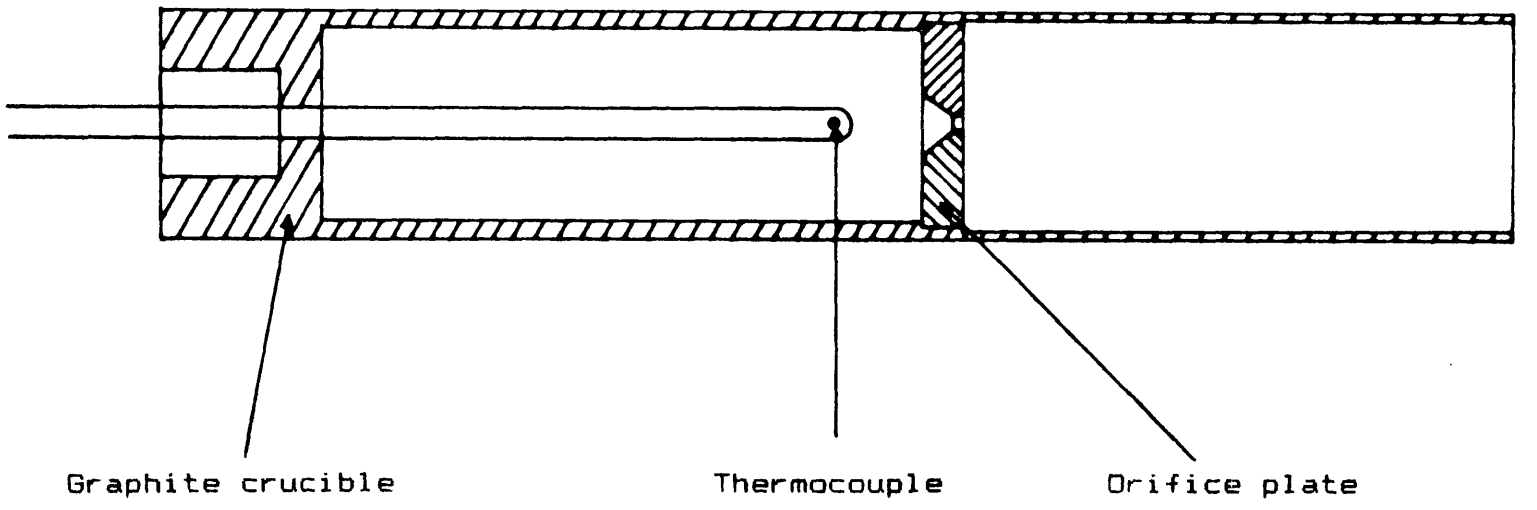

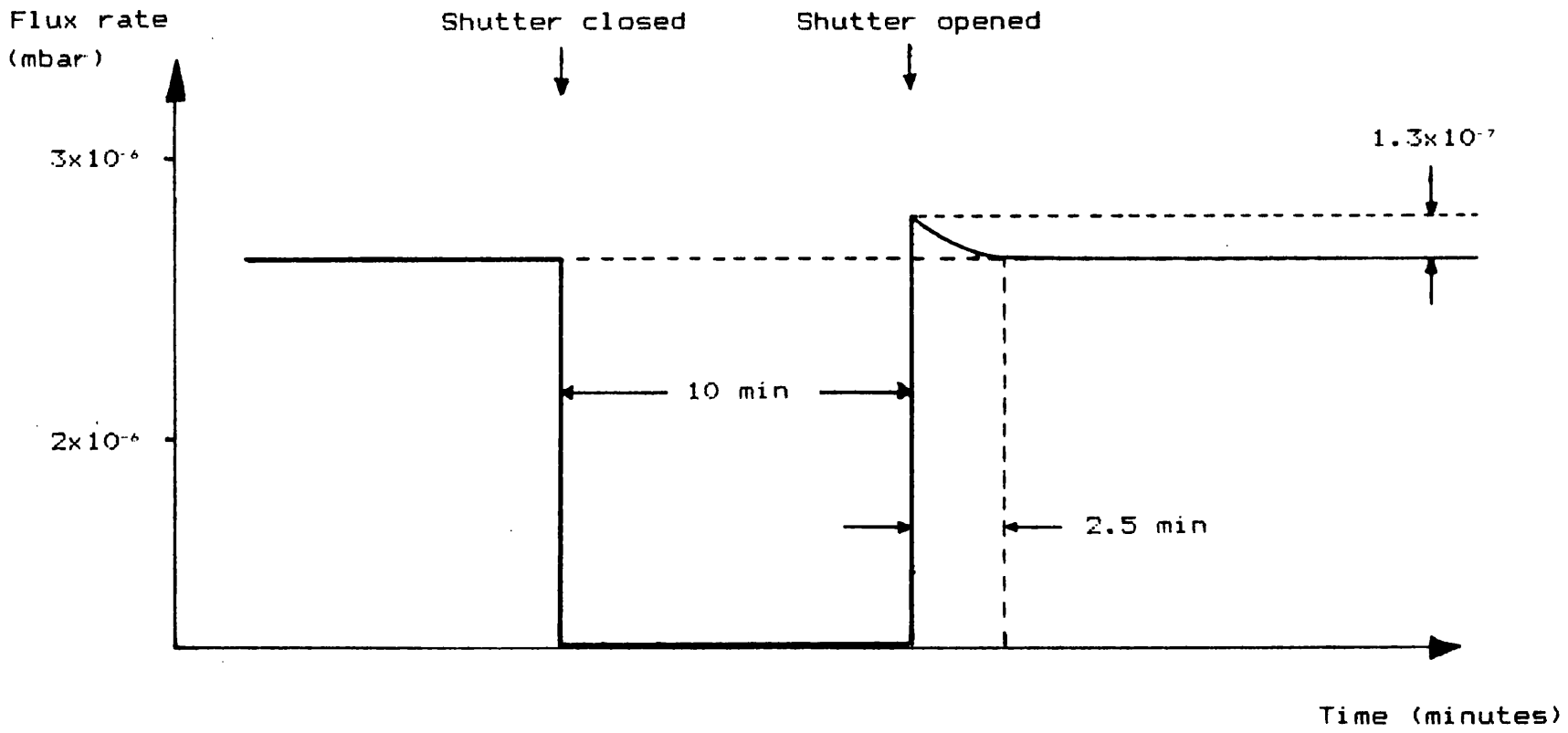


Fig(63). The decreased shutter effect resulting from the modified thermocouple position.

feedthrough as shown in Fig(64). The assembly consists of the heated substrate holder and the open ionisation gauge type beam flux monitor, the two items being positioned 90° to each other about the feedthrough axis.

The heated substrate holder shown in Fig(65) (customised Varian MBE 360 item) is a bayonet type of arrangement designed to accomodate molybdenum substrate blocks which are heated by radiation from a spiral filament heater mounted directly behind the block. Substrates are mounted onto the blocks with a Ga - In alloy (50 - 50% eutectic). This is a liquid at room temperature and the alloy adequately wets the back sides of polished lead chalcogenide and cleaved $BaF_2$ substrates so that they are held firmly in the vertical growth and storage positions. The back of the lead chalcogenide substrates are polished after epitaxy in order to remove the interdiffused alloy whereas it is simply removed with propanol from the $BaF_2$ substrates. The block temperature is measured by the integral tungsten / 26% rhenium - tungsten / 5% rhenium thermocouple, the thermocouple contact being the block itself. The wires are protected by the spring return plate which ensures no thermocouple contact with the block until the block has been turned into the lock position and the transfer rod is removed.

The beam flux monitor is an open - type

Fig(64). The substrate holder assembly (bottom view).

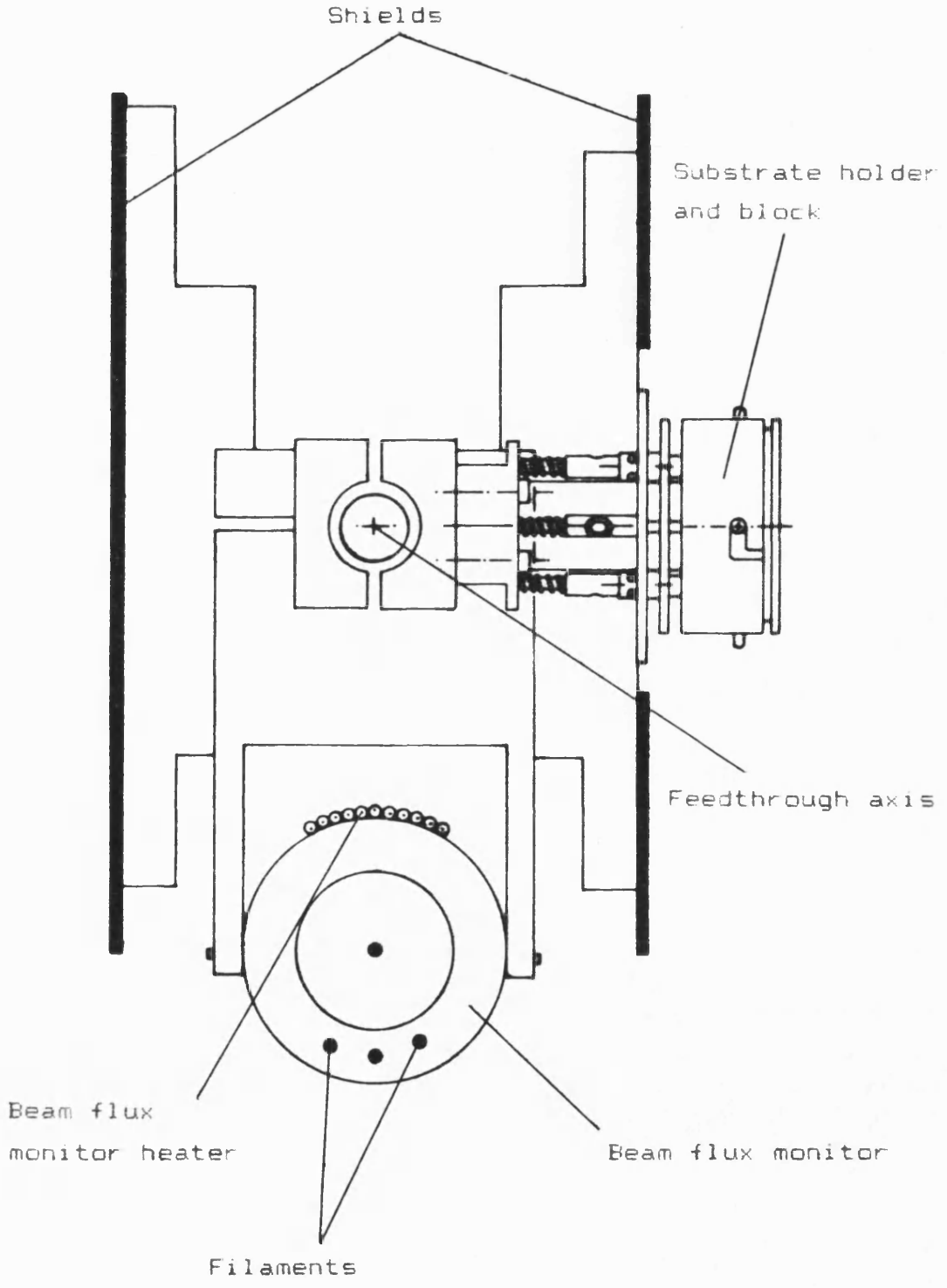

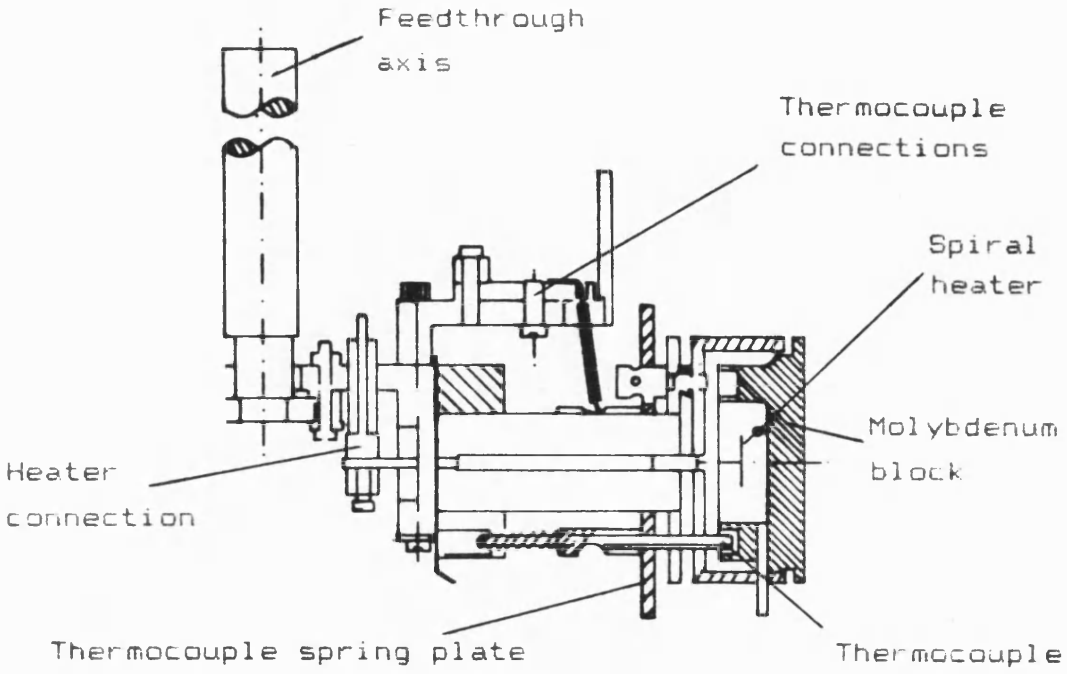


Fig(65). Heated substrate holder assembly.

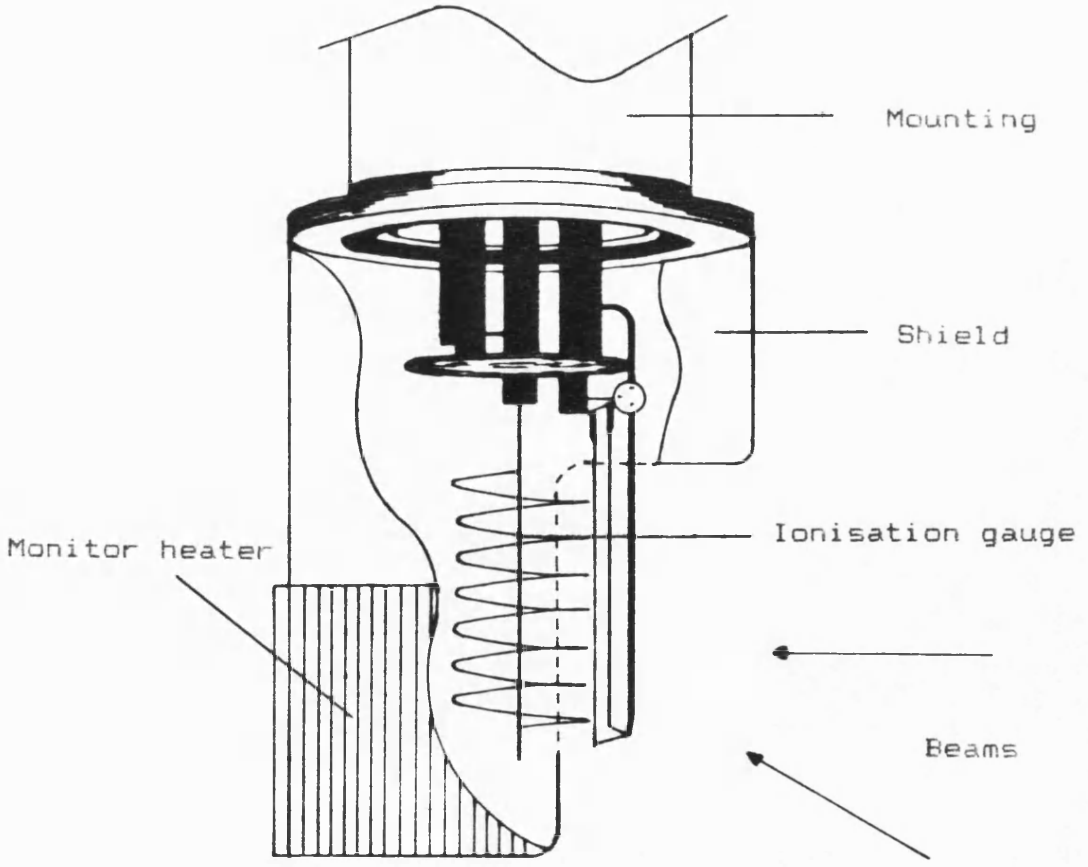


Fig(66). Side view of the beam flux monitor.

ionisation gauge (Varian type UHV 24) (Fig(66)) which measures the pressures of the incident beams over the background pressure when swung into the sample position. A heater positioned around the back shield enables the whole head to be outgassed thus reducing the problems associated with Se deposits. As mentioned in a previous section, the beam flux monitor pressures are not converted to actual flux rates since relative, and not absolute, flux rates are required in this work.

# 4) EPITAXIAL LAYERS AND ASSESSMENT

## 4.1) Introduction

The initial experiments designed to test the system under the constraints outlined in chapter 3 are described in sections 4.2 and 4.3. Section 4.4 shows how it is possible to dope the lead chalcogenides, with section 4.5 concentrating upon the properties of the new $Pb_{1-x}Eu_xSe$ alloy system.

## 4.2) Growth of binary films

The first film grown was PbSe deposited upon a $BaF_2$ substrate at 645K with a flux rate of $3x10^{-6}$ mbar for one hour. The resultant epitaxial film thickness was 4.8μm which can be expected when a unity sticking coefficient is considered and a 100% ionisation yield is assumed for the beam flux monitor. These assumptions predict a 5 $\mu mhr^{-1}$ growth rate.

Fig(67a) and Fig(67b) show the PbSe thickness distribution across the 30mm diameter sample holder for two different furnace geometries. The measurement technique uses the principle of light interference performed with a Mireau head mounted upon a Zeiss microscope. The interference fringes have a 2730Å period

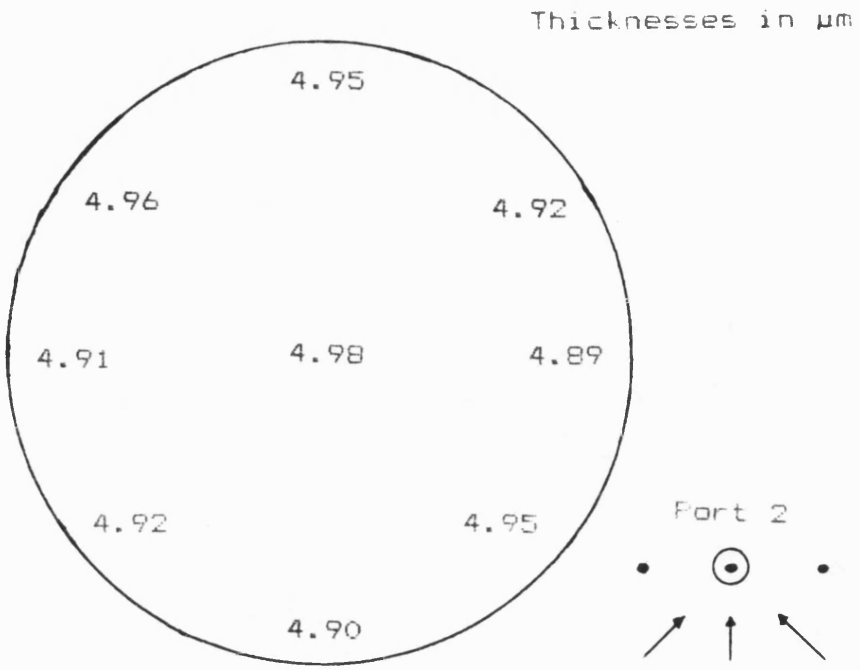


Fig(67a). PbSe film thicknesses measured from a furnace in port 2.

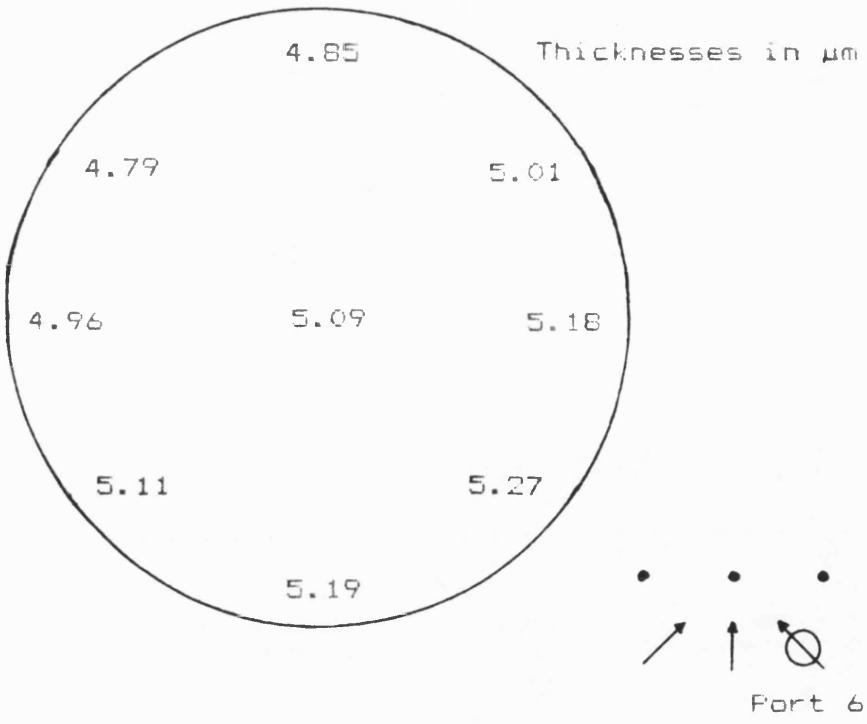


Fig(67b). PbSe film thicknesses measured from a furnace in port 6.

and thicknesses are measured by the fringe shift due to, for example, a sharp step. A method is used where the substrate is partially covered by a second substrate, the second being removed after epitaxy to reveal the step to be measured. This technique has been employed using $BaF_2$ substrates arranged around the block circumference for the case of the PbSe furnace being in port position 2 (top middle i.e. axially square) and port position 6 (bottom right i.e. 30° off two axes). The beam uniformity for port position 2 is excellent, having a deviation of approximately the measuring technique uncertainty (± 500Å). The results from port 6 show the expected non - uniformity across the substrate holder where the deviation in this case is ± 2500Å.

The growth rates for the PbSe furnace are constant between runs. This can be seen in Fig(68) where the thickness distributions of four samples grown one after another with identical growth conditions from a PbSe furnace in port position 2 are shown. The thicknesses of these samples show a variation between runs of less than ± 800Å, an excellent stability rate when it is considered that the PbSe furnace is re - calibrated to 3.0 ±0.01 $\times 10^{-4}$ mbar before each deposition, meaning that the furnace is at operating temperature for over 7 hours. Other experiments have

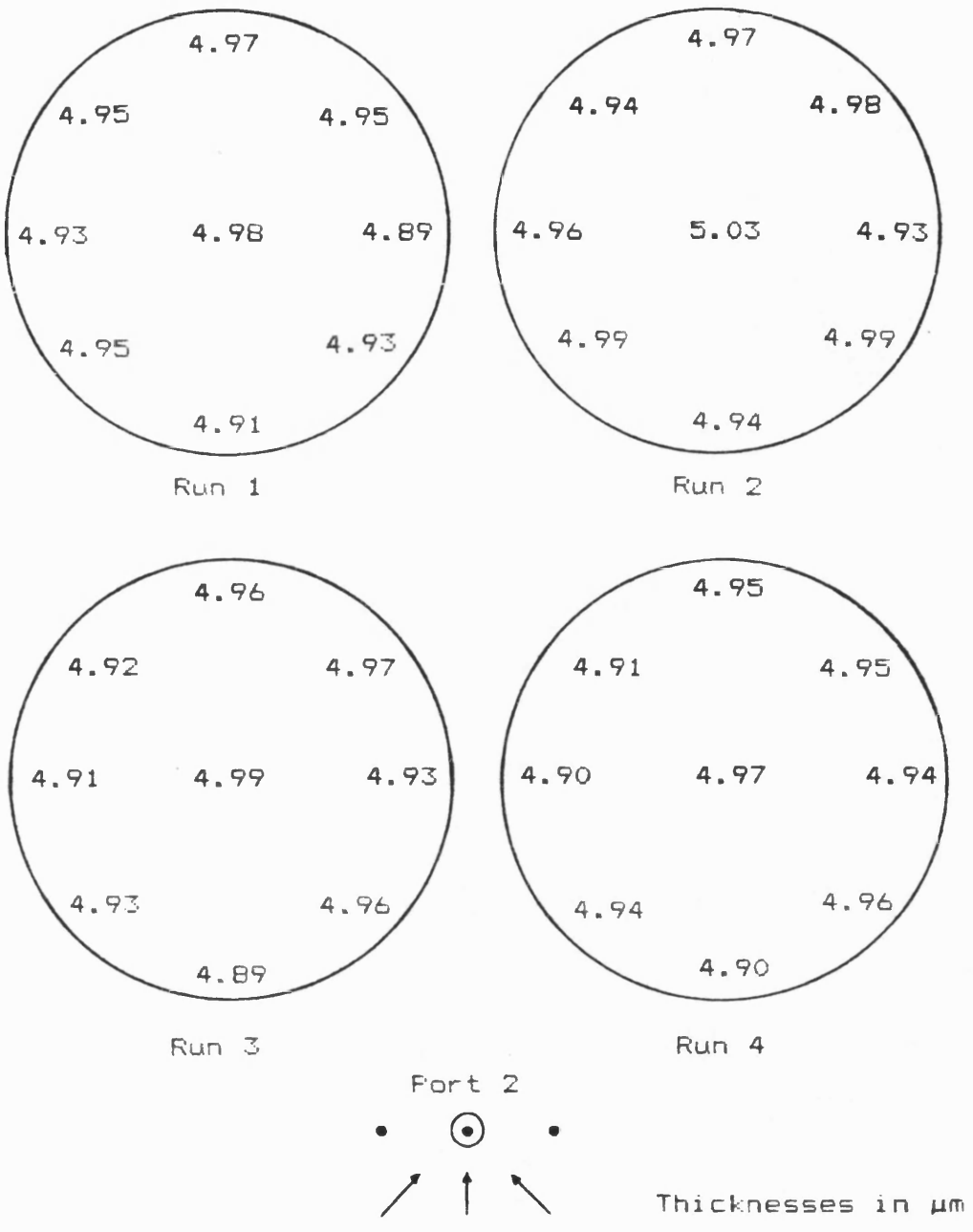


Fig(68). Thickness distributions from four consecutive runs resulting from PbSe loaded in port 2.

shown that these variations are achieved independent of the age of a furnace load. The vapour pressures of the lead chalcogenides given in section 3.3.1 indicate that similar results are to be expected for PbS, PbTe and SnSe.

The films described above have been investigated using a scanning electron beam microscope. The films deposited upon $BaF_2$ at substrate temperatures above 620K show a high quality morphology, disturbed only by cleavage lines formed from the [111] cleavage plane. Such a film is shown in Fig(69). Films deposited at lower temperatures are sooty in appearance and are polycrystalline as seen in Fig(70). The lower image is an image of the same sample but at a higher magnification. The films are not transparent which indicates that the nodules have developed after an initial substrate coverage. Epitaxial layers grown on polished PbSe substrates are found to have the same surface features as the underlying substrate as shown in Fig(71) where a faint scratch from polishing can be seen.

Dislocation etch pit counts were performed upon grown layers and upon PbSe substrates using a dislocation etch described by Norr (10g KOH in 10ml water, 1ml glycerol, 0.5ml 30% $H_2O_2$. Samples are cleaved and etched at 300K for 2 minutes) {107}. Typical etch pit counts

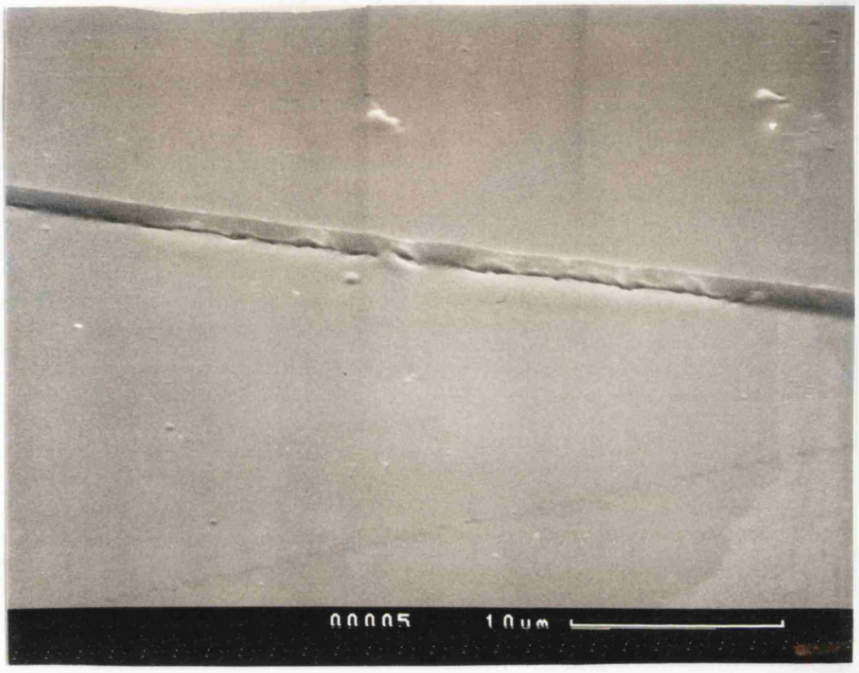


Fig(69). Scanning electron microscope image of a 3µm thick PbSe film grown on cleaved $BaF_2$ at 620K.

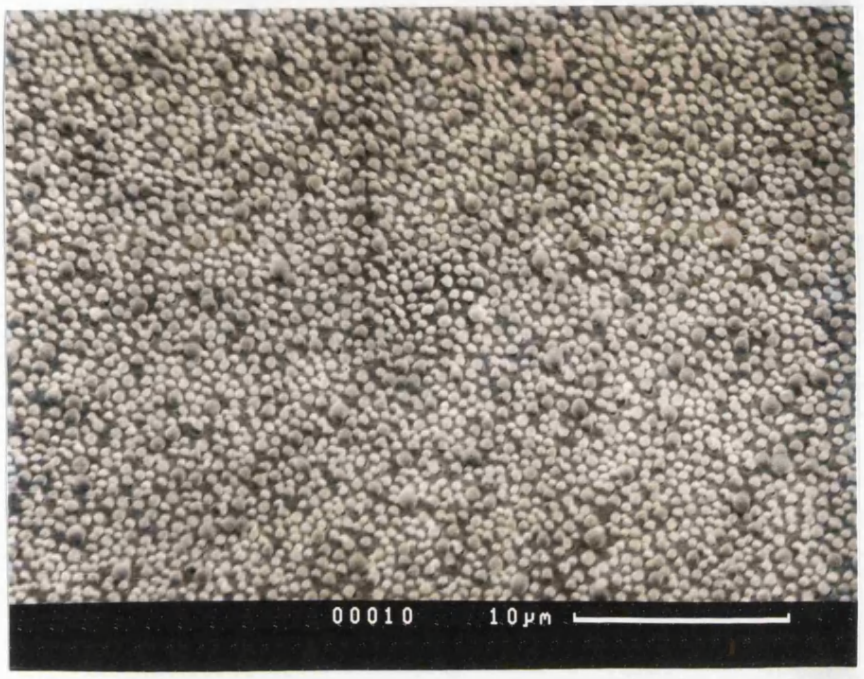


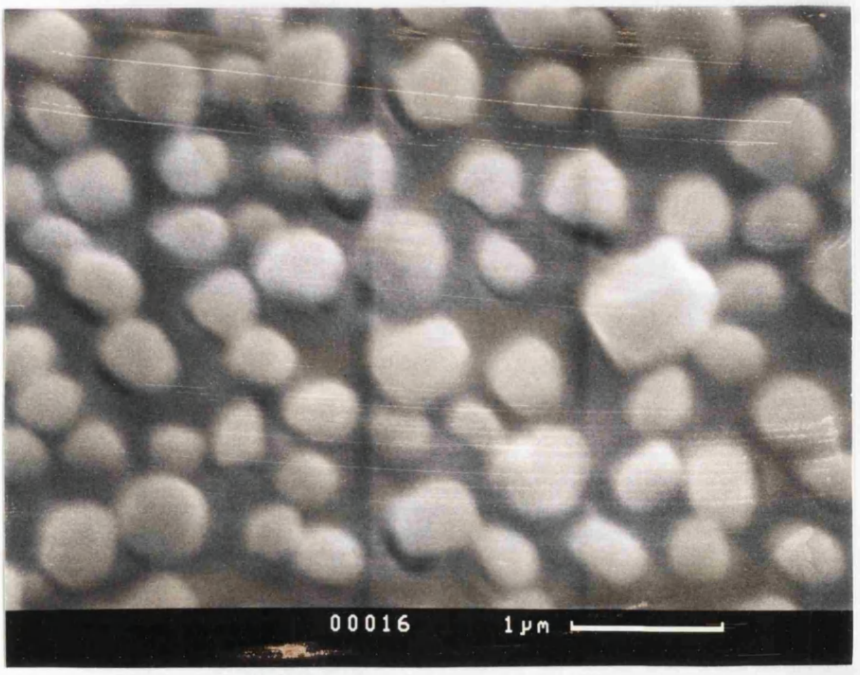


Fig(70). Scanning electron microscope image of a 3μm thick PbSe film grown on cleaved $BaF_2$ using a low substrate temperature (570K).

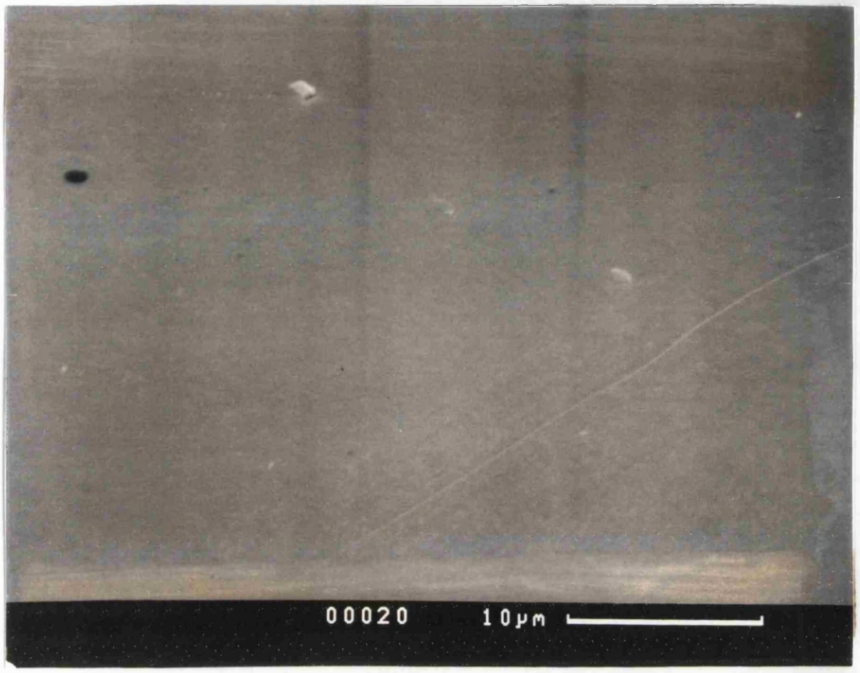


Fig(71). Scanning electron microscope image of a 3µm thick PbSe film grown on a polished PbSe substrate at 620K.

performed upon polished PbSe substrates were $10^4$ - $10^5$ $cm^{-2}$ and epitaxial layers upto 5μm grown upon such substrates generally exhibit an order of magnitude increase over that of the substrate.

A Perkin Elmer 983 infra - red spectrometer is used to obtain absorption spectra between 2μm (5000 $cm^{-1}$) and 55μm (180 $cm^{-1}$). The majority of the measurements have been performed upon films on $BaF_2$ substrates. $BaF_2$ has a cut - off wavelength of approximately 12.5μm (800 $cm^{-1}$) at room temperature as indicated by the transmission spectrum of a 2mm thick slice of $BaF_2$ supplied by the Korth company in Fig(72).

The room temperature absorption spectrum of a 4.8μm thick p - type PbSe film deposited onto $BaF_2$ is given in Fig(73). It shows an absorption edge at approximately 2250 $cm^{-1}$ corresponding to an $E_{g300K}$ value of 279 meV which agrees with the value quoted in Table (3). Similarly, a PbS spectrum is shown in Fig(74) and gives a 3340 $cm^{-1}$ absorption edge corresponding to an $E_{g310K}$ value of 421meV, also confirming the quoted Table (3) value. The above spectra exhibit interference caused by multi - reflections within the thin epitaxial layers. The change of scale on the wavenumber scale is to be noted.

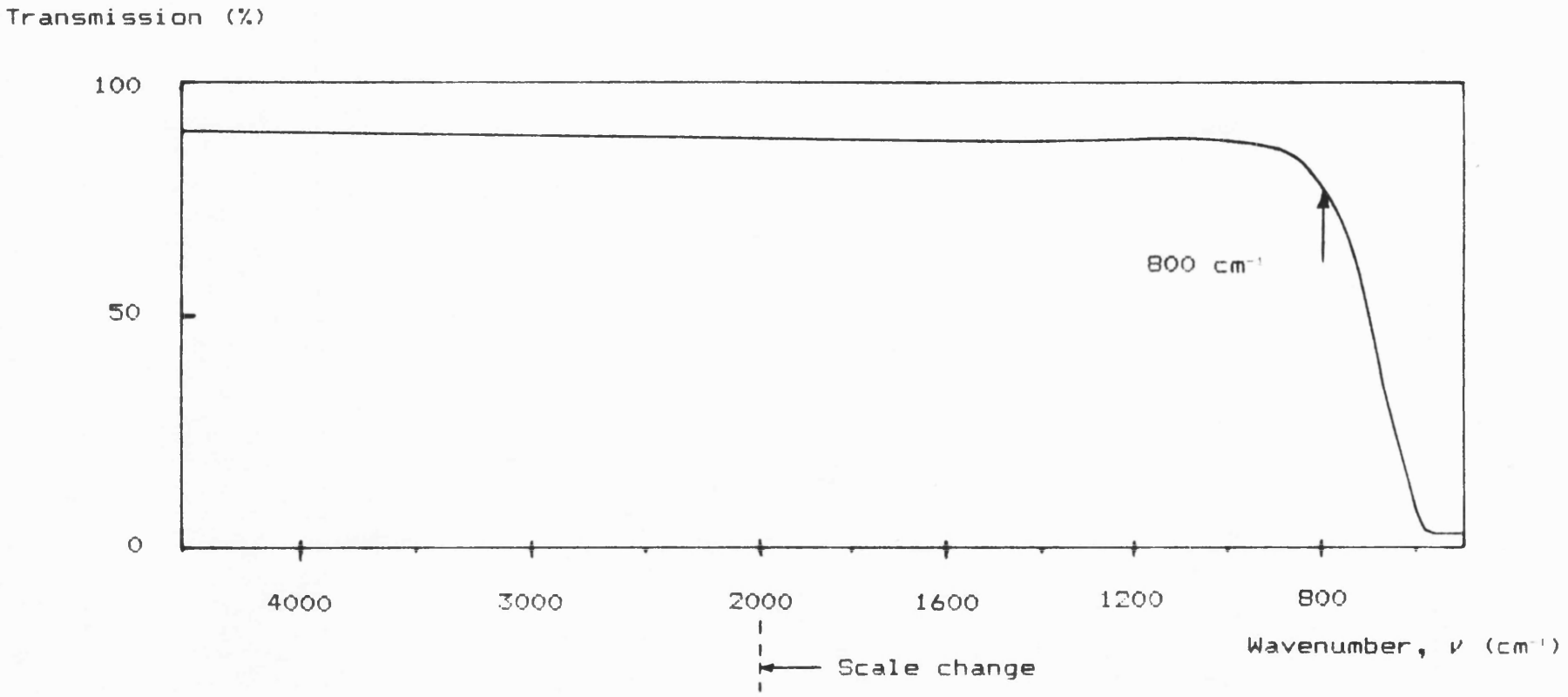


Fig(72). Transmission spectrum of a 2µm thick $BaF_2$ slice.

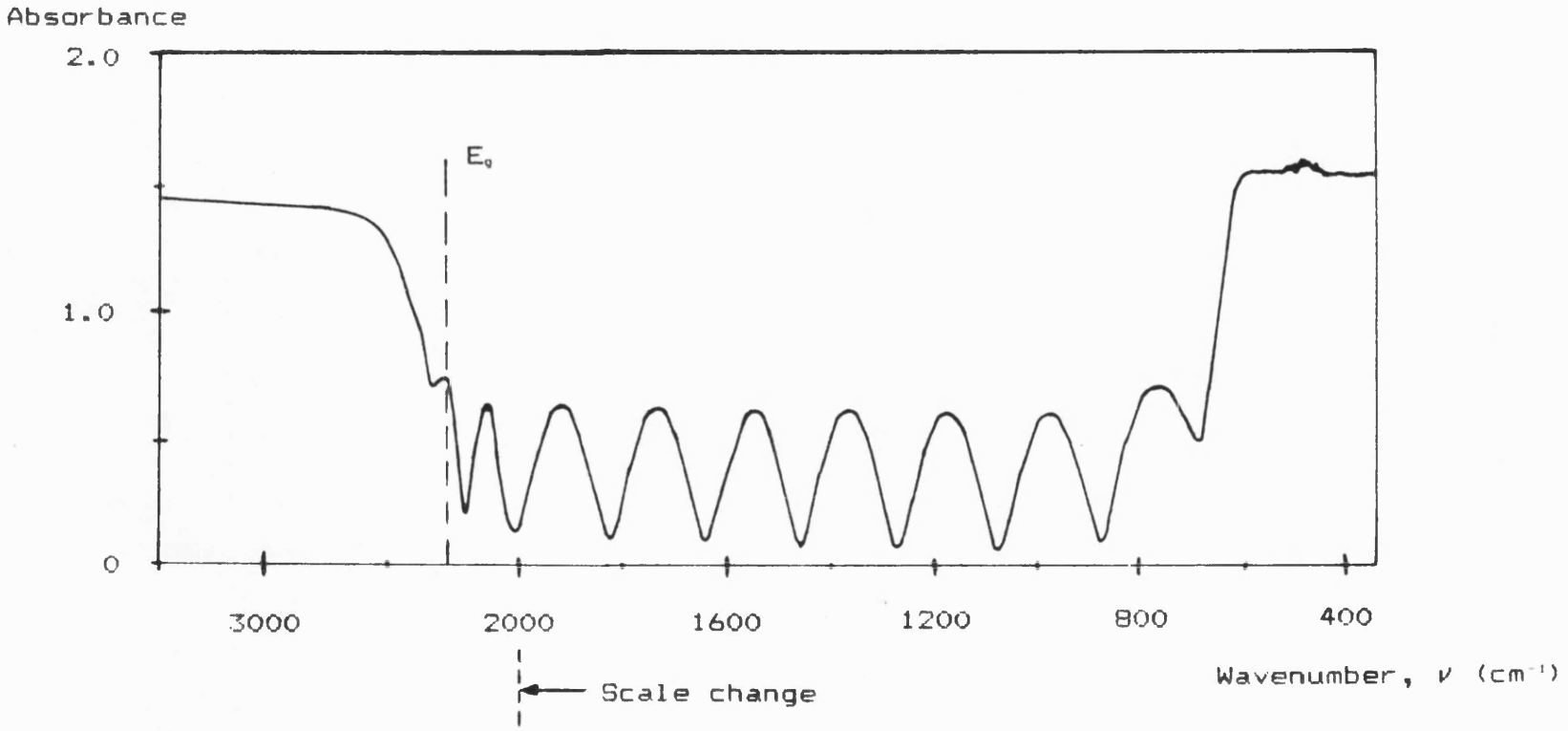


Fig(73). Absorption spectrum of a 4.8μm thick PbSe layer on $BaF_2$ at 300K.

Fig(74). Transmission spectrum of a 3μm thick PbS film on $BaF_2$ at 310K.

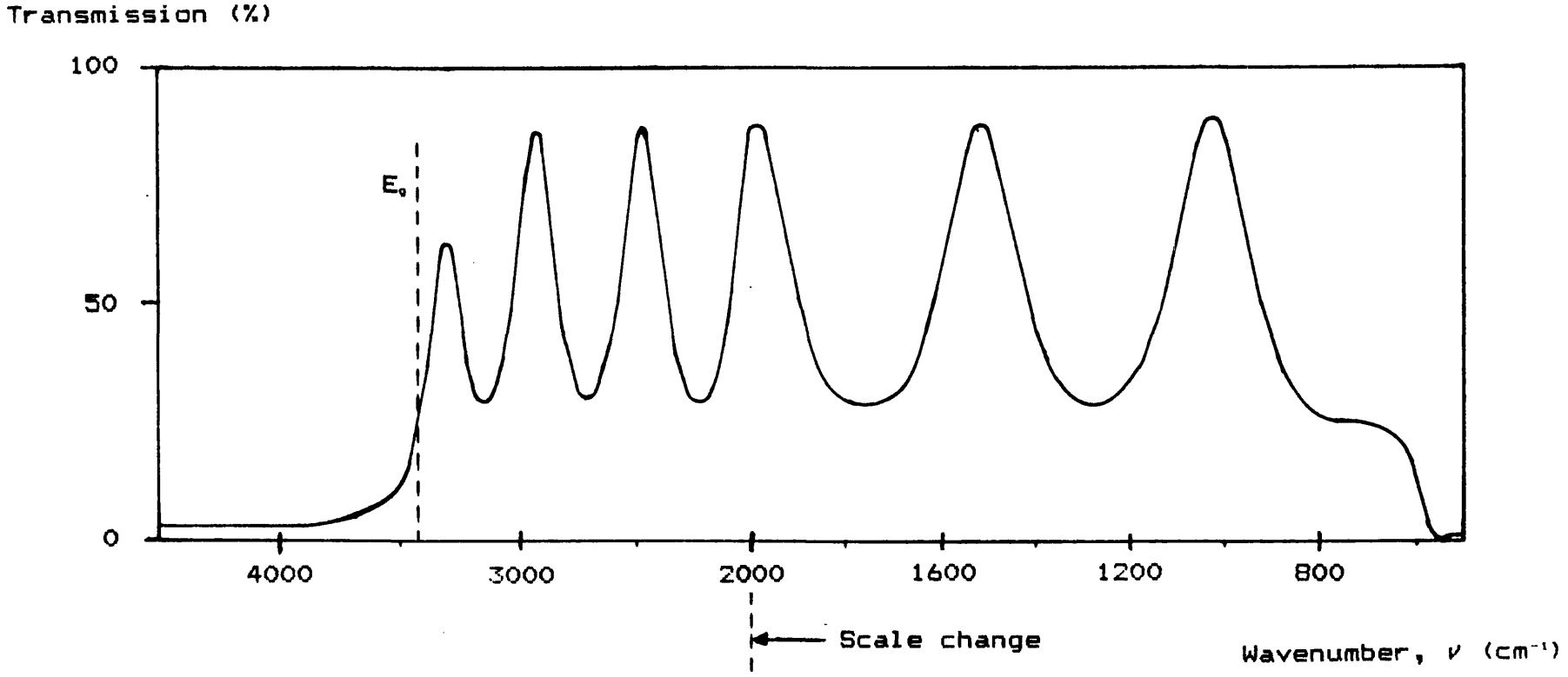

## 4.3) Growth of ternary films

The growth of $Pb_{1-x}Sn_xSe$ ternary films has been investigated to acquire the accuracy with which film compositions can be set and to check that the furnace requirements set out in chapter 3 are achieved.

A constant PbSe flux rate of $2.25 \times 10^{-4}$ mbar and a substrate temperature of 670K were used to deposit a four - layer $Pb_{1-x}Sn_xSe$ structure on $BaF_2$. The SnSe flux was increased for each 2500Å thick film, the beam flux monitor ratios of 0.05, 0.1, 0.2 and 0.4 being chosen. The deposition was interrupted for 15 minutes between each layer to allow for the stabilisation of the SnSe furnace. This structure has been investigated using secondary ion mass spectroscopy (SIMS) and X - ray diffractometry to observe diffusion effects and to attempt a calibration of the $Pb_{1-x}Sn_xSe$ film compositions to beam flux ratios.

The SIMS profile is depicted in Fig(75) {108}. Although the technique does not allow a direct calibration of the flux rate ratios to the composition, the results show that the compositions of the individual films are not depth - dependent and that there is no interdiffusion to be observed between the films. As a guide, the second layer has a tin content of approximately 0.078 ± 0.01 since its count rate agrees

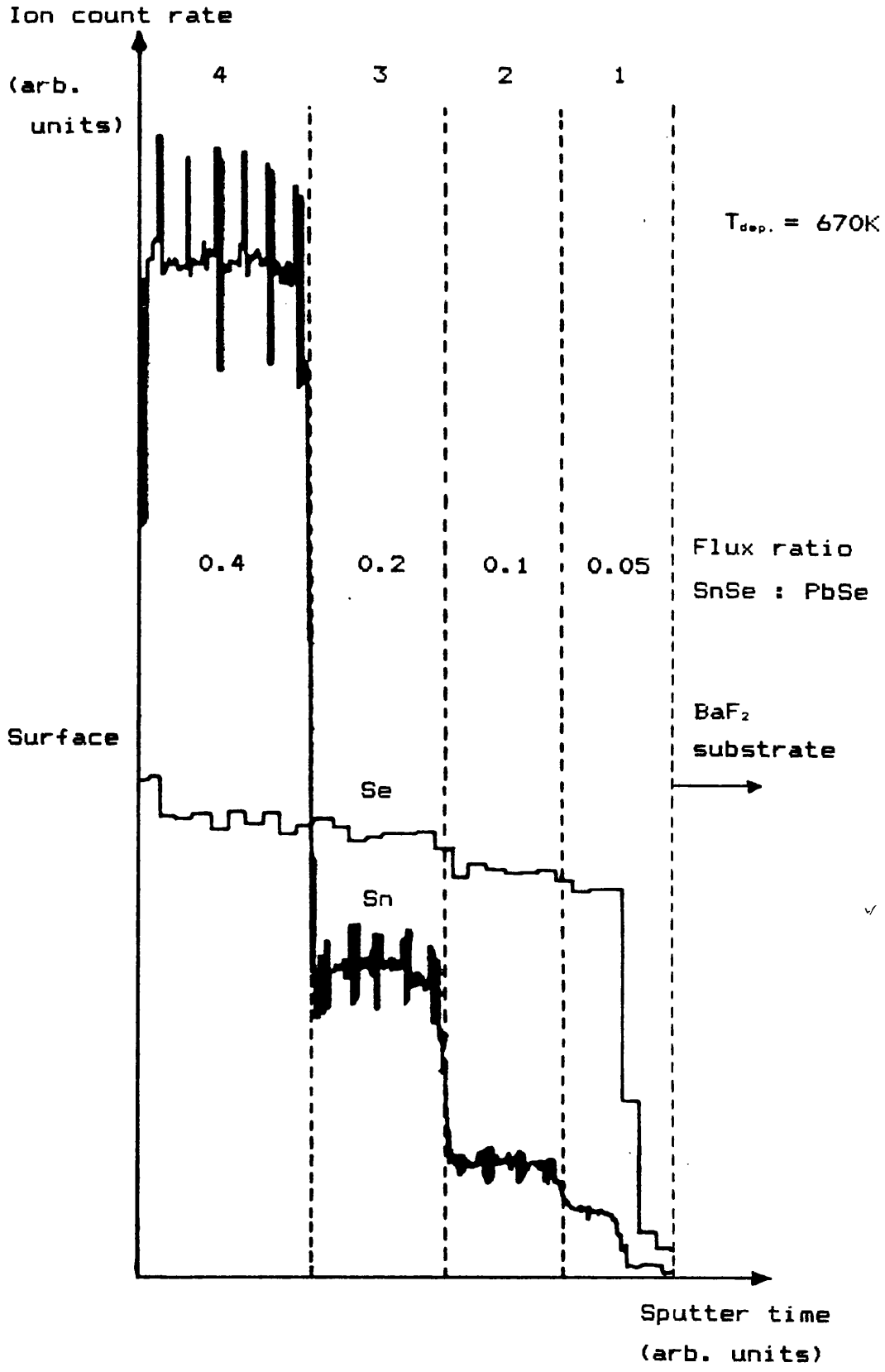


Fig(75). Secondary ion mass spectroscopy scan of a four - layer $Pb_{1-x}Sn_xSe$ structure on $BaF_2$ {108}.

closely with that taken from a calibration standard of composition $Pb_{0.932}Sn_{0.068}Se$.

A more direct method of calculating the composition of ternary films is by means of X - ray diffractometry. Here the strong lead chalcogenide [333] Cu K($\alpha$) reflections are used to detect the reflected angle shift between, for example, $Pb_{1-x}Sn_xSe$ and the standard PbSe or $BaF_2$ substrate peak. This shift can then be used to calculate the lattice constant shift and hence the composition through equation 48.

If $\lambda$ is the radiation wavelength, d the plane spacing then the Bragg condition for the reflection of X - rays at the Bragg angle $\theta$ can be written as follows

$$n\lambda = 2d \sin\theta \qquad (55)$$

The lead chalcogenides, as mentioned in section 2.2.2, are cubic and since

$$\frac{1}{d^2} = \frac{h^2 + k^2 + l^2}{a^2} \qquad (56)$$

where h, k and l are the Miller indicies of the reflection planes, then it follows that

$$a = \frac{\sqrt{27}\,\lambda}{2 \sin\theta} \qquad (57)$$

for the [333] plane first order reflections.

Fig(76) presents the resulting diffractometer

Fig(76). X - ray diffractometer scan of a four - layered $Pb_{1-x}Sn_xSe$ structure on $BaF_2$ using Cu($K\alpha_1$) and Cu($K\alpha_2$) radiation and the [333] reflection planes {109}.

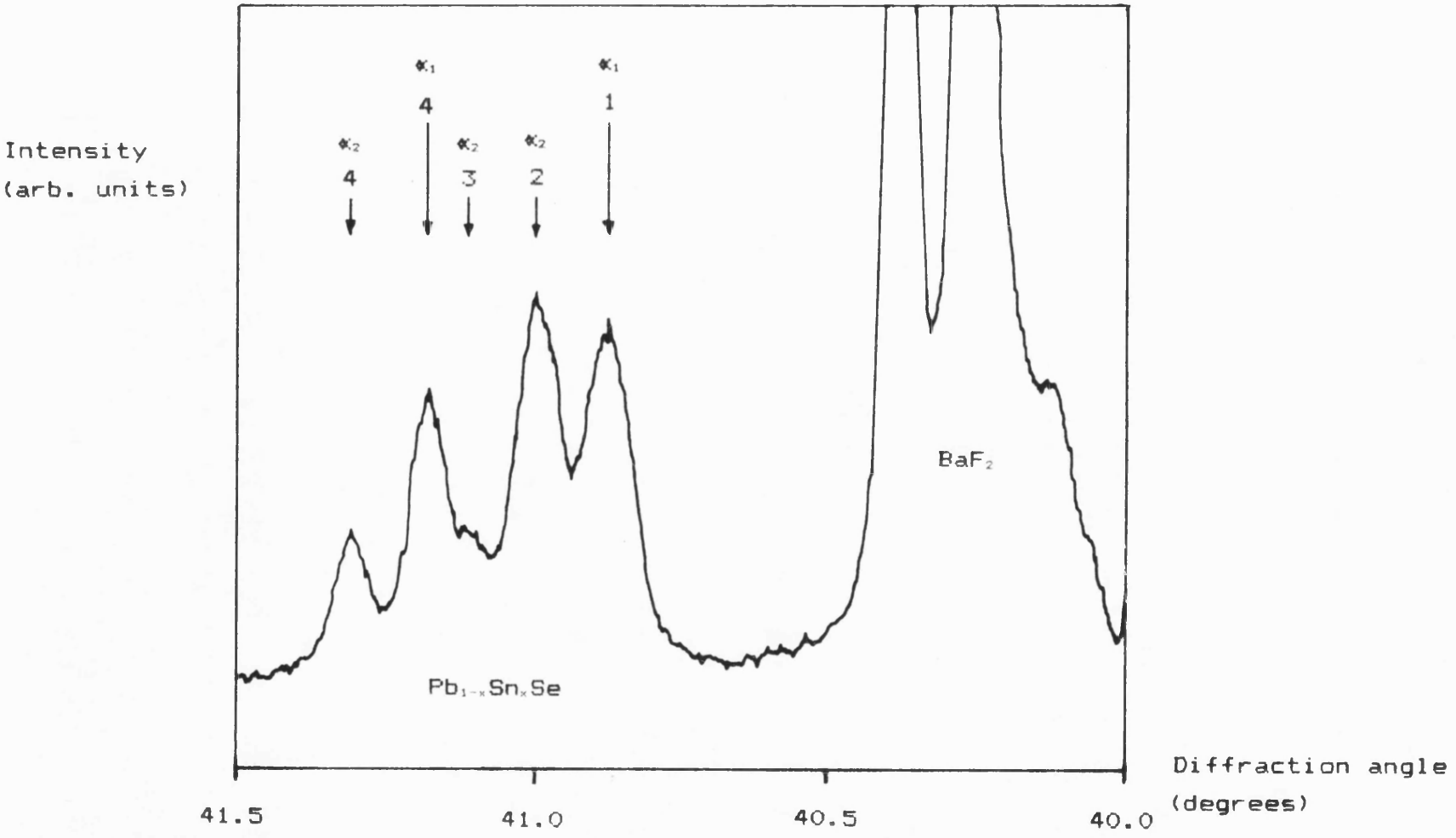

spectrum from the four - layer $Pb_{1-x}Sn_xSe$ structure (x = 0.05, 0.1, 0.2, 0.4 - MBE run number 18.1) described above [109]. It includes the strong BaF2 [333] peaks (at $2\theta = 80.52°$ and $2\theta = 80.76°$) and the weaker [333] reflections from the four $Pb_{1-x}Sn_xSe$ layers. A copper target gives radiation wavelengths of $K(\alpha_1)$ = 1.54056Å and $K(\alpha_2)$ = 1.54439Å. Table (6) shows the measured reflection angle, calculated lattice constant (from equation 57) and, using equation 48, the calculated Sn content. Note that the peaks are the result of both $K(\alpha_1)$ and $K(\alpha_2)$ reflections and that in the table, the $BaF_2$ and the first $Pb_{1-x}Sn_xSe$ film is calculated using $K(\alpha_1)$ radiation and the top three $Pb_{1-x}Sn_xSe$ films are calculated from $K(\alpha_2)$ radiation. The results show discrepancies between the beam flux ratio and the calculated Sn content of upto approximately 20% for the worst case (0.081 against 0.1 flux ratio), a value which will be justified later in this section.

The epitaxial films can be lifted off the $BaF_2$ substrates thus allowing X - ray powder photography measurements to be made, providing a different method for calibrating the beam flux monitor. A series of five $Pb_{1-x}Sn_xSe$ samples were grown, each 0.5μm thick deposited on cleaved $BaF_2$ substrates having beam flux ratios SnSe : PbSe of 0.03, 0.07, 0.12, 0.17 and 0.22. Chapman

| Layer | SnSe:PbSe | Angle 2θ | a / Å | x |
|---|---|---|---|---|
| $BaF_2$ | --- | 80.42° | 6.1997 | --- |
| | | ±0.010 | ±0.0015 | --- |
| $Pb_{1-x}Sn_xSe$ 1 | 0.05 | 81.69° | 6.1200 | 0.049 |
| | | ±0.010 | ±0.0015 | ±0.010 |
| $Pb_{1-x}Sn_xSe$ 2 | 0.10 | 82.00° | 6.1160 | 0.081 |
| | | ±0.010 | ±0.0014 | ±0.010 |
| $Pb_{1-x}Sn_xSe$ 3 | 0.20 | 82.24° | 6.1016 | 0.198 |
| | | ±0.010 | ±0.0014 | ±0.010 |
| $Pb_{1-x}Sn_xSe$ 4 | 0.40 | 82.62° | 6.0782 | 0.389 |
| | | ±0.010 | ±0.0014 | ±0.010 |

Table (6). Measured lattice constants and calculated x - values for a 4 - layer $Pb_{1-x}Sn_xSe$ structure using X - ray diffractometry (MBE 18.1).

has used K($\alpha_1$) radiation upon these layers and the results are given in Table (7) where in this case the 19th line is used corresponding to the [642] reflection planes {110}. The results of these investigations show a larger discrepency between measured and expected Sn contents. This can be explained by the the fact that in the latter measurements, the $BaF_2$ substrate has been removed thus allowing the lead chalcogenide layers to relax after the lattice mismatch associated with the $BaF_2$ substrate. This relaxation can lead to systematically higher x - values than expected.

The infrared spectrometer can not only be used to check the band gap of simple binary compounds but can also be employed to assess the tin content in the $Pb_{1-x}Sn_xSe$ system or the sulphur content in the $PbS_{1-x}Se_x$ system. The IR spectrum of the system is taken at a temperature T (K) and the band gap $E_g$ (meV) can be estimated hence allowing the x - value to be calculated using the following empirical formulae from Preier {111}:

$Pb_{1-x}Sn_xSe$:

$$E_g = 125-1021x + \sqrt{400+0.256T^2} \quad \text{meV} \qquad (58)$$

$PbS_{1-x}Se_x$:

$$E_g = 263-138x + \sqrt{400+0.256T^2} \quad \text{meV} \qquad (59)$$

| Sample | SnSe:PbSe | Angle 2θ | a / Å | x |
|---|---|---|---|---|
| MBE 68.1 | 0.03 | 140.70° ±0.01 | 6.1206 ±0.0018 | 0.044 ±0.015 |
| MBE 69.2 | 0.07 | 140.93° ±0.01 | 6.1164 ±0.0018 | 0.078 ±0.015 |
| MBE 70.2 | 0.12 | 141.32° ±0.01 | 6.1089 ±0.0019 | 0.139 ±0.015 |
| MBE 71.1 | 0.17 | 141.67° ±0.01 | 6.1024 ±0.0019 | 0.192 ±0.015 |
| MBE 72.1 | 0.22 | 141.85° ±0.01 | 6.0992 ±0.0019 | 0.218 ±0.015 |

Table (7). Measured lattice constants and calculated x - values for 5 $Pb_{1-x}Sn_xSe$ samples using [642] powder reflection planes {110}.

Due to the uncertainty of the absorption edge measurement, this technique allows only a qualitative assessment of the Sn/Pb or Se/S ratios. It is, however, a simple and relatively quick technique which has proved to be very useful in the initial system calibration work.

During the above work on composition values, it was observed that a certain amount of inhomogeneity of film composition was present across a $Pb_{1-x}Sn_xSe$ sample. A film of $Pb_{1-x}Sn_xSe$ (flux ratio SnSe : PbSe = 0.1) was grown with a substrate temperature of 645K using port 4 for SnSe (bottom 30°, left 30°) and port 6 for PbSe (bottom 30°, right 30°). Using a 1mm diameter sample and reference orifice, the film was measured at 9 points across the surface of a 15 x 15 mm $BaF_2$ slice positioned axially and squarely upon the substrate holder. The results of these measurements can be seen in Fig(77) where the average room temperature absorption edge is 1534 $cm^{-1}$ (6.52μm) with a maximum deviation of ± 34 $cm^{-1}$ (± 0.15μm). Using equation 58, this implies an x - value of 0.086 ± 0.005. This type of inhomogeneity can be tolerated when it is considered as an advantage to have different lasers across one laser slice emitting various wavelengths. However, if production type lasers are required with a customer - specified wavelength, a

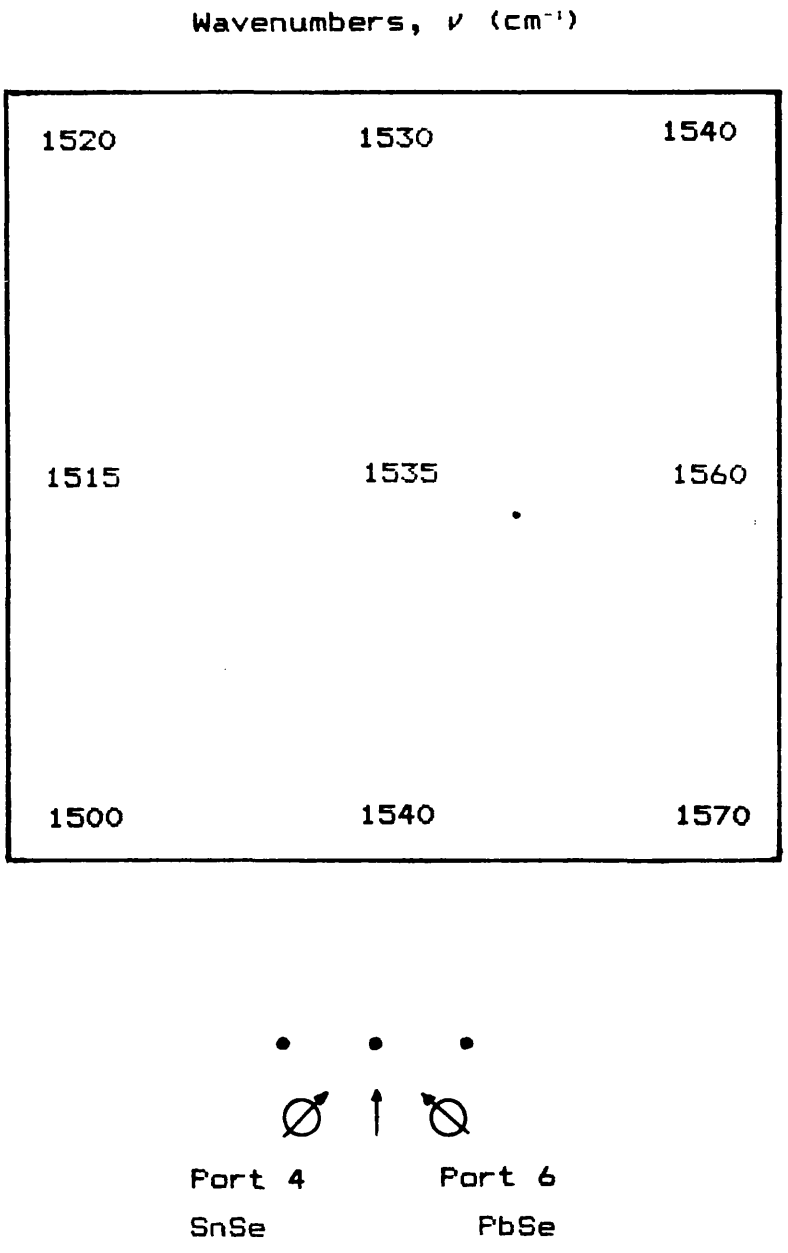


Fig(77). Absorption edge measurements across a $Pb_{0.9}Sn_{0.1}Se$ film grown on $BaF_2$ showing the inhomogeneity of such films.

rotating sample holder arrangement is needed.

The inhomogeneity explains the discrepencies between flux rate ratios and composition values discovered with the X - ray diffractometer. When it is also considered that different ionisation yields can be expected between different beam fluxes, the above X - ray diffractometry results show a good agreement and can be taken as a calibration level about the axis of the substrate holder.

The effect of substrate deposition temperature upon the composition of ternary films has been investigated using constant flux rate conditions for a multi - layer structure. Five 2500Å thick $Pb_{1-x}Sn_xSe$ layers were grown with a flux rate SnSe : PbSe = 0.1. Substrate temperatures of 720, 695, 670, 645 and 620K were chosen and Fig(78) shows the results of a SIMS profile through the sample {108}. This profile implies that a $Pb_{0.9}Sn_{0.1}Se$ layer is best grown using a substrate temperature of 645K where here the sticking coefficients of PbSe and SnSe are practically equal and close to unity. This is indicated by the fact that there is almost a one to one relationship between beam flux ratios and the composition factor x and total flux rate with growth rate. The sticking coefficients are definitely not precisely equal to unity because the composition factor

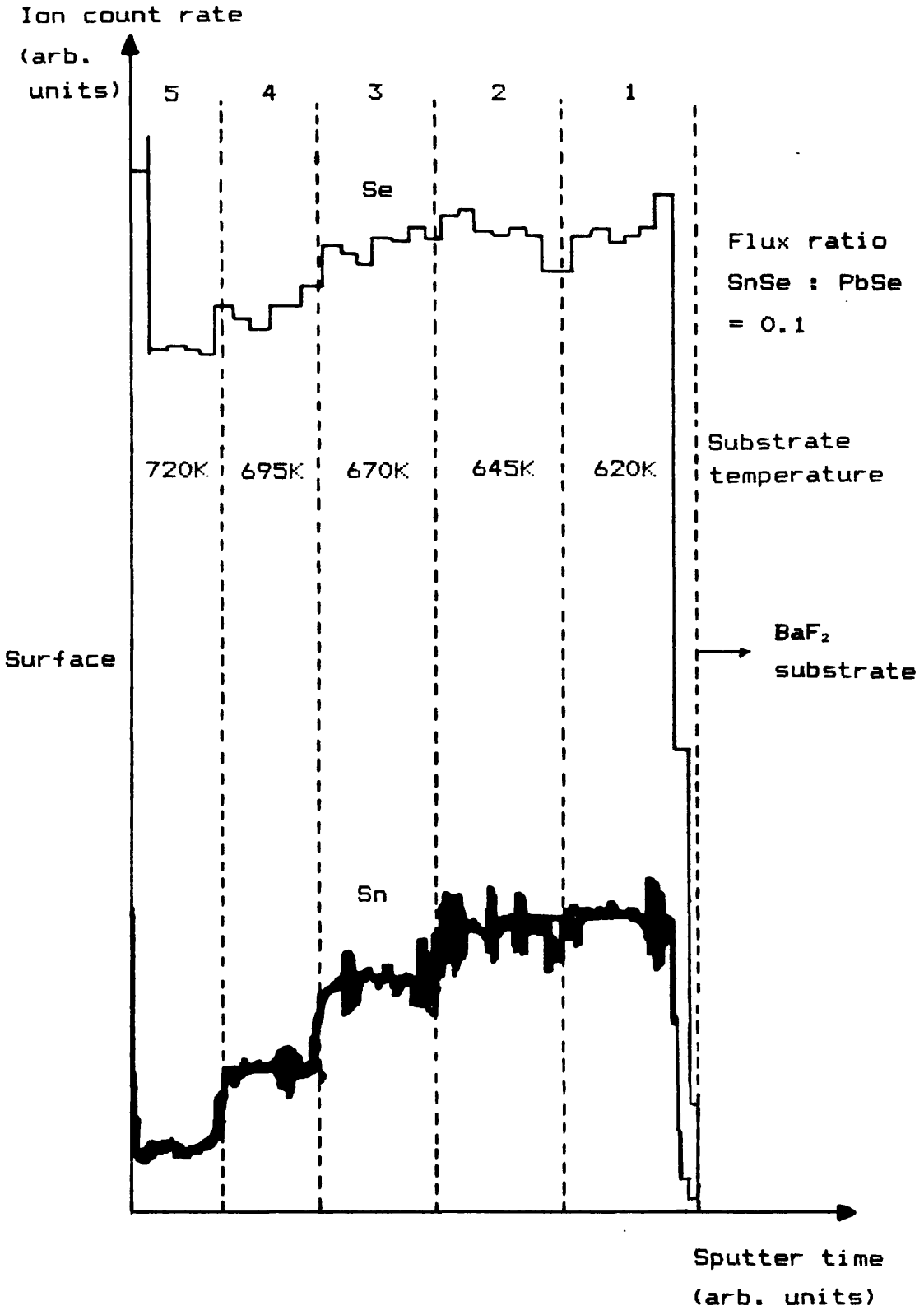


Fig(78). Secondary ion mass spectroscopy scan of a $Pb_{0.9}Sn_{0.1}Se$ structure grown on $BaF_2$ with five different deposition temperatures {108}.

shows the deposition temperature dependence for constant flux ratios above 645K.

## 4.4) Doping of lead chalcogenide MBE layers

In the epitaxial growth of lead chalcogenide laser diodes the p - n junction is normally created by introducing foreign atoms. The use of non - stoichiometric techniques performed by controlling elemental furnaces for accurate doping values is not preferred since vacancies diffuse much more quickly than foreign atoms and furnace control is difficult at the required dopant furnace temperatures. For example, in PbTe, $PbSe_{1-x}Te_x$ (all x) and $Pb_{1-x}Sn_xTe$ (x small), the p - n junctions diffuse with diffusion coefficients between $1x10^{-8}$ - $1x10^{-10}$ $cm^2s^{-1}$ at 670K whilst foreign atoms e.g. bismuth (n - type) and thallium (p - type) diffuse so slowly that at a temperature of 670K, no movement of a p - n junction can be observed over a period of hours {112}.

Binary and ternary lead chalcogenide epitaxial films deposited on an electrically neutral substrate are n - type since the more volatile chalcogen element resublimes during the growth process producing a surplus of chalcogen vacancies. However, under similar MBE metal - rich growth conditions, films grown upon p - type

substrates remain p - type due to the fast diffusion of lead vacancies to the growing surface. This diffusion is sufficient to maintain p - type conduction in films of upto 6μm thickness. Therefore a dopant acting as an acceptor will only be necessary to achieve defined carrier concentrations.

The doping in the work described in this thesis is a combination of two techniques: non - stoichiometric control (p - type; Se) and foreign atom incorporation (n - type; Bi and p - type; Ag).

4.4.1) N - type doping

It should be possible to anneal a p - type PbSe substrate in a chalcogen free atmosphere to form an n - type surface. Requirements are lead - rich growth conditions and sufficiently long annealing times at temperatures where the selenium will be lost through surface diffusion. It has been shown, however, that after the MBE - growth of p - type PbSe films on PbSe substrates, subsequent annealing at the growth temperature of 650K does not produce the expected surface n - type conduction {113}. The growth temperature is too low for sufficient selenium diffusion to occur without the addition of hydrogen in the atmosphere or lead upon the surface. These conditions are not possible within the

MBE system.

Increasing the annealing temperature to over 770K within short periods of time within the MBE system is also impractical and so, therefore, another approach to n - doping is necessary.

A dopant acting as a donor is necessary to convert p - type films to n - type and in the work here, controlled n - type doping will be performed by the foreign atom incorporation of the donor Bi. Bi occupies lead vacancies {114} and to ease its incorporation, it is sublimed as $Bi_2Se_3$. The selenium eases the creation of lead vacancies and hence enhances the incorporation of the Bi. It will be seen in section 4.3.3 that $Bi_2Se_3$ : PbSe flux rate ratios of approximately 0.001 produce n - type films with electron concentrations of $1x10^{19}$ $cm^{-3}$ and that concentrations of the order of $3x10^{20}$ $cm^{-3}$ can be produced {69}.

The specific work upon Bi - doping of the new laser material $Pb_{1-x}Eu_xSe$ is presented separately in section 4.5.2.

4.4.2) P - type doping

Initial laser structures, as described in chapter 5, were fabricated using an elemental Se furnace as the compensating p - type dopant source for p - type

lower confinement layers and active regions. It will be seen, however, that insufficient control of the Se furnace results in large differences in the carrier concentrations of the layers leading to inconsistent laser characteristics.

The diode laser requires the possibility of producing controlled, highly doped p - type layers. This has led to intensive experiments being performed to find a suitable p - type dopant and source. P - type doping of the lead chalcogenides has seen the use of various dopants, the majority of work published being on the $Pb_{1-x}Sn_xTe$ system {115} - {117}. The dopant most investigated is thallium and initial experiments connected with the work here on p - type doping considers Tl as a feasible material for use in the MBE of PbSe - orientated alloy systems.

P - type doping with Tl proves to be difficult and first experiments upon doping of PbSe with Tl were performed in a low pressure quartz reactor system due to the poisonous nature of Tl. Fig(79) is a diagram of a reactor tube with flowing nitrogen and hydrogen and a pressure of 1mbar with n - type PbSe source material at the gas inlet end and a substrate holder with a $BaF_2$ substrate positioned at the gas outlet end. A sloping temperature profile is positioned where the temperature

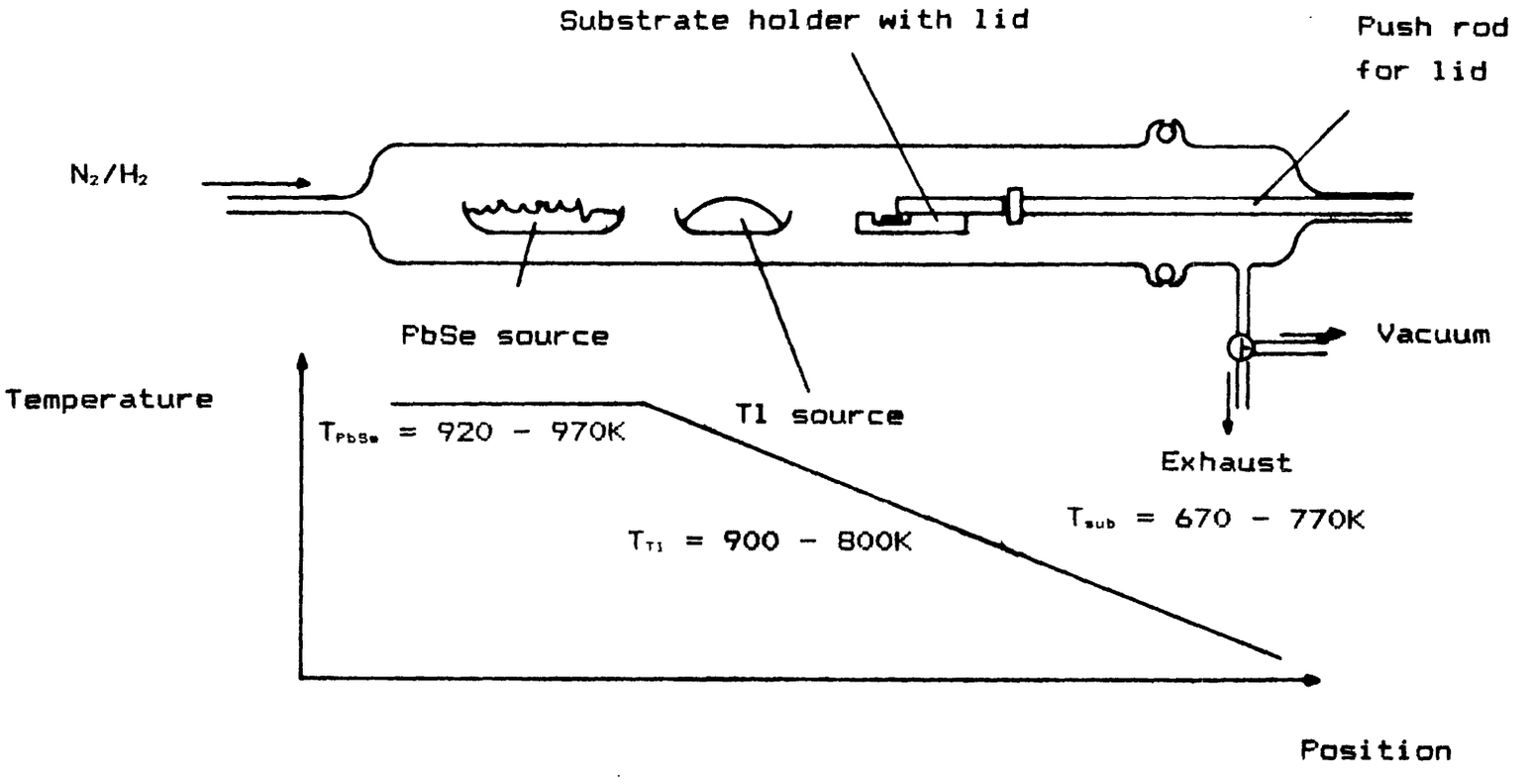


Fig(79). Reactor tube arrangement for thallium doping experiments.

of the PbSe is approximately 970K and that of the substrate 670K. The Tl is placed in a boat between the two, allowing the temperature and hence the Tl vapour pressure to be varied.

In contrast to the PbTe system {117}, every attempt to produce p - type PbSe resulted in n - type material. This occured also for $Pb_{1-x}Sn_xSe$ and PbS source materials and further investigations revealed that Tl will only be incorporated as an acceptor into PbSe and PbS in the presence of Se. Due to it's low vapour pressure, toxic nature and strong dependence upon the required simultaneous Se flux rate, thallium is not used in the MBE growth of PbSe or $Pb_{1-x}Sn_xSe$ systems. Silver is chosen as a likely candidate since it acts as an acceptor in Te - rich PbTe {117}, is non - toxic and due to it's vapour pressure data, can easily be loaded into one of the standard types of furnace described in section 3.4.3. The strong dependence of the silver doping effect upon the amount of Se compensation, however, is not known.

Results of work concerning p - type doping of lead chalcogenides are given in sections 4.4.4 (Se) and 4.4.5 (Ag) with section 4.5.2 describing the specific results of p - type doping work performed in the $Pb_{1-x}Eu_xSe$ alloy system.

4.4.3) Bismuth impurity n - type doping

N - type doping experiments were performed with a 1mm diameter orifice built into a standard Varian MBE cell having a resultant operation temperature of approximately 970K and producing a flux ratio $Bi_2Se_3$ : PbSe = 0.03. Electron concentrations measured of films grown with this flux ratio were in the region of $3x10^{20}$ $cm^{-3}$. Even with such high doping rates, Bi surface precipitation and surface defects were not observed.

Two runs were performed laying first a p - type layer onto a $BaF_2$ substrate covering this with an n - type layer and secondly a p - type layer covering an n - type layer on $BaF_2$. In both experiments the substrate temperature was maintained at 650K and each layer had a thickness of 3µm. Both runs produced the same result. A p - n junction was formed in the middle of the 6µm thick samples and showed no indication of diffusion in either direction to within the measurement accuracy of ± 0.5µm. It is, therefore, possible to produce n on p material and p on n material by simply operating the $Bi_2Se_3$ furnace shutter. It is to be noted that to produce n - type layers it is an advantage to maintain the Se flux since this enhances the incorporation of Bi through the increased formation of lead vacancies upon which the Bi

atoms are incorporated.

To produce electron carrier concentration values suitable for diode lasers, the $Bi_2Se_3$ flux has to be substantially lowered. Electron concentrations in PbSe of the order of $1x10^{19}$ $cm^{-3}$ are achieved with flux ratios as low as 0.0005, although the exact ratio is very difficult to measure accurately at these flux levels.

The use of Bi as a suitable dopant has also been shown in the $PbS_{1-x}Se_x$ and $Pb_{1-x}Sn_xSe$ systems and can successfully produce material with constant doping levels in the required range of $5x10^{18}$ - $2x10^{19}$ $cm^{-3}$.

4.4.4) Se - doped p - type MBE layers

The first p - type doping was carried out upon PbSe layers deposited onto $BaF_2$ substrates. Due to the unstable nature of the Se furnace, a series of doping experiments were not carried out, the resulting films being only tested for p - type conduction. In all cases, hole concentrations of $1x10^{17}$ - $5x10^{17}$ $cm^{-3}$ were obtained which have also been observed in the PbS, $Pb_{1-x}Sn_xSe$ ($x \leqslant 0.1$), $PbS_{1-x}Se_x$ ($0 < x < 1$) and $Pb_{1-x}Eu_xSe$ ($x \leqslant 0.01$) systems.

4.4.5) Silver impurity p - type doping

Experiments were performed to find the necessary

silver furnace parameters and geometries to incorporate Ag in the lead chalcogenides as an acceptor under MBE growth conditions. To ensure that the Ag will act as an acceptor and not as a donor, Se must be simultaneuosly sublimed to produce a chalcogene - rich environment in which Ag is substitutionally incorporated {117}. The beam flux ratio Se : PbSe = 0.1 has been used and as the results suggest, proves to be sufficient to enable the Ag atoms to occupy lead vacancy sites.

The results of preliminary doping tests show that a Ag furnace with an orifice of 2mm diameter situated in port 1 yields reproducible p - type conduction. Doping rates were measured between flux ratios Ag : PbSe = 0.0005 - 0.016, the results of which are given in Fig(80). The figure indicates that there is a Ag flux saturation level of 0.005, after which the hole concentration decreases to approximately $1x10^{18}$ $cm^{-3}$. Here the Ag is most likely being incorporated both substitutionally (acceptor) and interstitially (donor) and the material is, therefore, highly compensated. The carrier concentrations also show an abnormal temperature dependence in which the hole concentrations at 77K are higher than those measured at room temperature. An explanation of this type of behaviour is discussed in section 4.4.2.

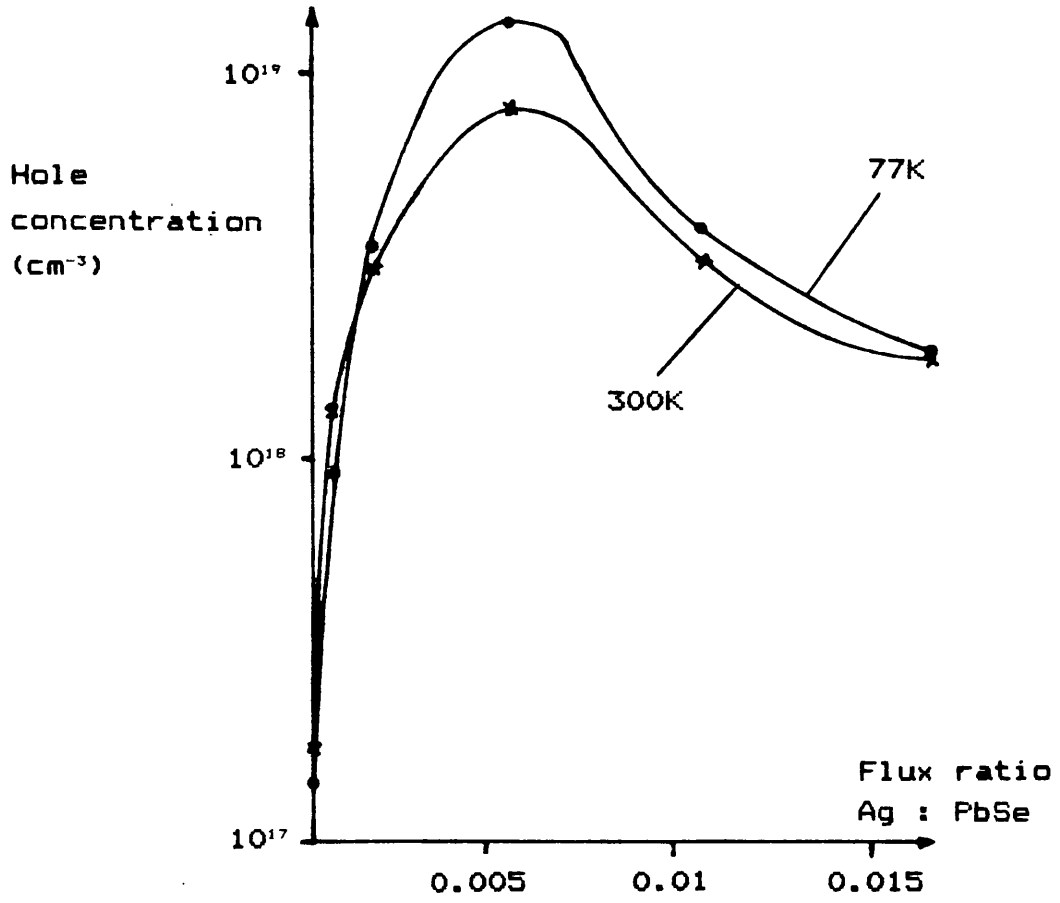


Fig(80). Hole concentration versus silver dopant flux rate in PbSe for 77K and 300K.

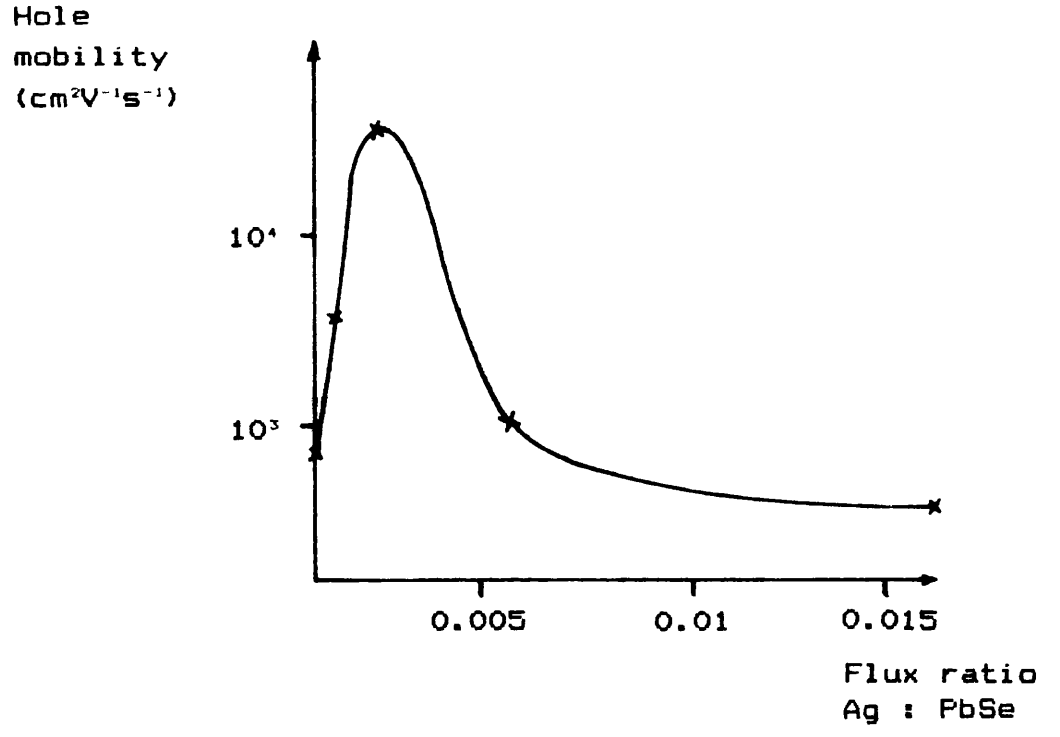


Fig(81). Hole mobility versus silver dopant flux rate in PbSe at 300K.

Fig(81) indicates the dependence of the room temperature hole mobility. A similar picture is seen as in the hole concentration, in this case the peak is at a Ag flux value of 0.0015. Since the hole concentration at this doping level is also high, this beam flux ratio of 0.0015 is used for subsequent laser structures. This value proves to provide adaquate, reproducible and constant doping levels which are not dependent upon constant Se flux levels being maintained.

## 4.5) The $Pb_{1-x}Eu_xSe$ alloy system

It will be seen in the following chapter that the $Pb_{1-x}Eu_xSe$ system offers very good confinement layer properties for short wavelength lead chalcogenide lasers due to the high band gap shift sensitivity to the Eu content. Hence the $Pb_{1-x}Eu_xSe$ alloy and the impurity doping characteristics have been extensively researched for different x values. Undoped, Bi - and Ag - doped $Pb_{1-x}Eu_xSe$ layers have been grown upon cleaved [111] $BaF_2$ substrates, the IR spectra, carrier concentrations and mobilities being measured.

### 4.5.1) Band gap measurements

Infra - red measurements have been performed upon the $Pb_{1-x}Eu_xSe$ material system grown by MBE with flux

ratios Eu : PbSe = 0 - 0.2 at a growth temperature of 645K. The layers are grown with a chalcogen - rich environment since Eu, like silver, is incorporated substitutionally within the Pb sub - lattice. A Se flux rate ratio of Se : PbSe = 0.1 is used and has proved to be sufficient to enable Eu and, where appropriate, additional Ag incorporation. A typical room temperature absorption spectrum is shown in Fig(82) for a flux ratio Eu : PbSe = 0.02 and where the film thickness is 3μm.

In subsequent laser structures, Eu has been loaded in port 2 (axially central) and, therefore, the series of growth experiments have been performed upon $Pb_{1-x}Eu_xSe$ films with this furnace geometry i.e. Eu in port 2 and PbSe in port 6. The absorption edge inhomogeneity for a 4μm thick sample is indicated in Fig(83) where the flux ratio Eu : PbSe = 0.02. The average absorption edge is 3766 $cm^{-1}$ (2.66μm) with a maximum deviation of ± 415 $cm^{-1}$ (0.32μm).

The dependence of the absorption edge upon the Eu content for x = 0 - 0.2 is given in Fig(84) in which it is seen that it shifts considerably to the required short wavelength end of the IR region. The measurements are taken from cleaved $BaF_2$ substrates situated at the centre of the substrate holder. Samples with x > 0.05 need higher Se flux rates and it was found that ratios

Fig(82). The transmission spectrum of a 3μm thick $Pb_{0.98}Eu_{0.02}Se$ film on $BaF_2$ at 300K.

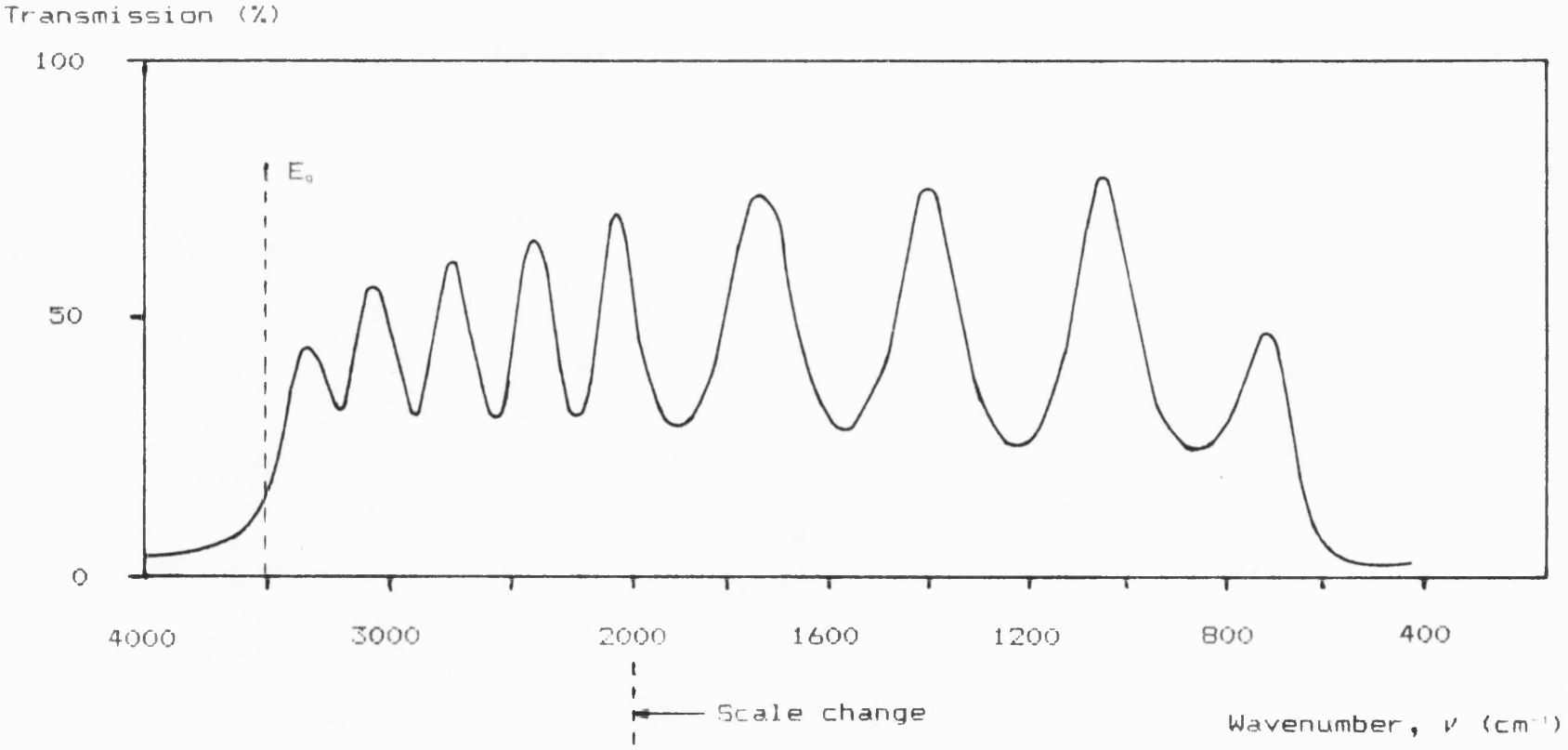

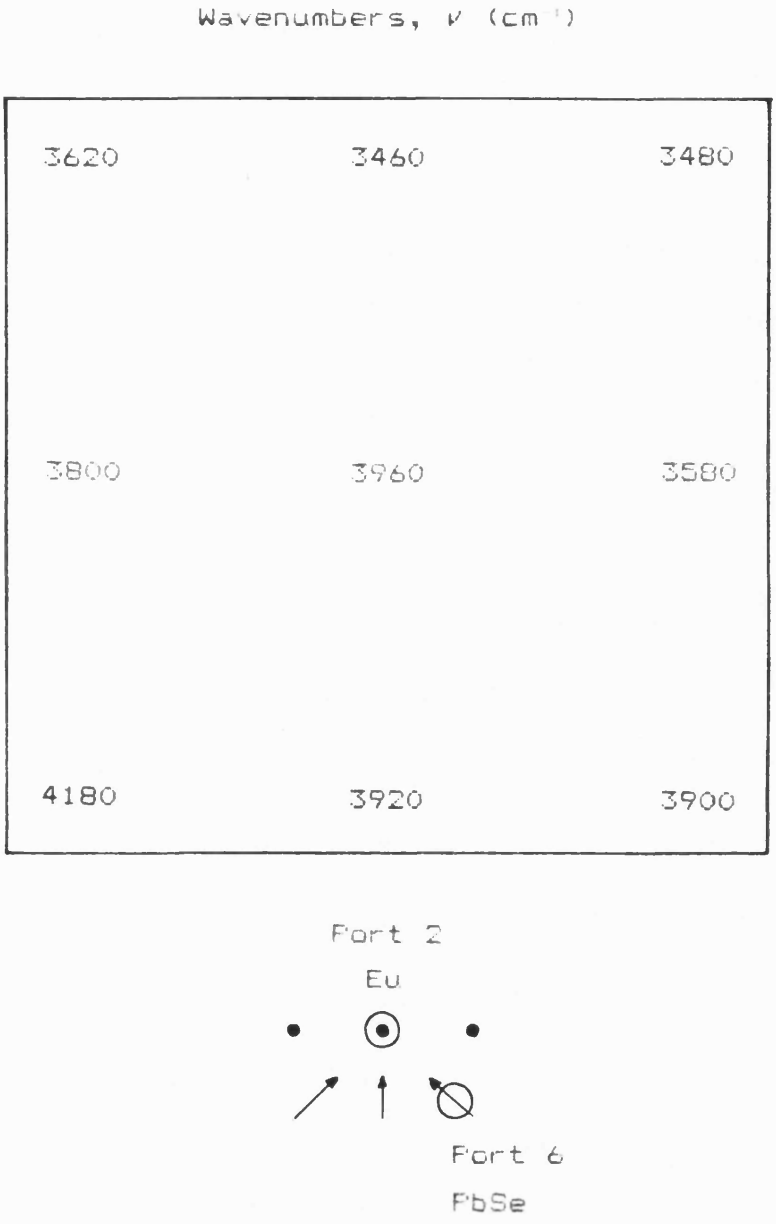


Fig(83). Absorption edge measurements across a $Pb_{0.98}Eu_{0.02}Se$ film grown on $BaF_2$ showing the inhomogeneity of such films.

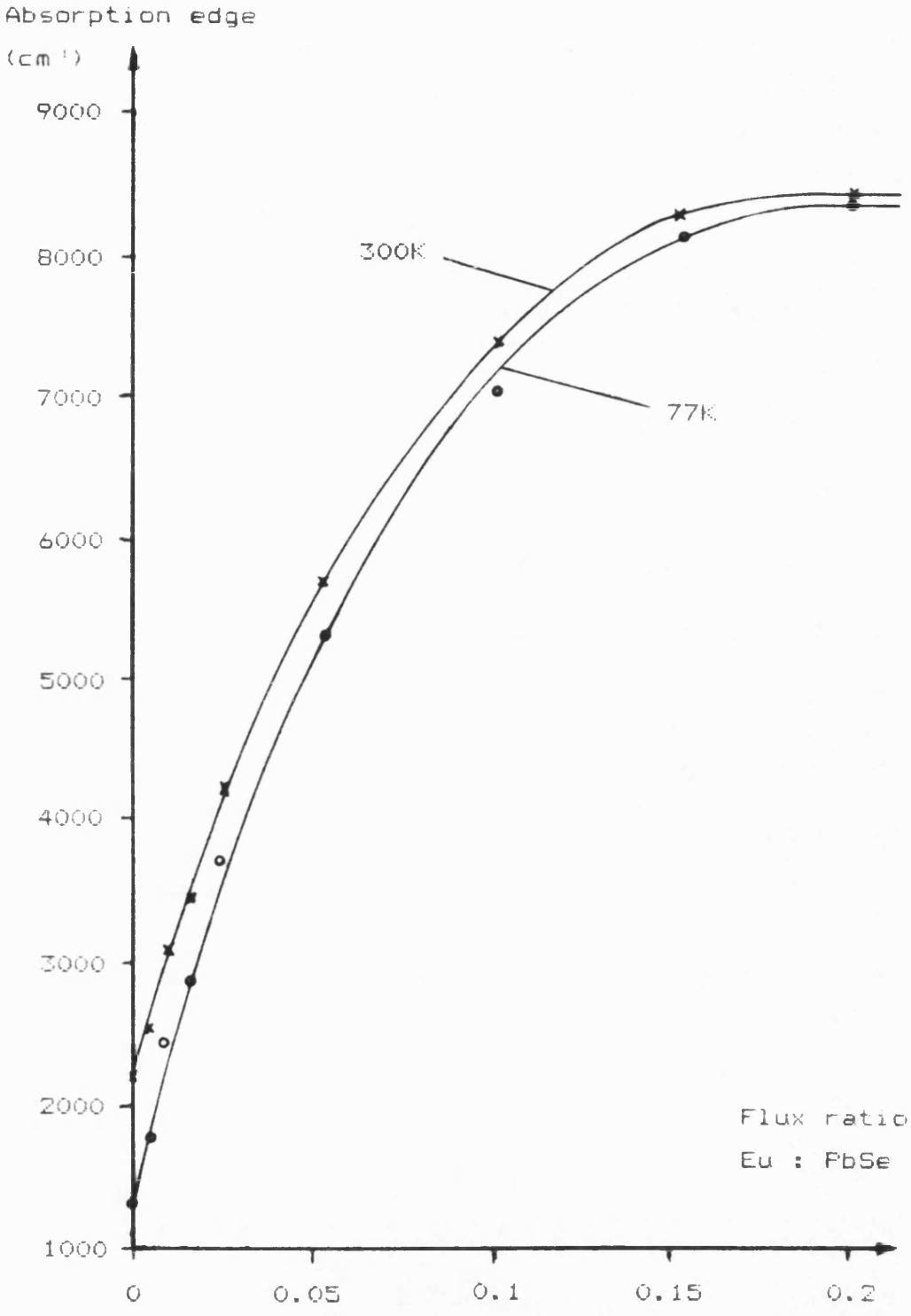


Fig(84). Absorption edge in $Pb_{1-x}Eu_xSe$ with varying Eu flux ratios at 77K and 300K.

Se = PbSe of upto 1.1 are necessary. Concentrations over x = 0.1 indicate a saturation of the band gap increase, probably due to interchanges between the 2+ state and the 3+ state of europium. For x > 0.15, the surface morphology suggests that the growth conditions are not suitable. A $Pb_{0.8}Eu_{0.2}Se$ film shows a similar surface morphology to that of a PbSe film grown at a low substrate temperature. Scanning electron microprobe analysis, however, indicates polycrystalline growth with no elemental precipitations. To produce crystalline $Pb_{1-x}Eu_xSe$ films where x > 0.15, the substrate temperature will probably have to be increased with a consequent increase in the Se flux. Further investigations are, however, outside the scope of this thesis and will not be discussed here.

Actual Eu contents of individual films have not been chemically investigated, therefore all x - values concerned with the Eu work indicate beam flux monitor ratios Eu : PbSe. Until there is evidence, however, against these ratios being directly read as Eu concentrations, it is assumed that the ionisation rates and sticking coefficients of PbSe and Eu are comparable and hence that the flux ratios correspond to the x - values.

4.5.2) The doping of $Pb_{1-x}Eu_xSe$

Five series of experiments have been carried out upon $Pb_{1-x}Eu_xSe$ epitaxial MBE films deposited on cleaved $BaF_2$ substrates. The films have a thickness of 4µm and were deposited with a substrate temperature of 650K. First measurements with 2µm thick layers show poor carrier mobility values due to interface state effects. Thicker samples eliminate this effect and also produce a higher measurement accuracy. The series consist of the following investigations (flux ratio Se : PbSe = 0.1 from section 4.4.4):

a) Undoped $Pb_{1-x}Eu_xSe$, x = 0, 0.004, 0.008, 0.015 and 0.025;

b) bismuth - doped $Pb_{1-x}Eu_xSe$ using the flux ratio $Bi_2Se_3$ : PbSe = 0.0005 from section 4.4.3 and the above x - values;

c) silver - doped $Pb_{1-x}Eu_xSe$ using the flux ratio Ag : PbSe = 0.0015 from section 4.4.5 and the above x - values;

d) $Pb_{0.985}Eu_{0.015}Se$ with Bi doping levels of 0, 1/2, 1, 2 and 4 times the flux value 0.0005;

e) $Pb_{0.985}Eu_{0.015}Se$ with Ag doping levels of 0, 1/2, 1, 2 and 4 times the flux value 0.0015.

Fig(85) shows the carrier concentration dependence upon Eu : PbSe flux ratio values and Fig(86)

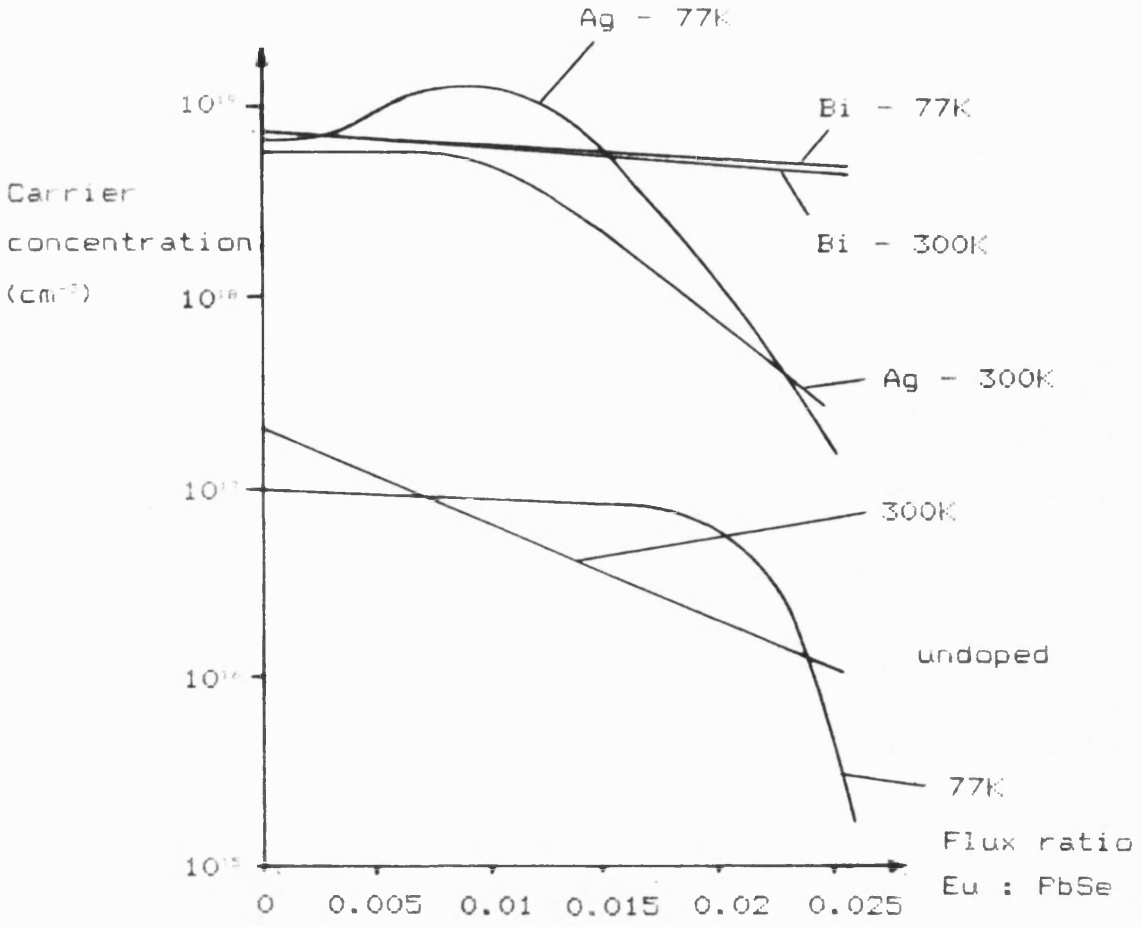


Fig(85). Carrier concentration for undoped, Bi - and Ag - doped $Pb_{1-x}Eu_xSe$ films at 77K and 300K.

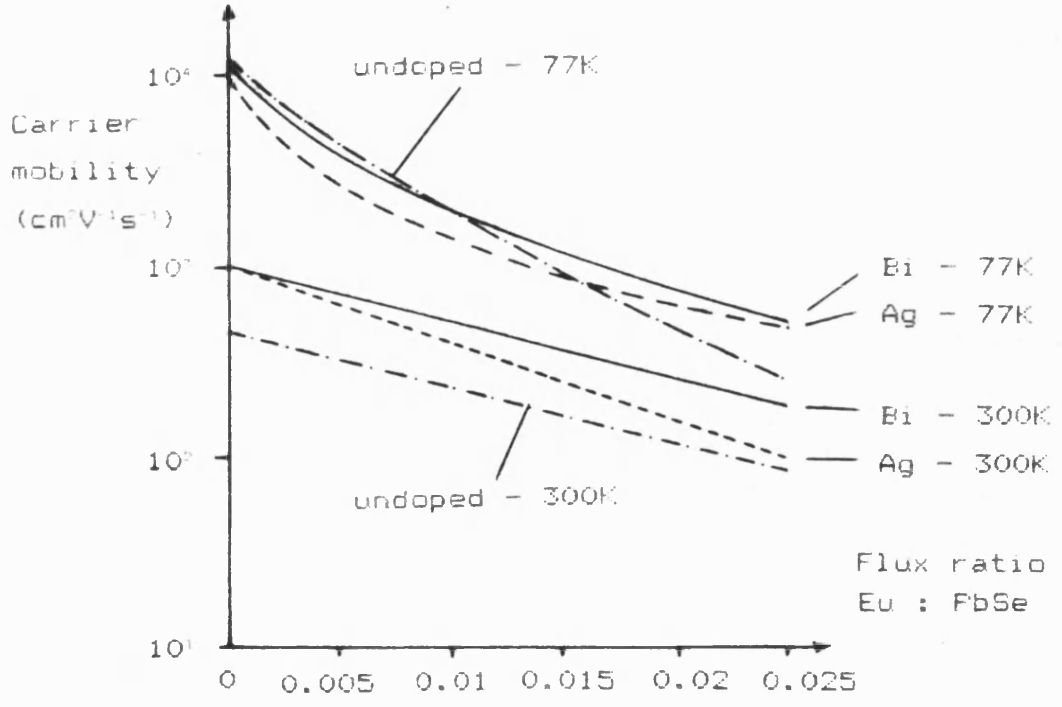


Fig(86). Carrier mobility for undoped, Bi - and Ag - doped $Pb_{1-x}Eu_xSe$ films at 77K and 300K.

the carrier mobility for the series a) - c). Bi is incorporated as a donor, the level of doping being nearly constant with increasing Eu concentration. Electron concentrations range between $7x10^{17}$ - $4x10^{18}$ $cm^{-3}$ for $x = 0 - 0.025$. This applies for both 77K and 300K which indicates that the donor levels are to be found in the conduction band as schematically shown in Fig(87). The figure shows an explanation of the temperature independence of the carrier concentrations to the doping levels and the observed temperature dependence of the band gap taken from the IR absorption measurements. The mobility at 300K decreases nearly linearly as to be expected from a crystal alloy system. At 77K the decrease is non linear and the mobility levels upto $x = 0.025$ show acceptable values for laser n - type doping work.

The hole concentrations of undoped and Ag - doped p - type $Pb_{1-x}Eu_xSe$ indicate a totally different dependence upon the Eu content. The carrier levels are highly dependent upon the Eu concentration ranging, for example, from $1.1x10^{19}$ ($x = 0.005$) - $1x10^{17}$ $cm^{-3}$ ($x = 0.025$) for Ag - doped material at 77K.

Fig(85) also shows that for both undoped ($0.007 < x < 0.024$) and Ag - doped ($x < 0.022$) p - type $Pb_{1-x}Eu_xSe$, the carrier concentrations exhibit an abnormal temperature dependence in that $p_{77K} > p_{300K}$.

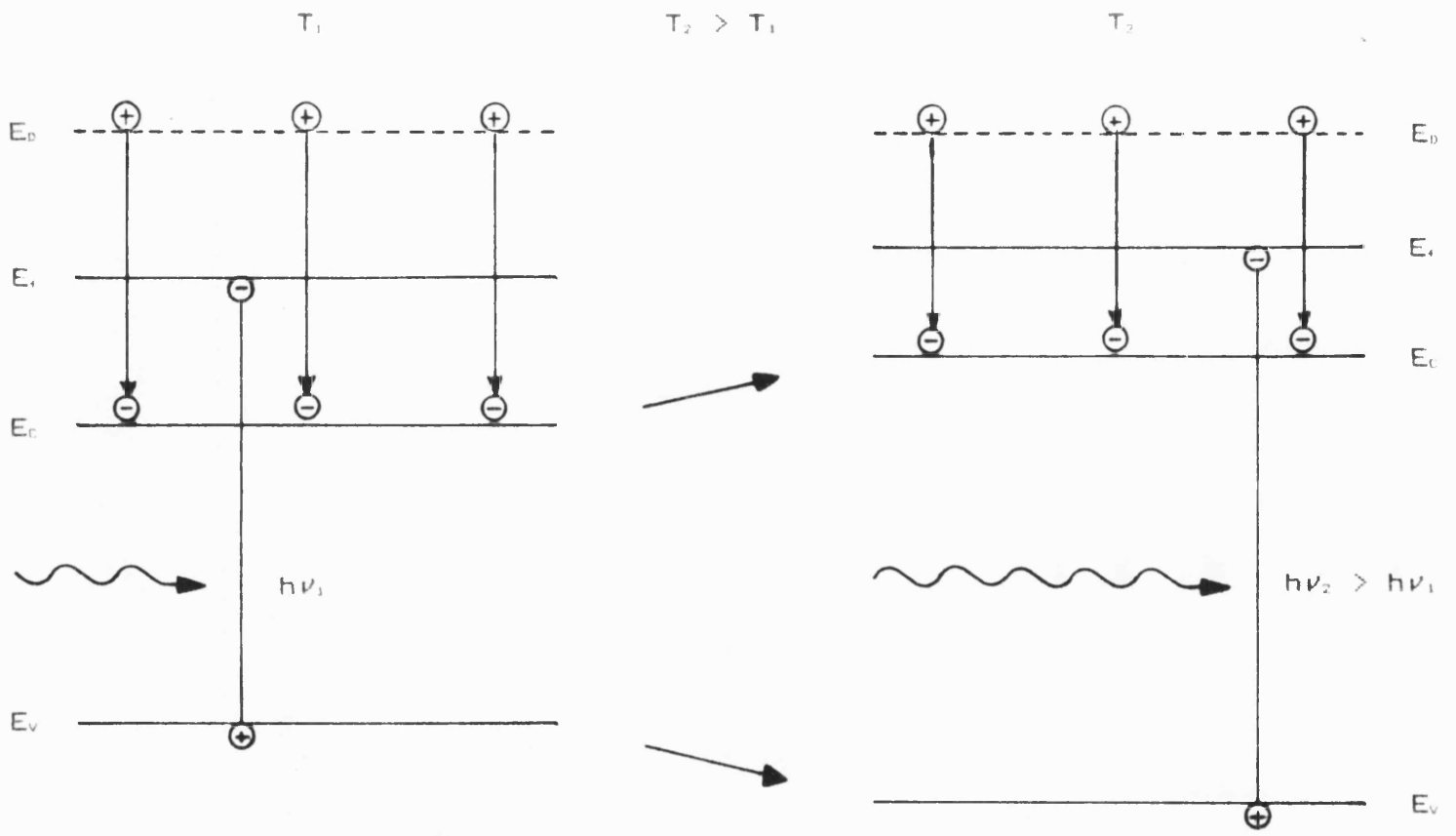


Fig(87). Energy diagrams for Bi - doped $Pb_{1-x}Eu_xSe$ films at temperatures $T_1$ and $T_2$ showing the postulated donor levels within the conduction band.

This abnormal effect has been observed in Ag - doped PbSe layers (section 4.4.5) and it is, therefore, assumed to be due to the Ag dopant. The effect can be qualitatively explained by a silver acceptor level sitting just below the top of the valence band as indicated in Fig(88). At room temperature, this level is partially ionised. If decreasing the temperature moves the top of the valence band away from the acceptor level then the carrier concentration will increase. Also, if the energy difference between the level and the bottom of the conduction band decreases slightly upon cooling, then there will be a small decrease in the absorption edge energy. These two material parameter characteristics are observed in Fig(84) and Fig(85) for x = 0. Fig(88) indicates the possible movement of $E_v$ with respect to the impurity level.

As the europium content is increased, the decreasing effect of the acceptor level can be explained by the movement of the Ag level into the forbidden gap as shown in Fig(89). For x > 0.02, the Ag level acts as an acceptor in the normal sense.

Fig(90) shows the temperature dependence of the carrier concentration from a Ag - doped $Pb_{0.985}Eu_{0.015}Se$ sample {118}. It shows an increasing hole concentration with decreasing temperature. From this it can be

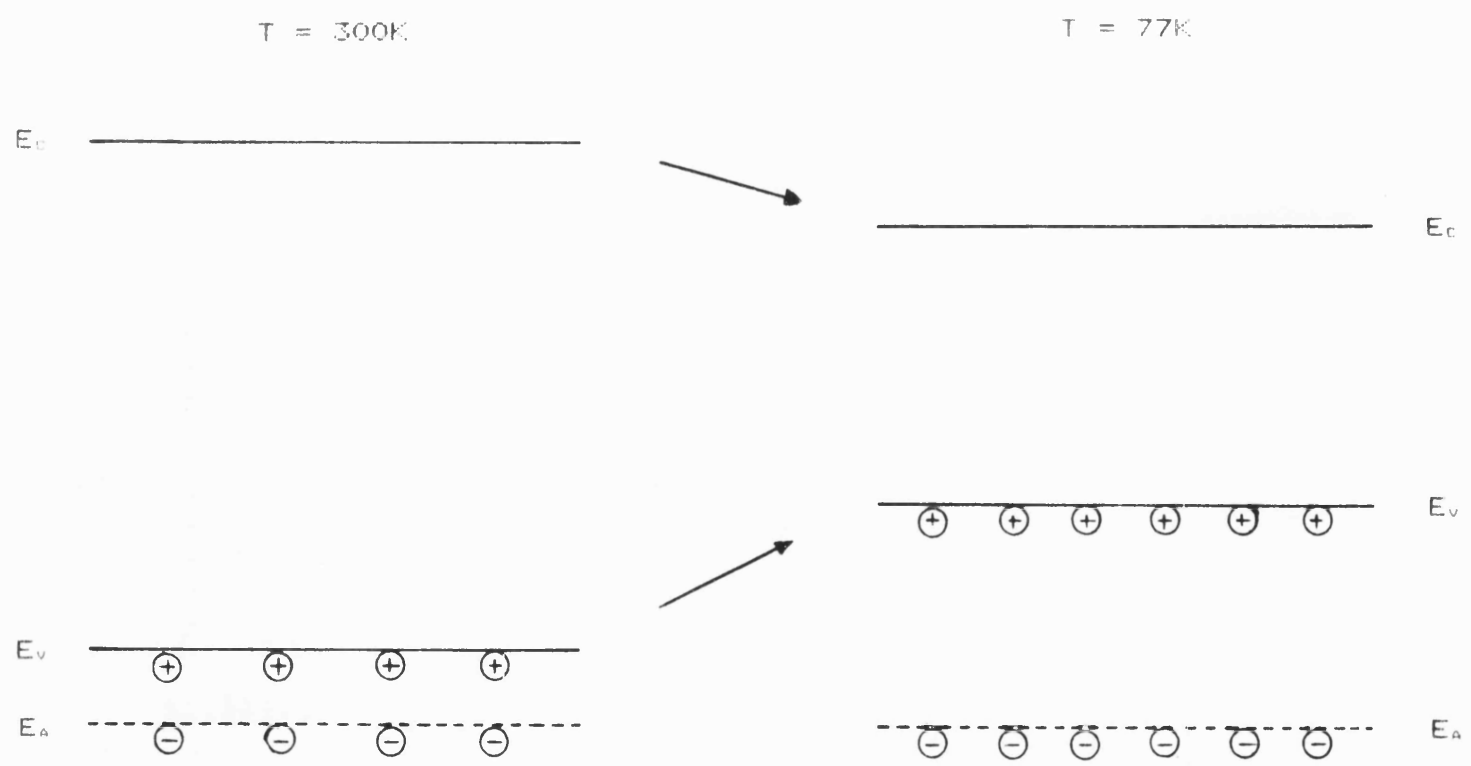


Fig(88). The idea of a silver acceptor level lying within the valence band at 300K and 77K.

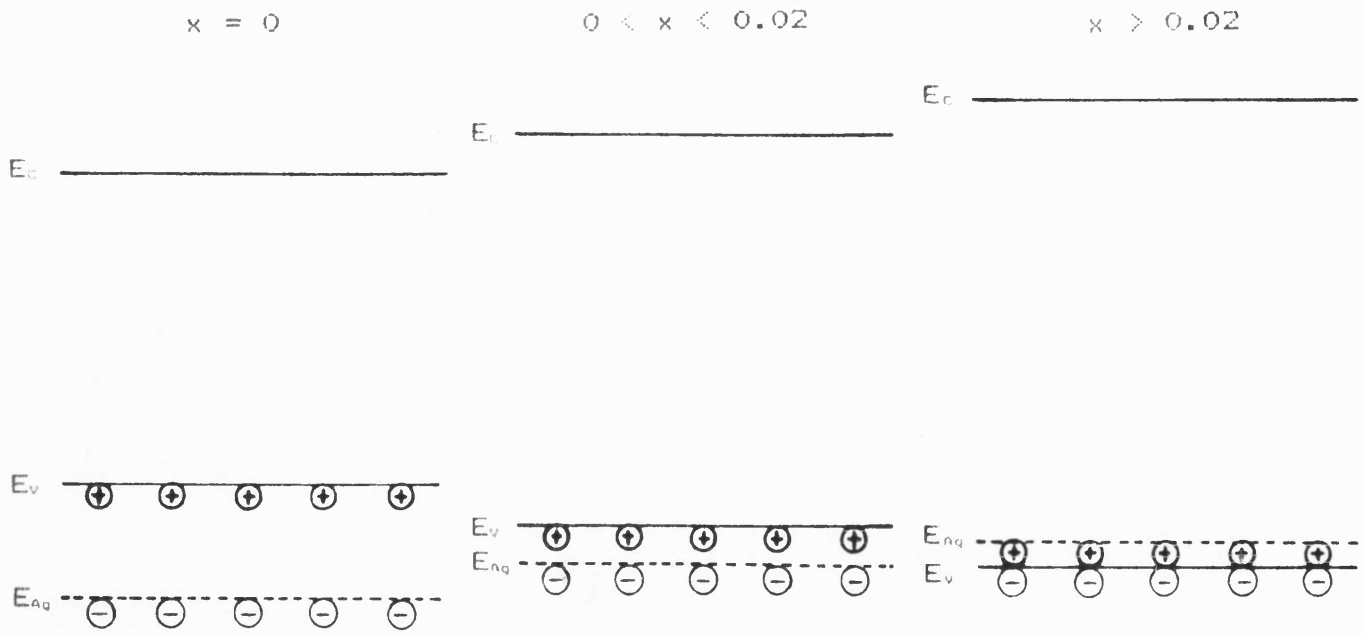


Fig(89). A qualitative explanation of the Ag acceptor level in the $Pb_{1-x}Eu_xSe$ alloy system showing schematically the location of the assumed acceptor gap as a function of the Eu content.

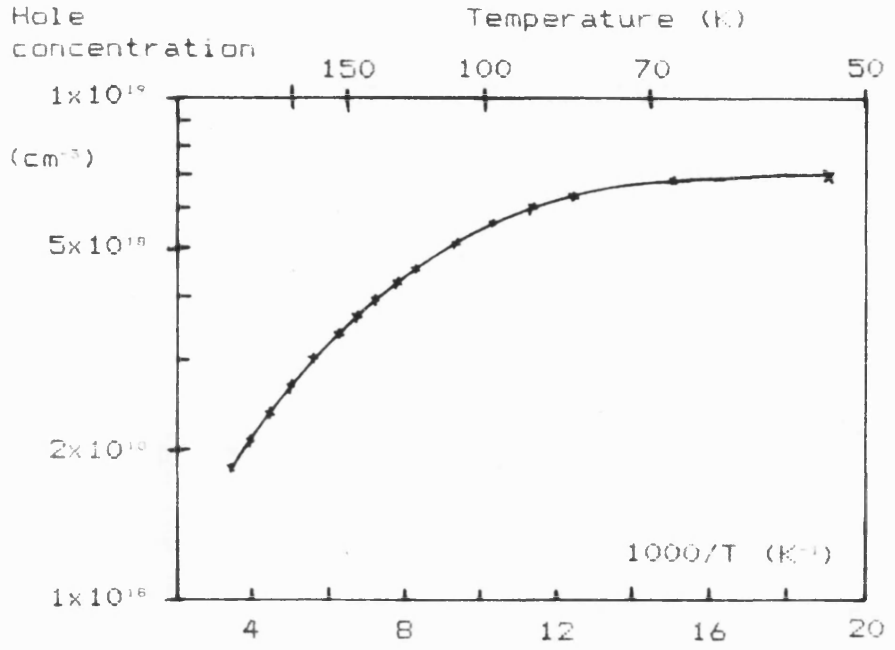


Fig(90). Temperature dependence of the hole concentration in a Ag - doped $Pb_{0.985}Eu_{0.015}Se$ layer {118}.

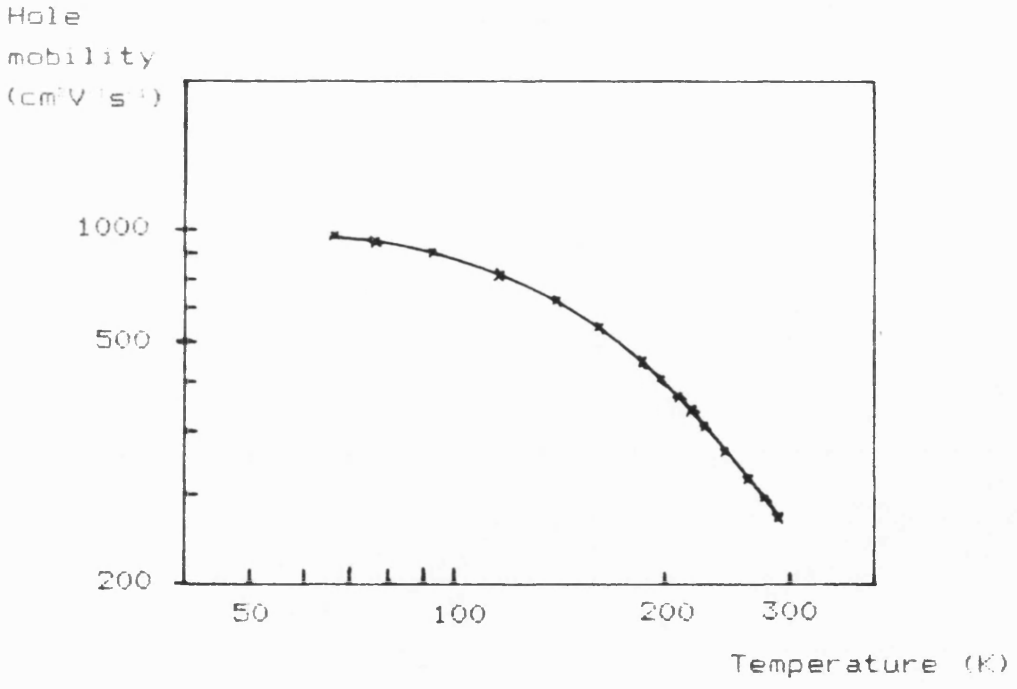


Fig(91). Temperature dependence of the hole mobility in a Ag - doped $Pb_{0.985}Eu_{0.015}Se$ layer {118}.

estimated that the Ag level is approximately 20meV below $E_v$.

In the undoped material, it is assumed that the lead vacancy level (an inefficient acceptor) is responsible for the abnormal carrier concentration temperature effect. It is known that these levels normally lie well below the top of the valence band in PbSe and have only a small influence upon the carrier concentration. If, however, the effect of Eu incorporation is to decrease the energy difference $E_v - E_{Pb}$, a Eu concentration is reached where the $E_{Pb}$ level moves from the valence band into the forbidden gap. This leads to a consequent reduction in the carrier concentration and Fig(85) indicates that this occurs for $x > 0.024$ in the 77K measurements.

The hole mobilities of Ag - doped and undoped $Pb_{1-x}Eu_xSe$ show a similar effect upon increasing the Eu content as that of Bi - doped samples (Fig(86)). The Ag - doped mobility values range from $7x10^3$ - $7x10^2$ $cm^2V^{-1}s^{-1}$ for x = 0 - 0.025 at 77K and undoped samples range from $1x10^3$ - $1.5x10^2$ $cm^2V^{-1}s^{-1}$ for x = 0 - 0.025 at 77K. The mobility dependence upon temperature of a Ag - doped $Pb_{0.985}Eu_{0.015}Se$ sample is shown in Fig(91) and exhibits a normal increase with decreasing temperature.

The effect of changing the dopant flux upon

carrier concentration in the $Pb_{0.985}Eu_{0.015}Se$ alloy system is shown in Fig(92). Fig(93) shows the dependence of the carrier mobility. These are the results of investigations d) and e) listed above. An increase of the Bi doping flux results in an increase in the electron concentration which saturates for this alloy at approximately $5 \times 10^{19}$ $cm^{-3}$ for $Bi_2Se_3$ : PbSe = 0.005. The mobility values gradually decrease with increasing Bi doping fluxes. On the other hand, hole concentrations resulting from Ag - doping are independent of the doping flux. Possible explanations are:

a) Due to a deficiency of lead vacancies, the Ag is being incorporated as a donor and as an acceptor impurity causing compensation;

b) additional Ag is not being incorporated due to a low sticking coefficient resulting from the high Eu content.

In both cases, an increase in Se flux should enable more Ag to be incorporated onto lead vacancy sites. The carrier concentrations resulting from the Ag flux discussed in section 4.4.5 are, however, adequate for the purposes of this work and further investigations have not been undertaken here.

To complete the results of series d) and e), Fig(94) presents the results of absorption edge

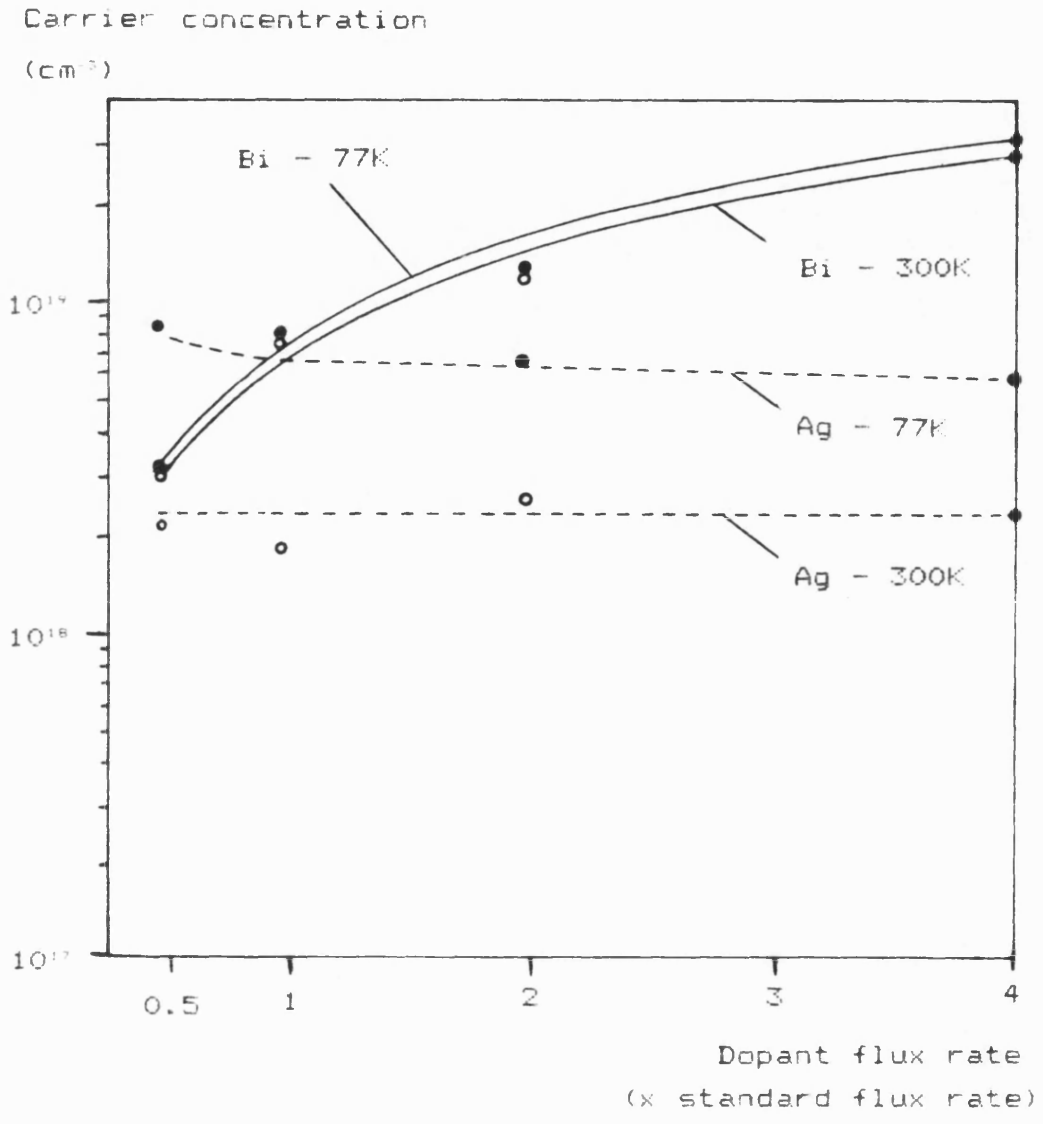


Fig(92). The effect of dopant flux ratios upon the carrier concentration of $Pb_{0.985}Eu_{0.015}Se$ layers. (The standard flux rate is that used in the previous diagrams).

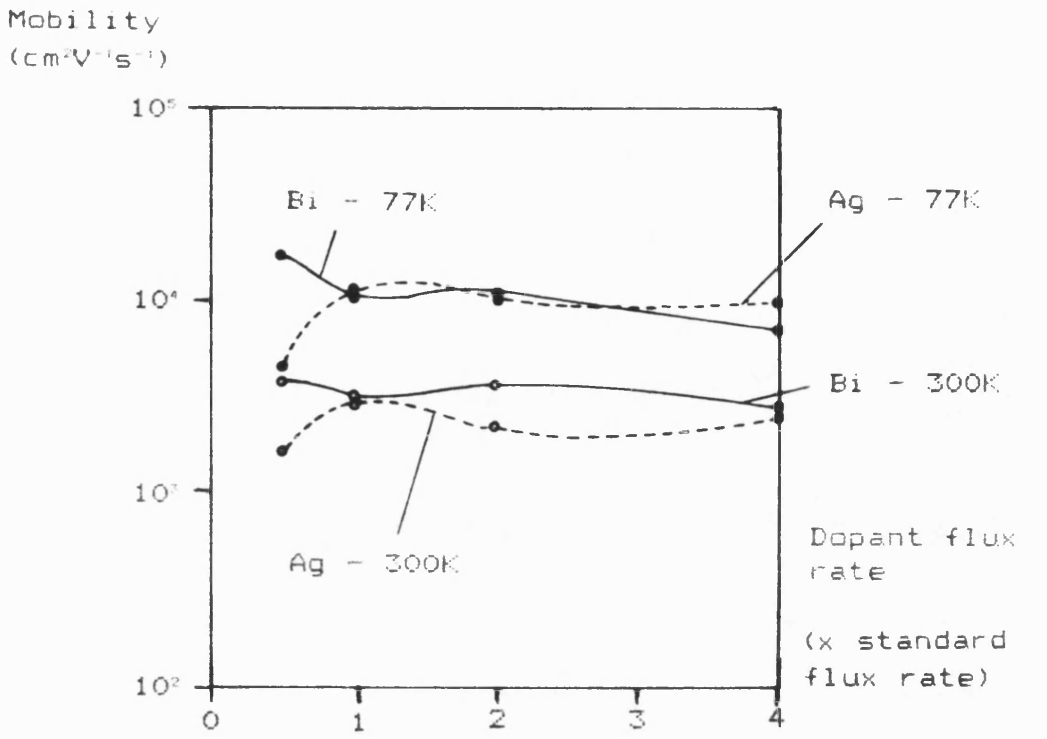


Fig(93). The effect of the dopant flux rate upon the carrier mobility of $Pb_{0.985}Eu_{0.015}Se$ layers.

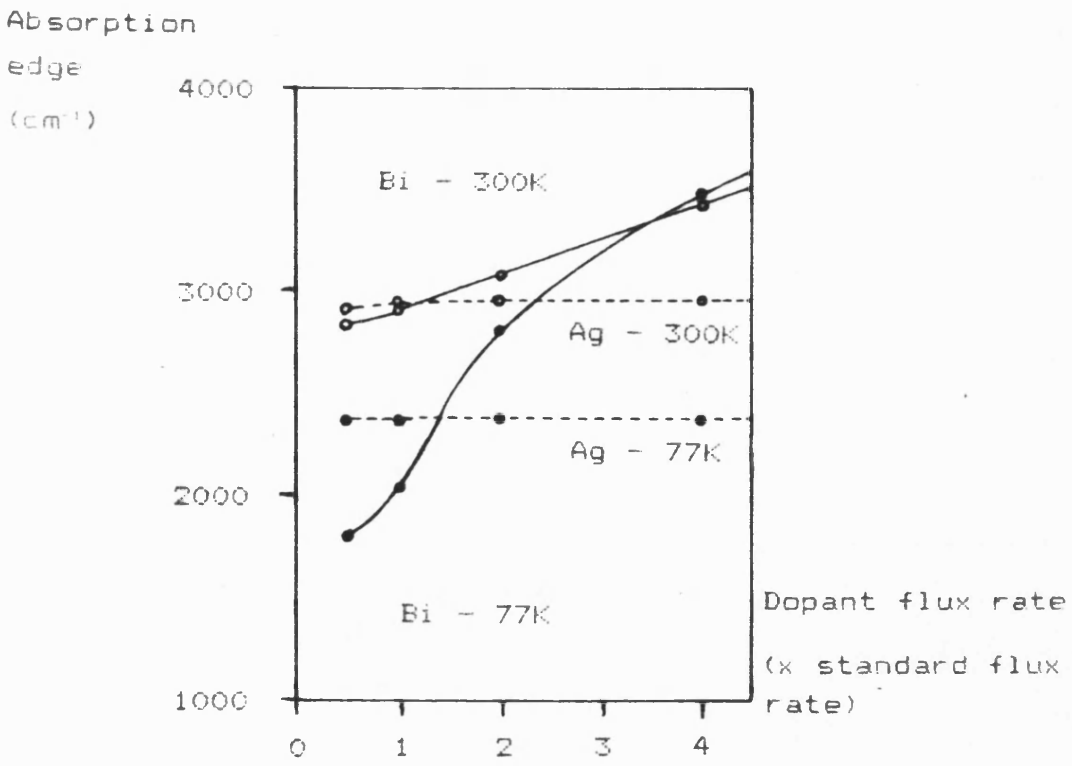


Fig(94). The effect of dopant flux rates upon the absorption edge of $Pb_{0.985}Eu_{0.015}Se$ layers.

measurements taken from IR spectra for increasing doping levels in which the Ag - doping curve confirms the relationship seen in the last two diagrams. The Moss - Burstein shift can also be seen for the Bi doping case and leads to the assumption that the E - $\underline{k}$ band diagram for the CB is very steep and very sensitive to the amount of Bi doping. The Ag dopant flux case, on the other hand, shows only an initial shift and further increases in the Ag flux rate produces no effect. This can be explained by a very flat E - $\underline{k}$ diagram for the VB or by the fact that the Ag is not being incorporated as stated above.

# 5) LASER STRUCTURES

## 5.1) Introduction

This chapter describes how the basic knowledge of growing single lead chalcogenide layers is used to fabricate infra red diode laser structures. Section 5.2 discusses the problems involved in contacting the lead chalcogenides whilst section 5.3 indicates the possibilities for insulation materials to structure these contacts. Section 5.4 gives an account of the structuring, mounting and testing of the diode lasers which are described in section 5.5.

## 5.2) Contacting

In the simplest of cases the semiconductor surface is free from intrinsic and extrinsic surface states. The position of the Fermi level is in this case fixed only by the electronic work function of the contacting metal. Metals with high work functions (Au, Pt etc.) form ohmic contacts with a p - type ideal surface and produce on the other hand a barrier on ideal n - type surfaces. Metals with small electronic work functions (In, Al etc.) are ideal for the reverse of the above conditions. These conditions are not, however, present in

the lead chalcogenides leading to the assumption that lead chalcogenide surfaces contain surface states {119}. The exact nature of these surface states is not known. The surface of a lead chalcogenide must, however, be of a varying metal / chalcogen ratio which is dependent upon the surface preparation techniques.

In bulk material, a lead vacancy acts as an acceptor centre. Such a vacancy at the surface will also be of acceptor nature and the density of these vacancies can be affected through the surface preparation technique. Chemical etching techniques, for example, attack the lead sub - lattice and produce lead vacancies leading to an acceptor - like surface. This condition is ideal for the fabrication of a p - type contact. In direct contrast, lead - rich surfaces contain chalcogen vacancies which have donor properties. Argon ion etching, for example, which attacks the chalcogen sub - lattice, produces a donor - like surface that is ideal for the manufacture of an n - type contact. In both cases, surface preparation techniques suitable for ohmic contacts can be enhanced by the deposition of a thin contacting material {119}.

The laser bonding material to the laser housing is in all cases indium. As In - diffusion barriers the metals Cr, Ni and Fe have been used. Through the course

of the investigations, tables of results for different contact material permutations have been drawn up and are given in Table (8) (p - type) and Table (9) (n - type).

Due to the lack of laser slice material, not all of the contacts listed in the tables have been tested for laser structures. The majority of lasers described in sections 5.5.1 - 5.5.7 have Pb/Ni/In and Au/Ni/In contacts unless otherwise stated.

## 5.3) Insulation for realising stripe geometries

The work here briefly describes three techniques used for the stripe contact geometry preparation:

a) Earth alkaline fluorides;

b) photoresist;

c) natural oxide.

Fig(95) shows the steps involved in a lift - off process developed using a combination of $CaF_2$, $MgF_2$ and $BaF_2$. The first three steps involve the evaporation and structuring of the water - soluble fluoride $BaCaF_2$. The final two steps utilise the lift - off technique by first evaporating the water resistant $MgF_2$ and then removing the $BaCaF_2$, photoresist and $MgF_2$ by washing. This leaves the required open stripe for the contacts.

The second type of insulating material is the photoresist. The majority of lasers produced have had

| Contact | Substrate material | Lifetime Months | Resistivity $x10^{-6}$ $\Omega$ $cm^{-2}$ | Comments |
|---|---|---|---|---|
| Au/Ni | PbSe | 6 | > 50 | Ni flakes off |
| Se/Au/Cr | PbSe | > 6 | 50 | Heat treatment required, Au flakes off |
| Se/Ag/Cr | PbSe | > 9 | 40 | Heat treatment required |
| Se/Fe | PbSe | 6 | 100 | Heat treatment required, corrosion |
| Au/Fe | PbSe + PbS | 6 | > 100 | Heat treatment required, corrosion |
| $As_2S_3$/Au | PbS | > 6 | 50 | Heat treatment required |
| $As_2S_3$/Fe | PbS | 6 | > 50 | Heat treatment required, corrosion |

Table (8). Data of p - type contacts studied.
The lifetime is estimated, the surface resistivities are typical and the comments point to notable characteristics.

| Contact | Lifetime Months | Resistivity $x10^{-5}\ \Omega\ cm^{-2}$ | Comments |
|---|---|---|---|
| In | 3 - 4 | < 10 | Mechanically stable, degrades |
| Pb/Ni | > 18 | 10 | Ni flakes off |
| In/Au | 3 - 6 | < 10 | Mechanically stable, can degrade |
| In/Cr | 3 - 6 | 20 | Difficult to structure |
| In/Fe | 6 | 50 | Possible corrosion |
| Al/Cr | > 9 | 20 | Difficult to structure |

Table (9). Data of n - type contacts studied. The lifetime is estimated, the surface resistivities are typical and the comments point to notable characteristics.

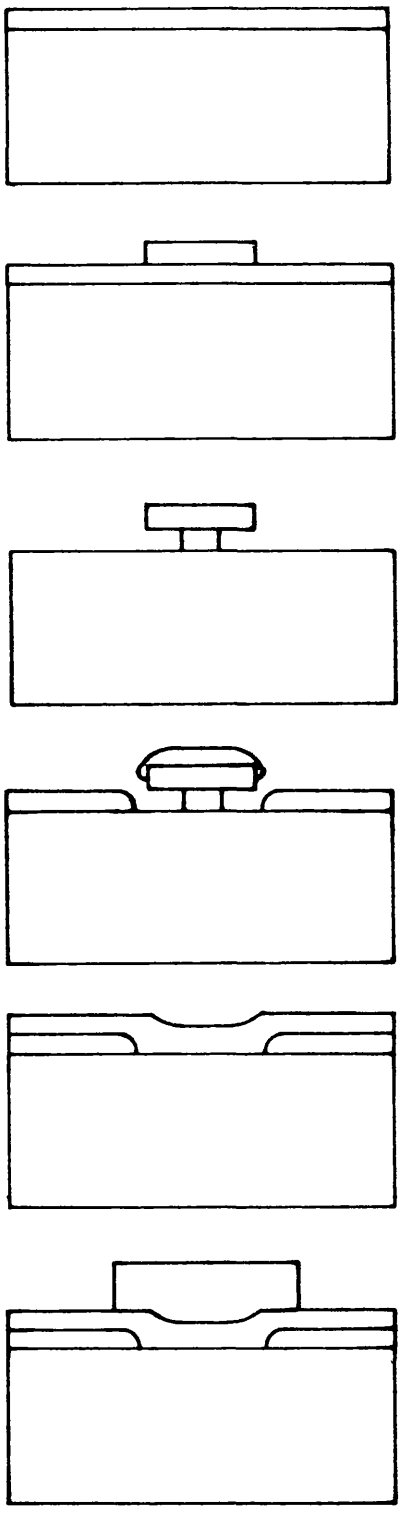


Fig(95). Fluoride lift - off process for forming n - contact stripe geometries.

n - contacts defined by this technique which is the simplest of the three described in this work. Fig(96) shows the process steps in detail.

The most technically - perfect of the three techniques is the method of forming the lead chalcogenide natural oxide for the insulation. Fig(97) shows the important steps involved in producing a laser chip using this concept.

## 5.4) Laser structuring and mounting

The samples are transferred after the MBE growth process to the loading chamber where they can be later retrieved through the loading port. $BaF_2$ control samples can be removed from the molybdenum MBE block by sliding the sample to the edge and removing the Ga - In alloy mechanically with propanol and chemically with hydrofluoric acid.

The PbSe laser slices are retrieved in the same manner as the $BaF_2$ except that the Ga - In alloy can only be removed by subsequent polishing due to the interdiffusion of the alloy into the PbSe substrate.

The slice is glued onto a glass polishing block substrate side (p side) up and is polished to the laser end thickness of 200µm using a combination of $Al_2O_3$ powders in a suspension of water and soap. A final

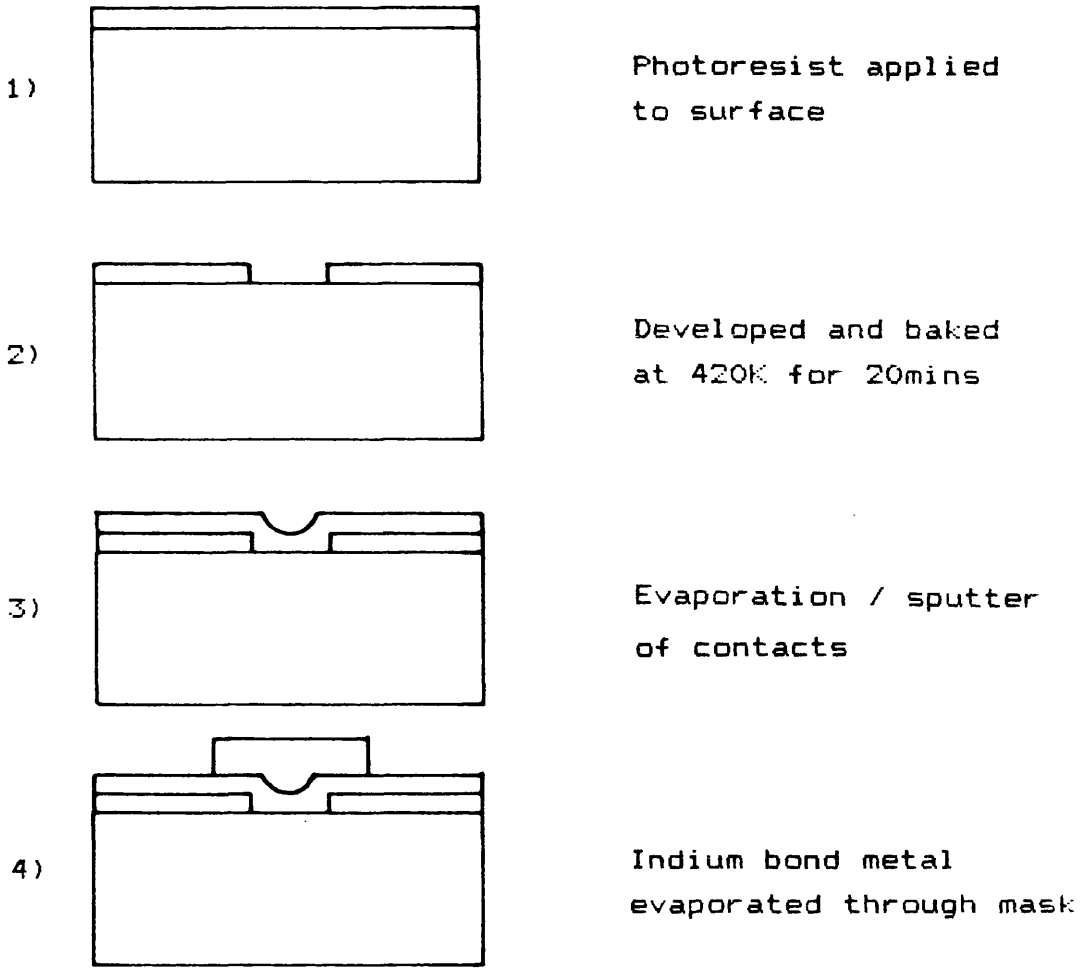


Fig(96). The use of photoresist for stripe contact definition and insulation.

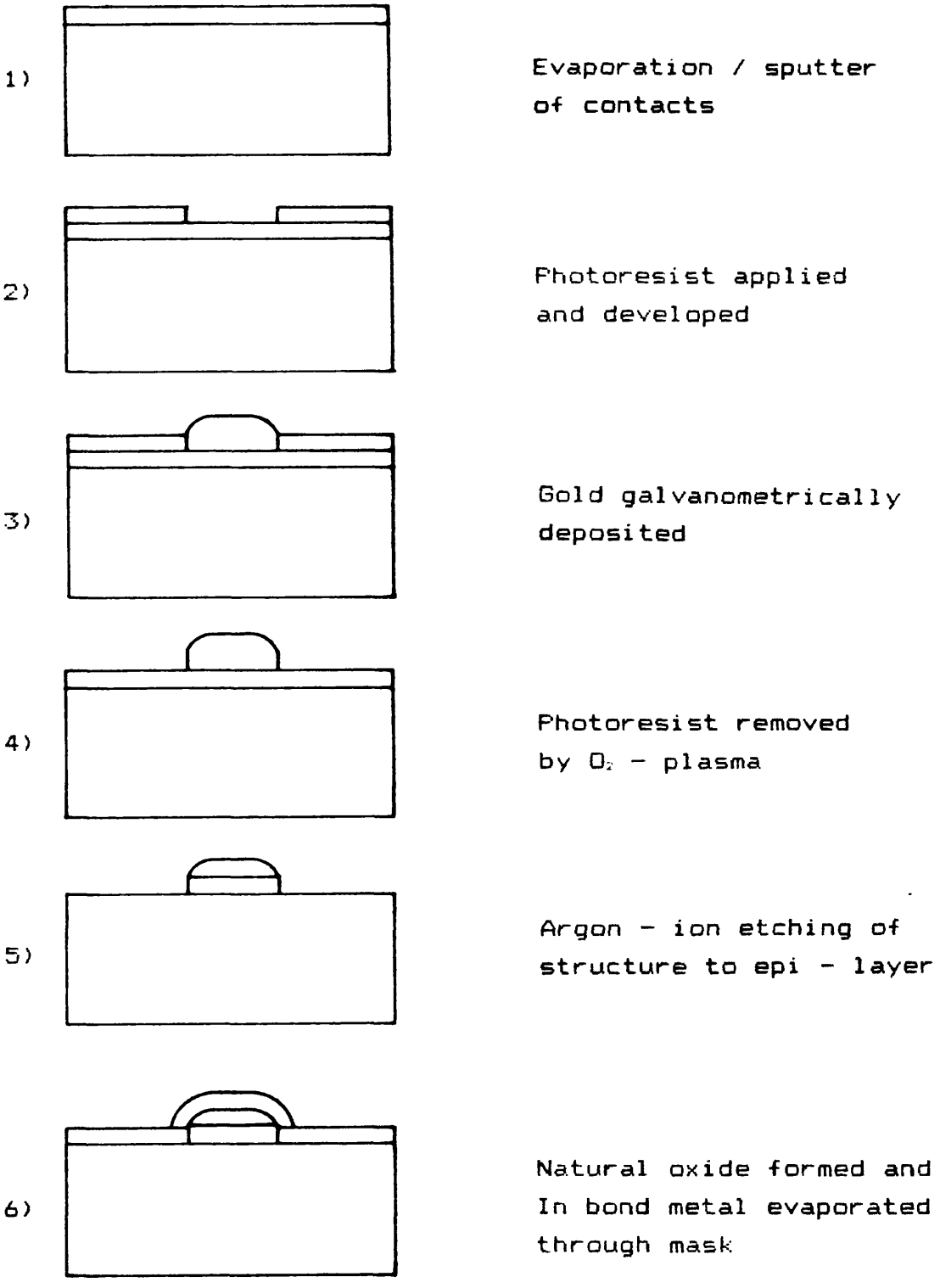


Fig(97). The use of the natural oxide for the laser chip passivation.

surface treatment with KOH polishing (final 30µm) ensures a reproducible surface for the immediate p - side contacting process.

The technique of fluoride insulation is used for the primary laser structures described later in sections 5.5.1 to 5.5.3. The major disadvantages of this construction lie with the hygroscopic nature of the fluoride insulating layer and the poor barrier qualities of the nickel diffusion barrier layer used in conjunction with the process.

The technique used for structures described in sections 5.5.4, 5.5.5 and 5.5.7 is the photoresist insulator. Lasers made using this technique exhibit poor mechanical stability of the n - contacts on and between the photoresist insulation. The process is, however, relatively easy to perform and has proved invaluable for quick laser slice testing.

The lasers presented in section 5.5.6 have been contacted using the natural oxide method and demonstrate the neatness and advantages of the technique. The diffusion barrier in this case was chromium and the most critical step is the etching of the stripe contacts using argon ions due to the small etching rate of chromium. The etching time must not be so long that the gold contact is etched away. Here a shorter time can be chosen since if

the chromium layer has not been etched, then the oxidation process will not function. The slice can then be returned to the ion milling machine for further etching and the process repeated until the start of the oxidation process indicates that the milling process is through the chromium layer and is hence complete.

In all three above cases, the bonding metal In is evaporated onto both sides of the completed slice. Approximately 10µm of In is deposited, the whole surface of the p - type substrate side and in 100µm - wide stripes over the structured windows on the n - side. The stripe form on the epitaxy side gives the advantages of better slice orientation and cleaving characteristics when mounting.

The first stage of the laser mounting is to cleave the laser slices into laser chips thus forming the necessary parallel resonator surfaces. The chips are at the end of the cleavage step approximately 300 x 300µm (cleavage dimensions) in the top perspective and 200µm thick (polished thickness). The chip is then mounted into the housing shown in Fig(98). The laser is positioned upon the In - coated silver block, p - side up, and is slowly raised to make a press contact with the In - coated silver band for the upper contact.

Laser testing is performed in two stages. Firstly

Fig(98). Laser diode housing.

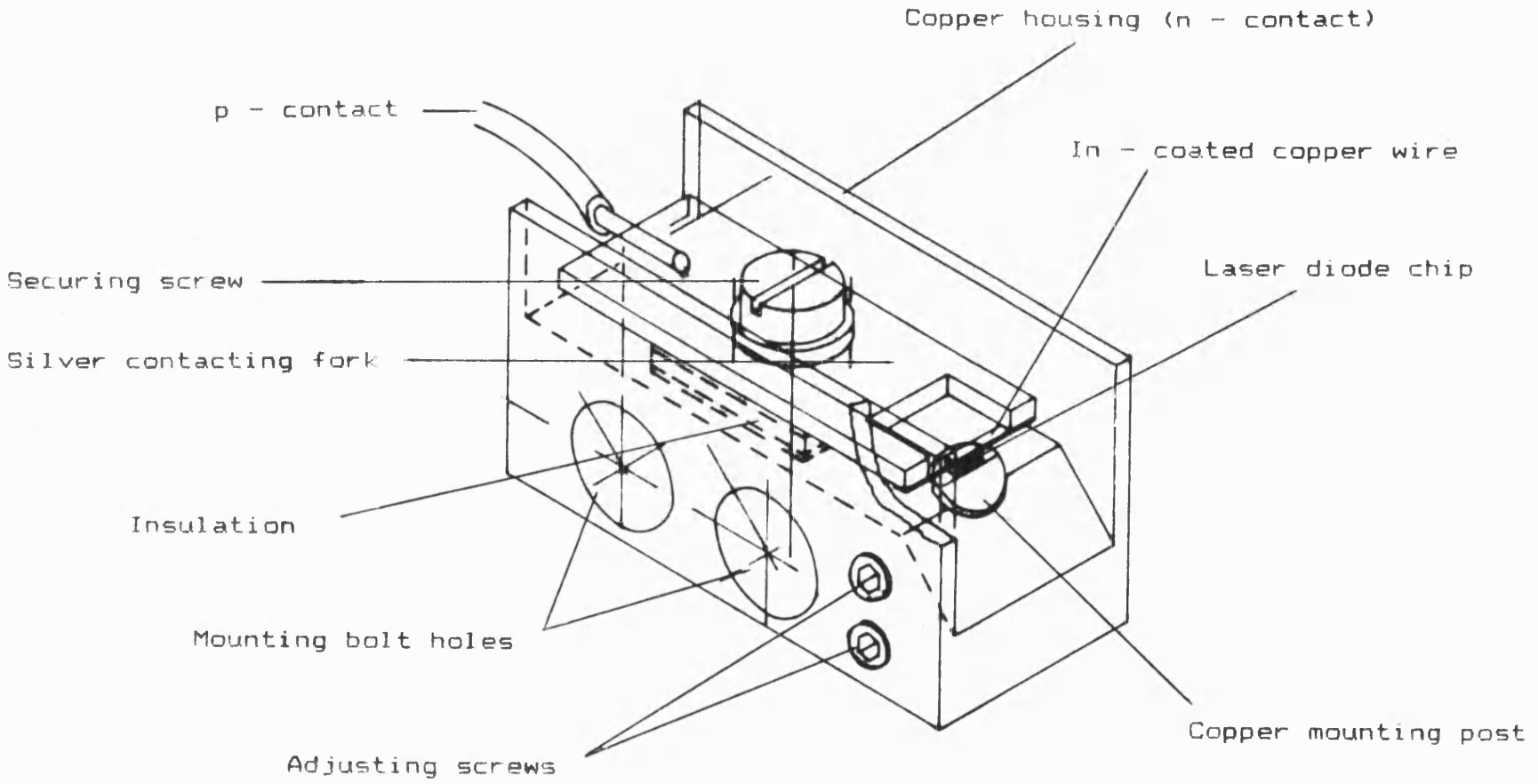

the laser is tested in a temperature - controlled environment with temperatures at and above liquid nitrogen. Here the chip is tested for laser emission, threshold current, power and I - V characteristics. Hence time can be saved when the chip at this stage does not lase or is of too poor a quality to warrant the second stage test.

The second stage testing includes a more accurate assessment of the above characteristics from above 20K with the addition of far field patterns and exact fine tuning rates. The fine tuning of a laser is measured with a germanium etalon ($\Delta\nu$ = 1/20 $cm^{-1}$). A calibration gas can be positioned in the beam inside a quartz tube with $BaF_2$ windows. Using the calibration gas, it is possible to search for lasers from a batch which have the exact emission wavelength with a sufficient fine tuning range needed for the spectroscopy of the gas in question.

## 5.5) Laser structures

This section describes the various laser structures fabricated using the MBE apparatus.

### 5.5.1) Cd - diffused $PbSe/Pb_{1-x}Sn_xSe/PbSe$ lasers

DH - laser structures of the PbSe / $Pb_{1-x}Sn_xSe$ / PbSe configuration were grown on p - type PbSe substrates

with carrier concentrations of approximately $3x10^{18}$ $cm^{-3}$. Due to the fact that at this point in time the Bi doping of the lead chalcogenides was still being investigated, the first set of lasers were grown without a p - n junction. The p - n junction was later formed by the diffusion of the n - dopant cadmium which has a diffusion depth control accuracy of ± 1µm.

Two basic types of laser structure were fabricated. These differed in the fact that one has an active layer of 3µm thickness and the other being 1µm thick. To ensure that the p - n junction is positioned correctly after the Cd diffusion process, both types of laser were repeated three times with differing top confinement layer thicknesses 3, 3.5 and 4µm. As a further variable, the laser slices were cleaved into two pieces after the epitaxy thus allowing two diffusion experiments to be performed. The first at 670K for 15 minutes and the second at 670K for 20 minutes. Schematic diagrams of two functioning Cd - diffused DH lasers are given in Fig(99) and Fig(100). The slice numbering shows the run number, followed by the slice number.

Fig(101) shows the first stage testing system curve for pulsed operation of laser 358,1 which has a 1µm thick active layer. It can be seen that the contact resistance is small and that the laser shows a typical

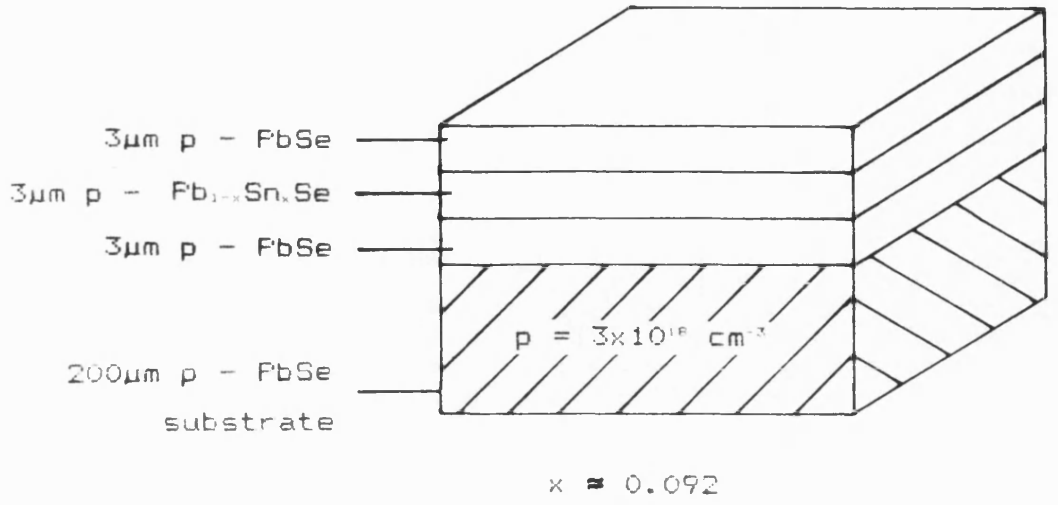


Fig(99). Schematic of laser 352,1 epitaxial layers. Structure is Cd - diffused at 670K for 20 mins after epitaxy to form p - n junction.

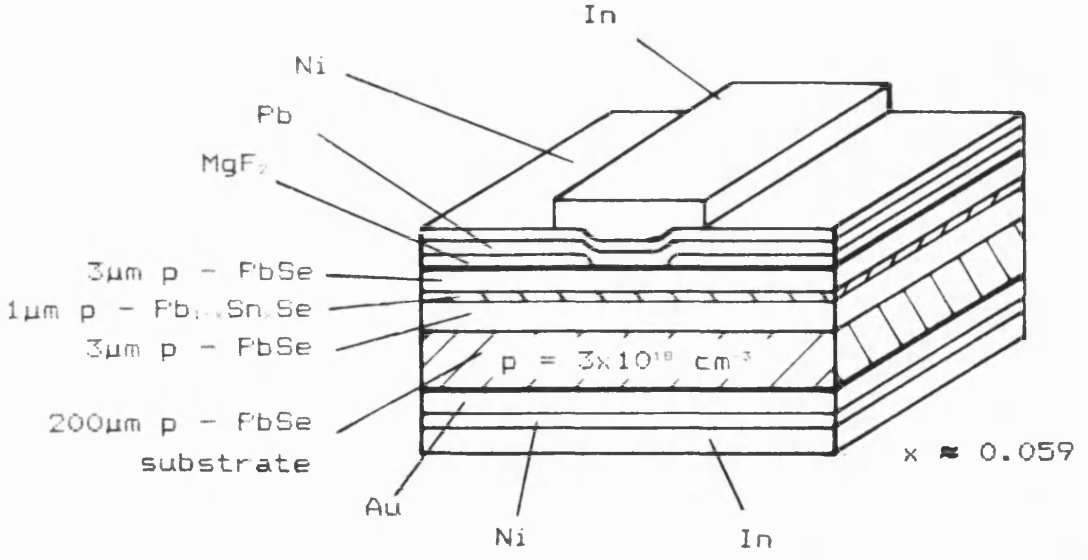


Fig(100). Schematic of laser 358,1 showing the use of the fluoride lift - off technique. Slice is Cd - diffused at 670K for 20 mins after epitaxy to form p - n junction.

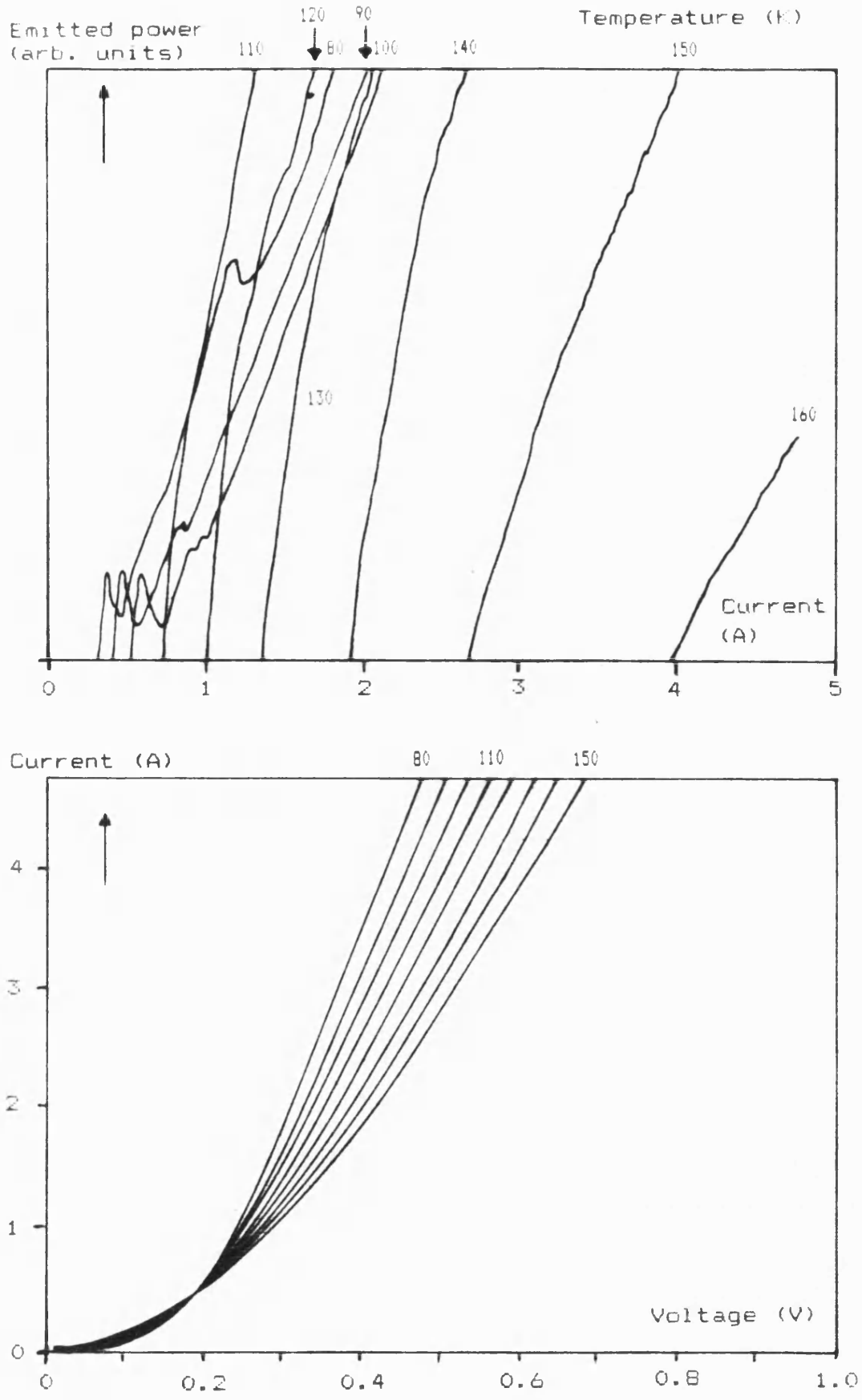


Fig(101). First stage laser test results of slice 358,1.

diode I - V characteristic. The threshold current at an operation temperature of 80K is 1A and the highest operation temperature is 160K. Table (10) gives the second stage test results for both laser 358,1 and the laser 352,1 which has the 3µm thick active layer. The wavelengths obtained at 80K indicate x composition factors of 0.059 and 0.092 respectively, the corresponding beam flux ratios SnSe : PbSe being 0.07 and 0.06. This indicates the problems concerned with the non - uniformity of the MBE process to achieve a required wavelength. Other lasers measured from the same slices show similar characteristics but with differing wavelengths according to the inhomogeneity experiments described in the previous chapter.

The characteristics of these DH lasers are comparable to those of the best diffusion technique lasers. This suggests that the quality of the grown films is as good as the single crystals grown by the sublimation technique with which the diffused lasers are fabricated.

### 5.5.2) Bi - doped PbSe/$Pb_{1-x}Sn_xSe$/PbSe lasers

The encouraging results of the Cd - diffused DH lasers show that the MBE method of fabrication is a viable technique. The next stage is to test the effect of

| Temperature (K) | $i_t$ (A) | Wavelength (μm) | Wavenumber ($cm^{-1}$) |
|---|---|---|---|
| 20 | 2.790 | -- | - |
| 30 | 2.035 | -- | - |
| 40 | 1.125 | -- | - |
| 50 | 0.960 | 20.592 | 486 |
| 60 | 0.925 | 19.152 | 522 |
| 70 | 0.960 | 17.856 | 560 |
| 80 | 1.075 | 16.302 | 613 |
| 90 | 1.280 | 15.310 | 653 |
| 100 | 1.750 | 14.222 | 703 |
| 110 | 2.450 | 13.264 | 754 |
| 120 | 4.340 | 12.192 | 820 |

Table (10a). Second stage test results for laser no. 352,1.
Note that the ZnS detector window absorbs for wavelengths > 20μm.

| Temperature (K) | $i_t$ (A) | Wavelength (μm) | Wavenumber ($cm^{-1}$) |
|---|---|---|---|
| 20 | 0.670 | 15.393 | 650 |
| 30 | 0.665 | 14.940 | 669 |
| 40 | 0.669 | 14.570 | 686 |
| 50 | 0.670 | 13.264 | 734 |
| 60 | 0.820 | 12.912 | 774 |
| 70 | 0.975 | 11.674 | 857 |
| 80 | 1.080 | 11.319 | 883 |
| 90 | 1.325 | 11.080 | 903 |

Table (10b). Second stage results of laser no. 358,1.

using Bi - doped layers to form the p - n junction. The experience gained through the diffused laser research suggests that Cd - doping would be at this stage more logical. Cadmium, however, when incorporated into the lead chalcogenides, diffuses rapidly thus hindering the manufacture of sharp heterojunction interfaces.

The first lasers using Bi incorporation were PbSe / $Pb_{0.97}Sn_{0.03}Se$ / PbSe DH devices with an emission wavelength in the 10μm region at 77K. A schematic diagram of such a structure can be seen in Fig(102). The first confinement layer, active layer and the first 2000Å of the top confinement layer is p - type material, achieved with the simultaneous sublimation of Se as described in section 4.3.4. The large metal vacancy site diffusion rate will supply to a certain extent holes from the p - type substrate to the growing film but to be sure of p - type growth, Se has been used throughout the structures. After 2000Å of the top confinement has been grown, the $Bi_2Se_3$ furnace is opened thus forming the p - n junction remote from the metallurgical interface between the active layer and the top confinement layer. This has been done since the heterostructure is not lattice matched and the interfaces may then lead to strong recombination. The possibility of producing fault complexes at these interfaces by Bi atoms is also reduced

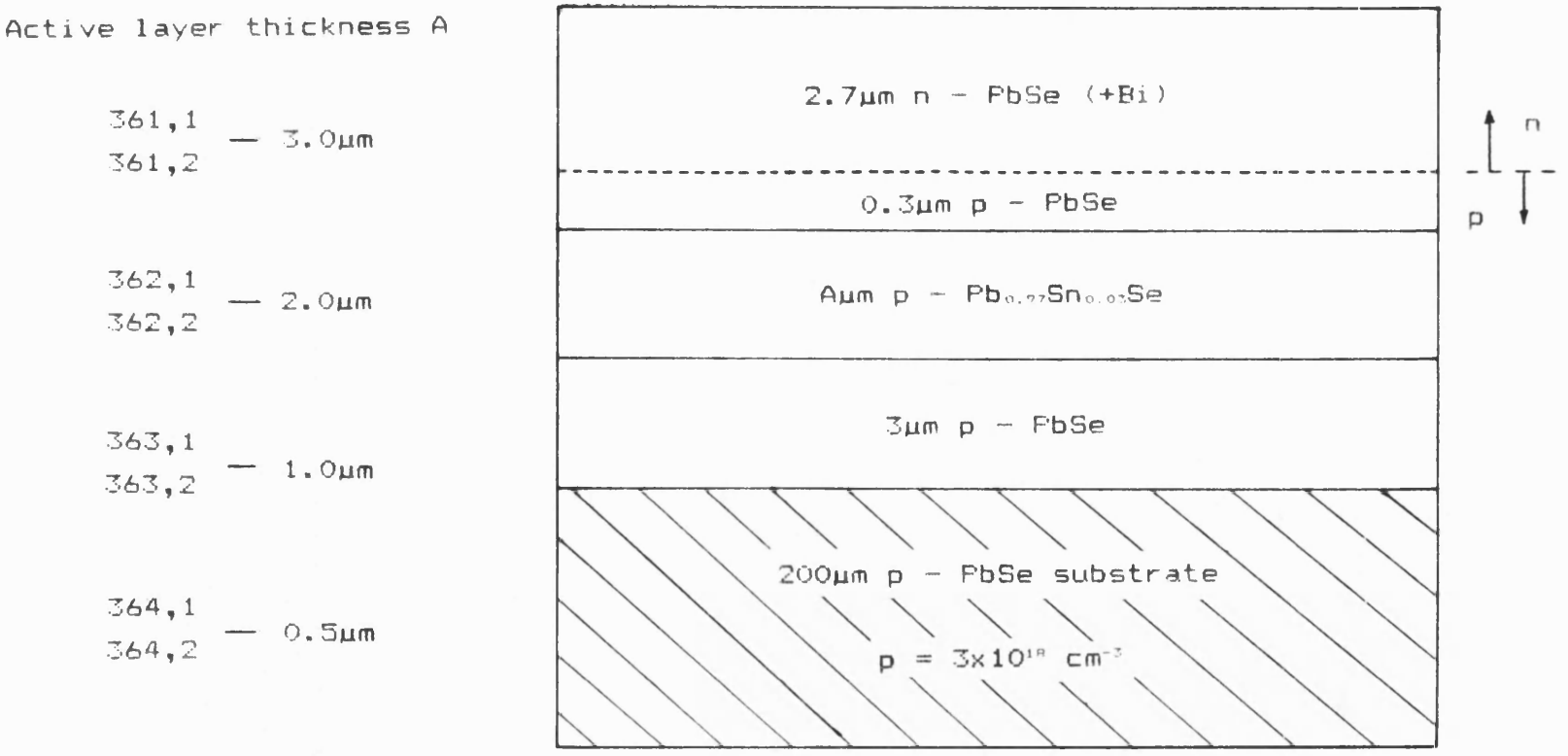


Fig(102). Layer details of first Bi - doped DH laser series grown in the MBE system.

by the design of the remote p - n junction.

A series of DH lasers were grown with active layer thicknesses (A) of 3, 2, 1 and 0.5μm. The maximum operation temperatures are obtained from laser 364,2 with an active layer thickness of 0.5μm. Maximum operation temperatures of 190K ($i_t$ = 5A) and 130K ($i_t$ = 0.5A) have been obtained for pulsed and continuous operation respectively and this is shown in the curve in Fig(103). The temperature tuning range was found from the second stage test to be 9.1μm (200K) to 11.9μm (25K) for pulsed operation and Fig(104) presents a current tuning mode spectrum for currents from 300 - 600mA at 55K in continuous operation. Fig(105) indicates the maximum operation temperature dependence upon active layer thickness found for these DH lasers. The diagram shows that the thinner active layer thicknesses produce higher maximum operation temperatures. This trend will, however, only remain until the confinement factor becomes such that optical confinement decreases for thinner active layer thicknesses.

The temperature dependence of the threshold current with respect to active layer thickness for two layers is shown in Fig(106). The respective $T_o$ values from equation 37 are also given. At high temperatures, the threshold current decreases with decreasing active

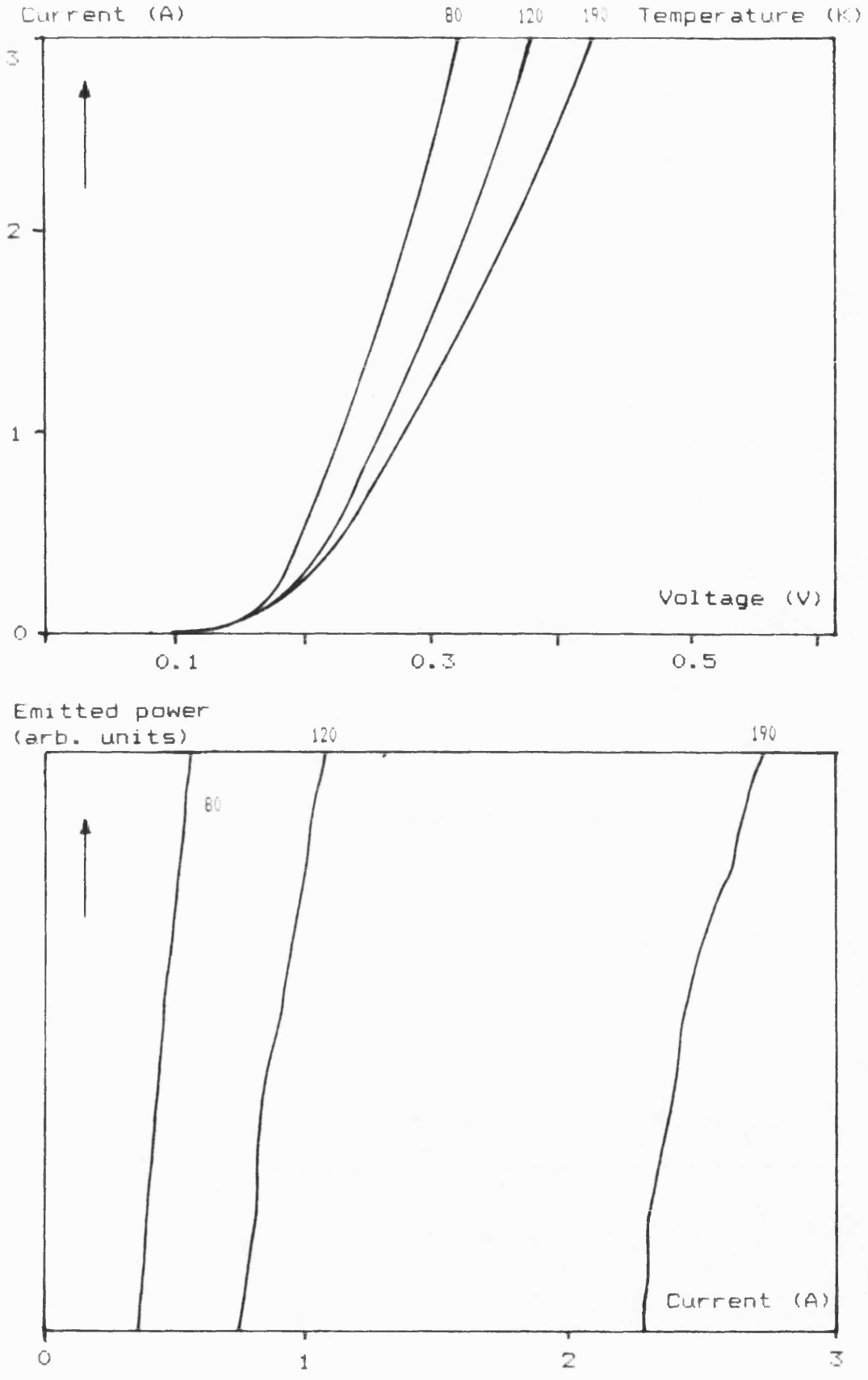


Fig(103). First stage test results of laser 364,2.

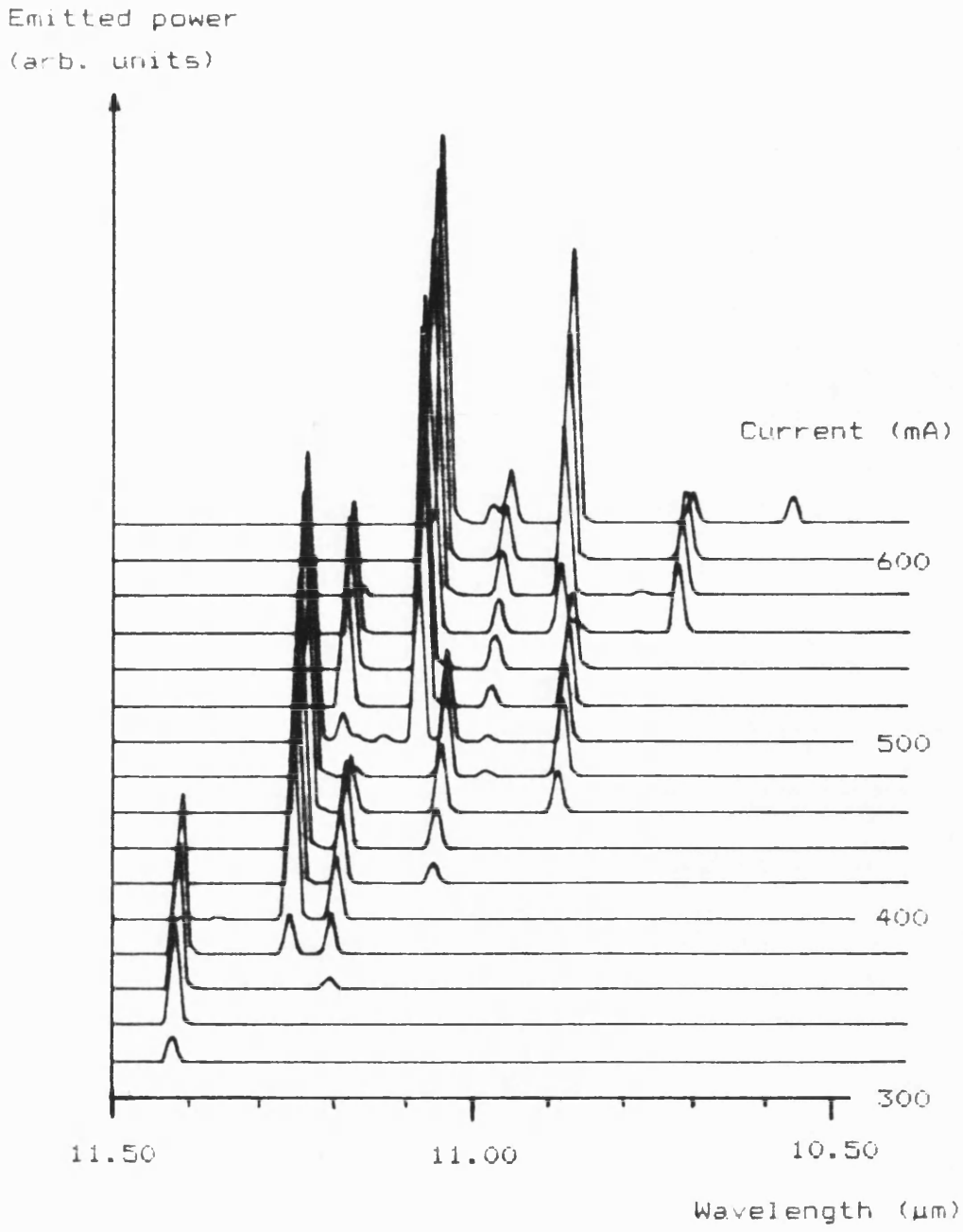


Fig(104). The tuning spectrum of laser 364,2 at 55K for different currents in continuous operation.

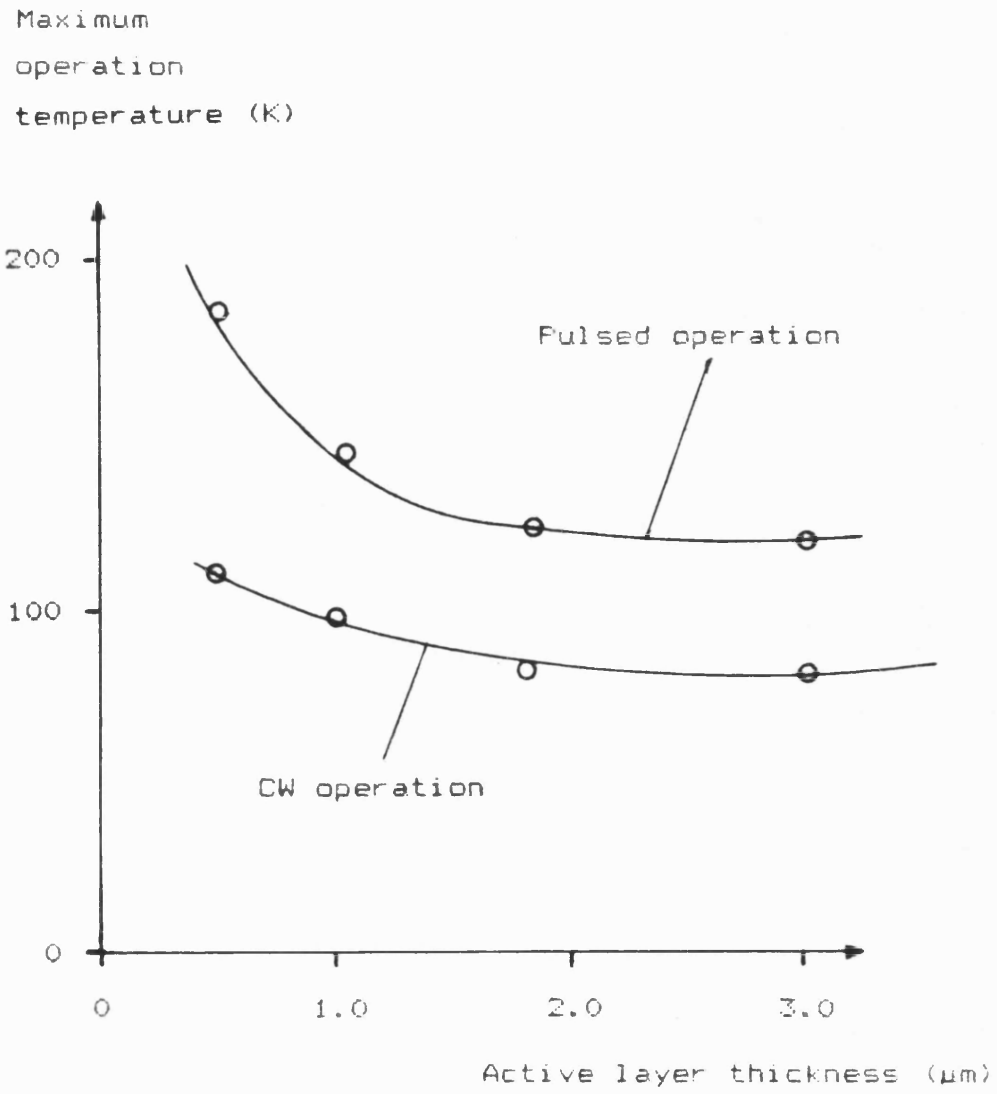


Fig(105). The dependence of the maximum operation temperature upon active layer thicknesses in PbSe / $Pb_{1-x}Sn_xSe$ DH lasers.

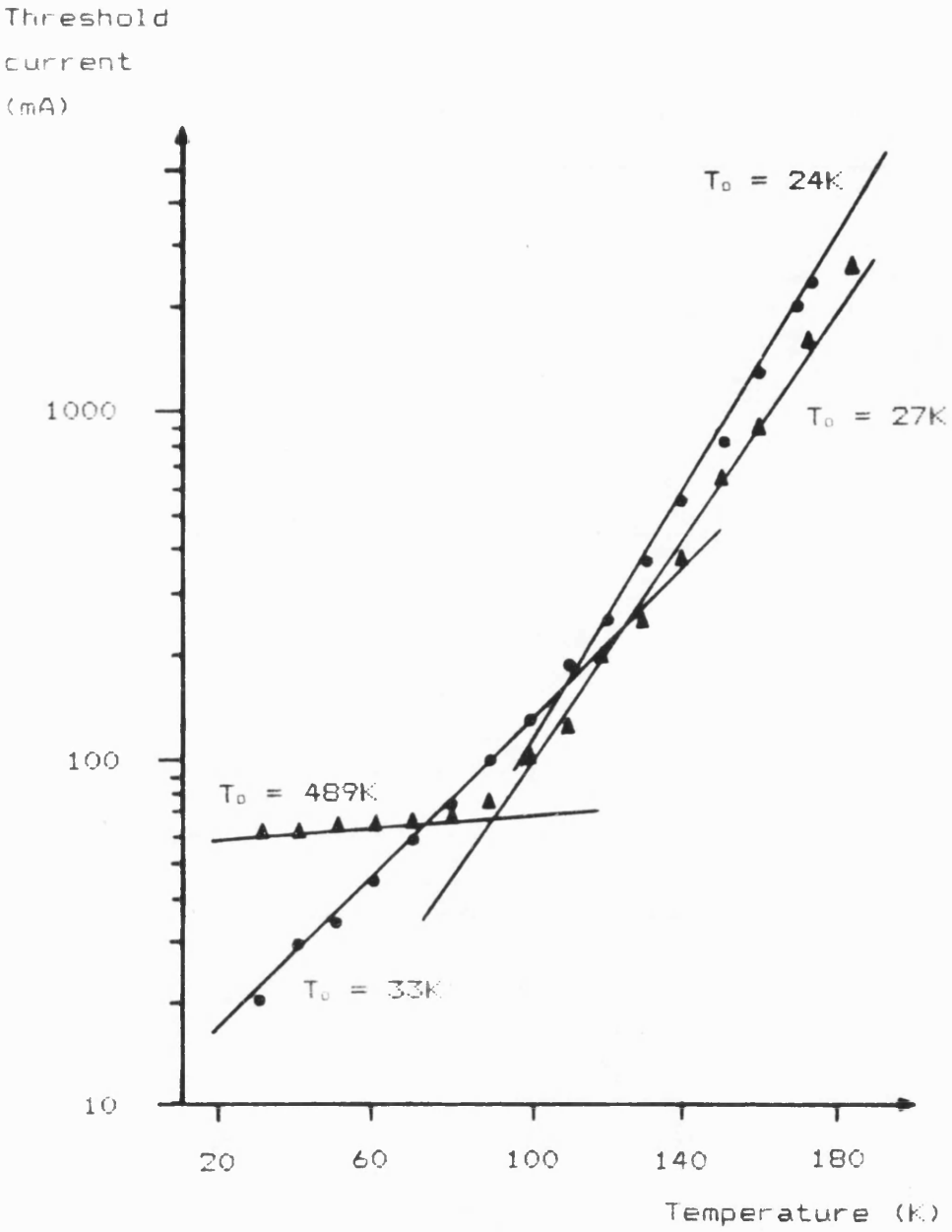


Fig(106). Threshold current dependence upon temperature for two different active layer thicknesses of a DH laser.

layer thickness through the decreasing effect of the electrical confinement. At low temperatures (20 - 70K) the threshold current of the device with the thinner active layer remains constant at a value higher than that obtained for the device with a thicker active region. The temperature independence in the former case can be explained by an increase in carrier recombination in the outer confinement layers which becomes more significant with thinner active layers. The carrier pair lead to an increase in the device current and the mechanism is further enhanced by the increasing emission wavelength as lower temperatures are approached. This effect is not significant for thick active layer devices where the main factor governing the dependence is still the decreasing effect of the electrical confinement.

### 5.5.3) $PbS/PbS_{1-x}Se_x/PbS$ DH lasers

Emission wavelengths shorter than that of the $Pb_{1-x}Sn_xSe$ lasers were attempted. PbS / $PbS_{1-x}Se_x$ / PbS DH lasers were fabricated with similar dimensions to those described in the previous section using Bi for the formation of the p - n junction. The final layer was a 0.5μm thick PbSe contact layer. This has been added to the structure to circumvent the contacting difficulties normally encountered with PbS. The Se content of the

active layer was set to give an approximate emission wavelength of 5.5μm. Using formula 59 this corresponds to an x - value of approximately 0.6 at 80K and the laser is schematically shown in Fig(107).

For an active region thickness of 0.5μm, the highest operation temperatures obtained were 210K in pulsed operation ($i_t$ = 5A) and 110K in continuous operation ($i_t$ = 0.35A). The tuning range of this laser was 5.5μm (110K) to 8.9μm (25K) in continuous operation. At 80K the wavelength measured was 5.7μm which corresponds to an exact x - value of 0.66 which agrees (within the expected error from inhomogeneity levels) to the set beam flux ratios.

### 5.5.4) $PbS_{1-x}Se_x/(PbS)_{1-x}(SnSe)_x/PbS_{1-x}Se_x$ lasers

The flexibility of the MBE technique as applied to lead chalcogenide diode lasers is well demonstrated by the third type of DH laser reported in this work. Wavelengths shorter than 8μm have been covered to 5μm using the $PbS_{1-x}Se_x$ alloy in the active layer. If, for example, the above $PbS_{1-x}Se_x$ composition is used for confinement layers, then, with the addition of Sn, an active layer of $(PbS)_{1-x}(SnSe)_x$ will improve lattice matching. This is qualatatively shown in Fig(108) for the region between PbS and PbSe. The diagram shows that for

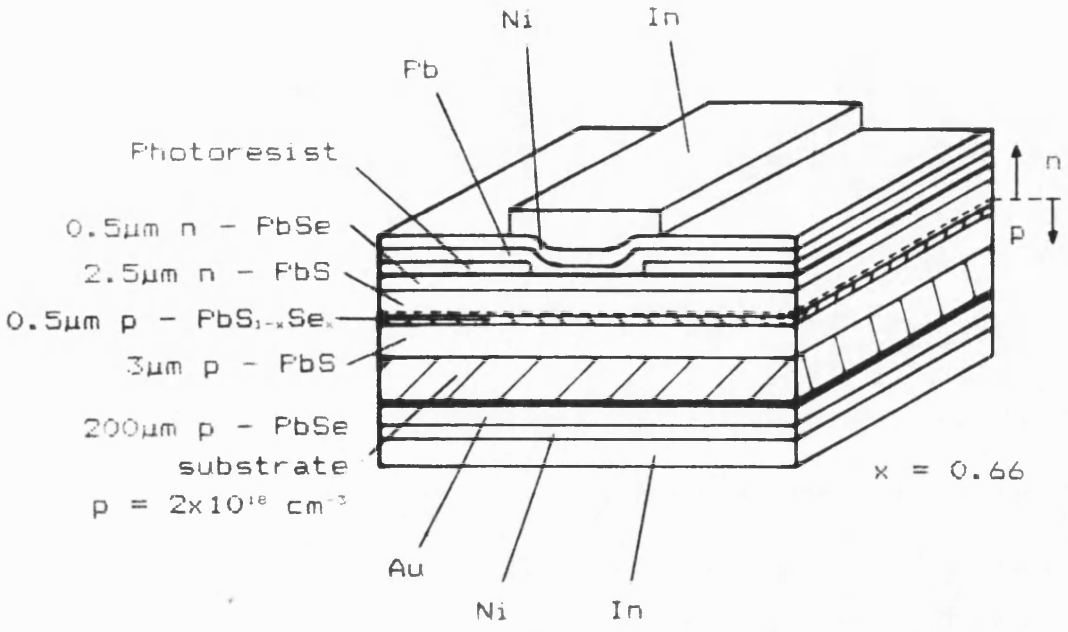


Fig(107). Schematic of the PbS / $PbS_{1-x}Se_x$ / PbS laser structure using the photoresist stripe geometry technique.

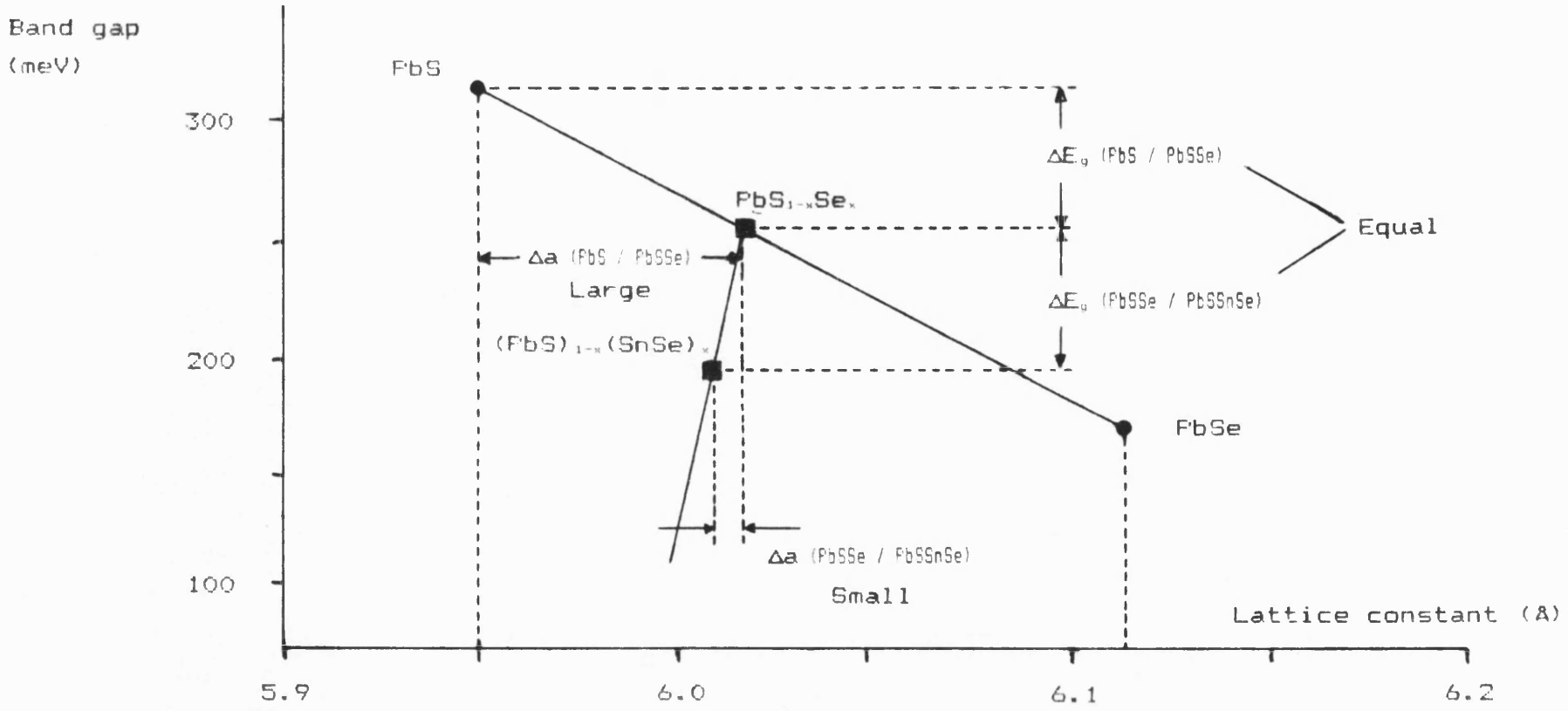


Fig(108). Qualitative explanation of the advantage in using $(PbS)_{1-x}(SnSe)_x$ in the active layer with $PbS_{1-x}Se_x$ confinement layers to reduce lattice mismatch.

an equal energy gap difference between the PbS / $PbS_{1-x}Se_x$ system and the $PbS_{1-x}Se_x$ / $(PbS)_{1-x}(SnSe)_x$ system, a large difference in the lattice matching factors is obtained. The lattice mismatch can, therefore, be considerably reduced by using the latter combination as indicated in the diagram.

The laser described here consists of 3µm thick $PbS_{1-x}Se_x$ confinement layers and an active layer of $(PbS)_{1-x}(SnSe)_x$ where the x - value has not been explicitly determined. However, from the device shown in Fig(109) with a 0.5µm thick active layer it can be deduced from the emission frequency that the band gap of the active film lies approximately 35meV below that of the $PbS_{1-x}Se_x$ confinement layers. These lasers function upto 135K in pulsed operation ($i_t$ = 5A) and upto 75K in continuous operation ($i_t$ = 0.4A). In continuous operation the laser can be tuned from 5.3 to 4.7µm with a temperature increase from 20 to 75K.

The maximum temperatures of the short wavelength lasers fall clearly behind the values obtained for lasers described in sections 5.5.1 and 5.5.2. An explanation for these lower values could be the unintentional low Sn content in the active layer thus producing a poor electrical confinement. This is analogous to the case of the PbSe / $Pb_{1-x}Sn_xSe$ DH laser where wavelengths below

x - not explicitly known

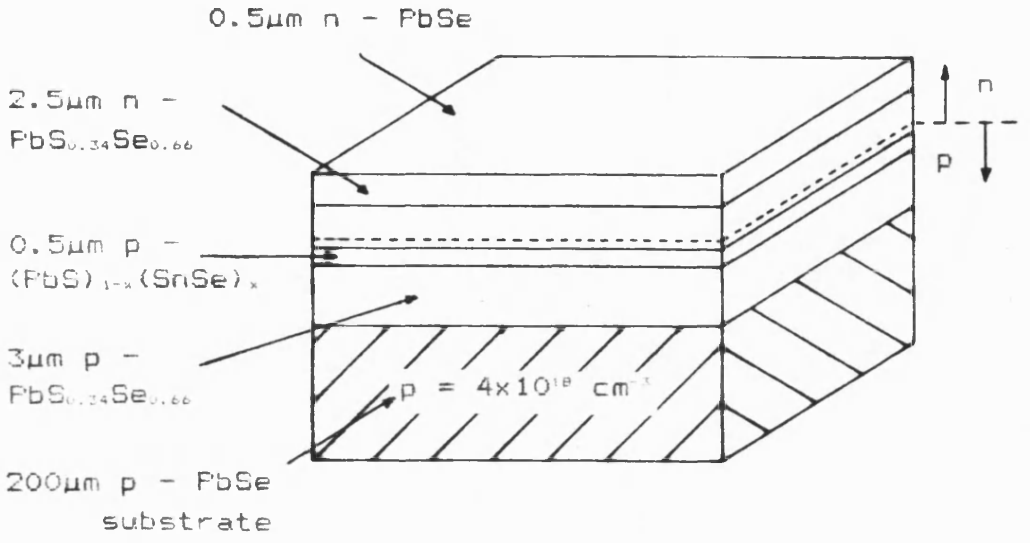


Fig(109). Schematic of the $PbS_{1-x}Se_x$ / $(PbS)_{1-x}(SnSe)_x$ / $PbS_{1-x}Se_x$ laser structure.

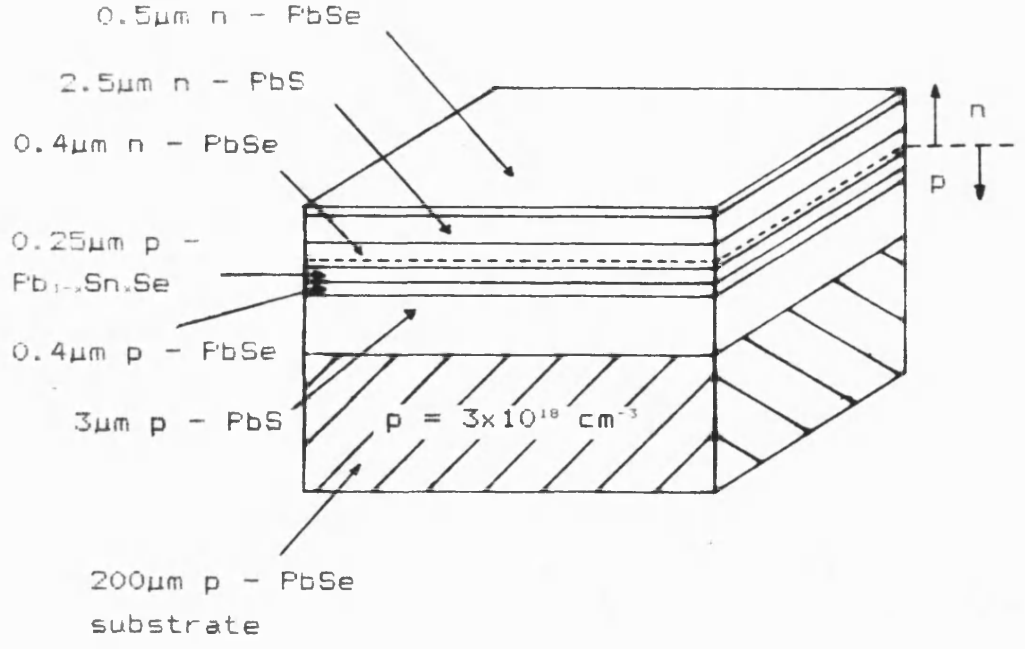


Fig(110). Schematic of the PbS / PbSe / PbSnSe / PbSe / PbS localised gain region laser.

10μm are not possible due to the poor confinement achieved by a small tin content as previously described in section 5.5.2.

5.5.5) Localised gain region diode lasers

To improve the low - temperature guiding for active film thicknesses even thinner than 0.5μm and to eliminate the low temperature threshold current effect, lasers were made with extra optical guiding layers thus forming the localised gain region laser. The lasers have a similar structure to those described in section 5.6.2 except that the active layer thickness is 0.25μm and the PbSe confinement layers are 0.4μm thick (i.e. d = 0.25μm + 2x0.4μm = 1.05μm). This whole structure is sandwiched between two PbS layers as depicted in Fig(110). The interfaces of the PbS / PbSe regions have a large lattice mismatch producing a high density of interface states but, however, offer a large difference in refractive index producing good optical confinement.

These lasers were expected to maintain their optical confinement and guiding even with smaller active region thicknesses. However, as Fig(111) indicates, the low temperature threshold current effect is not suppressed. The threshold current of this device decreases with increasing temperature, passes through a

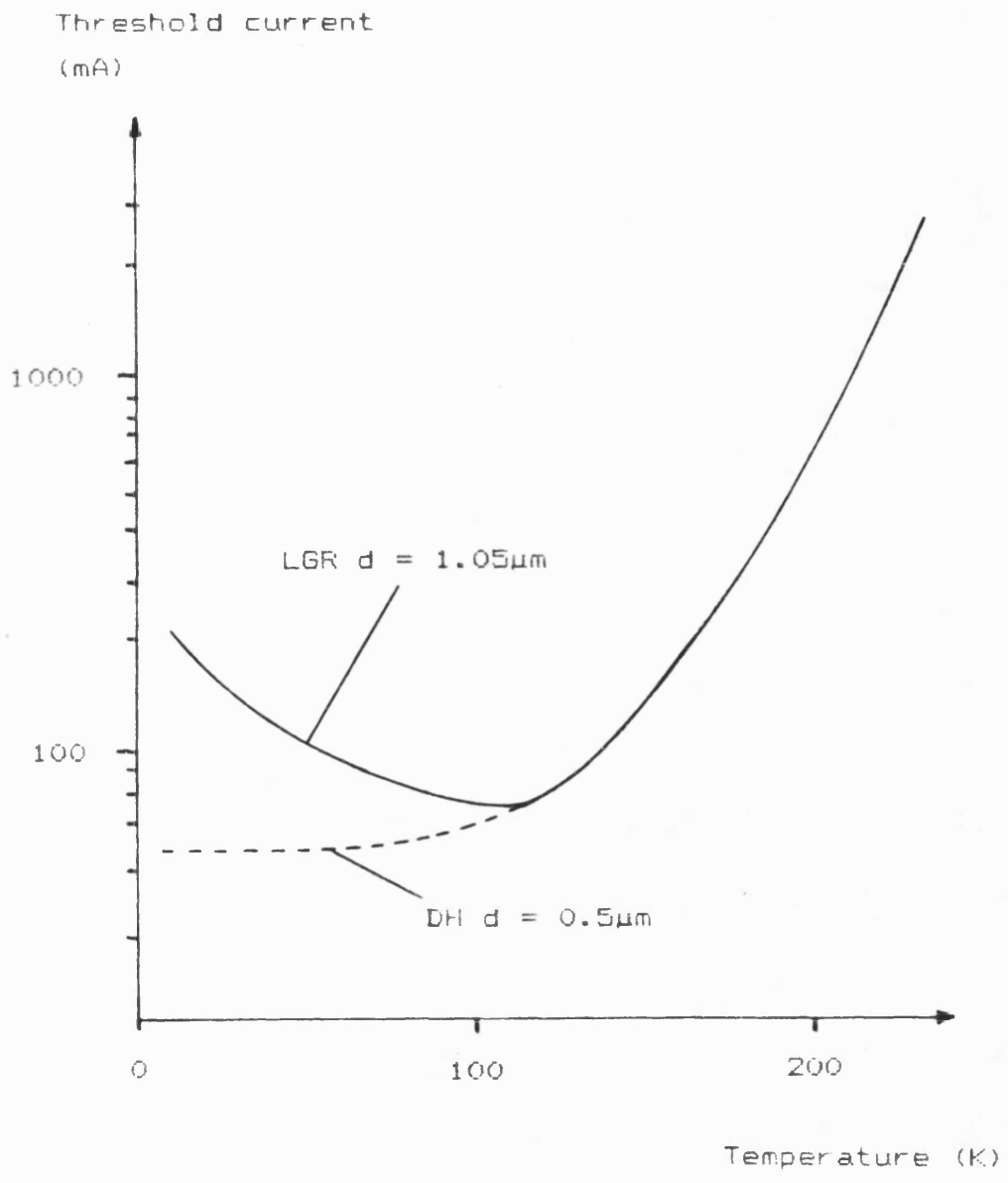


Fig(111). Temperature dependence of the threshold current for the localised gain region laser.

pronounced minimum located at 110 - 130K followed by the increasing high temperature branch.

In addition to this pronounced effect, laser emission occurs at two distinct frequencies corresponding to the composition of the active film and to the pure PbSe wave guide. This behaviour suggests that at low temperatures only a small fraction of the injected carriers become trapped in the potential well formed by the $Pb_{1-x}Sn_xSe$ active film. The majority of the injected carriers are swept across the active region and recombine in the PbSe wave guide behind the active film. This effect is a low temperature effect because at high temperatures the enhanced electron / phonon interaction eases the capture of the injected carriers into the well. This is schematically presented in Fig(112).

This effect could well be controlled by the positioning of the p - n junction. Investigations were, however, not undertaken as the structure is not suitable for short wavelength lead chalcogenide lasers. For shorter wavelengths, the difference in band gaps between the active region and confinement layers diminishes. A new type of structure is, therefore, required aimed at eliminating the low temperature effect and covering the required emission range.

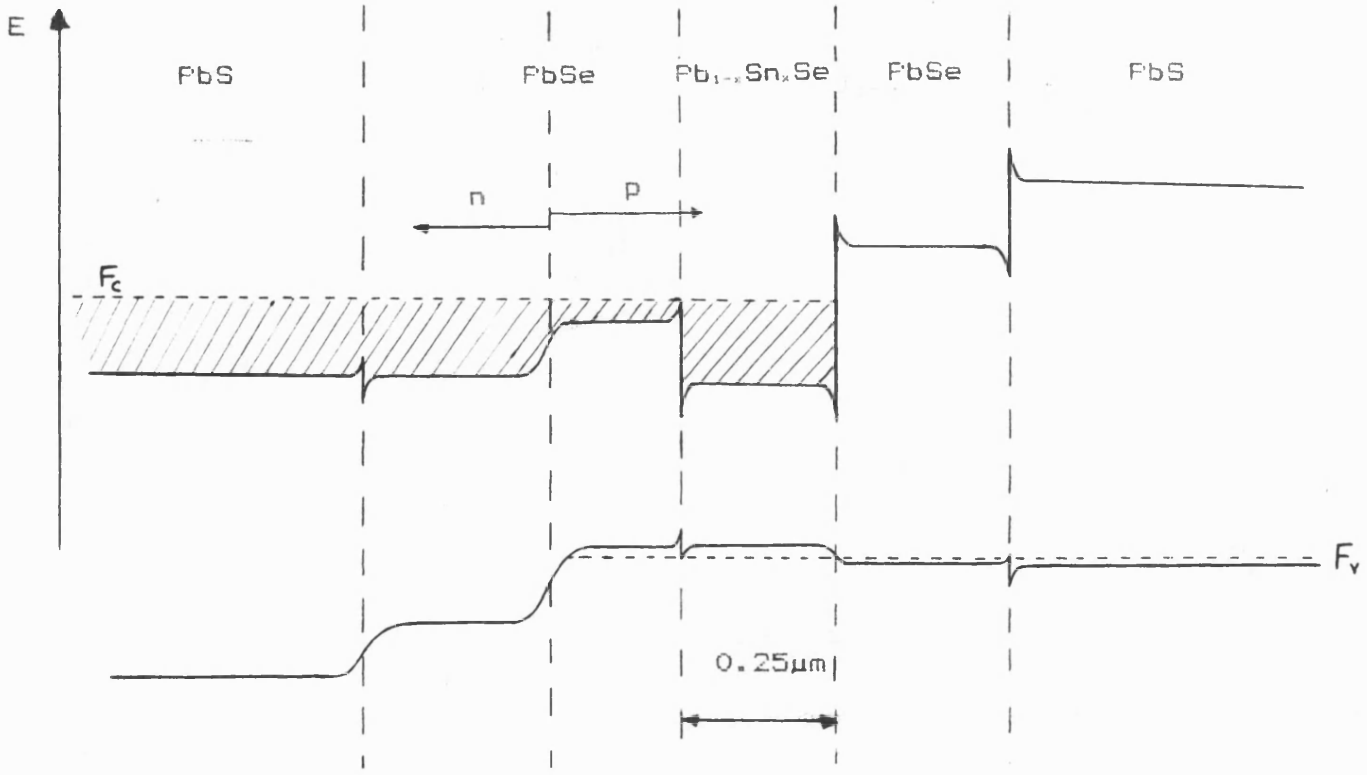


Fig(112). Injected carrier capture in the localised gain region laser showing the spill - over effect at low temperatures due to the lack of phonon interaction.

5.5.6) Graded refractive index lasers

The original goal of the project was to develop a single technology to cover the entire spectrum 3.5 - 20μm. The simple PbSe / $Pb_{1-x}Sn_xSe$ / PbSe DH structure covers the range 10 - 20μm but shorter wavelengths are only possible by using other materials with detrimentally large lattice constant differences. The simple DH laser could in theory be made to emit at shorter wavelengths by employing a quantum well in the active layer. Thin active layers, however, produce the enhanced low temperature effect described in the previous section and produce characteristically low output powers.

As mentioned in section 4.5.1, $Pb_{1-x}Eu_xSe$ shows a large increase in band gap energy for relatively small values of x. From the literature, it can also be deduced that for $x < 0.05$, the lattice constant mismatch is smaller than 0.1%. With reference to the work performed in section 4.5.1, showing the large increase in band gap energy possible, lasers were produced using $Pb_{1-x}Eu_xSe$ in the confinement layers. In addition to this, to increase the probability of injected carriers falling into the active region potential well, the $Pb_{1-x}Eu_xSe$ confinement layers were grown as a graded refractive index (GRIN) profile thus giving the structure a funnel - shaped band gap energy diagram as schematically shown in Fig(113).

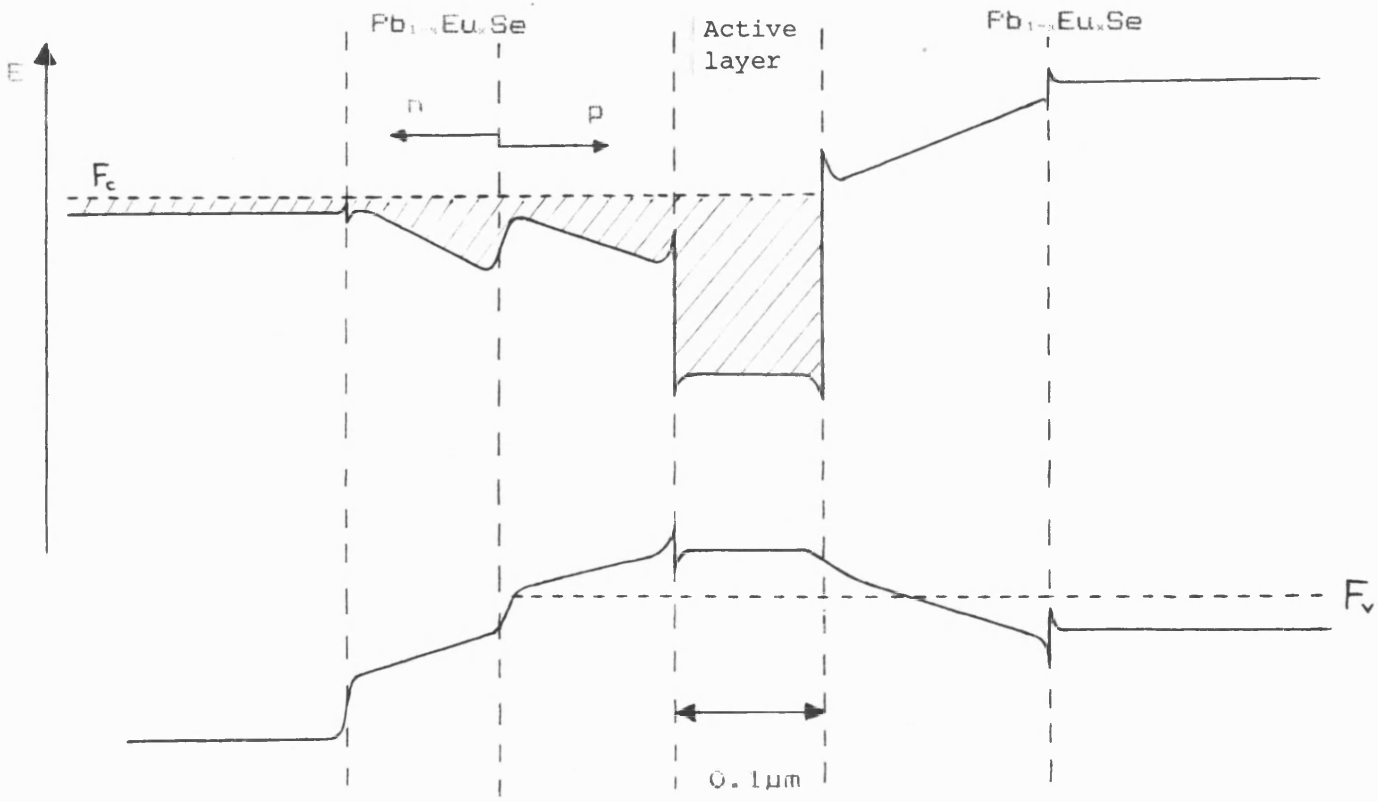


Fig(113). The graded refractive index laser energy diagram showing the concept of injected electron thermalisation into the active layer.

Two structures were grown consisting of 3μm thick $Pb_{0.97}Eu_{0.03}Se$ confinement layers with graded 0.5μm thick regions (x down to 0.01) sandwiching active layers of PbSe with thicknesses of 0.1 and 0.05μm. A third laser had a similar structure but with an active layer of $Pb_{0.9985}Eu_{0.0015}Se$ and a thickness of 0.1μm. The graded confinement layers were produced by slowly changing the Eu flux through regulating the Eu furnace temperature. This series of laser structures are presented in Fig(114) and were grown to indicate whether or not $Pb_{1-x}Eu_xSe$ can be used as confinement or active region material.

The characteristics of this type of laser show that practical, high quality IR diode lasers are possible by MBE epitaxial layer growth. The low temperature threshold current effect seen in the DH and LGR lasers described in sections 5.5.2 and 5.5.5 has disappeared due to the thermalising of the injected carriers by the funnel - shaped optical guide. The laser with the thickest PbSe active layer, however, already emits a slightly modified spectrum through the quantum effect and the laser with the 0.05μm thick active layer shows a surprisingly large quantum effect. This laser emits at 7.5 and 7.0μm at 20K, a shift of 1.4μm in the low energy emission over that of a pure PbSe laser with no quantum effect. The spectrum of this laser (431,9) is given in

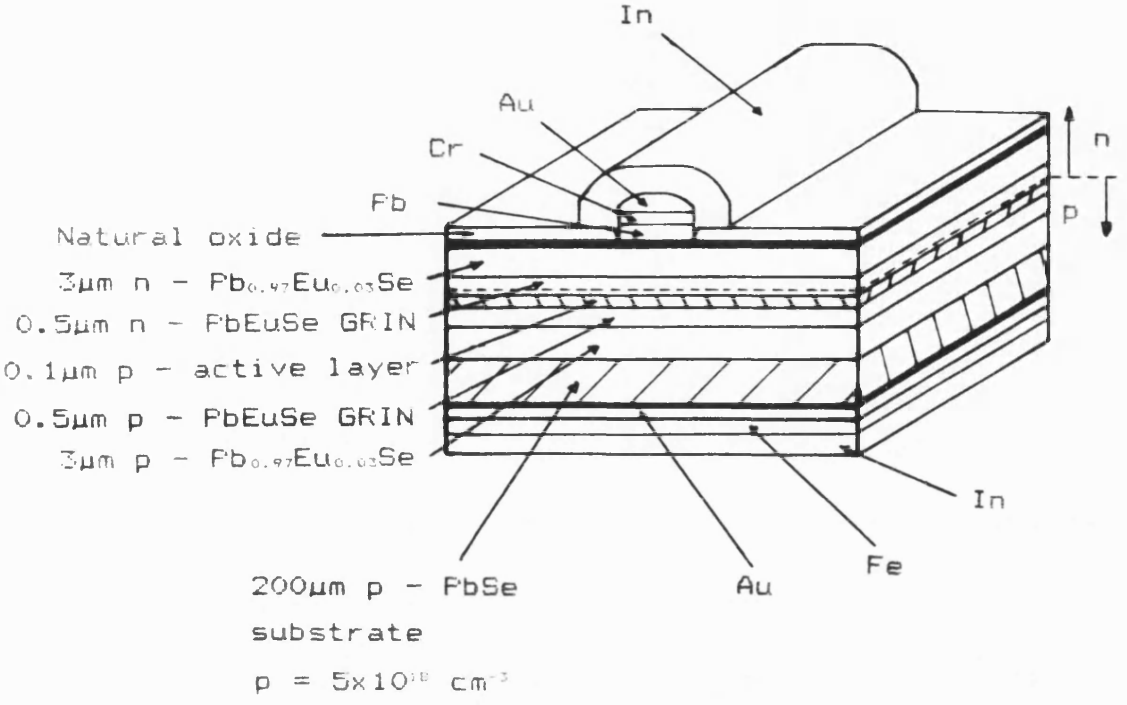


GRIN layers : $0.01 \overset{x}{\longleftrightarrow} 0.03$

Active layers : $Pb_{0.97}Sn_{0.03}Se$

$PbSe$

$Pb_{0.995}Eu_{0.005}Se$

Fig(114). Schematic of the $Pb_{1-x}Eu_xSe$ graded refractive index lasers using the natural oxide technique for device passivation.

Fig(115). The higher energy emission, which could come from a second subband, gives an approximate wavelength shift of 0.9μm. The spectra between 20 and 45K show that nearly all the total intensity concentrates in the two modes.

The maximum continuous wave operation temperature of the lasers were 163K and 135K for the active layer thicknesses of 0.1 and 0.05μm respectively. The value of 163K is one of the highest continuous wave operation temperatures ever reported for a lead chalcogenide diode laser. The characteristics of the laser with an active layer of $Pb_{0.995}Eu_{0.005}Se$ showed disappointing results. Only a few examples lased at temperatures of 20 - 45K with a high current pulse (3 - 5A). The wavelength of this laser was, however, the shortest, namely 3.7μm. Explanations for the poor $Pb_{1-x}Eu_xSe$ laser yield can be contributed to many factors rather than concluding from this single result that $Pb_{1-x}Eu_xSe$ is not a suitable active layer laser material. Possible problems could lie with the p - type doping, contacting or the incorrect positioning of the p - n junction.

### 5.5.7) Silver - doped DH lasers

The lasers described in sections 5.5.2 to 5.5.6 have p - n junctions fabricated with the identical

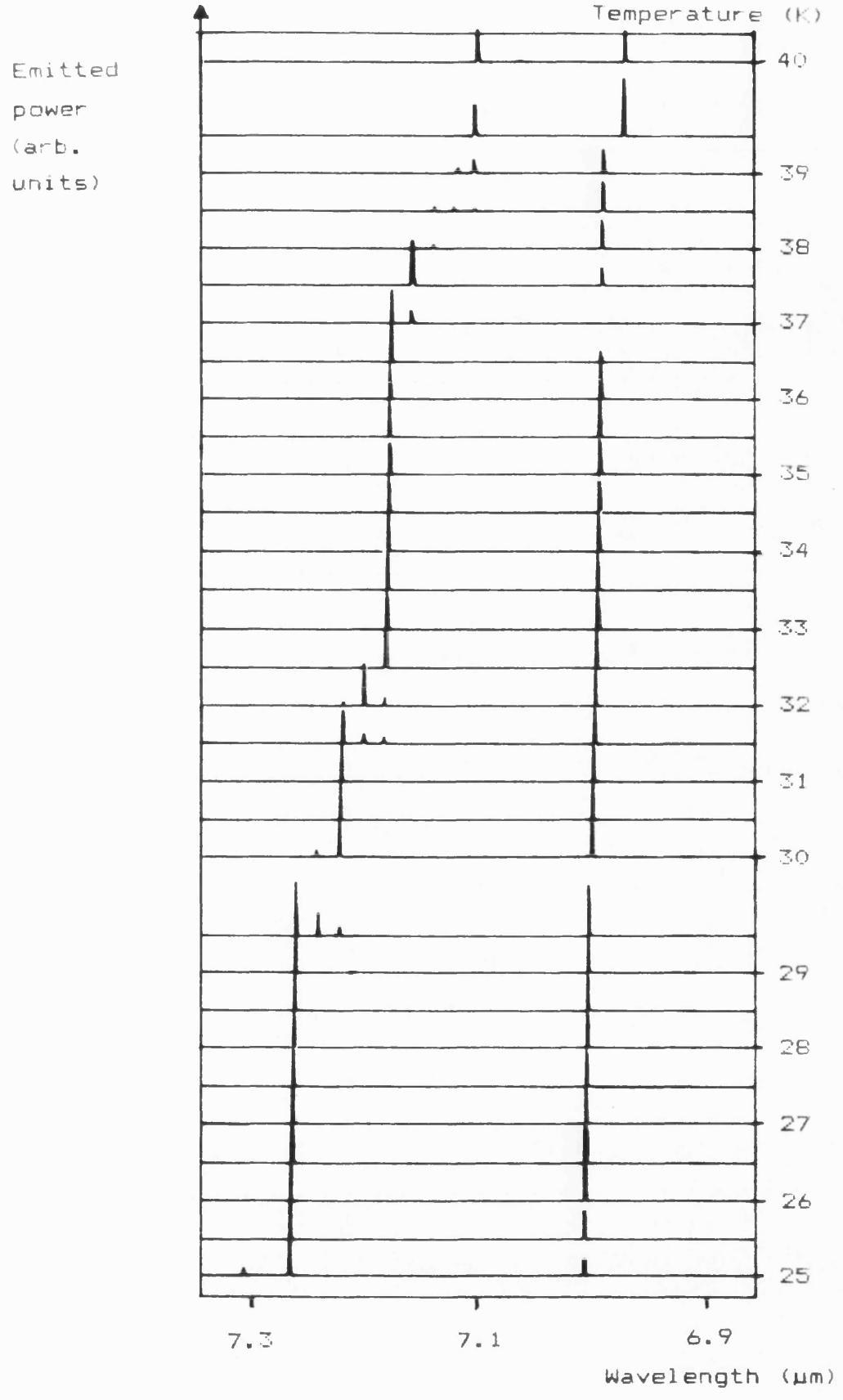


Fig(115). The temperature tuning spectrum of GRIN laser 431,9.

method. This has been achieved by the non - stoichiometric Se - doping for the p - side and, through the opening of the $Bi_2Se_3$ furnace shutter during growth, the n - side is produced through the impurity doping of Bi.

Chapter 4 has reported the results of impurity p - type doping of PbSe and $Pb_{1-x}Eu_xSe$ with silver. The work was undertaken due to the unsuccessful attempts to repeat some of the lasers reported in the previous sections. The common undefined factor between the laser structures is the relatively poor control of the Se furnace thus leading to different levels of hole concentrations in the first confinement layer and the active region.

Fig(116) shows the schematic of the first ever reported silver - doped DH lead chalcogenide diode laser. It exhibits the same basic construction as the lasers in section 5.5.2 except that the first confinement layer is Ag - doped to a level of $5x10^{18}$ $cm^{-3}$. The laser emits at 7.8μm at 80K which indicates a Sn content of 0.01 corresponding to the beam flux ratio SnSe : PbSe = 0.014 set during the deposition of the active layer. The maximum operation temperature in pulsed operation reaches 200K and the continuous wave operation maximum temperature is 120K. The laser has two modes and a

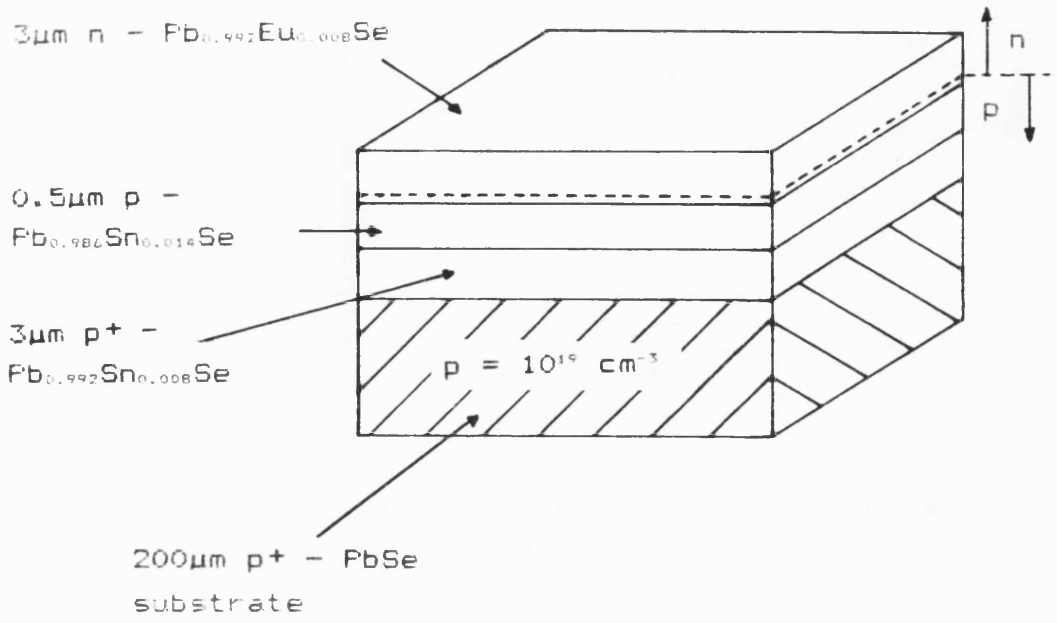


Fig(116). Schematic of the PbSe / $Pb_{1-x}Sn_xSe$ silver - doped DH laser.

threshold current of approximately 0.5A at 80K. Just as in the case of the stoichiometrically - doped DH lasers, the low temperature effect is again present due to the poor carrier confinement from the small band gap level difference. The lasers have been repeated within the MBE system with similar results. A repetition of lasers in previous sections was not possible and that lasers with defined Ag - doped first confinement layers are repeatable leads to the conclusion that silver doping is a necessity for commercially - orientated lead chalcogenide diode lasers fabricated by MBE.

## 6) CONCLUSIONS AND FUTURE WORK

A system has been designed for the manufacture of semiconductor infra - red diode lasers using the MBE technique of layer growth. The direct band gap lead chalcogenides exhibit band gaps which enable them to be considered for infra - red work between 2.5μm and 34μm. It has been shown that with careful design considerations specific to their high vapour pressures, the epitaxial growth and doping of the lead chalcogenides can be performed with reasonable control over ternary film composition and thickness. Experiments have shown that the materials can be doped n - and p - type using bismuth and silver respectively. Carrier concentrations of over $10^{19}$ $cm^{-3}$ are possible thus offering the possiblity of producing good confinement factors for heterostructure lasers.

The controlled growth of lead chalcogenide films has been used to manufacture a series of laser diode structures striving towards the goal of covering the infra - red spectrum from 3.5 - 20μm by employing a single unified technology based around the binary PbSe. From the three main types of laser fabricated in the project (double heterostructure, localised gain region and graded refractive index), the goal has been realised

in the graded refractive index type of structure - a structure which can only be grown successfully using the MBE technique of epitaxial growth. This type of structure is used throughout the entire required spectral range, the active layer materials and composition being chosen for a specific emission wavelength.

The stripe geometry lasers made from these films have reached maximum pulsed operation temperatures of 270K and contiuous operation temperatures of 163K which is within the reach of Peltier cooling systems thus making their inclusion into spectroscopic systems a much more practical and cheaper proposition. These maximum operation temperatures are some of the highest ever reported for the lead chalcogenides and are achieved by using the material $Pb_{1-x}Eu_xSe$ for the first time. The p - type first confinement layers of these lasers have relatively low hole concentrations ($10^{18}$ - $5x10^{18}$ $cm^{-3}$) and here further improvements are to be expected by the inclusion of the dopant silver. The characteristics of first silver - doped DH laser based upon the $Pb_{1-x}Sn_xSe$ material system shows great promise and after optimisation experiments, silver doping could prove to be a deciding factor upon the strive towards producing room temperature lead chalcogenide diode lasers.

The short wavelength end of the required spectrum

($3.5 < \lambda < 6\mu m$) presents more difficulties than the longer wavelength end ($6 < \lambda < 20\mu m$) for reasons explained in the text. More work upon the confirmation that $Pb_{1-x}Eu_xSe$ can be used within diode laser active layers has to be performed. Other alloy system candidates to be investigated could be $Pb_{1-x}Sr_xSe$ and $Pb_{1-x}Ca_xSe$. Measurements already carried out within the MBE system with the $Pb_{1-x}Sr_xSe$ alloy show a larger band gap shift with increasing Sr content than the $Pb_{1-x}Eu_xSe$ system with increasing Eu content. Mobilities are also higher and work must be carried out to investigate doping characteristics and eventual laser structures.

Improvements can be suggested in many aspects upon the constructional details of the MBE system itself. A system with eight furnaces arranged in a symmetrical circular form would give the advantage that every furnace would have an identical substrate - orifice distance, and giving the opportunity of loading an extra main PbSe source material furnace thus minimising the main system floodings to refill empty furnaces. This also presents the possibility of measuring flux rates during epitaxy. A system mounted upon a rotary feedthrough on the axis of the furnace flange could be rotated into each beam as required. The system could be a cross - beam type of construction thus enabling the measurement of beam fluxes

without influencing their paths to the substrate and hence in future offering computer control and assessment of more complicated structures (e.g. multi - quantum wells).

Work needs to be performed upon the shutter systems. The shutter effect can be minimised by tilting each shutter off the furnace axis thus reducing the heat back - scattering. In turn these shutters can be redesigned to be operated by electromagnets mounted upon a new type of furnace flanges. This gives added advantages including simplified construction, computer control, duty cycle operation thus allowing the accurate production of GRIN structures and the possibility of changing and cleaning shutters and collimators with each furnace refill.

These constructional changes would help the investigations into other possible laser structures to bring the maximum operation temperatures of the devices to more practical temperatures and to decrease the threshold currents required to produce laser action to increase stability and reliability. This could be achieved by the use of quantum well structures which also give the added advantage of producing the more difficult short wavelength lasers {120}.

The overall power output of the MBE lasers must

be improved and future investigations could be aimed in the direction of finding the conditions for more powerful devices. These conditions are reported to be the need of thicker active layers {120}. The conclusion to be drawn from the requirement of both high operation temperatures and high powers is that a compromise of the active layer thickness has to be found, the thickness actually used depending upon the application.

## 7) ACKNOWLEDGEMENTS

The author would like to thank Professor Dr. J. Hesse and Professor Dr. H.M. Preier of the Fraunhofer-Institut für Physikalische Meßtechnik for their support and kind permission to use the laboratory facilities. I am particularly indebted to Dr. K-H. Bachem (now with the Fraunhofer-Institut für Angewandte Festkörperphysik, Freiburg) for his invaluable help throughout the project.

It has been a pleasure to have been so carefully supervised by Dr. W. Clark of the University of Bath in his friendly and helpful manner and I would like to sincerely thank him.

Thanks are also due for the help and advice given by my colleagues Dr. H. Böttner, Frau M. Köhne, Frau B. Spanger, Herr G. Knoll, Mr. D.R. Ball MSc., Frau O. Prasse and Herr N. Schäl (now at the University of Giessen) of the technology group in the Institute's Optische Spektroskopie section, without which this thesis would have been impossible. A special thanks is due to Professor H.M. Preier, Dr. H. Böttner and Dr. M. Tacke for carefully reading and commenting upon the manuscript.

I appreciate the time and patience exhibited by

the members of the Institute's mechanical and technical drawing workshops. The appreciation extends also to the scientists and technicians who have performed measurements upon various work concerned with the thesis.

Finally I wish especially to thank my wife Sue for drawing with such care and patience the majority of the diagrams and for providing moral support during the long preparation of this thesis.

## 8) REFERENCES

{1} EINSTEIN, A.: Phys. Z. 18, 121 (1917).

{2} WEBER, I.: IRE-Transact. PG Ed.3, 1 (1953).

{3} BASOV, N.G.; PROCHOROV, A.M.: Zhurn, eksp. teoret. Fiz 431 (1954).

{4} SCHAWLOW, A.L.; TOWNES, C.H.: Phys. Rev., 112, 1940 (1958).

{5} MAIMAN, T.H.: Phys. Rev., 123, 1145 (1961).

{6} JAVAN, A; BENNETT, W.R.; HERRIOTT, D.R.: Phys. Rev. Lett., 6, 106 (1961).

{7} BERNARD, M.G.A.; DURAFFOURG, G.: Phys. Stat. Solidi, 1, 699 (1961).

{8} LEVINE, A.K.: Am. Sci., 51, 14 (1963).

{9} WEISER, K.; WOODS, J.F.: Appl. Phys. Lett., 7, 225 (1965).

{10} CUSANO, D.A.; KINGSLEY, I.D.: Appl. Phys. Lett., 6, 91 (1965).

{11} BENOIT à la GUILLAUME, C., DEBEVER, I.: Solid State Commun., 2, 145 (1964).

{12} HURWITZ, C.E.; KEYES, R.I.: Appl. Phys. Lett., 5, 139 (1964).

{13} CUSANO, D.A.: Solid State Communications, 2, 353 (1964).

{14} PHELAN, R.I.; REDIKER, R.H.: Appl. Phys. Lett., 6, 70 (1965).

{15} KRESSEL, H.; LADANY, I.: RCA company review, 36, 230 (1975).

{16} MARPLE, D.T.F.: Journ. of Appl. Phys., 35, 1241 (1964).

{17} SZE, S.M.: Physics of Semiconductor Devices, Wiley - Interscience, New York 710 - 715 (1969).

{18} CASEY, H.C.; PANISH, M.B.: Heterostructure Lasers, Academic, New York (1978).

{19} PILKUHN, M.H.: Physics Stat. Solidi, Vol. 25, 9 (1968).

{20} LASHER, G.J.; SMITH, W.V.: IBM Journal 8, 532 (1964).

{21} ROSENBERG, H.M.: The Solid State, Clarendon Press, Oxford, 108 (1975).

{22} BLACKMORE, J.S.: Electron. Communications, 29, 131 (1952).

{23} SMITH, R.A.: Semiconductors, Cambridge University Press, London, 22 (1959).

{24} NATHAN, M.I.: Proc. IEEE, 54, 1276 (1966).

{25} HOLONYAK, N.; KOLBAS, R.M.; DUPUIS, R.D.; DAPKUS, P.D.: IEEE J. Quantum Electron. QE-16, 170 (1980).

{26} HAYASHI, I.; PANISH, M.B.; REINHART, F.K.: J. Appl. Phys., 42, 1929 (1971).

{27} TSANG, W.T.; LOGAN, R.A.; VAN DER ZIEL, J.P.: Appl. Phys. Lett., 34, 644 (1979).

{28} KRESSEL, H.; NELSON, H.: RCA company review, 30, 106 (1969).

{29} PANISH, M.B.; HAYASHI, I.; SUMSKI, S.: J. Quantum Electron., QE-5, 210 (1969).

{30} ALFEROV, Z.I.; ANDREEV, V.M.; PORTNOI, E.L.; TRUKAN, M.K.: Fiz. Tech. Poluprov., 3, 1328 (1969).

{31} THOMPSON, G.H.B.: Physics of Semiconductor Laser Devices, Wiley - Interscience, 252 (1980).

{32} THOMPSON, G.H.B.: Ref(31), 158 (1980).

{33} PAOLI, T.L.; HAKKI, B.W.; MILLER, B.I.: J. Appl. Phys., 44, 1776 (1973).

{34} THOMPSON, G.H.B.: Ref(31), 271 (1980).

{35} SZE, S.M.: Ref(17), 726 (1969).

{36} MIYA, T.; TERUNUMA, Y.; HOSAKA, T.; MIYASHITA, T.: Electron. Lett., 15, 108 (1979).

{37} GOODMAN, C.H.L.: Solid State Electron Devices, 2, 129 (1978).

{38} ENG, R.S.; BUTLER, J.F.; LINDEN, K.J.: Tunable diode laser spectroscopy. Inv. Rev. Opt. Eng. Vol 19, No. 6, 945 - 960 (1980).

{39} LAWSON, W.D.; NEILSON, S.: Preparation of Single Crystals, Butterworth, 14-17 (1958).

{40} LAWSON, W.D.: J. Appl. Phys., 22, 1444 (1951).

{41} BREBRICK, R.F.; GUBNER, E.: J. Chem. Phys., 36, 1283 (1962).

{42} METZ, E.P.A.; MILLER, R.C.; MAZELSKY, R.: J. Appl. Phys., 33, 2016 (1962).

{43} BöTTNER, H.: Private communication, Fraunhofer Institut, IPM, Freiburg, West Germany (1983).

{44} IGAKI, K.; OHASHI, N.: J. Phys. Soc. Japan, 18 (Suppl. 2), 143 (1963).

{45} SATO, Y.; FUJIMOTO, M.; KOBAYASHI, A.: Jap. J. Appl. Phys., 2, 688 (1963).

{46} BREBRICK, R.F.; ALLGAIER, R.S.: J. Chem. Phys., 32, 1826 (1960).

{47} MILLER, J.F.; MOODY, J.W.; HIMES, R.C.: Trans. Metall. Soc., AIME 239, 342 (1967).

{48} CALAWA, A.R.; HARMAN, T.C.; FINN, M.; YOUTZ, P.: Trans. Metall. Soc., AIME 242, 374 (1968).

{49} HEINRICH, H.: Intern. Conf. on Lattice Defects in Semiconductors, Freiburg (1974).

{50} SCANLON, W.W.: Solid State Physics-Advances in Research and Applications, ed. Seitz, F. and Turnbull, D., Vol. 9, Academic Press, 104 (1959) combined with BLOEM, J.; KRöGER, F.A.: Z. Phys. Chem., Frankfurt 7, No. 1/2, 1 (1956) and BREBRICK, R.F.; SCANLON, W.W.: Phys. Rev., 96, 598 (1954).

{51} DALVEN, R.: Infrared Physics, Permagon Press, Vol.

9, 144 (1969) prepared from FUJIMOTO, M.; SATO, Y.: Jap. J. Appl. Phys., 5, 128 (1966) and BIS, R.F.: J. Phys. Chem. Solids 24, 579 (1963).

{52} PORTER, R.F.: J. Chem. Phys., 34, 583 (1961).

{53} DALVEN, R.: Infrared Physics, Permagon Press, Vol. 9, 145 (1969).

{54} KITTEL, C: Introduction to Solid State Physics, John Wiley, 3rd ed., Chapter 1 (1966).

{55} DALVEN, R.: Ref(53) 146 (1969).

{56} BIS, R.F.; FARABAUGH, E.N.; MUTH, E.P.: J. Appl. Phys., Vol. 47, No. 2, 739 (1976).

{57} ORIEL GmbH: Eigenschaften optischer Materialien, Darmstadt, West Germany (1981).

{58} NOVIKOVA, S.I.; ABRIKOSOV, N.K.: Fizika tverd. Tela 5, 1913 (1963); English trans.: Soviet Phys. Solid St., 5, 1397 (1964).

{59} DALVEN, R.: Ref(53) 146 (1969).

{60} KITTEL, C.: Quantum Theory of Solids, John Wiley, 213 (1963).

{61} LIN, P.J.; KLEINMAN, L.: Phys. Rev., 142, 478 (1966).

{62} SCANLON, W.W.: Ref(50) 83-137 (1959).

{63} BARDEEN, J.; BLATT, F.J.; HALL, L.H.: Atlantic City Photocond. Conf. Rep., John Wiley, 146 (1956).

{64} CARDONA, M.; GREENAWAY, D.L.: Phys. Rev., 133, A1685

(1964).

{65} ZEMEL, J.N.; JENSEN, J.D.; SCHOOLAR, R.B.: Phys. Rev., 140, A330 (1965).

{66} ALLGAIER, R.S.; SCANLON, W.W.: Phys. Rev., 111, 1029 (1958).

{67} PUTLEY, E.H.: Mat. used for Semiconductor Devices, Ed. HOGARTH, C.A., Interscience, 97-98 (1965).

{68} PUTLEY, E.H.: Ref(67) 101 (1965).

{69} BACHEM, K-H.; NORTON, P.R.; PREIER, H.M.: Proc. Int. Winter School on Heterostructures and 2-D Electronic Systems in Semiconductors, Mauterndorf, Austria, Feb 26 - Mar 2 (1984): Ed. BAUER, G.; KUCHAR, F.; HEINRICH, H.: Springer Verlag, Berlin, Heidelberg (1984).

{70} KOBAYASHI, A.; SATO, Y.; FUJIMOTO, M.: Physics of Semiconductors, Proc. 7th Int. Conf., Paris (1964); Ed. by HULIN, M.: Academic Press, 1257 (1964).

{71} CROCKER, A.J.: J. Phys. Chem. Solids, 28, 1903 (1967).

{72} STRAUSS, A.J.: J. Elect. Mat., Vol. 2, No. 4, 553-569 (1973).

{73} BREBRICK, R.F.; GUBNER, E.: Ref(41) 1283-1284 (1962).

{74} KOVAL'CHIK, T.L.; MASLAKOVETS, Iu. P.: Soviet Phys. Tech. Phys., 1, 2337 (1957).

{75} HESSE, J.: Sol. St. Dev. Conf., Tokyo (1976); Jap.

J. Appl. Phys., Vol. 16, Sup. 16-1, 297-304 (1977).

{76} SILBERG, E.; ZEMEL, A.: J. Electron. Mat., Vol. 8, No. 2, 99-109 (1979).

{77} PARTIN, D.L.: Journ. of Vac. Sci. Technol., B1, 174 (1983).

{78} PARTIN, D.L.: Journ. of Vac. Sci. Technol., 21, 1 (1982).

{79} PARTIN, D.L.: J. Electron. Mat., Vol. 12, No. 6, 917-929 (1983).

{80} STRAUSS, A.J.: Trans. Metall. Soc., AIME Vol. 242, 354-365 (1968).

{81} BREBRICK, R.F.; GUBNER, E.: Ref(41) 170 (1962).

{82} CALAWA, A.R.; HARMAN, T.C.; FINN, M.; YOUTZ, P.: Ref(48) 374 (1968).

{83} STRAUSS, A.J.: Ref(80). 364 (1968).

{84} HARMAN, T.C.; CALAWA, A.R.; MELNGAILIS, I.; DIMMOCK, J.O.: Appl. Phys. Lett., Vol. 14, No. 11, 333-334 (1969).

{85} STRAUSS, A.J.; HARMAN, T.C.: J. Electron. Mat., Vol. 2, No. 1, 71-85 (1973).

{86} HARMAN, T.C.: Journ. of Nonmetals, Vol. 1, 183-194 (1973).

{87} STRAUSS, A.J.: Trans., AIME 239, 794 (1967).

{88} SCANLON, W.W.: J. Phys. Chem. Solids, Vol. 8, 423-428 (1959).

{89} WEAST, R.C.: Ed. Handbook of Chemistry and Physics, 59th Ed. (1978): Chemical Rubber Company Press, Inc., Boca Raton, Florida, 103 (1978).

{90} PARTIN, D.L.: J. Electron. Mat., Vol. 13, No. 3, 493-504 (1984).

{91} WEAST, R.C.: Ref(89) 103 (1978).

{92} SILBERG, E.; ZEMEL, A.: Appl. Phys. Lett., Vol. 31, No. 12, 807-809 (1978).

{93} PREIER, H.M.; BACHEM, K-H.; BöTTNER, H.; BALL, D.R.; RIEDEL, W.J.: Proc. of SPIE Int. Soc. of Opt. Eng., 438, 10 (1983).

{94} LINDEN, K.J.; NILL, K.W.; BUTLER, J.F.: IEEE J., QE-13, 720 (1977).

{95} CARPENTER, R.; HAMER, M.F.; BICKLEY, W.P.; EDDOLLS, D.V.: Infrared Phys., Vol. 18, Pergamon Press, 193-197 (1978).

{96} GROVES, S.H.; NILL, K.W.; STRAUSS, A.J.: Appl. Phys. Lett., 25, 331 (1974).

{97} KASAI, I.; HORNUNG, J.; BAARS, J.: J. Electron. Mat., Vol. 4, No. 2, 299-311 (1975).

{98} ASTLES, M.G.; YOUNG, M.L.: J. Electron. Mat., Vol. 10, No. 1, 1-41 (1981).

{99} LUSCHER, P.E.: Solid State Technol., December 1977, 43-52 (1977).

{100} SOCRATES, G.: Thermodynamics and Statistical

Mechanics, Butterworths, London, 223 (1971).

{101} ABRIKOSOV, N. Kh.; BANKINA, V.F.; PORETSKAYA, L.V.; SHELIMOVA, L.E.: Semiconducting II - VI, IV - VI and V - VI compounds, Plenum Press, New York, 105 (1969).

{102} ROSMAN, R.: Private communication, Tel Aviv University, Israel (1985).

{103} MOON, R.L.; ANTYPAS, G.A.; JAME, L.W.: J. Electron. Mat., 3, 635 (1974).

{104} DALVEN, R.: Ref(53), 147 (1969).

{105} BIS, R.F.; DIXON, J.R.: J. Appl. Phys., 40, 1918 (1969).

{106} STEININGER, J.: Met. Trans., 1, 2939 (1970).

{107} NORR, K.: Polishes and etches for tin telluride, lead sulphide, lead selenide and lead telluride, U.S. Naval Ordnance Laboratory, White Oak, Maryland, U.S.A., 15 (1963).

{108} MAIER, H.: Institut für Halbleitertechnik, Basislabor, RWTH, Aachen, West Germany (1983).

{109} OTTO, G.: Geologische Schule, University of Freiburg, Freiburg, West Germany (1983).

{110} CHAPMAN, B.: School of Physics, University of Bath, Bath, England (1983).

{111} PREIER, H.M.: Applied Phys., (20), 189 - 206 (1979).

{112} BACHEM, K-H.; BöTTNER, H.: 4er Zwischenbericht,

Modenstabile IR - Diodenlaser, Fraunhofer Institut, IPM, Freiburg, West Germany 108 (1983).

{113} BACHEM, K-H.: 1er Zwischenbericht, Entwicklung optimal strukturierter Doppelhetero - Bleisalzdiodenlaser, Fraunhofer Institut, IPM, Freiburg, West Germany (1983).

{114} STRAUSS, A.J.: Ref(72) 553 - 569 (1973).

{115} PARTIN, D.; LO, W.: Low threshold current lead - telluride diode lasers grown by MBE, General Motors report GMR - 3349, Michigan, U.S.A. (1980).

{116} PARTIN, D.: High resolution doping profiles in $Pb_{1-x}Sn_xTe$ thin film structures, General Motors report GMR - 3444, Michigan, U.S.A. (1980).

{117} STRAUSS, A.J.: Ref(72) 553 - 569 (1973).

{118} HIESINGER, H.: Fraunhofer Institut, IAF, Freiburg, West Germany (1986).

{119} BACHEM, K-H.; BÖTTNER, H.: Ref(112) (1983).

{120} PARTIN, D.L.: Private communication, Michigan, U.S.A. (1985).

## 9) AUTHOR'S PUBLICATIONS AND CONFERENCES

a) BACHEM, K-H.; NORTON, P.R.; PREIER, H.M.: Ref(69) March (1984).

b) NORTON, P.R.; KNOLL, G.; BACHEM, K-H.: J. Vac. Sci. Technol., B3 (2), 782 - 783 (1985).

c) ZOGG, H.; NORTON, P.R.: SPG, Herbsttagung, Biel, Okt 1985, Helv. Phys. Acta., Band 59, 168 - 171 (1986).

d) ZOGG, H.; MAIER, P.; NORTON, P.R.: Mat. Res. Soc. Meeting, Boston 2 - 7 Dec 1985, Band 56, Apr (1986).

e) ZOGG, H.; NORTON, P.R.: IEEE Tech. Digest, IEDM 85, Washington D.C., 5.4, 121 - 124 (1985).

f) SHANI, Y.; KATZIR, A; BACHEM, K-H.; NORTON, P.R.; TACKE, M; PREIER, H.M.: Appl. Phys. Lett., 48 (18), 5th May, 1178 - 1180 (1986).

g) NORTON, P.R.; BACHEM, K-H.; TACKE, M.: 3rd Int. Sym. on Opt. and Optoelectronic App. Sci. and Eng., SPIE Proc. Vol. 659, Innsbruck, Austria, April (1986).

PUBLICATION A)

# MBE - A Tool for Fabricating IV-VI Compound Diode Lasers

K.-H. BACHEM, P. NORTON and H. PREIER

Fraunhofer-Institut für Physikalische Messtechnik
Heidenhofstrasse 8, D-7800 Freiburg

## Abstract

The molecular beam epitaxy (MBE) and the closely related hot wall epitaxy (HWE) techniques are excellent tools to fabricate lead chalcogenide hetero structures for device applications. Whenever exact compositions of a ternary or quaternary film are required, like in lasers, the MBE method is best suited. Lattice matched PbTe-based and non lattice matched PbSe-based laser structures have been realized for the 4 to 12 µm wavelength range. While no significant difference exists between lattice matched and non lattice matched devices, both kinds exhibit much larger operation temperatures than diffused homojunction diodes. The properties of an MBE-system specially designed for the growth of lead chalcogenides are described in detail. Characteristic data of PbTe- and PbSe-based DH lasers are presented and compared with those of homojunction devices.

## 1. Introduction

Quite a variety of lead chalcogenide heterostructures have been fabricated by molecular beam epitaxy and the related technique of hot wall epitaxy. The main purpose for growing these heterostructures was to prepare double hetero-structure laser diodes /1 - 4/ with properties superior to those of diffused homojunction lasers. In addition, also detectors of the kind PbTe-PbSnTe /5/ and PbS-PbSSe /6/ have been fabricated using evoporation techniques.

Most of the laser structures realized to date have lattice mismatched heterojunctions, like PbTe-PbSnTe-PbTe /1/ or PbS-PbSSe-PbS /2/. The properties of these devices were already superior to homojunction lasers in spite of the lattice mismatch. The most significant improvement was the maximum operation temperature which was raised up to 120 K from a value of about 80 K for homojunction lasers.

Recently lattice matched double hetero structures with PbEuSeTe active and confinement layers as well as PbSnTe active layers and PbSnYbTe confinement layers were prepared successfully at GENERAL MOTORS (GM). The PbEuSeTe- diodes have been operated at 4.06 µm up to 147 K cw, the highest operation temperature observed so far in lead chalcogenide lasers. With the lattice matched PbSnTe-diodes a cw tuning range from 10.3 µm (at 10 K) to 7.1 µm (at 128 K) has been realized. However, if the pulse properties are considered, no large differences between lattice matched lead telluride and non lattice matched lead sulfide

selenide lasers has been noticed. Apparentely lattice matching is less important in the second system. The higher cw operation temperatures obtained for telluride based structures are not significant because the cw temperature is strongly effected by the properties of the contacts and bounding technique. This leads to the conclusion that not inherent laser properties but rather a superior contacting procedure leads to the high cw operation temperatures of the GM lasers. In this paper the MBE system used in our laboratory for the fabrication of lead chalcogenide heterostructures is described. Design and performance of the evaporators are discussed in detail, since both effect most critically the control of layer composition. The properties of PbSe-PbSnSe-PbSe and PbS-PbSSe-PbS lasers are discussed and compared with published data.

## 2. Evaporation Techniques

Deposition of lead chalcogenides including Sn-containing ternary or quaternary compounds is most straightforward accomplished by evaporation techniques. All lead- and tin chalcogenides vaporize already at moderate temperatures /7/. Practical beam flux densities in the order of $10^{13}$ to $10^{15}$ $cm^{-2}s^{-1}$ are obtained at temperatures below 1100 K. The lead chalcogenides vaporize almost undissociated. Besides PbX(X = S, Se, Te) no other compounds are found in the gas phase and congruent subliming compositions exist within the stability region of the solids. The vaporization behaviour of the tin chalcogenides is more complex, their vapor consists of $X_2$, SnX, $SnX_2$, $Sn_2X_3$ and $Sn_3X_4$, but SnX is the major constituent. SnTe, and SnSe, evaporate incongruently. Therefore, the source composition shifts into the two-phase region. Complications do not arise from this complexity because a two-phase source provides vapor pressures just as well defined as a congruently subliming one-phase source. Alternatively to compound source materials, elemental source materials have been successfully employed /8/. However, this approach has been abandoned since it was found that closer stoichiometry control and therefore lower carrier concentrations are achievable by growth from sources of the binary compounds /8/. Only in cases where elemental source materials are inevitable, these are used in combination with binary compound source materials. For example, in order to deposit ternary lead chalcogenides containing rare earth or earth alkali elements, it is neccessary to use elemental source materials because the chalcogenides of these elements cannot be evaporated at practical temperatures due to their extreme thermal stability.

Assuming binary source materials are used and these materials are evaporated from thermocouple controlled Knudsen cells, the beam flux stability can be derived from the temperature dependence of the vapor pressures of the binaries /7/. Considering that the evaporators are operated at a temperature of 1000 K and taking into account that a state-of-the-art thermocouple controlled feedback system provides a relative temperature

accuracy of 0.2 to 0.5 K, it can be estimated that the vapor pressures of lead and tin chalcogenides are accurate within 0.2 to 0.5 percent inside the Knudsen cells. Thus, the composition of a molecular beam combined from the beams of Knudsen cells would be accurate within approximately 0.4 to 1 percent. The same kind of precision is expectable for the composition of ternary films for constant deposition temperature. Considering the most critical case of a $PbSe_{1-x}Te_x$ film to be lattice matched to a given substrate, it follows that lattice matching down to a precision of $5 \times 10^{-4}$ should be achievable. An even better composition control is expected if the beam is not combined from two individually temperature controlled Knudsen cells but the two cells are combined inside one temperature controlled heater /5/. In this case temperature fluctuations effect the vapor pressures in both cells in the same direction. However, one has to consider that the higher stability of the beam composition is gained on expense of flexibility.

The above presented estimations are based on vapor pressure calculations, the technical limitations resulting from the relative accuracy of the temperature control system, and assuming ideal Knudsen cells. In reality, the evaporation cell is a complex device whose behaviour is critically dependent on its design and operation conditions. Differently from III-V-compound deposition systems where open evaporators have to be used for obvious reasons, in lead salt deposition systems, Knudsen cell like evaporators are usually prefered. The vapor pressures of the lead and tin chalcogenides approach the mbar region already at convenient temperatures around 800 °C. Therefore, evaporation cells with millimeter sized orifices can be used. Such a cell provides a beam flux rate of the order of $10^{15}$ $cm^{-2}$ $s^{-1}$ at a distance of 15 cm, which is sufficient ot obtain growth rates of a few µm per hour. Figure 1 shows a schematic view of the cells we are using for evaporation of binary compounds. The orifice has a diameter of about 1.5 mm. The temperature inside the cell is not uniform, but decreases from the bottom toward the open end. Therefore the source material, loaded with as crushed pieces, sublimes towards the cover where it forms a solid block with a channel in its axis. The thermocouple is fed through the bottom of the cell and its tip is placed where the block is formed. The vapor pressure in the cell corresponds to the temperature of the open surface of the block because this surface is the hotest part of the block. Fig. 1 shows the beam flux rate obtained from such a cell in dependence of time for uninterrupted operation and unchanged set point of the temperature controller. The beam flux rate has been measured at the substrate position with standard ion gauge. The conversion factor between pressure reading and beam flux rate has not been determined. Therefore the beam flux rates are given in pressure units. For orientation, a PbSe beam flux rate corresponding to $3 \times 10^{-6}$ mbar measured at the substrate position yields a growth rate of 11 Å per second for a deposition temperature of 350 °C and for a combined beam of PbSe and SnSe with rates corresponding to $3 \times 10^{-6}$ mbar and $2 \times 10^{-7}$ mbar, respectively, yield a ternary film with a Sn content of approximately 10 % (atomic

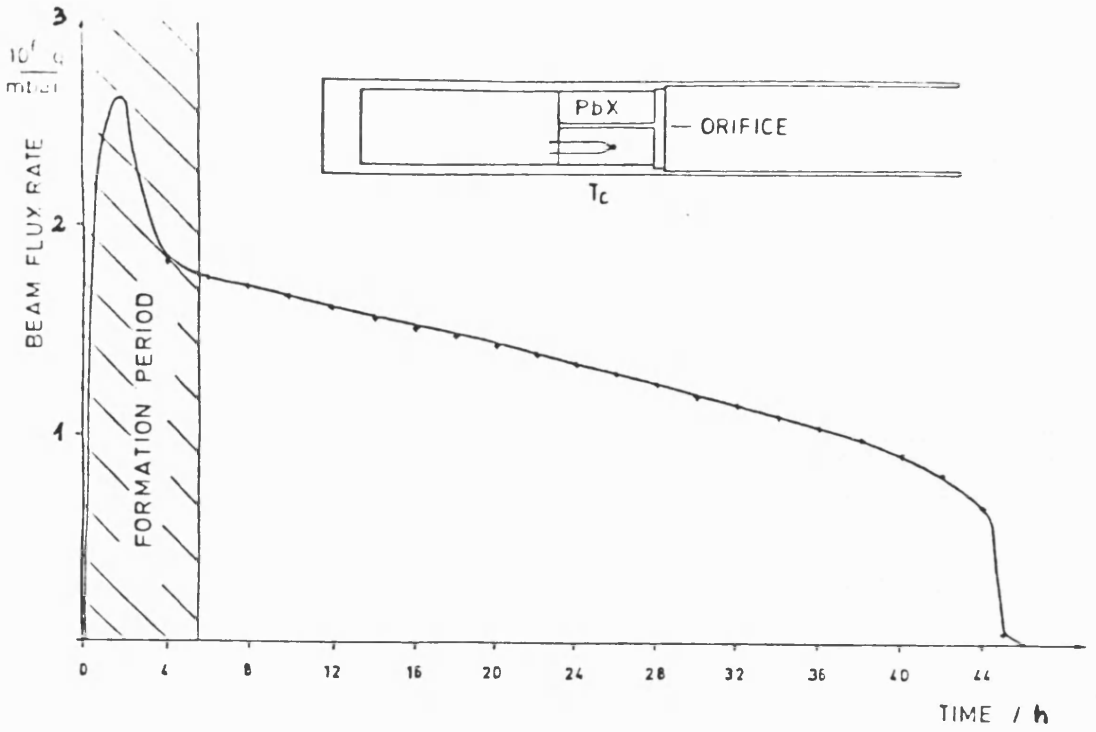


Fig. 1:
Dependence of beam flux rate on operation time for an evaporator shown schematically in the inset.

fraction). The dependence of beam flux rate on time as shown in Fig. 1 is typical. For the first few hours of operation of a freshly loaded cell the beam flux is not controllable. In this period the material sublimes into the colder part of the cell thereby forming a solid block. When sublimation is completed the flux stabilizes and becomes precisely controllable. The steady decrease of the beam flux rate in dependence of operation time results from the axial temperature gradient in the cell. Slightly modified cells are employed for evaporation of Se and Bi selenide. These species are used for control of stoichiometry and n-type doping. For these purposes only small beam flux rates, typically in the range of $10^{-9}$ to $10^{-8}$ mbar, have to be provided. Thus only small sized low temperature operated cells are required. The low operation temperatures, typically 300 and 600 °C, request for a special heater design because radiation coupling between heater, cell and thermocouple is weak in the low temperature regime. With appropriately designed cells, a beam flux stability at the above mentioned level of better than 20 % is obtained. This accuracy is sufficient for the desired purposes.

The SIMS-profile of a four layer PbSnSe structure is shown in Fig. 2. The PbSe flux rate was 1,5 x $10^{-6}$ mbar, the SnSe flux rate was increased in steps. The ratio of the flux rates q(SnSe)/q(PbSe) is indicated in the diagram. The deposition was interrupted for 15 minutes between adjacent films in order to reach steady state source conditions for the SnSe cell. The data have not been smoothed, but even without sophisticated data processing procedures it can be seen that the composition

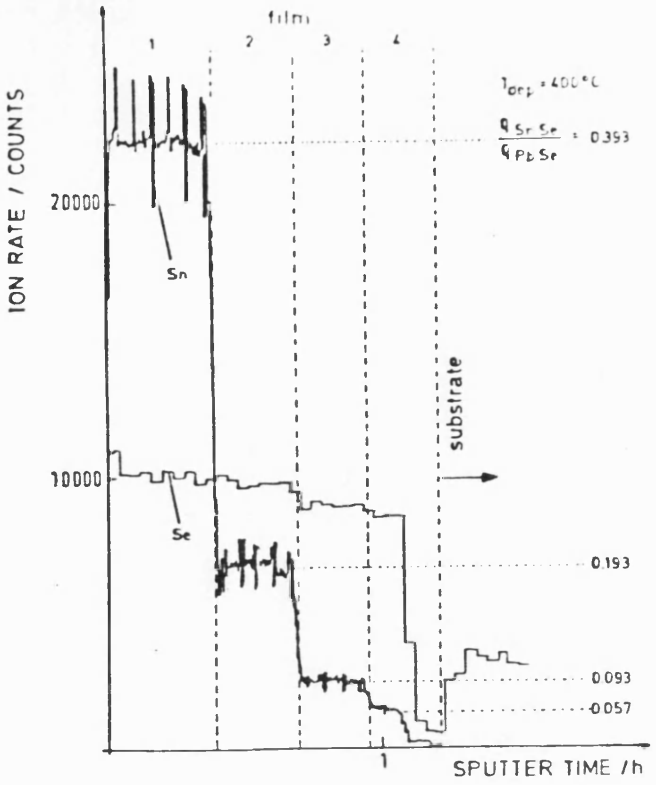


Fig. 2:
SIMS-profile of a layer structure consisting of $Pb_{1-x}Sn_xSe$-films with 4 different compositions deposited at a temperature of 400 °C.

in each film is reasonable constant. The total thickness of the multilayer is approximately 1 µm. Therefore, the interface regions are broadened due to sputter effects. Nevertheless, the transition between the first and second film is still abrupt although the deposition temperature is 400 °C. The laser structures are usually grown at lower temperatures (350 - 375 °C). Multiquantum well structures should be obtainable with relative ease. The ion rate axis and the sputter time axis do not correspond linearly to composition and depth, respectively, because of SIMS typical matrix effects. For orientation, the third layer has a tin content of 6.8 ± 0.1 %. Its count rates agreed precisely with those of a calibration standard of the composition $Pb_{0.932}Sn_{0.068}Se$.

The substrate holder is uncritical in lead salt deposition systems because of the typical low deposition temperatures (350 - 400 °C) and small substrate areas (1 - 2 $cm^2$). The commercially available substrate station from VARIAN, originally designed for depositon of III-V-compounds, is well suited.

The PbSnSe- and PbSSe-laser structures, being described later, have been grown under background pressures ranging from 5 x $10^{-10}$ mbar up to 3 x $10^{-9}$ mbar. PARTIN /3, 4/ has deposited PbSnTe-laser structures under apparently identical vacuum conditions. These vacuum conditions are standard for an UHV-system obtained after backout at medium temperatures (≃ 150 °C). It is important to notice that, up to now, no one has proven that such low background pressures are neccesary

for deposition of laser active materials in an MBE-system. In HWE systems PbSSe-laser structures with excellent performance /2/ have been grown under vacuum conditions of about $10^{-7}$ mbar, far beyond UHV standard. It has been claimed that, in contrast to the HWE-technique, the MBE-technique is less tolerable as far as background pressure is concerned. However, experimental proof to support this judgement has not been presented yet as far as we know. Independently of the outcome of appropriate experiments, an MBE-system for deposition of lead chalcogenide based compounds should meet UHV-standards. Lead chalcogenide compounds containing rare earth and earth alkali elements will most likely require UHV conditions and these compounds are the ones to close the gap in the laser emission spectra between the more classical lead tin chalcogenide lasers and the III-V-compound lasers.

PbSe and PbS films grown from binary source materials which have been prepared by the procedure described above are always n-conducting ($3 \times 10^{17}$ - $1 \times 10^{18}$ $cm^{-3}$). The stoichiometry of the starting material has no significant effect on the carrier concentration. Carrier concentration and type of conductivity of the deposited films can be controlled by adjusting the deviation of stoichiometry via coevaporation of Se or by intentionally doping with foreign elements.For telluride rich systems, doping with Tl and Bi is the common procedure for growing p- and n-type films, respectively /9/. We prefer a combination of both techniques. Bi is employed for growing n-type films and p-type conductivity is achieved by deposition under Se rich conditions. Doping experiments have shown that Tl is not incorporated as acceptor if coevaporated with PbS and PbSe under typical metal rich deposition conditions in the MBE-system. Films covered with Tl-droplets formed during deposition in high Tl-flux remained n-conducting. This finding is contrary to results of doping experiments in PbTe /9/. In this material Tl forms an acceptor like center in chalcogen rich as well as metal rich matrix. Contrary to Tl Bi is a well behaving efficient n-type dopant in PbS, PbSe, $PbS_{1-x}Se_x$ and $Pb_{1-x}Sn_xSe$. Electron concentrations up to $10^{20}$ $cm^{-3}$ have been obtained in PbSe at a deposition temperature of 400 °C and a PbSe flux rate of $3 \times 10^{-6}$ mbar, a Bi rate of $10^{-7}$ mbar and a Se rate of $10^{-7}$ mbar. Carrier concentrations in the range of $2 - 5 \times 10^{18}$ $cm^{-3}$ require Bi fluxes of $10^{-9}$ mbar. This is the typical doping level of the active regions of our laser structures.

## 3. Laser structures

The work on lead salt laser structures is currently concentrated on lead telluride and lead selenide based systems.

At GENERAL MOTORS several attempts have been made to realize short wavelength lasers selecting quaternary telluride systems whose band gaps are larger than the lead telluride band gap. The experimental results on lead germanium and lead ytterbium

tellurides showed that these systems are less attractive for laser fabrication. Ge containing laser structures could not be prepared, because of the extraordinary small sticking coefficient of Ge. For Yb containing materials a complex doping behaviour has been reported. A DH-laser structure emitting at about 10 µm with an active PbSnTe layer and PbSnYbTe confinement layers operated up to 128 K (cw). The maximum temperature for pulsed operation of this particular laser has not been reported. Although the reported cw temperature is the highest achieved for a 10 µm laser, the temperature exceeds the best values for diffused lasers operating at the same wavelength only slightly. For diffused PbSnSe lasers with Sn contents of 3 % and 7 % we have obtained maximum operation temperatures of 170 and 160 K, respectively, for pulsed operation and of 115 K for continuous operation.

Excellent results have been obtained with lead europium telluride lattice matched DH-laser structures /4/. High operation temperatures up to 190 K for pulsed operation and 147 K for continuous operation have been reported.

Compared with the more sophisticated lattice matched structures realized by GENERAL MOTORS, the DH-Laser fabricated by our group are rather simple. We have prepared three types of structures. Long wavelength laser structures consisting of PbSe confinement layers and an active PbSnSe film. The structure is deposited on a p-type PbSe substrate; The first confinement layer and the active film is Se-doped (p-type) and the upper confinement layer is Bi-doped. The structure with the thinnest active film (0,5 µm) operated up to 190 K for pulsed operation ($I_{th}$ = 5 A) and up to 125 K for continuous operation ($I_{th}$ = 0,5 A). The tuning range was 9.1 to 11.9 µm for cw operation. In a series of structures with different thicknesses of the active layers (0,5, 1, 2, 3 µm) the maximum operation temperature drops steadily down to the temperature typically achieved with diffused lasers (150 K). In Fig. 3 the dependence of threshold current on operation temperature for two of these lasers is shown for pulsed operation. One laser has an active film thickness of 0.5 µm and the other has an 1 µm thick active film. For high temperatures both lasers show almost identical behaviour, but for low temperatures the temperature dependence is markedly different indicating that different loss mechanims are dominating at low temperatures. This behaviour is typical for these two batches.

The second type is an PbS/$PbS_{1-x}Se_x$/PbS-structure ($x \simeq 0.9$) deposited on a p-type PbSe substrate. This laser structure operates up to 210 K in pulsed operation ($I_{th}$ = 5 A) and up to 110 K in continuous operation ($I_{th}$ = 0.35 A). The thickness of the active film was chosen to be 0.5 µm. The dependence of optical output power on laser current and different operation temperatures for one of these lasers is shown in Fig. 4. The full scale intensity corresponds to an output power of approximately 1 mW. The power scale is not linear because of non linear wavelength dependent detector response. In the upper part of Fig. 4 output power versus current curves for a diffused laser are presented.

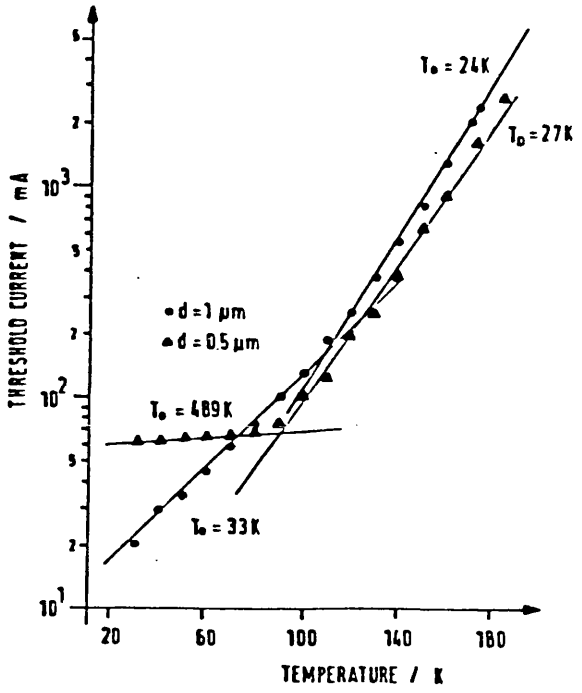


Fig. 3:
Threshold current versus temperature for two $Pb_{1-x}Sn_xSe$ DH-lasers with an active film thickness of 0.5 and 1 µm.

The third structure consists of PbS confinement layers and a quasi-ternary active layer of $(PbS)_{1-x}(SnSe)_x$. The x-value has not been determined explicitly, but from the emission frequency of the laser it can be deduced that the band gap of the active film is approximately 35 meV smaller than the bandgap of the PbS confinement layers. These lasers operate up to 135 K in pulsed and up to 75 K in continuous operation ($I_{th}$ = 0.4 A) and tune from 5.3 to 4.75 µm in the temperature range of 20 to 75 K. The maximum operation temperatures of the short wavelength lasers fall clearly behind the values obtained for the other type of lasers. The step in the refractive index between active layer and confinement layer is most likely to small for sufficient optical confinement.

The results are summarized in table 1:

| laser structure | maximum operating temperature (K) pulse | cw | cw tuning range (µm) |
|---|---|---|---|
| PbEuSeTe-PbEuSeTe-PbEuSeTe | 190 | 147 | 4.93 - 4.06 |
| PbYbSnTe-PbSnTe-PbYbSnTe | ? | 128 | 10.7 - 7.1 |
| PbSe-PbSnSe-PbSe | 190 | 125 | 11.9 - 9.1 |
| PbS-PbSSe-PbS | 210 | 110 | 8.95 - 5.48 |
| PbS-PbSnSeS-PbS | 135 | 75 | 5.3 - 4.75 |

Table 1: Properties of MBE grown DH-lasers

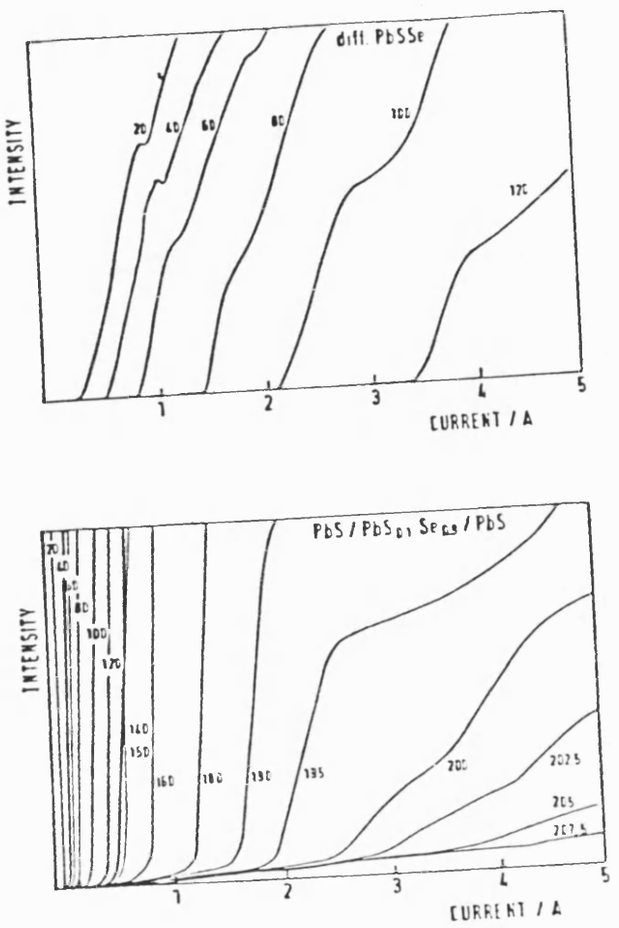


Fig. 4:
Dependence of optical output power of a DH-laser and of a diffused homojunction laser on current for different temperatures indicated in the graphs in degrees K.

## 4. Conclusions

The fabrication of lead chalcogenide laser structures by the MBE-technique is relatively easy. The major constituents and doping materials evaporate at convenient temperatures and the beam fluxes can be controlled. Lattice matched laser structures of the PbTe type and non lattice matched lasers of the PbSe type have been realized. Concerning the highest operation temperatures obtained for the various types of lasers a particular feature of extrem practical importance has to be noticed. Non lattice matched DH-lasers based on PbSnSSe reach higher operation temperatures under pulsed conditions than lattice matched laser structures based on telluride rich systems prepared by the same deposition technique. It should be mentioned that the highest operation temperature (230 K) has been reported for a PbS/PbSe/PbS structure /2/. The lattice mismatch is almost 3 % for this combination. From this fact it certainly cannot be deduced that lattice mismatch is uneffective in the lead sulfide selenide system. However, there is evidence that lattice matching is of minor importance at least in PbSe/PbSnSe/PbSe-structures. In the latter case, the maximum operation temperature increases with decreasing thickness of the active film in the investigated range from 3 to 0.5 μm. This indicates that a non-radiative recombination process at the interfaces is most likely not the dominating loss mechanism. However, more fundamental studies are necessary to clarify this point. For example it is not known whether the mismatch dislocations themselves or only the combination of mismatch dislocations and dopants create an effective non-radiative recombination center. In this context it is worthwhile to notice that in all the laser structures we have fabricated so far it was avoided to dope the interfaces. The pn-junctions have been placed after the first 2000 Å of the confinement film have been deposited undoped. Concerning fabrication of short wavelength lasers, rare earth element containing lead chalcogenide systems are apparently better suited than Ge, Mn or Cd containing systems.

## Acknowledgement

This work is sponsored by the German Ministry for Research and Technology (Contract 13 N 5281). The films and DH-lasers have been prepared with the help of H. BÖTTNER, M. KÖHNE, G. KNOLL, O. PRASSE and N. SCHÄL which is highly appreciated.

## References

1. J.N. WALPOLE, A.R. CALAWA, T.C. HARMAN, and S.H. GROVES: Appl. Phys. Lett. 28, 552 (1976).

2. H. PREIER, M. BLEICHER, W. RIEDEL and H. MAIER: Appl. Phys. Lett. 28, 669 (1976).

3. D.L. PARTIN: J. Vac. Sci. Technol. B1 (2), 174 (1983).

4. D.L. PARTIN: Proceedings of the SPIE conference on "Tunable Diode Laser Development and Spectroscopy Applications", San Diego, August 25 - 26, 1983, Vol. 438, p. 17.

5. H. HOLLOWAY and J.N. WALPOLE, Prog. Cryst. Growth Charac. 2, 49 (1979).

6. R.B. SCHOOLAR, J.D. JENSEN, and G.M. BLACK: Appl. Phys. Lett. 31, 620 (1977).

7. A.V. NOVOSELOVA, V.P. ZLOMANOV, S.G. KARBANOV, O.V. MATVEYEV and A.M. GAS'KOV: Progress in Solid State Chemistry, Vol. 7, eds. H. REISS and J.O. McCALDIN; p. 85 (1972), Pergamon Press.

8. D.L. SMITH and V.Y. PICKARDT: J. Electr. Mat. 5, 247 (1976).

9. D.L. SMITH and V.Y. PICKHARDT: J. Electrtochem. Soc., 125, 2042 (1978).

CONFERENCE B)

# Summary Abstract: Fabrication and properties of PbSe/$Pb_{1-x}Sn_xSe$ DH-laser structures

P. Norton, G. Knoll and K.-H. Bachem

*Fraunhofer Institut für Physikalische Meßtechnik Heidenhofstrasse 8, D-7800 Freiburg, Federal Republic of Germany*

(Received 15 September 1984; accepted 15 October 1984)

PbSe/PbSnSe/PbSe double heterostructure (DH-laser) and PbS/PbSe/PbSnSe/PbSe/PbS localized gain region (LGR)-lasers emitting in the 10 to 16 $\mu$m range, have been fabricated from molecular beam epitaxy (MBE)-grown film structures.

The MBE apparatus is equipped with commercially available evaporation furnaces fitted with Knudsen cells made from graphite. The cells are specifically trimmed to obtain a high beam flux rate stability. This is important because the bandgap of the ternary PbSnSe is very critically dependent on the Sn content.

The deposition of the ternary PbSnSe is relatively easy because of a well-behaving growth mechanism. The binary source materials PbSe and SnSe are simultaneously evaporated to produce $Pb_{1-x}Sn_xSe$. In the temperature range of 350 to 400 °C, the sticking coefficients of PbSe and SnSe are apparently close to unity. This is indicated by the fact that there is an almost one to one relationship between beam flux ratios and composition factor $x$, and total flux rate with growth rate. However, the sticking coefficient is definitely not precisely equal to unity because the composition factor shows a weak deposition temperature dependence for constant flux ratios.

SIMS depth profiles show that the interfaces between films of different compositions are abrupt on a laser device-orientated scale and that the composition through a layer remains constant within the typical SIMS accuracy.

PbSe, PbS, and $Pb_{1-x}Sn_xSe$ films grown on substrates not effecting the stochiometry of the deposit (e.g. $BaF_2$) are always $n$-type ($3\times10^{17}$–$10^{18}$ $cm^{-3}$) indicating metal-rich growth conditions. In this respect these materials behave similarly to the PbTe system.[1] However, contrary to the PbTe system, lead precipitation has never been observed.

Films deposited on $p$-type PbSe substrates convert to $p$-type conductivity even if they are deposited under metal-rich conditions due to the high diffusivity of Pb vacancies moving from the substrate into the growing film. By taking advantage of this behavior, only one foreign $n$-type dopant is necessary to produce a $p$-$n$ junction. Bismuth has been chosen because of its small diffusivity and high doping efficiency. Electron concentrations up to $10^{20}$ $cm^{-3}$ in PbSe at a substrate temperature of 400 °C for a flux rate ratio Bi:PbSe of 1 : 30 have been achieved. Typical doping levels for laser structures require a ratio of approximately 1 : 3000 which is still within limits of control.

The structures have been grown upon chemically polished $p$-type PbSe substrates ($2$–$5\times10^{18}$ $cm^{-3}$). The first confinement layer and active film are not intentionally doped and are, therefore, $p$ type for reasons explained above. The upper confinement film is doped $n$ type with Bi.

PbSe/$Pb_{1-x}Sn_xSe$/PbSe laser structures have been fabricated with confinement layers of 3 $\mu$m thickness on either side of active layer regions of thicknesses ranging from 3 to 0.5 $\mu$m. The maximum operating temperaures of these lasers increases with decreasing active layer thickness. For the thinnest active film, maximum operating temperatures of 190 and 130 K have been obtained for pulsed and continuous operation, respectively.

At high operating temperatures, the threshold current decreases with decreasing active layer thickness as expected. However, at low temperatures (20–70 K) the threshold current of the device with the thinnest active region, remains surprisingly constant on a value higher than that obtained for the devices with thicker active regions. This suggests that in this device a new loss mechanism is controlling the threshold current/temperature dependence. Amongst different explanations for this low temperature behavior, it was speculated that optical wave guidance is becoming inefficient because of the increasing emission wavelength with decreasing operation temperature.

To improve the low temperature guiding for films even thinner than 0.5 $\mu$m, we have added additional outer optical confinement layers of PbS. This structure, commonly named a localized gain region (LGR) structure, consists of a 0.25 $\mu$m thick $Pb_{1-x}Sn_xSe$ film imbedded into a 1 $\mu$m thick PbSe film and cladded by optical confinement PbS layers of 3 $\mu$m thickness. Contrary to our expectations this laser exhibited an even more mysterious low temperature threshold current/temperature dependence. The threshold current of this device decreases strongly with increasing temperature, passes through a pronounced minimum located at 110–130 K, followed by the increasing high temperature branch.

In addition to this strange characteristic, laser emission occurs at two distinct frequencies corresponding to the composition of the active film and to the PbSe wave guide. This behavior suggests that at low temperatures only a small fraction of the injected carriers become trapped in the potential well formed by the active film. The majority of the injected carriers are swept across the active region and recombine in the PbSe wave guide behind the active film. This effect is a low temperature effect because at high temperatures the enhanced electron/phonon interaction eases the capture of the injected carriers into the well.

Although these structures are not lattice matched, the operation temperatures obtained are higher than those reported for lattice-matched PbSnTe–DH structures emitting in the same wavelength region.[2] The problems arising from inefficient carrier entrapment at low temperatures can be surmounted by replacing the plain PbSe wave guide by a

 0734-211X/85/020782-02$01.00  

$Pb_{1-x}Eu_xSe$ film having a funnel-shaped bandgap profile in the middle of which the active layer is located. For this type of laser, cw operation has been obtained up to 163 K. Details of these laser structures will be reported elsewhere.

[1]H. Holloway and J. N. Walpole, Prog. Cryst. Growth Charact. 2, 49 (1979).
[2]D. Kasemset, S. Rotter, and C. Fonstad, J. Electron. Mater. 10, 863 (1981).

PUBLICATION C)



# EPITAKTISCHE IV-VI-SCHMALBANDHALBLEITER-SCHICHTEN AUF Si FUER IR-SENSORSYSTEME

H. Zogg, ETH Hönggerberg, HPT, CH-8093 Zürich
P. Norton, Fraunhofer-Institut für phys. Messtechnik, D-7800 Freiburg i. Br.

Zusammenfassung : Bleichalkogenidschichten wurden mit MBE (MolekularStrahl-Epitaxie) bzw. HWE (HeissWand-Epitaxie) und mittels einer MBE-$(Ca,Ba)F_2$ Zwischenschicht auf (111)Si abgeschieden. Wir berichten über die strukturellen und elektronischen Eigenschaften solcher Schmalbandhalbleiter-Schichten. Die Zusammensetzungen (Bandlücken) der Bleichalkogeniden wurden dabei so gewählt, dass die Grenzwellenlängen darin hergestellter IR-Sensoren den atmosphärischen 3-5 µm- bzw. 8-14 µm Fenstern angepasst sind. Damit wird die Herstellung von monolithischen Sensorsystemen für Wärmebildkameras möglich mit photovoltaischen IR-Sensoren im Bleichalkogenid und aktiven Schaltungen (Multiplexierung, Verstärkung) im Si-Substrat.

Einleitung : Epitaktische IV-VI Schmalbandhalbleiterschichten werden seit etwa 1970 mit HWE oder MBE auf (111)-Oberflächen von $BaF_2$-Einkristallen aufgewachsen und darin photovoltaische IR-Sensoren fabriziert. Mit den Zusammensetzungen (Pb,Sn)Se, Pb(S,Se) und (Pb,Sn)Te kann der Bandabstand kontinuierlich zwischen ca. 0.3 eV und <0.1 eV, entsprechend Grenzwellenlängen von <3 µm bis >15 µm der IR-Detektoren, eingestellt werden [1,2]. Der Gitterfehler zwischen $BaF_2$ und Bleichalkogenid beträgt weniger als 5% und ist nicht kritisch für erfolgreiches Wachstum.

Einkristalline $BaF_2$(111) Schichten können auch auf Si(111) Substraten mit MBE abgeschieden werden, wobei die Gitterkonstante des $BaF_2$ um 14% grösser als die des Si ist. Eine dünne $CaF_2$ Zwischenschicht dient dabei der Gitteranpassung an der Si Grenzfläche [3,4].

Auf diese $(Ba,Ca)F_2$/Si Substrate haben wir erstmals hochqualitatives epitaktisches PbSe [3,5] abgeschieden. In dieser Arbeit berichten wir über die Eigenschaften von PbTe und $Pb_{0.96}Sn_{0.04}Se$ auf $(Ba,Ca)F_2$/Si. Erste IR-Sensoren wurden in diesen Schichten bereits realisiert, welche Grenzwellenlängen von 5.8 µm (PbTe) und 9.7 µm ($Pb_{0.96}Sn_{0.04}Se$) bei 87K aufweisen und deren Empfindlichkeit nahe dem Photonenrauschen (für 295K Hintergrundstrahlung und $180^o$ Blickwinkel) liegen [6].

Herstellung : PbTe und PbSe wurden mit HWE in Schichtdicken von einigen µm bei ca. 400°C abgeschieden. Zur Herstellung von (Pb,Sn)Se Schichten wurde die MBE Anlage am Fraunhofer IPM in Freiburg i.Br., welche primär für die Epitaxie hochdotierter Schichten für IV-VI Laserdioden eingerichtet ist, verwendet. Dank separaten PbSe- unbd SnSe- Quellen in dieser Anlage ist eine genaue Kontrolle des Pb/Sn Verhältnis, welches die Bandlücke bestimmt, möglich. Wird nur mit binären Quellen gearbeitet, resultieren sowohl mit MBE als auch mit HWE n-Typ Schichten, während durch Mitverdampfen des entsprechenden Chalkogens Se oder Te die Ladungsträgerkonzentration nach p-Typ verschoben wird. Für die Herstellung von IR-Sensoren nach unserer Schottkydiodentechnik werden p-Typ Schichten benötigt.

Mikrostrukturen und mechanische Spannungen : Glatte Oberflächen mit gelegentlichen Fehlern resultierten in n-Typ Schichten ohne zusätzliche Chalkogenverdampfung. Röntgenographische Gitterkonstantenbestimmungen an PbSe Schichten ergaben Werte, die innerhalb der Messgenauigkeit ($<10^{-3}$) mit den Gleichgewichtswerten übereinstimmten. Mechanische Spannungen, die auf Grund der ca. 7 mal höheren thermischen Ausdehnung der Bleichalkogenide (und auch $(Ca,Ba)F_2$) gegenüber Si beim Abkühlen auftreten sollten, sind demnach weitgehend relaxiert. Wurden die Proben etwas erwärmt, verschoben sich die Röntgenlinien sofort (d.h. innerhalb der wenigen Minuten dauernden Messvorbereitung) zu den der Gitterkonstanten bei der aktuellen Probentemperatur entsprechenden Gleichgewichtslagen. Dies lässt auf athermische Relaxation des PbSe schliessen. Zusätzlich unterstützt wird diese Annahme durch Interferenzkontrastmikroskopie: Parallele Linienmuster wurden in den drei [110]-Richtungen beobachtet, die offenbar Gleitstufen im {100}[110] Gleitsystem der Bleichalkogenide entsprechen und beim Abkühlen der Proben von der Wachstumstemperatur entstanden sind.

Wird bei der Epitaxie der Chalkogen-Dampfdruck zur Herstellung von p-Typ Schichten erhöht, so wird für Schichten auf massiven $BaF_2$ Einkristallen die Qualität nicht verändert. Dies war auch für HWE-PbTe Schichten auf $(Ca,Ba)F_2$/Si mit zusätzlicher Te Quelle der Fall. Bei Se-haltigen Materialien auf $(Ca,Ba)F_2$/Si trat dagegen eine drastische Verschlechterung der Schichtqualität auf: Blasen von einigen µm Durchmessern, die sich quer durch die gesamte Schicht inklusive $(Ca,Ba)F_2$ ausdehnten, bedeckten mindestens Teile der Oberfläche [3]. Unterhalb weggeplatzten Blasen war mit der Mikrosonde ausser Si nur etwas Se, aber kein Pb oder Ba, nachweisbar. Ursache dieser

Blasen sind wahrscheinlich durch Fehler in der $(Ca,Ba)F_2$ Schicht bis zur Si-Oberfläche durchdiffundierte Se-Atome mit anschliessender Si-Se Oberflächenreaktion, die sich verheerend auf die Schichthaftung auswirkt. Wurde in der MBE Apparatur der zusätzliche Se-Fluss erst nach etwa 1 µm Schichtwachstum eingeschaltet, blieb die auch während der Epitaxie beobachtbare Schicht anfänglich noch völlig spiegelnd. Erst nach einer gewissen weiteren Wachstumszeit, die in grober Uebereinstimmung mit Se-Diffusionszeiten durch den ohne zusätzlichen Se-Fluss gewachsenen Teil der Schicht ist, traten Blasen (sichtbar als makroskopische Aufrauhung der Oberfläche) auf. Diese Gebiete waren vorerst an "Schwachstellen" des Substrates lokalisiert, z.B. am aufliegenden Rand der Schattenmaske oder an der eingeritzten Substratbezeichnung, und breiteten sich allmählich über die ganze Probe aus. Die Blasen entstehen also bereits während des Schichtwachstums. Sie können durch folgende Effekte verursacht sein: Hohe Kompressionsspannungen während des Wachstums (grössere Gitterkonstante von $BaF_2$ gegenüber Si!) lassen die Schicht um Schwachstellen des Substrates in Blasen aufwölben; oder Reaktionsprodukte der Si-Se Oberflächenreaktion erzeugen einen lokalen Gegendruck mit dem selben blasenbildenden Effekt. Im Rasterelektronenmikroskop direkt beobachtete Gleitstufen an solchen Blasen sind Zeugen von hohen mechanischen Spannungen, die mindestens zeitweise geherrscht haben müssen.

Hallbeweglichkeiten : Mit HWE hergestellte n-PbSe [3] sowie PbTe Schichten auf $(Ca,Ba)F_2/Si$ weisen ebenso hohe Hallbeweglichkeiten wie massive Einkristalle auf (Fig. 1). Typische Werte guter Proben liegen bei 1000 $cm^2/Vsec$ bei RT, steigen mit approximativ $T^{-5/2}$ mit sinkender Temperatur T an (akustische Phononenstreuung mit temperaturabhängigem Bandabstand) und sättigen oberhalb $10^5$ $cm^2/Vsec$ (Verunreinigungsstreuung). Mit MBE hergestellte Schichten wiesen dagegen eine 2-5 mal kleinere Beweglichkeit auf (Fig. 2), und zwar sowohl für auf $(Ca,Ba)F_2/Si$ als auch auf massivem $BaF_2$ hergestellte Schichten. Wir vermuten deshalb, dass diese verkleinerten Werte durch die noch nicht optimierte Wachstumsprozedur der wenigen bisher mit MBE hergestellten Schichten verursacht sind. Weiter wurden p-Typ Proben, die für die Sensorherstellung vorgesehen waren, zur Vermeidung der Blasenbildung inhomogen hergestellt, indem die Se-Quelle erst während der zweiten Hälfte des Schichtwachstums eingeschaltet wurde. Die unvollständige Homogenisierung der Ladungsträgerkonzentration über die Schichtdicke wurde in der Berechnung der Hallwerte nicht berücksichtigt. Diese etwas kleineren Hallbeweglichkeiten sind

jedoch für Substrate, die für die Herstellung von IR-Sensoren benutzt werden, mindestens bei unserem jetzigen Stand der Entwicklung, ohne Bedeutung [1,6].

Den Herren Prof. Melchior und Prof. Baumgartner, ETH Zürich, sei an dieser Stelle für die Förderung der vorliegenden Arbeit herzlich gedankt. Die MBE Anlage konnte dank dem grosszügigen Entgegenkommen von Herrn Dr. Preier, Fraunhofer Institut für phys. Messtechnik, Freiburg i.Br., benutzt werden, wofür wir ebenfalls unseren besten Dank aussprechen. Weiter danken wir Herrn P. Waegli, ETH Zürich, für die zahlreichen Untersuchungen am Rasterelektronenmikroskop. Die Gruppe für Rüstungsdienste, Bern, hat das Projekt finanziell unterstützt.

Referenzen

[1] H. Holloway, Physics of Thin Films 11, 103, 1980.
[2] A.C. Bouley, T.K. Chu, G.M. Black, Proc. SPIE 285, 26,1981.
[3] H. Zogg, M. Hüppi, Appl. Phys. Lett. 47, 133, 1985.
[4] H. Zogg, M. Hüppi, P. Maier, R. Knobel, SPG Tagung Okt. 1985, dieser Band.
[5] H. Zogg, W. Vogt, H. Melchior, Infrared Phys. 25, 333, 1985.
[6] H. Zogg, P. Norton, Technical Digest, Int. Electron Device Meeting IEDM, Washington D.C. Dec. 1985, im Druck.

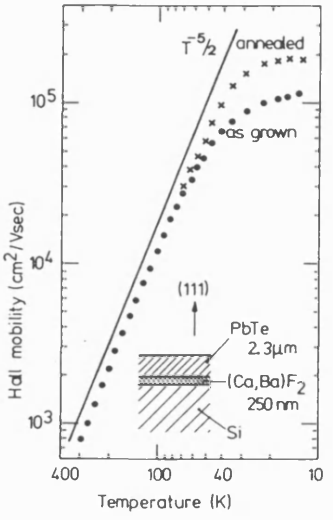


Fig.1: Hallbeweglichkeit von epitaktischem n-PbTe ($n=2.6\cdot10^{17}$ $cm^{-3}$) auf (Ca,Ba)$F_2$/Si

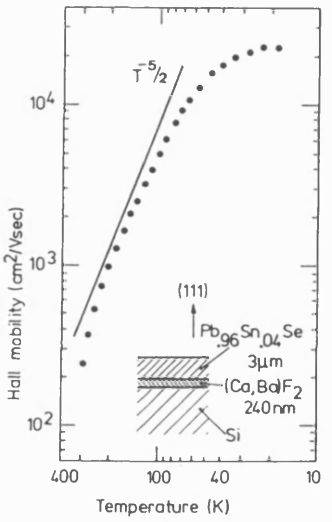


Fig.2: Hallbeweglichkeit von epitaktischem p-(Pb,Sn)Se ($p=2\cdot10^{17}cm^{-3}$ auf (Ca,Ba)$F_2$/Si

Mat. Res. Soc. Meeting, Boston 1985, Dec. 2-7

Preprint CONFERENCE D)

# MBE GROWTH OF NON-LATTICE MATCHED (Ba,Ca)$F_2$, (Pb,Sn)Se/(Ba,Ca)$F_2$ AND CdTe/(Ba,Ca)$F_2$ ON Si SUBSTRATES

H. ZOGG, P. MAIER and P. NORTON*
Swiss Federal Institute of Technology, AFIF, CH-8093 Zürich, Switzerland
*Fraunhofer Institut f. phys. Messt., D-7800 Freiburg, Fed. Rep. of Germany

ABSTRACT

Graded (Ca,Ba)$F_2$ layers consisting of near lattice matched $CaF_2$ at the Si interface and of $BaF_2$ with 14% increased lattice constant at the top surface were grown by molecular beam epitaxy (MBE) on Si(111). Smooth and crackfree layers exhibiting Rutherford backscattering (RBS) channeling minima below 5% were obtained. Device quality epitaxial layers of PbTe, PbSe and (Pb,Sn)Se were grown on top of these structures. Mechanical stress at 300K was relaxed by athermal mechanisms in the fluoride- as well as in the Pb-salt films. - In preliminary runs, epitaxial CdTe-layers were obtained on Si(111) using the same fluoride-buffer film technique and which showed clear SEM electron channeling patterns.

## INTRODUCTION

Since the first publications on MBE of IIa-fluorides [1,2], high quality layers of these insulators have been grown on an increasing number of semiconductor materials. Due to the unique complete miscibility of the $CaF_2$-$SrF_2$ and $SrF_2$-$BaF_2$ sequence, a close lattice match can be achieved for most of the semiconductors commonly used for device applications (Fig. 1). Compound structures like GaAs/(Ca,Sr)$F_2$/GaAs [3], Si/$CoSi_2$/$CaF_2$ [4], or Si/$CaF_2$/Si [5-7] have also been prepared having in mind possible vertical integration or insulation in 3-dimensional IC-applications.

Most of these structures reported to date consist of binary or mixed fluorides with a more or less close lattice match to the substrate, but with constant compositions of the fluoride layer.

However, a variety of more general applications becomes feasible by grading the composition of the fluoride layers across their thickness in a manner, that lattice match at the interface to both the bottom- and the top epitaxial semiconductor is obtained. This has been found to be possible even over the extreme range of compositional tunability with $CaF_2$ (a=0.54 nm) and $BaF_2$ (0.62 nm) as end-members at the opposite interfaces, thus providing a link for up to 14% lattice mismatch [8]. The two semiconductors connected by the fluoride buffer may therefore have very different latttice constants and may belong to different systems.

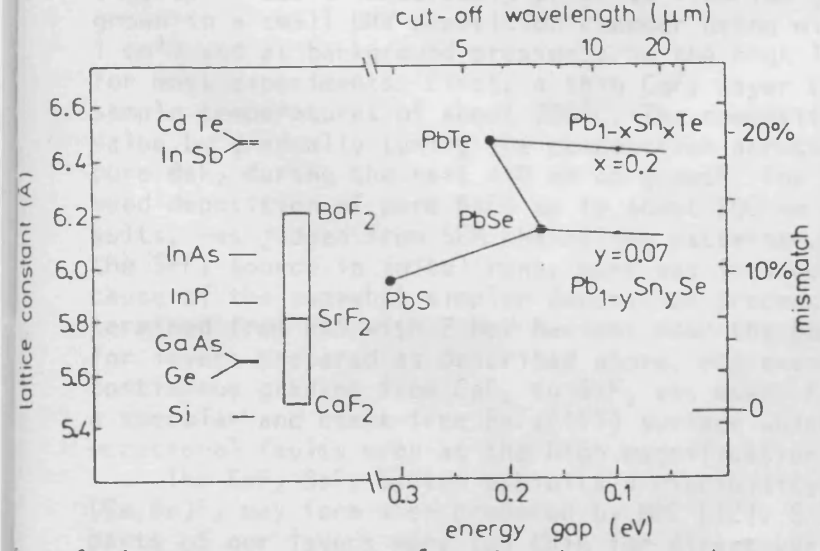


Fig. 1. Lattice constants of semiconductors and IIa-fluorides, and band gap values of Pb-chalcogenides. Miscibility is indicated by solid lines.

The technique has been applied for the first time in Si/(Ca,Ba)$F_2$/PbSe structures [8,9] with lattice mismatches at the interfaces to the Si and PbSe of 0.6% and 1.3% at room temperature, respectively, and with the rest of the mismatch accommodated in the graded part

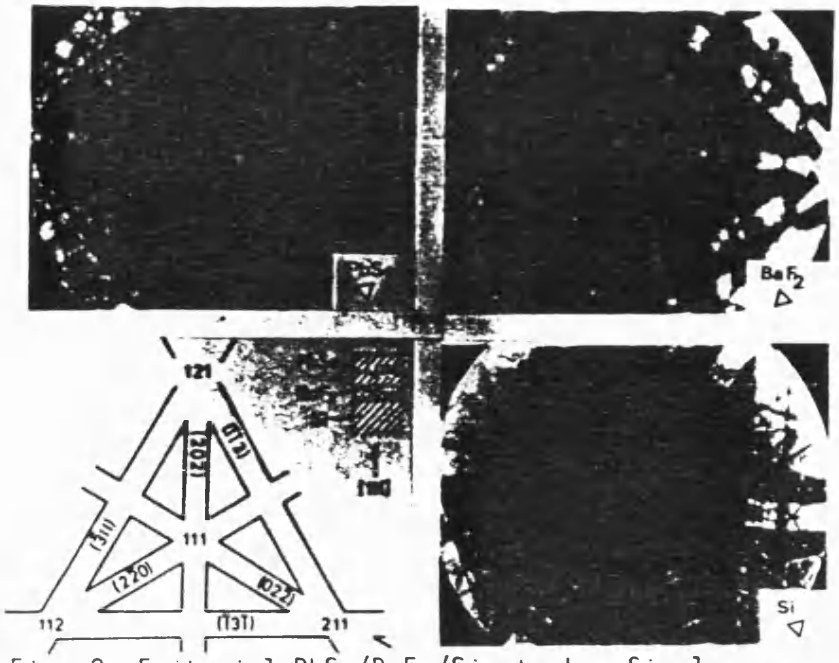


Fig. 2. Epitaxial PbSe/$BaF_2$/Si stacks. Single crystal SEM electron channeling patterns of Si, $BaF_2$ and PbSe surfaces, and schematic drawing of the most important reflection bands. Note the twinned lattice orientations of succeeding layers.

of the fluoride buffer layer. Fig. 2 shows electron channeling patterns illustrating the single crystal nature of such structures. As is well known with bulk $BaF_2$ [10], MBE grown $BaF_2$ surfaces also form suitable substrates for epitaxial narrow gap Pb-chalcogenides. Photovoltaic IR-sensors on Si suited for operation in the 3-5 or 8-12 um atmospheric window have recently been demonstrated by using this technique and with PbTe or (Pb,Sn)Se for the top layer [11]. This offers promising applications for IR-optoelectronics like IR-focal plane arrays for thermal imaging applications with signal multiplexing and preamplification circuitry integrated in the Si substrate.

For further applications requiring less lattice mismatch accommodation or other substrate materials than Si, graded fluoride buffers with mixed end compositions within the $CaF_2$-$SrF_2$-$BaF_2$ sequence may be used. Mixed fluorides with adequate quality and various constant compositons have already been grown by different groups [3,7,12], and, as will be shown below, graded parts in such layers do not seem to deteriorate their quality.

## EXPERIMENTAL Si(111)-$CaF_2$-$BaF_2$ SEQUENCES

Si(111) wafers were cleaned either in hot $HNO_3/H_2SO_4$ with subsequent oxide removal in HF or by growing a volatile oxide which was removed by in situ heating up to 850°C immediately prior to fluoride growth. Fluoride layers were grown in a small UHV deposition chamber using miniature Ta- or C-crucibles (0.1-1 $cm^3$) and at background pressures in the high $10^{-8}$ mbar range during deposition for most experiments. First, a thin $CaF_2$ layer (≈1-10 nm) was deposited at sample temperatures of about 700°C. The composition was then graded to the $BaF_2$ value by gradually tuning the composition across the $CaF_2$-$SrF_2$-$BaF_2$ sequence to pure $BaF_2$ during the next ≈10 nm of growth. The layers were terminated by continued deposition of pure $BaF_2$ up to about 200 nm thickness. Since comparable results, -as judged from SEM channeling patterns-, were obtained even by omitting the $SrF_2$ source in inital runs, work was focused on the $CaF_2$-$BaF_2$ sequence because of the somewhat simpler deposition procedure. $X_{min}$ values below 5%, as determined from RBS with 2 MeV He-ions near the $BaF_2$ surface, were obtained [9,13] for layers prepared as described above, and even if an abrupt transition without continuous grading from $CaF_2$ to $BaF_2$ was used. Fig. 3 shows a micrograph of such a specular and crack-free $BaF_2$(111) surface which appears smooth apart from some occasional faults even at the high magnification used.

The $CaF_2$-$BaF_2$ System exhibits a miscibility gap, but metastable mixed $(Ca,Ba)F_2$ may form when prepared by MBE [12]. Since the continuously graded parts of our layers were too thin for direct verification of a true $(Ca,Ba)F_2$ lattice, some layers with mixed $(Ca,Ba)F_2$ compositions up to the outer surfaces were grown at 600°C. These layers consisted of two phases with lattice constants of the $BaF_2$-rich part corresponding to the value at the equilibrium

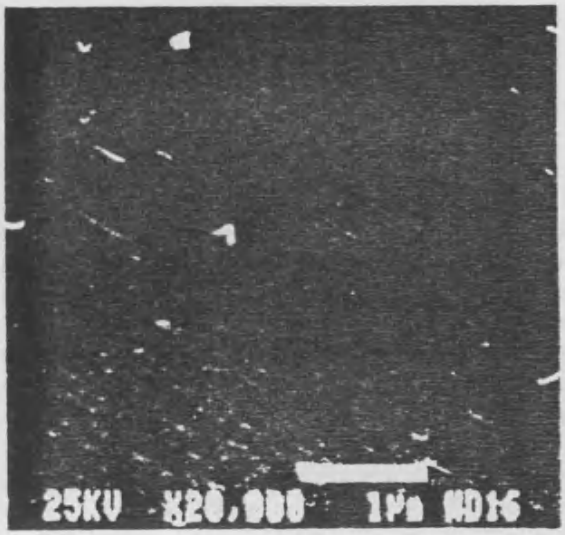


Fig. 3. SEM micrograph of epitaxial $BaF_2$-$CaF_2$ on Si(111).

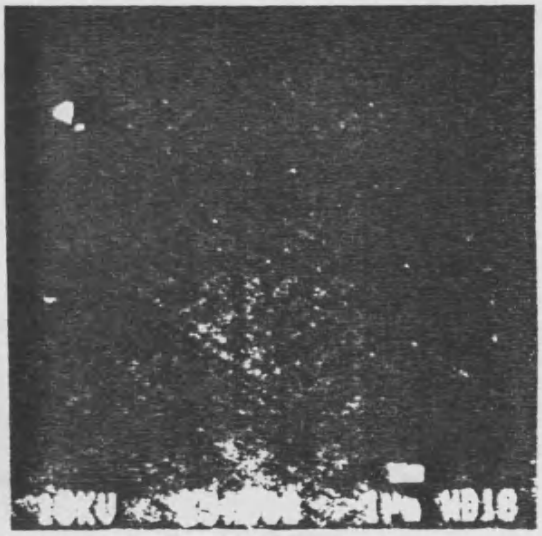

Fig. 4. SEM micrograph of epitaxial PbSe on $BaF_2$-$CaF_2$ on Si(111).

miscibility gap. A considerable part of the Ba and Ca is diffused towards the surface or Si-interface, respectively, leading to a Ba enrichement near the outer surface. It therefore does not seem likely that the thin graded parts terminated with pure $BaF_2$ form a true metastable phase under our deposition conditions. Metastable $(Ca,Ba)F_2$ would possibly result at lower growth temperatures and "cleaner" environement. However, if a continuos grading is desired, the $CaF_2$-$SrF_2$-$BaF_2$ sequence offers an alternative.

According to RBS channeling data along <110> and <114> directions and SEM channeling patterns, it was concluded that most of our layers consisted of predominantely type B orientation (i.e. with the lattice rotated 180° about the normal to the <111>surface compared to the Si lattice). RBS- and SEM-channeling, however, are unsuited to detect small amounts of type A (with the same lattice orientation as the substrate) grains in a B-matrix. By simple X-ray diffraction (XRD) with $CuK\alpha$ radiation at (440)-planes, an up to 10 fold increased sensitivity for twin detection was achieved: Bragg reflections of such planes occur with 3-fold symmetry every $(2n)\cdot 60^0$ (n=1,2,3) angle when the sample is rotated around an axis normal to the <111>surface (with the detector held fixed) if one type of orientation only is present. Additional reflections occur at $(2n+1)\cdot 60^0$ from twinned parts. The ratio of the intensities of the two sets of reflections provides an estimate of the volume ratio of the two types of orientations. In fact, a large fraction, but not all, of our graded layers consisted of pure type B, with type A fraction below 2% (XRD sensitivity limit), but some layers exhibited up to 15 % type A grains in the B matrix although they were prepared using similar procedures. This 15%-amount of A-orientations remained undetected in SEM- or RBS-channeling. The origin of these irreproducibilities seems to be related to the first stages of growth and depends on details of the experimental conditions which are not fully understood at present.

## PbTe AND (Pb,Sn)Se ON $BaF_2$-$CaF_2$-Si(111)

PbTe and PbSe with up to a few um thickness were grown by HWE (hot wall epitaxy) at about 400°C. To grow (Pb,Sn)Se, MBE was employed because of the much better control of the Sn/Pb ratio which determines the bandgap [11,13]. Binary source materials were used with an additional chalcogen source for tuning the carrier concentrations from the high $10^{17}/cm^3$ n-range (with the source shut off) to p-type with increasing chalcogen source temperature. Fig. 4 shows a micrograph of the specular surface of a PbSe layer. Bulklike Hall mobilities were obtained over the whole 300K to 10K range, increasing from about 1000 $cm^2$/Vsec at 300K up to $3\cdot 10^5$ $cm^3$/Vsec below 20K for PbTe and n-type PbSe [9,13].

With the additional Se-source switched on, an unexpected phenomenon occured which is not observed when growing on bulk $BaF_2$(111) or n-type layers on (Ba,Ca)$F_2$/Si: Blisters up to about 10 um in diameter cover parts of the surface (Fig. 5). They are formed during growth, bow up and some of them crack away together with the fluoride buffer layer so that further growth at these areas is polycrystalline. The glide planes visible at the bowed parts are indicative of plastic deformation during growth. The origin of these blisters is most probably due to Se which has diffused through faults in the fluoride layer. This caused a reaction with the Si-surface that either developed gases causing bow out or that caused an area of decreased adhesion with subsequent separation because of possible compressive stresses during growth. However, only about 1/100 of a monolayer of Se from the additional source impinges on the sample during growth of a 1 um thick film. The density of the blisters was only weakly dependent on the growth conditions, but decreased with improved quality of the fluoride layers in the course of further development. Such blisters were observed only in PbSe and (Pb,Sn)Se with additional elemental Se-deposition, but not in n- or p-type PbTe.

## MECHANICAL STRESSES

Since the thermal expansion coefficients of the IIa-fluorides and of the Pb-chalcogenides ($\cdot 2 \cdot 10^{-5}$/K at RT) are about 7 times larger than the values for Si, mechanical stresses have been expected to occur when the sample was cooled down to RT after growth, in addition to those possibly built in during growth [9,11]. Strains in the layers have therefore been determined using different methods.

RBS channeling angular scans around <111>- and <110>-directions were recorded for ≈200 nm thick fluoride layers. The angle between these two directions is 35.26° in an unstrained cubic lattice. If the layers are strained, the resulting tetragonal distortion of the fluorite lattice manifests itself by a changed angular position of the channeling minimum of the Ba-signal compared to that of Si. Fig. 6 shows that a possible displacement of the two curves is below our measurement accuracy of about 0.05°, corresponding to a strain below 0.2%.

XRD determinations of the lattice plane spacings perpendicular to the surface were performed for fluoride- as well as for PbSe-layers. Again, a possible tetragonal distortion was below ≈0.1% of the lattice constant (accuracy limit). Furthermore, when heating the sample up to about 100°C in a heating stage of the Diffractometer, the positions of the Bragg reflections shifted immediatly (i.e. faster than it was possible to determine the line positions) to the new equilibrium values for bulk material as if no mechanical constraints from the Si-substrate were present.

We conclude that stress relaxation is therefore not thermally activated for


Fig. 5. Blisters in p-PbSe. These blisters are due to faults in the fluoride layer and occur in PbSe and PbSnSe only if additional elemental Se is deposited

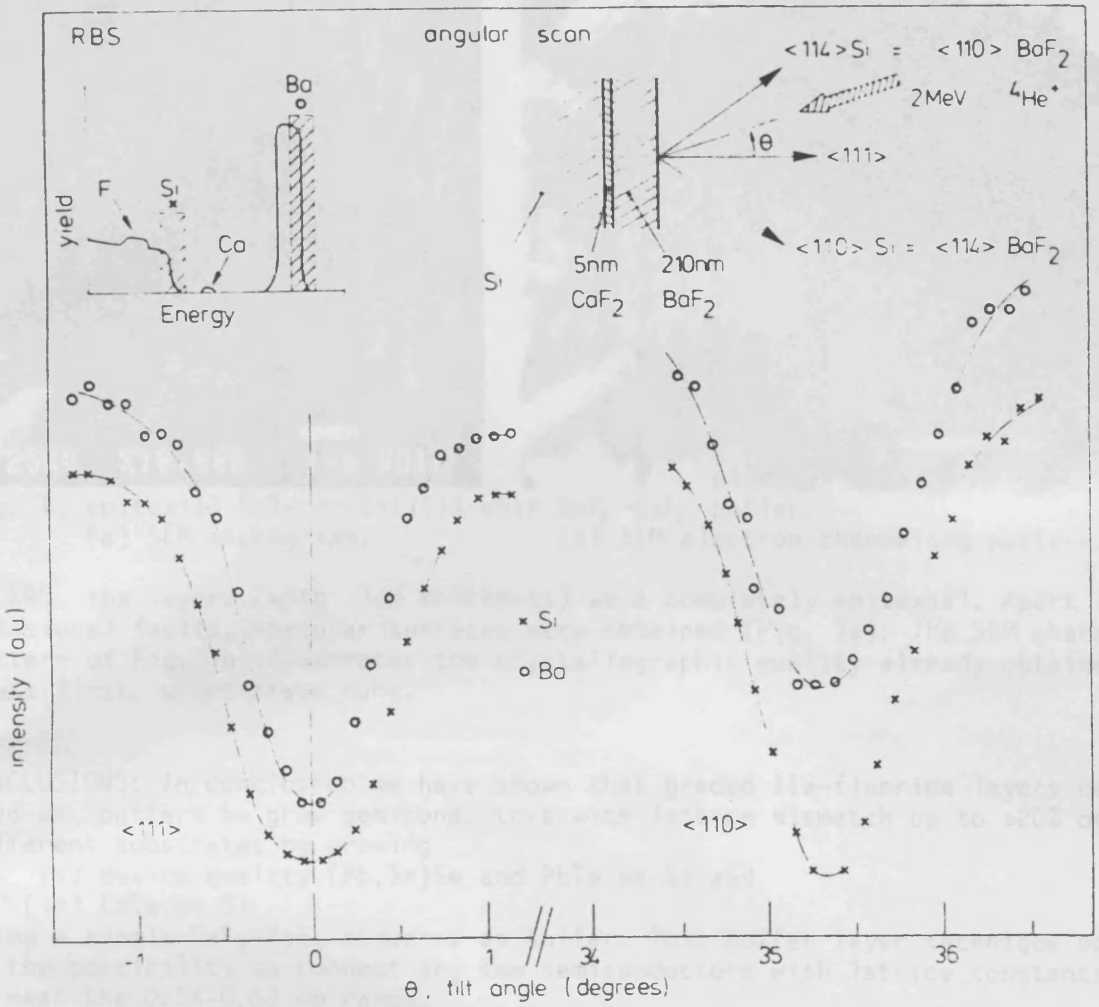


Fig. 6. RBS angular scans around <111>- and <110>-lattice directions showing no measurable tetragonal distortion. Note that the ordinate scales are not normalised and different for each curve.

epitaxial PbSe as well as for $BaF_2$ layers. The lines in the SEM micrograph of PbSe in Fig. 4 (which was taken at reduced beam voltage and glancing incidence to enhance the surface topography contrast) are parallel to <110>-directions and can be interpreted as slip traces of the {100}<110> slip system of the Pb-chalcogenides. The same lines were observed in PbTe and (Pb,Sn)Se layers.

Probably, slip near room temperature is responsible for the stress relaxation in $BaF_2$, too. $BaF_2$ is known to be softer than $CaF_2$, but complete stress relaxation in $CaF_2$ layers on Si has been observed very recently if their thickness was above 250 nm [15].

## EPITAXIAL CdTe ON $BaF_2$-$CaF_2$-Si(111)

Epitaxial CdTe on Si would open the door to the important HgCdTe system for IR- and optoelectronic applications, but with the possibility to use the Si-substrates for signal processing on a VLSI basis. As indicated in Fig. 1, the lattice constant of CdTe lies somewhat above the range covered by the IIa-fluorides. However, as CdTe has been grown on rather large mismatched substrates like GaAs and shows a "self healing" tendency with increasing growth away from the interface, an exact lattice match does not seem to be an unavoidable prerequisite for growth of high quality layers.

In preliminary experiments, we have deposited CdTe onto Si using the same graded $CaF_2$-$BaF_2$ buffer technique as described above. CdTe was then evaporated

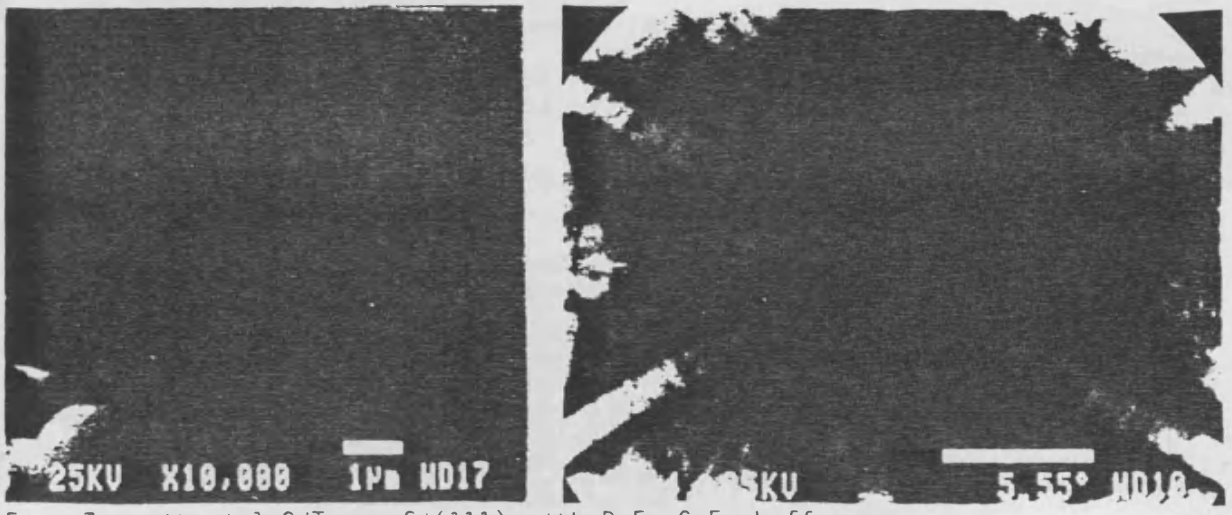


Fig. 7. epitaxial CdTe on Si(111) with $BaF_2$-$CaF_2$ buffer.
(a) SEM micrograph, (b) SEM electron channeling pattern.

to XRD, the layers (with 1um thickness) were completely epitaxial. Apart from occasional faults, specular surfaces were obtained (Fig. 7a). The SEM channeling pattern of Fig. 7b illustrates the crystallographic quality already obtained in these first, unoptimised runs.

CONCLUSIONS: In conclusion we have shown that graded IIa-fluoride layers can be used as buffers to grow semiconductors with lattice mismatch up to ≈20% on different substrates by growing

(i) device quality (Pb,Sn)Se and PbTe on Si and
(ii) CdTe on Si

using a simple $CaF_2$-$BaF_2$ sequence as buffer. This buffer layer technique opens up the possibility to connect any two semiconductors with lattice constants in or near the 0.54-0.62 nm range.

Mechanical stresses possibly resulting from the different thermal expansions of the layers and substrate have been found to be relaxed in $BaF_2$ as well as in Pb-salt films.

ACKNOWLEDGEMENTS: The authors wish to thank Dr. Pixley, Dr. Stüssi and Dr. Nobel for the kind help to use their RBS-apparatus, W. Vogt for growth of PbSe and P. Wägli for the skilled application of the SEM. This work was sponsored by the Swiss Defense Technology and Procurement Agency.

[1] R.F.C. Farrow, P.W. Sullivan, G.M. Williams, G.R. Jones, D.C. Cameron, J. Vac. Sci. Technol. 19, 415, 1981.
[2] T.Asano, H. Ishiwara, Jap. J. Appl. Phys. Suppl 21-1, 187, 1982.
[3] S. Siskos, C. Fontaine, A. Munoz-Yague, J. Appl. Phys. 56, 1642, 1984.
[4] J. M. Phillips, W. M. Augustynjak, Proc. Mat. Res. Soc. Meeting, Boston, Dec. 1985, to be published.
[5] T. Asano, Y. Kuriyama, H. Ishiwara, Electron. Lett. 21, 386, 1985.
[6] H. Onoda, T. Katoh, N. Hirashita, M. Sasaki, Techn. Digest IEDM, Washington D.C. Dec. 1985, p. 680.
[7] L.J. Schowalter, R.W. Fathauer, AVS nat. Symp., Nov. 1985, to be published.
[8] H. Zogg, W. Vogt, H. Melchior, Infrared Phys. 25, 333, 1985.
[9] H. Zogg, M. Hüppi, Appl. Phys. Lett. 47, 133, 1985.
[10] H. Holloway, Phys. Thin Films 11, 105, 1981.
[11] H. Zogg, P. Norton, Techn. Digest IEDM, Washington D.C. Dec. 1985, p. 121.
[12] P.W. Sullivan, R.F.C. Farrow, G.R. Jones, J. Cryst. Growth 60, 403, 1982.
[13] H. Zogg, W. Vogt, H. Melchior, Proc. SPIE 587, to be published.
[14] H. Zogg, P. Maier, M. Ospelt, Thin Solid Films 129, 329, 1985.
[15] S. Hashimoto, J.-L. Peng, W.M. Gibson, L.J. Schowalter, R.W. Fathauer, Appl. Phys. Lett. 47, 1071, 1985.

PUBLICATION E)

Reprinted from IEDM — INTERNATIONAL ELECTRON DEVICES MEETING, Washington, D.C., December 1-4, 1985

# HETEROEPITAXIAL PbTe-Si AND (Pb,Sn)Se-Si STRUCTURES FOR MONOLITHIC 3-5 μm AND 8-12 μm INFRARED SENSOR ARRAYS

H. Zogg and P. Norton*

Swiss Federal Institute of Technology
CH-8093 Zürich, Switzerland

*Fraunhofer-Institut für Physikalische Messtechnik
Heidenhofstr. 8, D-7800 Freiburg, Fed. Rep. of Germany

## ABSTRACT

Epitaxial layers of narrow gap PbTe and (Pb,Sn)Se have been grown on Si substrates, and used for the first time to fabricate intrinsic photovoltaic IR-sensors on Si for the 3-5μm and 8-12μm range. The narrow gap semiconductors were grown on the $BaF_2$ side of a graded $(Ca,Ba)F_2$ buffer film which served to overcome the large lattice mismatch (up to 19%) to the Si. The backside illuminated IR-devices revealed resistance area products at 87K of up to $4\Omega cm^2$ for PbTe (cut -off wavelength 5.8μm), and up to $0.5\Omega cm^2$ for (Pb,Sn)Se with 9.7μm cut-off. These values come close to or exceed the photon noise limit (for 295K background radiation, 180° FOV, 50% quantum efficiency). The results open up the possibility to construct large monolithic IR-FPA's (focal plane arrays) with IR-sensors in the narrow gap semiconductor and signal processing in the Si.

## INTRODUCTION

In this work, we present first realisations of photovoltaic IR-sensors for the 3-5μm and 8-12μm atmospheric transmission window fabricated in a heteroepitaxial narrow gap semiconductor layer grown on Si. Although still far from being optimised, the technique appears to be suited for monolithic narrow gap semiconductor on silicon IR-FPA's for thermal imaging applications. Such monolithic FPA's would be much simpler to construct than the present hybrid bump-bonded HgCdTe/Si combinations.They would circumvent the high number of hybrid interconnects needed between each sensor and Si signal processing circuitry which complicates fabrication procedures especially for large two-dimensional staring arrays.

Narrow gap PbTe and (Pb,Sn)Se and a graded $(Ca,Ba)F_2$ buffer layer were used for the present work. These combinations were chosen because

a) Epitaxial IV-VI (Pb,Sn)Se, (Pb,Sn)Te and Pb(S,Se) narrow gap semiconductors can be grown in device quality on bulk $BaF_2$(111) faces by MBE (molecular beam epitaxy) or HWE (hot wall epitaxy). Background noise limited photovoltaic IR-detectors have been fabricated in such layers [1]. They are compositionally tunable covering the full range for thermal imaging applications (Fig.1).

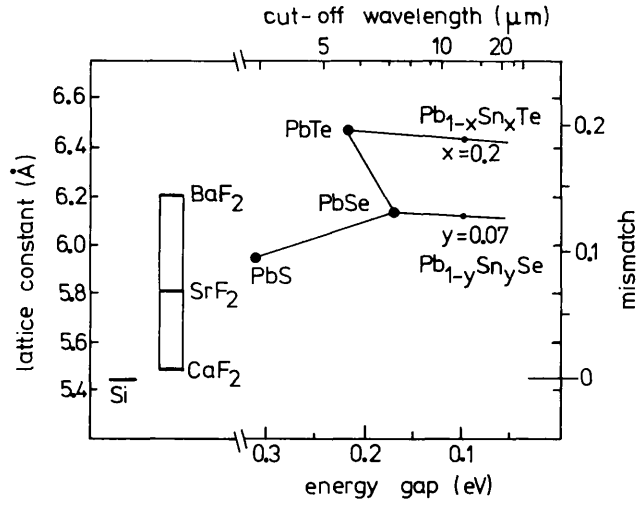


Figure 1 Epitaxial Si / IIa-fluorides / IV-VI narrow gap semiconductors: lattice constants and band gap values.

b) Group IIa fluorides $CaF_2$, $SrF_2$, $BaF_2$ and mixtures thereoff find increasing interest as epitaxial insulators that can be grown by rather simple MBE-procedures on most semiconductors. Examples are $CaF_2$ on Si [2], $(Ca,Sr)F_2$ on GaAs [3], $SrF_2$ on InP [4], or $BaF_2$ on PbSe [5]. In some cases, a second semiconductor layer was grown on top of these structures to form e.g. Si/$CaF_2$/Si with a MOS transistor in the top Si layer [6], GaAs/$(Ca,Sr)F_2$/GaAs [3], or PbSe/$BaF_2$/PbSe [7] with integrated IR-sensors.

c) In a previous study [8], we prepared epitaxial Si(111)/$(Ca,Ba)F_2$/PbSe structures with the buffer layer consisting of near lattice matched $CaF_2$ at the Si interface (mismatch 0.6% at 300K), and of $BaF_2$ with 14% increased lattice constant at the PbSe



CH2252-5/85/0000-0121 $1.00 © 1985 IEEE

interface. N-type PbSe top layers grown in this way were of a high quality. P-type layers showed some blistering due to Se interactions (probably Se which had diffused through the buffer and caused localised interactions at the Si surface), but it was possible to fabricate first IR-sensitive Schottky diodes in these layers. It is the purpose of the present work to show that the technique is not limited to PbSe. Using PbTe or (Pb,Sn)Se instead of PbSe, the sensitivity range can be tailored to the atmospheric transmission windows for practical applications.

## EXPERIMENTAL

The graded $(Ca,Ba)F_2$ layers were grown on Si(111) wafers by MBE at background pressures in the $10^{-8}$mbar range during deposition. $CaF_2$ and $BaF_2$ were evaporated from two independent Ta or graphite crucibles. After a substrate anneal of up to 850°C, a thin (1-10nm) layer $CaF_2$ was deposited at 700°C, followed by a near abrupt transition to $BaF_2$. In order to reduce mechanical strain because of the higher thermal expansion of the fluorides compared to Si, the substrate temperature was then lowered to 350°C and deposition of pure $BaF_2$ was continued up to about 200nm thickness.

Interference contrast microscopy showed crackfree, nearly structureless surfaces for the better layers except for a few occasional faults. Secondary electron (SEM) micrographs revealed small triangular hillocks in the sub micron range with resemblance to epitaxial $CaF_2$ on Si(111) surfaces [2].

Rutherford backscattering ion channeling studies with 2 MEV $He^+$ ions showed values $\chi_{min}$ of the backscattering yield of the Ba-signal below the surface peak (=yield ratio in the crystallographically oriented to random directions) down to 3.3% in the <111>-, and 2.6% in the <110>-direction [8]. Such low values are indicative of excellent crystallographic qualities of the layers, although they possibly may contain a rather large number of dislocations [2]. As checked with RBS channeling, X-ray diffraction and electron channeling, the layers were of type B orientation compared to the Si substrate, i.e. the fluorite lattice is rotated 180° around the <111> surface normal (twinned orientation).

PbTe layers were then deposited in a separate HWE furnace at 400°C. As p-type layers with concentrations in the low $10^{17}$ $cm^{-3}$ range are required for our device fabrication schedule as described below, additional Te was deposited simultaneously for tuning the carrier concentration to p-type. Contrary to the case of PbSe growth, this was possible without problems, i.e. no degradations (blisters due to chalcogen reactions) were observed when the chalcogen pressure in the HWE apparatus was increased. As grown layers showed essentially bulk Hall mobilities, i.e. ∿1000 and 30000$cm^2$/Vsec at 300K and 77K, respectively, with the typical $T^{-5/2}$ increase with decreasing temperature T, and saturated above $10^5 cm^2$/Vsec below 20K.

$Pb_{0.96}Sn_{0.04}Se$ was grown up to a few µm thickness on top of the $Si/(Ca,Ba)F_2$ structures by MBE at 375°C. MBE instead of HWE was used because MBE with separate PbSe- and SnSe-effusion cells allows a precise control of the Pb/Sn ratio which determines the band gap. An additional Se source was used to obtain p-type layers. In order to prevent blistering of the layers due to Se-vapor interactions, the Se source was shut off during the first part of growth. Hall mobilities of these layers (and of layers grown on bulk $BaF_2$ for reference purposes) were about a factor 3 lower than for PbTe or PbSe grown by HWE. As it is well known that high mobility PbTe and PbSnSe (on bulk $BaF_2$) can be obtained by MBE as well as by HWE [1], we attribute these lower values to the unoptimised growth procedure of our few layers prepared with the MBE apparatus at the Fraunhoferinstitut at Freiburg which is primarily used for highly doped IV-VI narrow gap materials for IR-laser applications. However, a very high Hall mobility is not necessarily a prerequisite for device fabrication [1]; at the present state of development of our IR-devices, we do not believe that this lower Hall mobility is the limiting factor concerning performance.

IR-sensitive Schottkydiodes were prepared by vacuum deposition of a dot of Pb for the blocking-, and of Pt for the ohmic contact through hard masks. A layer of polycrystalline $BaF_2$ was used to define the active area and for contact insulation [1,7]. This technique is well established and yields backside illuminated devices with typical reflection loss limited quantum efficiencies of about 50% without antireflection coating.

## RESULTS

The structures withstanded repeated cooling down to 10K and heating up to 150°C without more change in electrical properties than usually encountered in layers grown on bulk $BaF_2$. The different thermal expansion coefficients of Si ($2.6 \cdot 10^{-6}$/K) and of the IIa-fluorides and IV-VI semiconductors (both $\sim 2 \cdot 10^{-5}$/K) are therefore not detrimental to the rather thin (few µm range) layers used in this work. Smooth, mirror like surfaces were maintained and no cracks were detectable. Areas up to $5*8 mm^2$ have been grown without problems of adherence as long as no or only minor blistering due to Se-reactions mentioned above occured. However, smaller areas will possibly be advantageous because of reduced mechanical strains caused by temperature changes.

Fig. 2 and 3 show the I-V characteristics and spectral response at 87K of a PbTe and a $Pb_{0.96}Sn_{0.04}Se$ Schottky diode on $(Ca,Ba)F_2/Si$ substrates. The measured cut-off wavelengths are ∿5.8µm and 9.7µm,

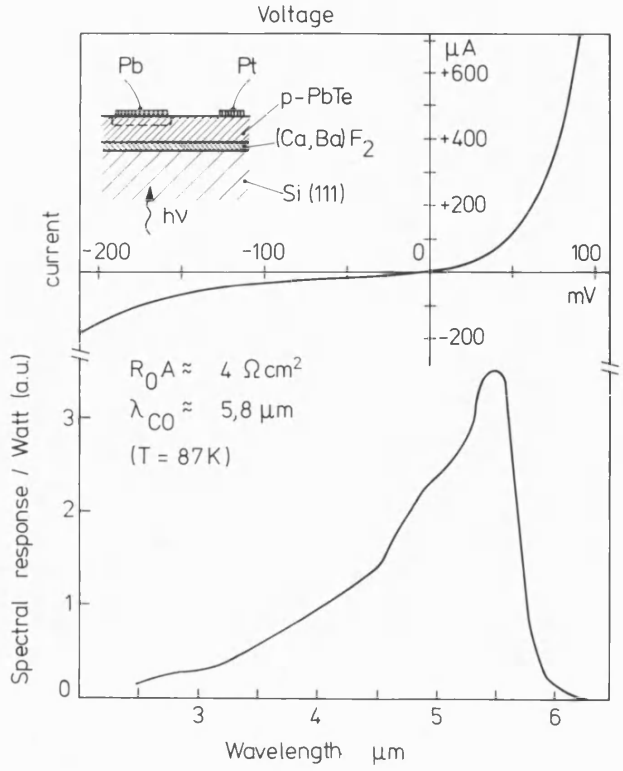


Figure 2 I-V characteristics and spectral response of a backside illuminated heteroepitaxial PbTe on $(Ca,Ba)F_2/Si$ photodiode.

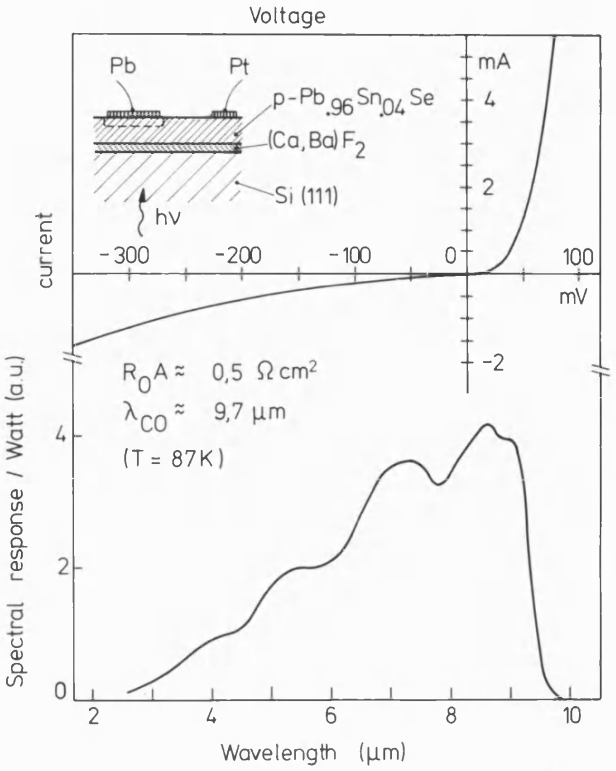


Figure 3 I-V characteristics and spectral response of a backside illuminated heteroepitaxial $Pb_{0.96}Sn_{0.04}Se$ on $(Ca,Ba)F_2/Si$ photodiode.

respectively, at that temperature. The spectral response shows the expected behaviour of a near ideal photovoltaic sensor, but with the response modulated due to interference effects. Resistance area products at zero bias $R_0A$ (which are proportional to the square root of the detectivities $D^*$) were up to $4\Omega cm^2$ for PbTe and up to $0.5\Omega cm^2$ for $Pb_{0.96}Sn_{0.04}Se$ photodiodes. As shown in Fig.4, these $R_0A$ products lie near or above the calculated values at which the photon background noise for 295K radiation and 180° field of view (FOV) is equal to the junction noise. The $R_0A$ obtained earlier for a PbSe diode on $(Ca,Ba)F_2/Si$ substrates with some blisters extending through the active area [8] is also included in this figure for comparison.

Although the present sensors were obtained using growth and fabrication procedures which were rather crude and far from being optimised, useful detectivities for terrestrial applications have already been obtained. A large potential for improvement seems possible with a better understanding and optimisation of the numerous technology and device parameters and by using more elaborate techniques for device fabrication, e.g. pn-

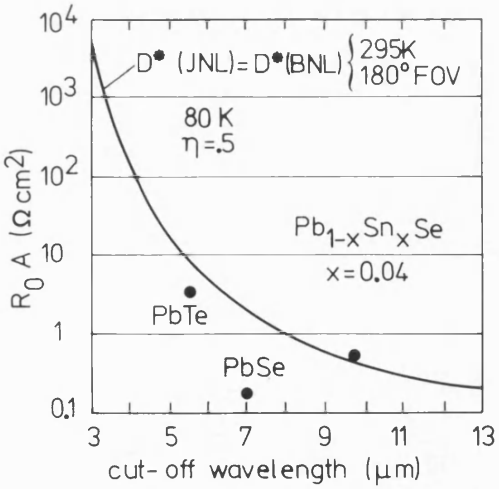


Figure 4 Points: Experimental resistance area products $R_0A$ of IV-VI narrow gap IR-photodiodes on $(Ca,Ba)F_2/Si$. Solid line: calculated $R_0A$ at which the background noise limit (for 295K, 180° FOV) is equal to the junction noise limit with junction at 80K and 50% quantum efficiency (from Ref.1)

junctions formed by diffusion or ion implantation instead of Schottky diodes which are very sensitive to the surface structures.

## CONCLUSIONS

High quality epitaxial IV-VI narrow gap semiconductor layers have been grown onto Si substrates by MBE or HWE using composition graded (Ca,Ba)$F_2$ buffer films to overcome the large lattice mismatch (up to 19%). Near background noise limited photovoltaic IR-devices for terrestrial thermal imaging applications have been demonstrated in these layers for PbTe with 5.8μm cut-off wavelength and for $Pb_{0.96}Sn_{0.04}Se$ with 9.7μm cut-off at 87K. Other compositions covering the range from below 3μm to above 15μm may be used, too. These first results clearly demonstrate the applicability of this rather simple technique to large monolithic IR-FPA's. The narrow gap IV-VI semiconductor layer may contain a line or area array of photovoltaic intrinsic IR-sensors and the Si may be used for signal multiplexing and amplification.

The graded (Ca,Ba)$F_2$ layers can be prepared with good quality. They may be applied as graded epitaxial insulator- and buffer- films in stacks of different non lattice matched heteroepitaxial monolithic semiconductors. As high quality mixed $XF_2$ (X=Ca, Sr, Ba and mixtures thereoff) crystals have already been prepared, lattice constants between 0.54 and 0.62nm may be tailored using a layer within the completely miscible $CaF_2$-$SrF_2$-$BaF_2$ sequence.

Acknowledgments: The authors would like to thank Prof.H.Melchior, ETH Zürich for his interest and support of the present work, and Dr.H.Preier, IPM Freiburg for his permission to use the Institute MBE system.

## REFERENCES

[1] H.Holloway,"Thin film IV-VI semiconductor photodiodes", Physics of Thin Films 11, 1980, pp. 105-203.

[2] L.J.Schowalter, R.W.Fathauer et.al., "Epitaxial growth of $CaF_2$ on Si", J.Appl.Phys.58, 1985, pp.302-308.

[3] S.Siskos, C.Fontaine, A.Munoz-Yague, "GaAs/(Ca,Sr)$F_2$/GaAs lattice-matched structures grown by molecular beam epitaxy", Appl.Phys. Lett. 44, 1984, pp.1146-1148.

[4] C.W.Tu, S.R.Forrest, W.D.Johnston Jr., "Epitaxial InP/fluoride/InP(001) double heterostructures grown by molecular beam epitaxy", Appl. Phys.Lett.43, 1983, pp.569-571.

[5] H.Zogg, W.Vogt, H.Melchior, "Epitaxial growth of $BaF_2$ films onto PbSe and electronic properties of the interface", Appl.Phys.Lett. 45 (3),), 1984, pp.286-288.

[6] T.Asano, Y.Kuriyama, H.Ishiwara, "Fabrication of MOSFETs in Si/$CaF_2$/Si heteroexpitaxial structures", Electron.Lett.21, 1985, pp.386-38787.

[7] W.Vogt, H.Zogg, H.Melchior, "Preparation and properties of epitaxial PbSe/$BaF_2$/PbSe structures", Infrared Phys.25 (4), 1985, pp.611-614.4.

[8] H.Zogg, M.Hüppi, "Growth of high quality epitaxial PbSe onto Si using a (Ca,Ba)$F_2$ buffer layer", Appl.Phys.Lett.47 (2), 1985, pp.133-13535.

PUBLICATION F)

# 77 K cw operation of distributed Bragg reflector $Pb_{1-x}Sn_xSe$/$Pb_{1-x-y}Eu_ySn_xSe$ diode lasers

Y. Shani and A. Katzir
*School of Physics and Astronomy, Tel Aviv University, Tel Aviv 69978, Israel*

K.-H. Bachem, P. Norton, M. Tacke, and H. M. Preier
*Fraunhofer-Institut für Physikalische Messtechnik, Heidenhofstrasse 8, D-7800 Freiburg, Federal Republic of Germany*

(Received 14 January 1986; accepted for publication 11 March 1986)

Distributed Bragg reflector $Pb_{1-x}Sn_xSe/Pb_{1-x-y}Eu_ySn_xSe$ double heterostructure stripe geometry diode lasers were fabricated using molecular beam epitaxy. We observed cw single mode operation between the heat-sink temperatures 66 and 81 K at $\lambda \approx 7.8\,\mu$m with an average tuning rate of 0.8 $cm^{-1}$/K. Single mode continuous tuning over a relatively wide range of 6 $cm^{-1}$, with an average tuning rate of 0.026 $cm^{-1}$/mA, was obtained at 77 K.

Lead salt lasers are commonly used as tunable radiation sources for ultrahigh resolution spectroscopy and infrared heterodyne detection. Lasers for these applications should fulfill the following requirements for optimum performance: emission in a single mode with wide continuous tuning and high power, a small wavelength dependence on temperature or current fluctuations, and cw operation of the laser at temperatures $T > 77$ K.

These are not obtained simultaneously in a standard, Fabry–Perot (FP) laser. Distributed feedback (DFB) lasers and distributed Bragg reflector (DBR) lasers combined with laterally confined double heterostructures are suitable devices satisfying these requirements.

DFB and DBR PbSnTe lasers had been reported before, but they were not operated cw at $T > 77$ K.[1–5] In addition, the only lasers which operated cw ($T < 50$ K)[2] did not have a "clean" single mode spectrum. Here cw operation of a corrugated lead salt laser at 77 K is reported for the first time.

The structure of this laser is shown in Fig. 1. The layers were grown on a $p$-type PbSe ($p = 1.15 \times 10^{19}$ $cm^{-3}$) substrate by molecular beam epitaxy (MBE). At first a 3-$\mu$m-thick $p$-type layer of $Pb_{1-x-y}Eu_ySn_xSe$ ($x = 1.4\%$, $y = 0.8\%$) doped with Ag was deposited. Then a 1-$\mu$m-thick $p$-type $Pb_{1-x}Sn_xSe$ ($x = 1.4\%$) active layer was deposited, followed by a 2-$\mu$m-thick $n$-type $Pb_{1-x-y}Eu_ySn_xSe$ ($x = 1.4\%, y = 0.8\%$) (doped with Bi) upper cladding layer. The lattice mismatch of these layers should be quite small due to the fact that the lattice constant of EuSe is only $\sim 1\%$ larger than that of PbSe, and thus Eu admixture hardly changes the lattice constant. Using conventional photolithographic techniques, 1-mm-wide stripes of baked photoresist were aligned along the (100) direction. A layer of 0.55 $\mu$m thickness was removed from the top cladding in the region between the photoresist stripes by using $Ar^+$ ion beam etching. Periodic corrugations were now fabricated in these etched regions, using first a holographic photolithography step and then a second ion beam etching step.[6]

The grating grooves had trapezoidal shape, and were parallel to the photoresist stripes. The period ($\Lambda$) and the depth of the corrugation were 0.80 and 0.55 $\mu$m respectively. The grating period was chosen to provide first order Bragg reflection. All the photoresist was then removed by plasma etching, and the corrugated regions were covered with baked photoresist as an isolator. The last process steps were the fabrication of 25-$\mu$m-wide window stripes perpendicular to the corrugation grooves and the application of metal contacts. By cleaving, lasers of 370 $\mu$m active length, 650 $\mu$m corrugated section length, and 400 $\mu$m width were fabricated. The lasers were mounted in standard packages with the $n$ side facing an indium plated copper stud.

The lasers were tested at low temperatures using a closed cycle helium refrigerator. Laser emission was observed from the cleaved mirror (opposite to the Bragg reflector, see Fig. 1) under pulsed conditions (6-$\mu$s pulses at 1-kHz repetition rate) and cw conditions. The total resistance of the lasers was about 60 m $\Omega$ at 80 K. Spectra of the laser radiation were recorded with a monochromator. The absolute experimental error of the wavelength is less than 1%.

One of the lasers, whose characteristics are being reported here, operated as an ordinary FP multimode laser for heat-sink temperatures up to 130 K in the cw mode and up to 180 K in the pulse mode. In a certain temperature range around 77 K it worked as a DBR laser; in the range 66–81 K in the cw mode and in the range 75–90 K in the pulse mode. At the lower operating temperature, DBR cw lasing was obtained for currents up to three times the threshold current, and more than five times the threshold current in the pulsed mode. The threshold current was about twice that obtained for regular FP lasers which were fabricated from the same wafer (having the same length), except for the DBR operating region where it was only 40% higher. At 77 K the threshold current density was 4 $kA/cm^2$ at both cw and pulse operation. In Fig. 2 a spectrum of the cw DBR region is shown for different temperatures and injection currents. The intensity scales of the individual curves were chosen so that the peak intensities look comparable. The maximum power of 0.2 mW was obtained at 7.82 $\mu$m, 700 mA, and 70 K. The FP mode intensities outside the DBR operation range are smaller by an order of magnitude. The temperature tuning rate was between 0.6 and 1.0 $cm^{-1}$/K, while the tuning rate of a conventional multimode FP laser is about 4.5 $cm^{-1}$/K. The spectrum usually contains only one mode and sometimes two modes for a spectral range of some 20 $cm^{-1}$. Mode hopping was also observed.

 0003-6951/86/181178-03$01.00  

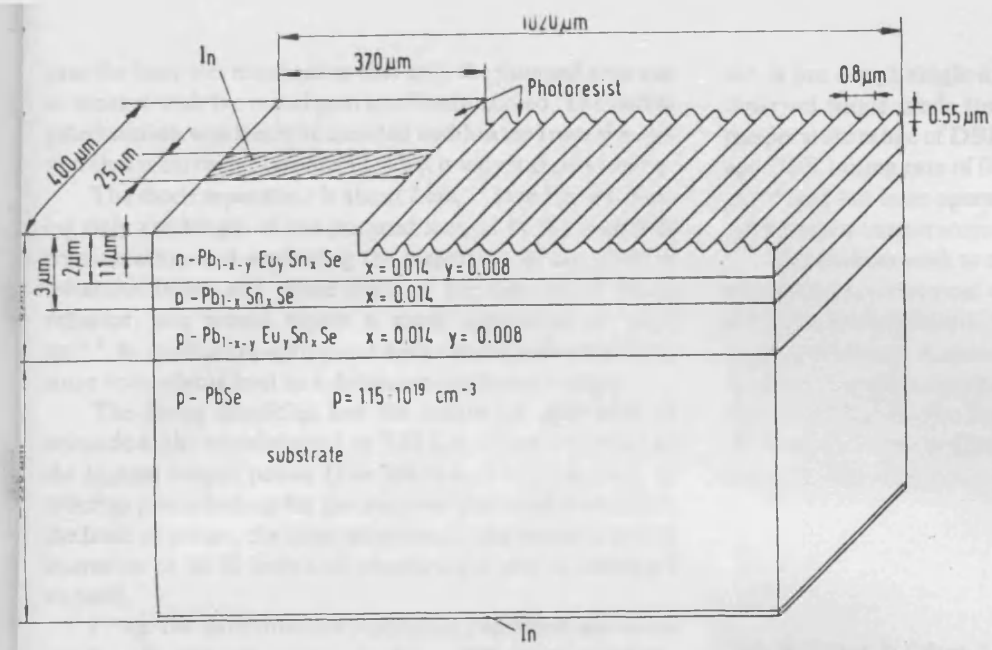


FIG. 1. Schematic description of the distributed Bragg reflector (DBR) laser.

The modes are very "clean" and measurements with a spectral resolution of 0.3 $cm^{-1}$ revealed no further lateral mode structures, and a ratio of more than 200:1 between maximum peak power and noise was obtained. A more detailed spectrum of the laser at 77 K is shown in Fig. 3. Here a mode hopping between 440 and 450 mA can be clearly observed. From 450 mA (7.841 $\mu$m) to 680 mA (7.804 $\mu$m) the laser operated in one single mode over a continuous tuning range of 6 $cm^{-1}$. At 77 K, a maximum power of about 0.15 mW was obtained at a current of 650 mA. At 680 mA a hysteresis of the mode hopping behavior was observed. While increasing the current, the mode hopping occurred between 680 mA (7.804 $\mu$m) and 690 mA (7.790 $\mu$m); but while decreasing the current, the mode hopping occurred between 680 mA (7.790 $\mu$m) and 670 mA (7.806 $\mu$m).

Analyzing the tuning characteristics as a function of current in the DBR range, we obtain a mode tuning rate of $\sim$0.026 $cm^{-1}$/mA, while the overall tuning rate is $\sim$0.035 $cm^{-1}$/mA. In FP lasers one observes a comparable mode tuning and an overall tuning of $\sim$0.1 $cm^{-1}$/mA, which is determined by the gain tuning.

The mode hopping is due to the difference between the overall tuning rate of the Bragg condition, which is determined by $dN_{\text{eff},c}/dI$, and the tuning rate of a single mode, determined by $dN_{\text{eff},g}/dI$, where $N_{\text{eff},c}$ and $N_{\text{eff},g}$ are the effective refractive indices in the corrugated and the pumped regions, respectively, and $I$ is the current. These tuning rates differ less than the mode and gain tuning rates that determine the mode hopping characteristics of FP lasers. Hence we can expect a considerably larger single mode tuning range.

If the DBR section is kept at constant temperature, no tuning of the Bragg condition should be observed. In our

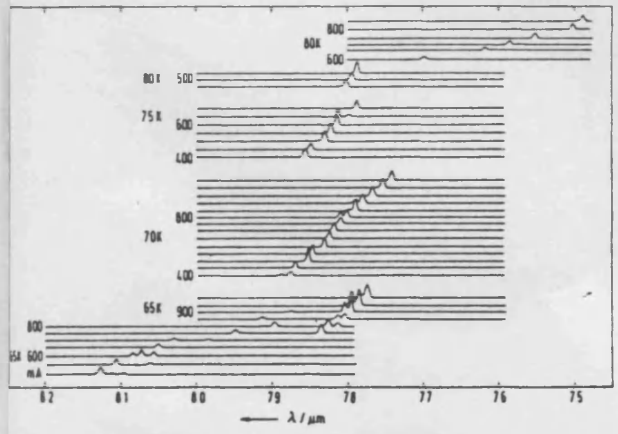


FIG. 2. DBR cw spectrum as a function of the temperature (5 K steps) and the injection current (50 mA steps). The intensity scale is different for each temperature and current measurement.

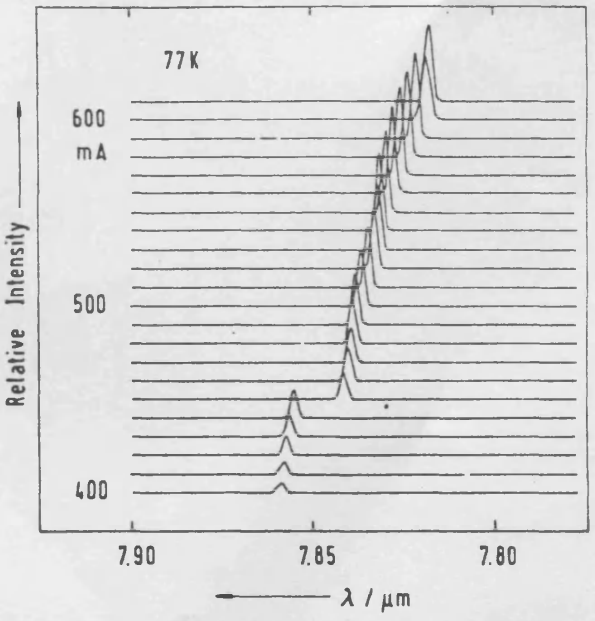


FIG. 3. Emission spectrum of a DBR laser, operated cw mode, as a function of the injection current (10 mA steps) at 77 K.

case the laser was mounted so that only the pumped area was in contact with the metal post and hence cooled. The corrugated section was freely suspended and heated from the section that is carrying the current. That is why it shows tuning.

The mode separation is about 2 $cm^{-1}$ (see Fig. 3). Taking only the length of the pumped section of the laser into consideration and neglecting the dispersion of the effective refractive index and phase shifts of the distributed Bragg reflector, one would expect a mode separation of $\sim 2.7$ $cm^{-1}$, in qualitative agreement with the experimental data, since both effects lead to a decreased mode separation.

The Bragg condition and the maximum gain seem to coincide at the wavelength $\lambda = 7.82\,\mu m$, where we observed the highest output power ($I = 700$ mA, $T = 70$ K, cw). In order to give a feeling for the temperature conditions inside the laser structure, the same wavelength was found in pulsed operation at 86 K heat-sink temperature and at threshold current.

From the experimental resonance condition we calculate the effective refractive index $N_{eff,c}$ of the corrugated section. The value $N_{eff,c} = \lambda/2\Lambda = 4.89$ is reasonable for a $Pb_{1-x}Sn_xSe/Pb_{1-x-y}Eu_ySn_xSe$ waveguide. In order to verify this number, we used the published refractive index of $Pb_{1-x}Sn_xSe$.[7] The refractive index of $Pb_{1-x-y}Eu_ySn_xSe$ was calculated from Ref. 7 using the parameters of $Pb_{1-x}Sn_xSe$ except the energy gap. With the same set of data we derived $\kappa L \sim 1.5$, where $\kappa$ is the coupling coefficient and $L$ the length of the corrugated section.

In conclusion, we have described the fabrication and performance of a DBR $Pb_{1-x}Sn_xSe/Pb_{1-x-y}Eu_ySn_xSe$ laser. It has a high single mode output power of 0.2 mW. We observed single mode tuning ranges of up to 6 $cm^{-1}$. The temperature range of DBR operation was 15 K with an average DBR tuning rate of 0.8 $cm^{-1}/K$. This is the first corrugated lead salt laser operating cw at temperatures above liquid nitrogen temperature.

The authors wish to thank Dr. H. Böttner for contributions to the experimental work and Dr. Reli Rosman and Dr. E. Kapon for helpful discussions. Y. Shani wants to especially acknowledge E. Kapon for introducing him to this subject of research and his continued interest and advice. This work was supported by the German Ministry for Research and Technology in the project 13 N 5277. Support by the U. S.-Israel Binational Science Foundation is also acknowledged.

[1] J. N. Walpole, A. R. Calawa, S. R. Chinn, S. H. Groves, and T. H. Harman, Appl. Phys. Lett. 29, 307 (1976).
[2] J. N. Walpole, A. R. Calawa, S. R. Chinn, S. H. Groves, and T. H. Harman, Appl. Phys. Lett. 30, 524 (1977).
[3] H. H. Hsieh and C. G. Fonstad, IEEE J. Quantum Electron. QE-16, 1039 (1980).
[4] E. Kapon, A. Zussman, and A. Katzir, Appl. Phys. Lett. 44, 275 (1984).
[5] E. Kapon and A. Katzir, IEEE J. Quanum Electron. QE-21, 1947 (1985).
[6] The procedure is like that described in Refs. 4 and 5 except for the holographic setup which is similar to that described by D. V. Podlesnik, H. H. Gilgen, R. M. Osgood, Jr., and A. Sanchez, Appl. Phys. Lett. 43, 1083 (1983).
[7] Y. Shani, R. Rosman, and A. Katzir, IEEE J. Quantum Electron. QE-21, 51 (1985).

CONFERENCE G)

# $Pb_{1-x}Eu_xSe$ for IR device applications

P. Norton, K.H. Bachem*), M. Tacke

Fraunhofer-Institut fuer Physikalische Messtechnik
Heidenhofstrasse 8, D-7800 Freiburg, West Germany

## Abstract

$Pb_{1-x}Eu_xSe$ is a promising material for IR devices. The band gap becomes larger with the relative content of Europium. The preparation of $Pb_{1-x}Eu_xSe$ by molecular beam epitaxy and the properties of these layers will be described.

## Introduction

There are two main reasons, why $Pb_{1-x}Eu_xSe$ is a promising new material for IR devices. With increasing Europium content, the band gap of PbEuSe becomes rapidly larger. With 1.5 % Eu, the absorption edge is approximately 3400 $cm^{-1}$ at room temperature, compared to roughly 2300 $cm^{-1}$ for PbSe. Second, the lattice constant is hardly expected to change upon admixture of Europium, since the lattice mismatch of PbSe and EuSe is only about 2 %. Thus the PbEuSe system lends itself for the construction of heterostructures.

In this paper we shall first describe the growth of $Pb_{1-x}Eu_xSe$ by molecular beam epitaxy (MBE) and then discuss the electrical and optical material characteristics.

## Growth of $Pb_{1-x}Eu_xSe$ by MBE

$Pb_{1-x}Eu_xSe$ films have been grown in a MBE apparatus that had been specially designed for IV - VI compounds[1]. As substrates we use $BaF_2$ or PbSe. The conductivity data of samples grown on $BaF_2$ were superior for freshly cleaved slices as compared to additionally polished $BaF_2$ substrates. The growth temperature of 350 - 400 °C that is known for best results on PbSe layers was also used for $Pb_{1-x}Eu_xSe$ up to x = 20 %. As dopants both Silver and Bismuth were used for p-type and n-type material.

For growth of $Pb_{1-x}Eu_xSe$ layers, we use the constituent materials PbSe, Se, and Eu. Selenium has to be added in order to incorporate the Europium atoms on metal sites. Most layers have been grown with the selenium atom flux being about 12 % of the PbSe flux. For PbSe layers, this results in p-type material. If no selenium were added, PbSe layers would be n-type due to the elevated sample temperatures and the higher partial pressure of selenium as compared to lead. Using the 12 % selenium flux, $Pb_{1-x}Eu_xSe$ could be grown up to x = 5 %. Films with higher Europium concentration did not have monocrystalline appearance for this Se flux rate. In order to get to higher Europium concentrations, the selenium flux had to be increased. For the highest, x = 0.2 a selenium flux of 110 % of the Europium flux yielded good results.

Use of Europium requires good vaccuum conditions, since it reacts readily with oxygen. If our standard growth temperature is used, oxide layers are not visible, and the samples are stable when kept in the atmosphere. However, it is probably still advisable to finish a heterostructure by a thin PbSe cap layer for protection.

## Electrical Characteristics

Samples grown on $BaF_2$ were characterized by measurement of the Hall effect in Van der Pauw geometry. There was no large difference between samples of thickness 2 µm and 4 µm, provided the $BaF_2$ substrates were freshly cleaved. Thus the disturbed region adjacent to the interface is small. With polished substrates, the mobility of 2 µm thick samples was drastically reduced.

The 300 K carrier concentration of $Pb_{1-x}Eu_xSe$, grown nominally undoped, decreases nearly linearly with the Europium content from $2 \times 10^{17}$ $cm^{-3}$ for x = 0 to $10^{16}$ $cm^{-3}$ for x = 0.025. This material is p-type, probably because it is selenium rich. At 77 K, the carrier concentration is constant and equal to about $10^{17}$ $cm^{-3}$ up to x = 0.02, and then decreases rapidly, so that at x = 0.025 the concentration is only approximately $7 \times 10^{15}$ $cm^{-3}$. The 77 K carrier concentration is larger than that at 300 K in the region x = 0.1 to x = 0.23.

---

*) present address: Fraunhofer-Institut fuer Angewandte Festkörperphysik, Eckerstrasse 4, 7800 Freiburg, West Germany

The same qualitative behaviour is found in samples doped with silver at a dopant flux of 0,07 % of the PbSe flux. However, for x = 0 the concentration is approximately 6 $10^{18}$ $cm^{-3}$ for 77 K and 300 K. We qualitatively explain this behaviour with a level near the valence band edge that resonates with the band edge or gets degenerate with the band. The relative position depends on the band gap size and hence varies with Europium concentration and temperature.

n type material behaves different in that its carrier concentration remains nearly unchanged at 7 $10^{18}$ $cm^{-3}$ for x = 0 to x = 0.025 and 77 K as well as 300 K. The bismuth doping flux was 0.05 % of the PbSe flux for the set of samples used for these measurements. This result supports the assumption that the a typical p-type results can be explained by a specific constellation of an acceptor level.

The mobilities of Bi, Ag and undoped samples differ at a given temperature and Europium concentration by about ±20 %. They drop at 300 K by about 50 % when x is raised to 0.025, whereas at 77 K the mobility is nearly reduced by an order of magnitude in the x = 0.025 material.

With the Selenium flux of 12 %, the carrier concentration of Silver doped material saturates at a silver flux of about 0.04 %. Any excess silver is probably incorporated upon interstitial sites and does not seem to influence the electrical properties. Bismuth doped material showed an increasing carrier concentration with increasing dopant flux up to the highest flux of 0.2 %, where a carrier concentration of 2 $10^{19}$ $cm^{-3}$ was found at 300 K and 77 K. The mobility of the free carriers of p- and n-type samples is nearly independent of the flux rates that we used, 0.05 % to 0.2 % for Bismuth and 0.07 % to 0.24 % for silver.

## Optical Characteristics

Transmission measurements of the $Pb_{1-x}Eu_xSe$ samples showed that the absorption edge shifts steadily with increasing Europium content. The position of the absorption edge as well as its rate of change depend on the dopant and its concentration. We observed tuning rates between 900 $cm^{-1}$ and 600 $cm^{-1}$ per % Europium.

The transmission interferences that were observed at energies below the absorption edge indicated that the $Pb_{1-x}Eu_xSe$ has good optical properties for 0 x 0.025. This result was confirmed by the excellent performance of diode lasers kthat incorporated PbEuSe as cladding layers. The optical data of these lasers were consistent with a refractive index variation that is only due to the increasing band gap. This leads to a reduced refractive index at increased Europium content, which is highly desirable for cladding layers of the active region of lasers.

## Discussion

In view of the optical and electrical properties as described above, $Pb_{1-x}Eu_xSe$ lends itself as amterial for infrared devices. Grown by MBE, it allows the fabrication of advanced heterostructure devices, as were already described e. g. for lead salt detectors[2]. A major advantage of this system is the small lattice mismatch between PbSe and EuSe that might render the use of quarternery alloys for lattice matching unnecessary. SIMS data show, that the MBE grown Europium concentration variation within a heterostructure is stable, so that fine structures like superlattices are feasible[3].

First experiments for the determination of the band offsets of p-PbSe/$Pb_{1-x}Eu_xSe$ heterostructures indicate that the valence band discontinuity is small[4]. Thus one should be able to construct heterostructures with $Pb_{1-x}Eu_xSe$ of high Europium content as transparent conductive layer on top of a $Pb_{1-x}Eu_xSe$ structure with x matched to the desired optical performance. Due to a small valence band offset such a structure would not induce any undesired barrier in photovoltaic devices.

The admixture of Europium to PbSe for increasing the bandgap with a small change in the lattice constant can be analogously transferred to $Pb_{1-y}Sn_ySe$. We have grown corresponding quarternary $Pb_{1-x-y}Eu_xSn_ySe$ with success. Heterostructure lasers with a band tailoring by modification of only the Europium content of this material show good results. Thus the long-wave PbSe limit of the $Pb_{1-x}Eu_xSe$ system can be reduced, if one seeks for heterostructures for IR devices operating near e. g. 10 µm wavelength.

## Acknowledgements

This work was supported by the German Ministry for Research and Technology in the project 13 N 5277. The authors thank H.M. Preier and H. Böttner for helpful discussions and cooperation.

## References

1. K.H. Bachem, P. Norton, and H. Preier, "MBE - A Tool for Fabricating IV - VI Diode Lasers, in: Two-Dimensional Systems, Heterostructures, and Superlattices; G. Bauer, F. Kuchar, H. Heinrich, ed., Springer, 1984.
2. H. Holloway, J.N. Walpole, "MBE Techniques for IV - VI optoelectronics devices" Prog. Crystal Growth Charact. 1979, Vol. 2, B.R. Pamplin, ed., Pergamon Press Ltd.
3. M. Maier, private communication.
4. A.A. Eisenbeiss, H. Heinrich, private communication.